3-23-2018

Design, Buildup, and Testing of a Radial Rotating Detonation Engine for a Compact Auxiliary Power Unit

Riley Huff

Design, Buildup, and Testing of a Radial Rotating Detonation Engine for a Compact Auxiliary Power Unit

THESIS

Riley Huff, Second Lieutenant, USAF

AFIT-ENY-MS-18-M-266

DEPARTMENT OF THE AIR FORCE
AIR UNIVERSITY

AIR FORCE INSTITUTE OF TECHNOLOGY

Wright-Patterson Air Force Base, Ohio

AFIT-ENY-MS-18-M-266

DESIGN, BUILDUP, AND TESTING OF A RADIAL ROTATING DETONATION ENGINE FOR A COMPACT AUXILIARY POWER UNIT

THESIS

Presented to the Faculty

Department of Aeronautics and Astronautics

Graduate School of Engineering and Management

Air Force Institute of Technology

Air University

Air Education and Training Command

in Partial Fulfillment of the Requirements for the

Degree of Master of Science in Aeronautical Engineering

Riley Huff, B.S.

Second Lieutenant, USAF

March 2, 2018

AFIT-ENY-MS-18-M-266

DESIGN, BUILDUP, AND TESTING OF A RADIAL ROTATING DETONATION ENGINE FOR A COMPACT AUXILIARY POWER UNIT

THESIS

Riley Huff, B.S.
Second Lieutenant, USAF

Committee Membership:

Dr. Marc D. Polanka
Chair

Dr. Frederick R. Schauer
Member

Lt Col James L. Rutledge, PhD
Member

Maj Levi M. Thomas, PhD
Member

Abstract

Recently there has been a need for rapid response power generators on aircraft of all sizes. Not only do the current power generators consume a large portion of the aircrafts usable volume, they are also extremely heavy for the amount of power that they can produce; therefore, a need for compact, lightweight Auxiliary Power Units (APU) with high power density has arisen. A novel solution to this problem comes in the form of coupling a Rotating Detonation Engine (RDE) with a turbine generator. RDEs operate on an approximately constant volume detonation process, similar to that of the Humphrey Cycle, which has the potential for more power extraction over conventional gas turbine combustors. Previous work on RDE turbine integration has shown promise, but a modification leading to a more compact form with higher power density would be beneficial. Therefore, a new type of RDE referred to as the Radial Rotating Detonation Engine (RRDE) has been developed. This design is based on a disk-shaped device within which reactants flow from the outer radius, detonate, and then exit the inner radius.

The goal of this project was to design a modular RRDE to use as a testbed for evaluating this novel layout as a detonation based combustor. While radial flow RDE have been attempted elsewhere, this project marks the first instance of this layout being used for power extraction. In the RRDE used for this project the flow is routed into a compact centrifugal turbocharger to extract the power. Next, the operability of the RRDE was characterized to determine the limits in RRDE operation and areas for potential improvement. This testing included varying the height of the detonation channel, the nozzle area ratio of the RRDE, the mass flux through the RRDE, and the equivalence ratio at which the device was operated. These results showed a nozzle

area ratio of 0.6 provided an optimal point of operation for the RRDE. The results also showed at higher mass fluxes and lower equivalence ratios, the RRDE would transition into higher wave mode operation. Overall, the operability mirrored that of conventional RDEs with similar injection schemes, with the main difference being the location of the detonation wave had significantly more variation due to layout of the RRDE.

Finally, the Radial RDE was coupled with the turbocharger turbine and power and efficiency measurements were accomplished. The RRDE APU configuration was tested at a range of nozzle guide vane flow angles in an attempt to condition the flow prior to the turbine. As an APU, the RRDE showed significant increases in power density, up to $10x$, over conventional gas turbine based APUs. Though room exist for improvement in this device, the potential for a detonation engine based APU was shown for the first time. This development opens up a new opportunity for the Air Force to rapidly generate power with a high power density APU for use in various applications such as airborne directed energy weapons.

Acknowledgements

I would like to first thank AFIT for allowing me to conduct this research and AFRL for sponsoring the project. I want to thank everyone in the D-Bay lab for welcoming me into their area of expertise and teaching me everything they know. A special thanks to Matt Fotia, John Hoke, Andy Naples, and 1LT Micheal McClearn for the help with the design process and answering all of my questions along the way. I would also like to thank Dr. Fred Schauer for allowing a fresh 2LT gain valuable experience in your lab. I would like to thank my advisor for the continuous improvement of my skills as a student, researcher, writer, and presenter. I would like to thanks my roommates for their support along the way and having people to talk to about things other than my thesis. Finally, I would like to thank my family: my brother for keeping me grounded through this process as he pursues his academic dreams, my grandma who always called at just the right time, and my parents for being the reason I am the man I became and for the great example they set.

Riley Huff

Table of Contents

Page

List of Figures

Figure Page

List of Tables

List of Symbols

Symbol		Page
$\dot{m}_{corr}$	Corrected Mass Flow Rate	92
a	Speed of Sound	93
η_{th}	Thermal Efficiency	94
Q_{in}	Energy Input	94
C_D	Discharge Coefficient	98
A_o	Sonic Nozzle Orifice Area	98
P_t	Total Pressure	98
T_t	Total Temperature	98
R	Specific Gas Constant	98
r_c	Initial Channel Radius	98
h_c	Initial Channel Height	98
V_a	Wavespeed	115
V_{CJ}	Chapman-Jouguet Velocity	115
$\dot{W}_s$	Shaft Power	155
τ	Torque	155
$\dot{W}_{out}$	Power Output	165
V_{APU}	APU Volume	165
m_{APU}	APU Mass	165

List of Abbreviations

Abbreviation		Page
APU	Auxiliary Power Unit	1
GTE	Gas Turbine Engine	1
RDE	Rotating Detonation Engine	2
PGC	Pressure Gain Combustion	2
RRDE	Radial Rotating Detonation Engine	2
RIT	Radial Inflow Turbine	3
DERF	Detonation Engine Research Facility	7
CPC	Constant Pressure Combustor	9
PDE	Pulse Detonation Engine	10
FJ	Fickett-Jacob	12
ZND	Zeldovich, von Neumann, and Døring	12
CJ	Chapman-Jouguet	16
DDT	Deflagration to Detonation Transition	21
AFRL	Air Force Research Lab	24
WPAFB	Wright Patterson Air Force Base	24
NGV	Nozzle Guide Vane	36
CTAP	Capillary Tube Average Pressure	43
ITP	Infinite Tube Pressure	43
MAF	Mass Air Flow Sensor	78
FFT	Fast Fourier Transform	86
ICE	Internal Combustion Engine	95
BSFC	Brake Specific Fuel Consumption	95

DESIGN, BUILDUP, AND TESTING OF A RADIAL ROTATING DETONATION ENGINE FOR A COMPACT AUXILIARY POWER UNIT

I. Introduction

Aircraft today require an increasing amount of electrical energy to power everything from the aircraft's computer system to reading lights for passengers. This energy is typically created in one of two ways: pulling power directly off the main engines, or through the use of a stand alone Auxiliary Power Unit (APU). Using the main engines as the source for this energy has a direct reduction in the performance of the engine as the power generator is a parasitic loss added to the engine's shaft. Using an auxiliary power unit allows for the performance of the the main engines to be unaffected, provided the APU does not use bleed air from the main engine. Modern APUs are incredibly complex pieces of machinery that combine a conventional Gas Turbine Engine (GTE) with an electrical generator. However, these devices are bulky and heavy for the power they output.

In recent decades the United State Air Force has shown increased interest in high powered, airborne directed energy weapons. These devices require 10^3 - 10^6 W of power which is taxing on the aircraft's energy production. An example of this system is the YAL-1 Airborne Laser which was mounted to a modified Boeing 747. Operating a system like this for multiple laser fires places a heavy burden on the electrical power generation of the aircraft.

With an aircraft the size of the 747, additional APUs could be installed without a spatial issue; however, the Air Force also envisions a future where these airborne lasers would be used on fighter sized aircraft. This presents an issue with the power

generation for these smaller aircraft. First, harvesting this energy off the main engines will be detrimental to the performance of the aircraft, and second, there is little available space on a fighter aircraft for a high power APU to mount.

Another issue with conventional, gas turbine based APUs is the long start up times. These devices require on the order of minutes before they are ready and able to activate the generators and product energy. This means the laser would have to wait an extended period of time between shots, or the APU would need to be on constantly, which wastes fuel. With these airborne lasers, it would be beneficial to have an APU that can spool up and produce energy nearly instantly, but also not have to be continuously operated when it is not needed.

The reasons above created the need for a compact, power dense, rapid response APU. A possible solution to these concerns involves the coupling of Rotating Detonation Engine (RDE) to a turbine to create a compact APU. RDEs offer multiple benefits over conventional combustors, like the ones used in gas turbine based APUs. These benefits include shorter combustion lengths, instant power generation, and a more efficient method of turning chemical energy in the fuel into usable energy. These devices fall into the realm of Pressure Gain Combustion (PGC), which means the combustion products exit the combustor at a higher pressure than the reactants that enter.

This project will discuss the design, buildup, and testing of a novel Radial Rotating Detonation Engine (RRDE) for application as an detonation based APU. An RDE of this orientation has yet to be tested in the United States, and testing the efficacy of this device for power extraction has never been conducted. This effort was able to experimentally prove that a radial flow path RDE can establish and maintain a detonation. Furthermore, this project will discuss the operation of this new device in an attempt to determine an ideal operating condition for the APU. Finally, this

project will discuss the results of coupling the RRDE with a Radial Inflow Turbine (RIT) from a commercial turbocharger opening up a new possibility for a compact power source with rapid response for periodic power loads such as airborne directed energy weapons.

1.1 Rotating Detonation Engine APU

Rotating Detonation Engines are physically complex, yet mechanically simple devices that operate using continuously propagating detonation waves to combust a mixture of reactants. The detonation wave consist of a leading shock wave that provides the activation energy for the combustion process and combustion zone that provides the energy release to drive the leading shock wave. These devices conventionally feature an annular flow area where fresh reactants enter the channel on one end, are then combusted by the circumferentially running detonation wave, and then exit the channel at the other end, shown in Figure 1. With these devices, as long as fresh reactants are provided to the channel the detonation will continue to propagate. More detail on RDEs and their operation will be discussed in Section 2.2.2.

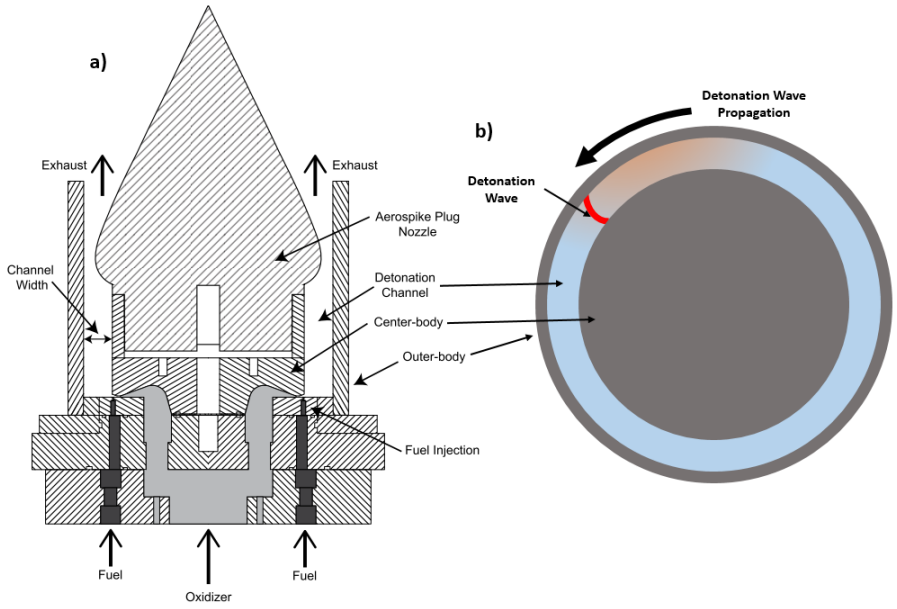

Figure 1. Rotating Detonation Engine Layout and Operating Scheme. (a) side view modified from [1] & (b) top view.

The design of a compact APU is centered around having a compact combustor, which a RDE provides, as well as a compact turbine generator. For this reason a RIT from a turbocharger was used for the power extraction portion of the APU. Radial turbines are rugged devices mostly used in the automotive field as turbochargers. These devices inlet hot gases in the radial direction and expand the products through the turbine and a 90° turn before ejecting them in the axial direction. The benefit of a radial turbine over an axial turbine include the reduced radius of the turbine and increase pressure ratio at which they operate. This means a single stage of radial turbine can replace multiple stages of axial turbine, which keeps the overall size more compact. They also operate more efficiently at lower flow rates and power outputs under roughly 5 kW. These were the reasons behind selecting a radial turbine for use in this project; however, mounting a radial turbine with a RDE created other issues.

Figure 2 shows two cases of the side effects of coupling a RIT to a conventional RDE. Because the flow path of a conventional RDE is mostly axial, the products

would either need to turn 90° before entering the turbine (a) or be ducted through a scroll before entering the turbine (b), a layout used by automotive turbochargers. If turning the flow inward were attempted a region of high heat load would occur, shown in red in (a). Ducting the flow would solve this problem; however, it would increase the size of the device, which would negatively impact the compactness of the APU. These results created the need for a new type of RDE, one in which the flow is radial instead of axial.

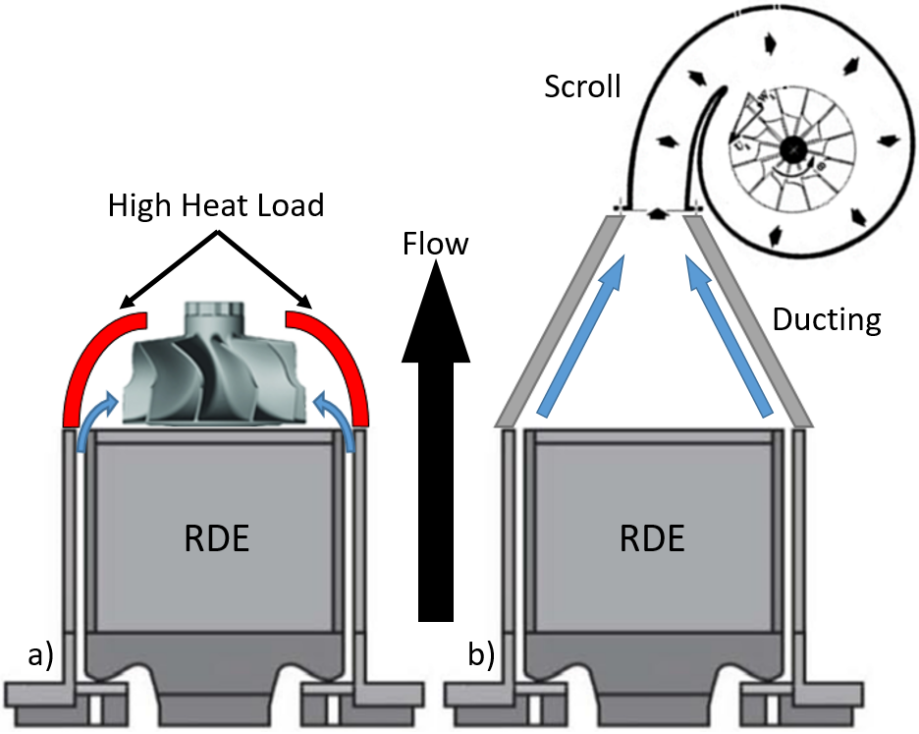

Figure 2. Conventional RDE with a Radial Inflow Turbine. (a) conventional RDE direct mount & (b) conventional RDE ducted mount

With a Radial RDE, the flow is injected, and remains, in the radial direction. This means the exit of the RRDE matched the desired flow direction of the turbine without need the 90° turning or the long ducting like with conventional RDEs. This leads to the possibility of the RRDE being a more feasible solution for a compact APU. The concern was that a design of this type had never been tested before in the United States. It was uncertain if this device would be able to detonate, and have

the detonation be sustained, let alone have an operability range which would enable the coupling of a turbine downstream.

An example of the flow path for a RRDE is shown in Figure 3, with a side view (a) and the top down view as if the top of the RRDE was removed and the channel was exposed (b). With this design, fresh reactants are supplied from the outer radius of the device. The detonation wave still propagates in the circumferential direction; however, with the RRDE, the detonation wave extends out in the radial direction instead of the axial direction. Like a conventional RDE, as long as there is constant supply of fresh reactants to the channel the detonation should continue to propagate. More detail on the functionality of this novel design will be discussed in Section 2.2.3, Section 2.3.3, and Section 3.2.

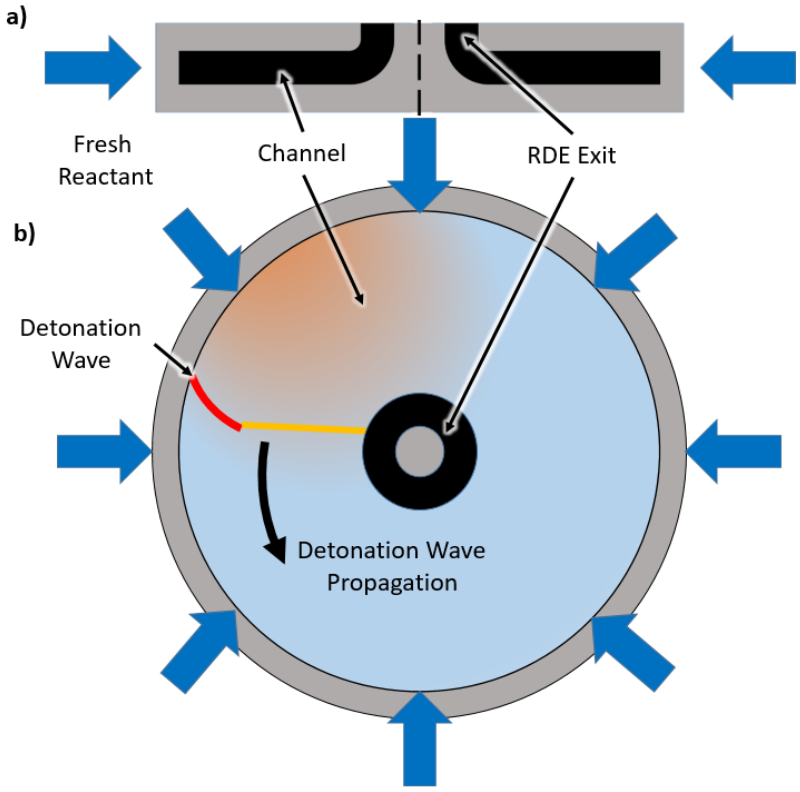

Figure 3. Radial RDE Layout and Operating Scheme. (a) side view & (b) top view.

1.2 Research Objectives and Methodology

There are three main objectives of this project. The first was to design a modular, hydrogen-air Radial RDE to initially verify this new layout would sustain a detonation wave and then to study the performance of this novel layout compared to conventional RDEs. This design process took the geometry of conventional RDEs as well as the turbocharger turbine and created a device that works as both a stand alone combustor and a compact APU. As part of this design process, flexibility was integrated into the RRDE in a manor that allows for testing of other geometries, other fuels, and other minor design changes without the need for a complete redesign.

To achieve this objective, a modular design was created that mirrored the injection scheme and some of the geometry of a conventional RDE operated at the Detonation Engine Research Facility (DERF). This design features modularity that will allow for the testing of the RRDE as a stand alone combustor with variable areas of the channel, air injector, and nozzle exit. More detail of these design features will be discussed in Section 3.2.2. The RRDE design also features the ability to alter the fuel injection scheme, which would allow for the future testing of alternate fuels or fuel injection scheme to improve the RRDE operation. Finally, this design allowed for mating of the off the shelf, Garrett GT3582R turbocharger which was selected for this project due to its compact design, high RPM operating range, and its high mass flow capability for a turbocharger of this size.

The second objective of this project was to successfully operate the RRDE on hydrogen and air, and establish the operating regime of this new device. This data enables the comparison of trends seen in conventional RDEs. Because of the uniqueness of this flow scheme, new trends and operating characteristics were expected, and the examination of these differences provide inputs for future RRDE designs or modifications. This data will also be used to find areas within the operating map that

will allow for higher performance of the RRDE.

This objective was achieved by actually operating the RRDE on hydrogen and air. The detonability of hydrogen allowed for a wide operation range but certain configuration changes resulted in increase operating range as well as the presence of multi-wave operation. This testing was conducted using four main variables: channel height/area, nozzle area, mass flow through the RRDE, and the equivalence ratio. It should be mentioned that though the air injection area at the throat of the device was adjustable, testing was only conducted at one injection area ratio for this project. Section 3.4.2 will discuss the design space investigated, while Section 4.2 will discuss the operational results within that design space.

Finally, the most important objective of this project was to couple the RRDE with a turbine and examine the power output of this device. There are a multitude of sub-objectives that could stem from creating a novel APU configuration, but this project focused on the power output and the efficiency of the APU, and compared the results to conventional APUs in use today. The performance metrics that were used for this comparison are the specific power output of the turbine and the device's thermal efficiency. More discussion of how these are calculated will be given in Section 3.4.1.

This objective was achieved through the testing of the RRDE coupled to the turbocharger turbine. Design challenges with pairing the two, and the design of guide vanes to condition the flow for the turbine are discussed in Section 3.2.3. Like the stand alone testing, there were multiple variables changed throughout the APU operation including the mass flow and equivalence ratio. Furthermore, variation in the flow angle of the exhaust entering the turbine was also examined. The results of this testing will be discussed in Section 4.6.

II. Literature Review

To design, build, and characterize the operation envelope a Radial RDE it is best to first understand how these devices function. This requires knowledge on the fundamentals of detonation combustion, which will be discussed in Section 2.1. It also includes understanding the differences between a Constant Pressure Combustor (CPC), the combustor in a typical gas turbine engine, and a Pressure Gain Combustors, (PGC), a detonation cycle based combustor. These details will be given in Section 2.1.1. The effects of geometry and operating regime of previously operated PGCs will provide a starting ground for the design of the novel RRDE, given in Section 2.2.2.2. This thesis is also interested in coupling the RRDE with a Radial-Inflow Turbine, (RIT) in order to create a rapid response Auxillary Power Unit. Marrying a RIT with a PGC is another area of research that must be examined to ensure a successful pairing of the two devices, and will be touched on more in Sections 2.3 and 2.4. Deep understanding of these topics are all critical to the success of this project, and more depth and detail will be discussed throughout this chapter.

2.1 Detonation Fundamentals

To understand how a PGC can harness the benefits of detonation combustion, understanding of the fundamental physics behind detonations and what separates them from conventional deflagration combustion is required. The first step involves knowing the difference between deflagration combustion and detonation combustion. These distinctions will also help give insight on why detonation combustion is favorable to deflagration in certain cases. Section 2.1.1 will explore these key differences and also discuss the potential benefits PGCs see over their CPC counterparts.

The physics of a detonation event and the models used to predict how the deto-

nation process completes is also crucial information; Section 2.1.2 and Section 2.1.3 will provide an in depth discussion of these models and how they are used to predict detonation performance.

2.1.1 Detonation vs. Deflagration.

A detonation is a supersonic combustion event that features a leading shockwave and a combustion process. These two characteristic of the detonation are coupled due to the fact that the combustion creates the energy to sustain the shockwave, and the shockwave provides the compression and temperature rise, and therefore, the activation energy to initiate the combustion process. This event is different from a deflagration combustion event in a few ways The first difference is a deflagration combustion event occurs at subsonic velocities unlike the detonation event that proceeds supersonically. Another distinction is that a detonation sees a high initial pressure and temperature increase due to the leading shockwave, which leads to a pressure increase during the detonation. For this reason, a device which uses detonations to complete the combustion process is referred to as a Pressure Gain Combustor, (PGC). The two most studied pressure gained combustors are the Pulse Detonation Engine (PDE) and Rotating Detonation Engines, (RDE). The details and differences between these two combustors will be examined in Section 2.2.

The next difference between detonations and deflagrations is the end states of these processes. Detonations conclude with a higher pressure, temperature, and density compared to deflagrations at the same initial condition. These results are due to the leading shockwave and will be further discussed in Section 2.1.2 and Section 2.1.3. Detonations products exit the combustor at a higher pressure than they entered, instead of a slight loss in pressure seen in CPC. The increased exit pressure has many applications in which a detonation combustor could produce the same exit pressure

as a conventional combustor, but would require a lower initial pressure entering the combustor. This means a decrease in compressor stages which leads to a smaller, lighter gas turbine engine.

Another key feature of detonation combustion that set it apart from deflgration combustion is detonations produce a lower amount of entropy compared to a deflagration process. The conventional model for gas turbine engine is the Brayton Cycle. This cycle describes a constant pressure combustion process and an example of the Temperature, T, vs. Entropy, s, plot and the Pressure, P, vs Volume, $\forall$, plot is shown in Figure 4 (a) and (b) respectively. These represent an ideal Brayton cycle process, where the area between the curves represents the available work from the process. While this cycle closely models a CPC cycle, it cannot accurate predict the work available in a PGC cycle due to the increase in pressure during combustion. Figure 4 also shows the cycle analysis for the Humphrey Cycle, which is a constant volume model and features an increase in pressure during the combustion process. It can be seen that the Humphrey Cycle is able to produce more available work due to the fact that the combustion process generates less entropy that the constant pressure combustion.

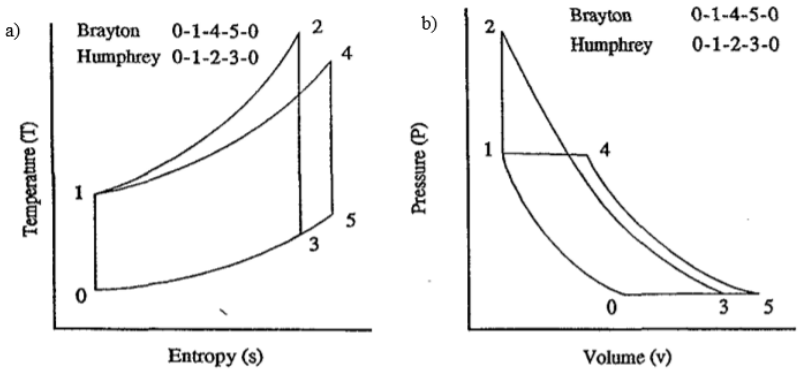

Figure 4. Temperature vs. Entropy (a) and Pressure vs. Specific Volume (b) Plots for Brayton and Humphrey Cycle.[2]

There are a multitude of cycles proposed to model the PGC cycle, not just the

Humphrey Cycle. The main three include the Humphrey Cycle, Fickett-Jacob (FJ) Cycle, and Zeldovich, von Neumann, and Dȍring (ZND) Cycle. All of these cycles account for the pressure gained during the combustion event in some manner, with the latter two representing detonation cycles. Figure 5 shows an idealized form of the Temperature vs. Entropy (a) and the Pressure vs Volume (b) plots for the three cycles. The FJ Cycle provides even more work out compared to the Humphry Cycle and the ZND Cycle provides more available work on top of that. The FJ Cycle accounts for the Chapman-Joguet conditions post-detonation, the fundamentals of this will be discussed further in Section 2.1.2. The ZND Cycle account for the post-detonation conditions and the post-shock conditions, which allows for higher pressure and temperature over the other cycles. More detail on the fundamentals of the ZND Cycle will be discussed in Section 2.1.3.

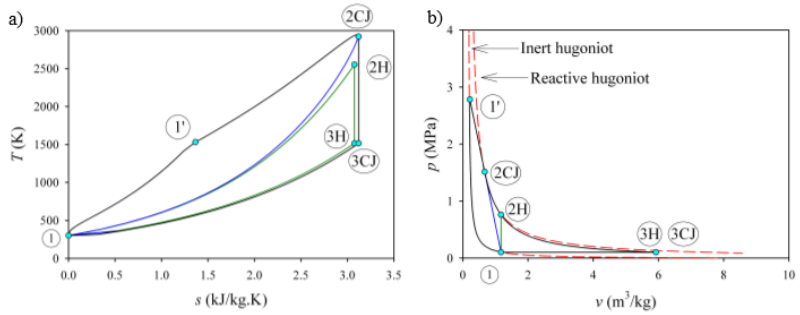

Figure 5. Temperature vs Entropy (a) and Pressure vs. Specific Volume (b) Plots for Humphrey Cycle $(1 \rightarrow 2H \rightarrow 3H \rightarrow 1)$**, Fickett-Jacobs Cycle** $(1 \rightarrow 2CJ \rightarrow 3CJ \rightarrow 1)$**, and ZND Cycle** $(1 \rightarrow 1' \rightarrow 2CJ \rightarrow 3CJ \rightarrow 1)$**.[3]**

2.1.2 Rayleigh Lines, Rakine-Hugoniot Curve and Chapman-Joguet Points.

By simultaneously solving the continuity and momentum conservation equations and the state equations, Rayleigh was able to combine the relationships into one equation known as the Rayleigh Line Equation (Equation 1). The Rayleigh Line

Equation relates the pressures and densities, pre- and post-reaction, to the mass flux of the system.[4]

$$-\dot{m}''^2 = \frac{P_2 - P_1}{\frac{1}{\rho_2} - \frac{1}{\rho_1}} \tag{1}$$

where $\dot{m}''$ is the mass flux per unit time into the system, P is pressure, and ρ is density. To best understand what this equation means, it is easiest to rearrange the Rayleigh Line into a linear equation and plot the results.

$$P = a\nu_2 + b \tag{2}$$

where ν is the specific volume, $\frac{1}{\rho}$, and a is the slope given by:

$$a = -\dot{m}''^2 \tag{3}$$

and b is the intercept given by:

$$b = P_1 + \dot{m}''^2\nu_1 \tag{4}$$

Figure 6 shows an example of the Rayleigh line plotted using the same initial conditions, but varying the mass flux. Figure 6 has many details that are important to understand if one wants to fully grasp the fundamentals behind a detonation event. The first is that the plot is divided into multiple regions, of which only two are accessible. The regions marked A and B are invalid solution spaces because they require a negative mass flux into the system to occur. This leave the second and fourth quadrant for valid solutions spaces. The second quadrant represents a pressure gain combustion event while the fourth quadrant is a pressure loss combustion. These two regions also correspond to detonation and deflagration combustion, respectively. Furthermore, as the mass flux into the system increases, the slope of the line becomes more negative, with the vertical dashed line representing an infinite mass flux and the horizontal dashed line representing zero mass flux.

The Rayleigh Line Equation gives a method for solving both the continuity and momentum equation. However, it does not provide any information on how the

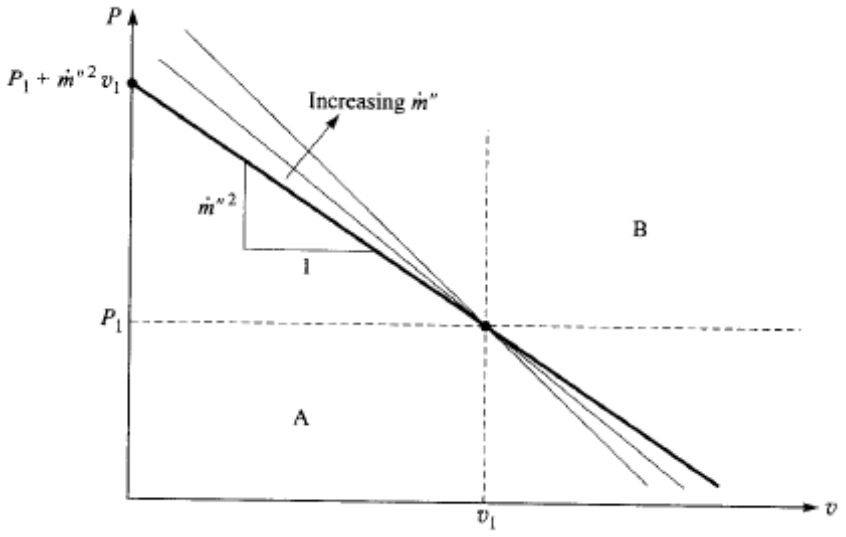

Figure 6. Plot of multiple Rayleigh lines for a given set of initial conditions.[4]

reaction is occurring. For this reason, the actual solution for the system could lay anywhere along the Rayleigh Line. In order to find its exact location, the energy equation must be consulted.

Under the assumption of an ideal gas, Rankine and Hugoniot were able to combine continuity, momentum and the energy equation, along with the ideal gas relations, to achieve the Equation 5.[4]

$$q = \frac{\gamma}{\gamma - 1}\left(\frac{P_2}{\rho_2} - \frac{P_1}{\rho_1}\right) - \frac{1}{2}\left(P_2 - P_1\right)\left(\frac{1}{\rho_1} + \frac{1}{\rho_2}\right) \tag{5}$$

where γ is the ratio of specific heats and q is the specific heat release. The Rankine-Hugoniot Equation allows for the relation of pressures and densities to the heat release per unit mass, q, of the system. The combination of the Rayleigh Line and the nonlinear, Rankine-Hugoniot Curve will now allow for the solution of the state of the system, assuming the heat release per unit mass, q, is known.

Figure 7 shows an example plot of the Rankine-Hugoniot Curve for a given initial condition. The Rankine-Hugoniot curve is plotted in bold, while the dashed lines are

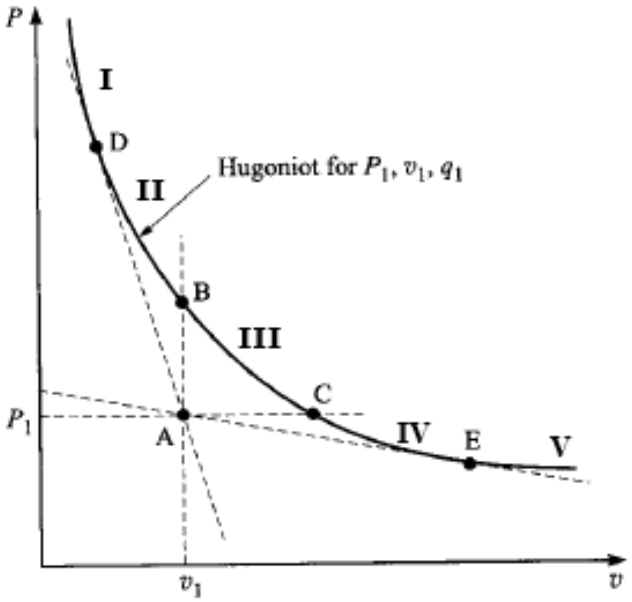

Figure 7. Plot of a Rankine-Hugoniot Curve.[4]

Rayleigh Lines. This plot is analogous to Figure 6, where the point A in Figure 7 is the same initial condition from Figure 6. In this plot the purely horizontal dashed line, AC, represents the zero mass flux Rayleigh Line, while the purely vertical dashed line, AB, represents the infinite mass flux Rayleigh Line. The dashed line, AE, represents a low mass flux Rayleigh Line, while the dashed line, AD, represents a high mass flux Rayleigh Line. Again, the first and third quadrants are areas of invalid solutions.[4]

Figure 7 has more details about how the combustion process is taking place. For a given heat release, mass flux, initial pressure, and density for the solution to the system can be found. Solutions fall along five distinct regions of the Rankine-Hugoniot Curve. Region I is the line section that extends from D off to infinity, Region II falls between points B and D, Region III runs from B to C, Region IV is from C to E, and, finally, Region V is the section starting at point E and extends to infinity. These regions represent different combustion events depending on where they fall along the Rankine-Hugoniot Curve.[4]

Point D and E correspond to significant combustion events and are known as

the Chapman-Jouguet (CJ) points. These are the points of tangency of between the Rankine-Hugoniot curve and the Rayleigh lines. The upper CJ point, D, is a detonation event in which the speed of the combustion wave is sonic with respect to the speed of sound of the products of combustion. This point is also where detonation events tend to occur; any detonation that falls above or below this point will converge back to the upper CJ point. The lower CJ point, E, represents a deflagration event where the combustion also occurs at sonic speeds.

The CJ points also serve as a boundary for where real, sustainable combustion events occur. For the upper branch of the Rankine-Hugoniot line detonations will converge on the upper CJ point, and for the lower branch, deflagration events have never occurred below the lower CJ point. Another way to think of this results is by consulting Figure 7. Notice that because the CJ points are points of tangency with the Rayleigh lines, any line that corresponds to a combustion event outside of the CJ points will have a Rayleigh line that also crosses the Rankine-Hugoniot line at a point inside of the CJ points. The Upper CJ point corresponds to a solution where detonation events are attained and sustained. At this point the combusted gases are moving relative to the shock wave at the sonic velocity and the detonation is stable. The lower CJ point is a solution for deflagration events that also occur at sonic velocities; however, these combustion events are not driven by a shock wave.[4]

The two CJ points also hold significance in terms of the entropy creation during combustion events. Figure 8 shows the relationship of the entropy created during the combustion process, y-axis, versus the specific volume, ν.[4] Figure 8 is broken up into the same regions as Figure 7. This plot shows that the two CJ points correspond to the minimum and maximum entropy creation points in detonation events. One side note is that even though this plot shows the two CJ as the local minimum and maximum, they do, in fact, represent the absolute minimum and maximum for real combustion

events because combustion rarely, if ever, occurs in Region I or Region V. The most important feature of this graph, and a large reason detonation combustion is such a studied field, is the fact that the upper CJ point is at a lower entropy production relative to the lower CJ point. This means that for the same initial condition and desired heat release, the detonation event will produce less entropy, leading to less losses in the process. Finally, the lower losses due for detonation events leads to more efficient conversion of the energy stored in the fuel into usable energy.[4]

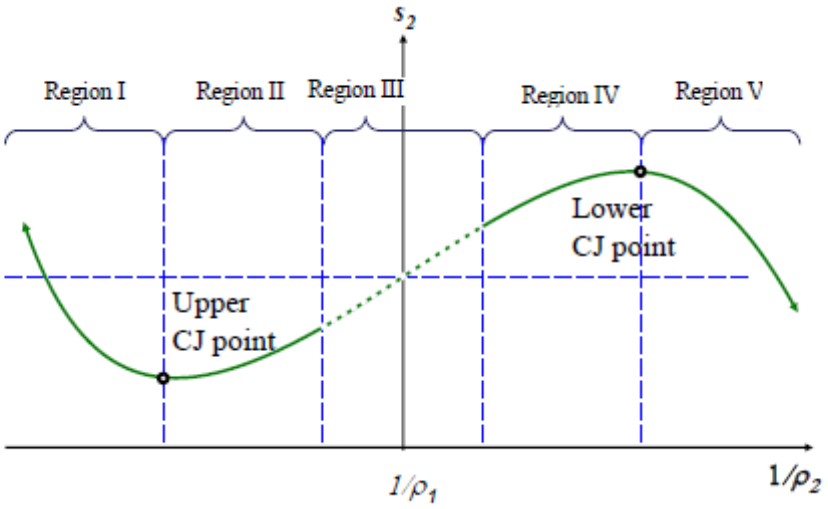

Figure 8. Entropy vs. Specific Volume for different combustion events.[5]

2.1.3 Zel'dovich, von Neumann and Døring.

Zel'dovich, von Neumann and Døring all took the previously mentioned one dimensional models of detonations and dove deeper into the features of a detonation. They separately hypothesized that there are three distinct events within a detonation that describe how the process unfolds. These features of a detonation, shown in Figure 9, are a leading shock, followed by an induction zone where the pre-combustion processes occur, and finally followed by the combustion itself.

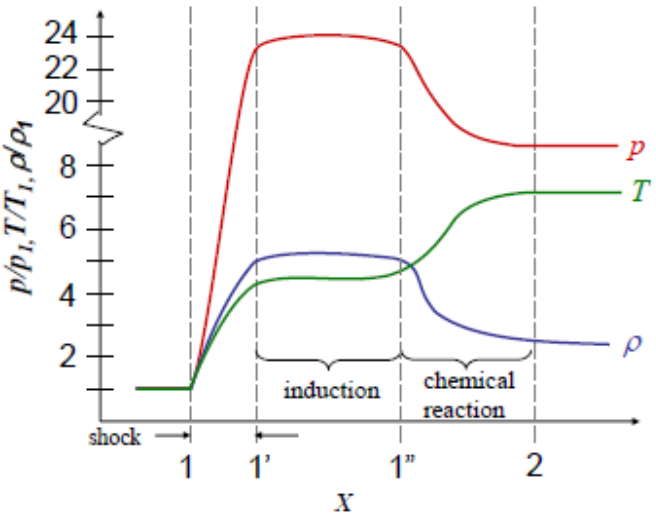

Figure 9. ZND Structure.[5]

Figure 9 tracks the pressure, temperature and density of the gases as the detonation proceeds from left to right and it breaks the three events into their own region: the shock from 1 to 1', the induction zone from 1'to 1", and the chemical reaction zone from 1"to 2.

Initially all of the properties are constant pre-shock, but as they move across the shock they see a rapid increase in pressure, temperature and density. This is an expected result that agrees with the isentropic shock relations and is referred to as the von Neumann spike. Because the shockwave is infinitesimally thin, on the order of the mean free path of the molecules, it is highly unlikely that the chemical reaction will occur in this region.

Next, the gases proceed through the induction zone. As the gases enter this region they have a large amount of internal energy provided by the shock, sufficiently more than the activation energy of the combustion reaction; however, in order for the chemical reaction to proceed, the molecules must collide and start the precursor reactions. This involves breaking down the fuel and dispersing those products into the oxidizer in the surrounding air. The gases at this stage stay at roughly the same

pressure, temperature and density.

Once there is sufficient mixture of air and decomposed fuel particles the chemical reaction begins. At this stage the combustion occurs which corresponds to a rapid, dramatic increase in temperature, and a decrease in pressure and density. Despite the loss in pressure during the chemical reaction zone, the overall detonation process concludes with an increase in pressure, temperature, and density. This model provides a more detailed description of how a detonation unfolds; however, it is still and one-dimensional model and does not account for the two- or three-dimensional effects on the structure of the detonation.

2.1.4 Detonation Structure.

Unlike the theories discussed in Sections 2.1.2 and 2.1.3, detonation waves are not one dimensional and are not formed by a single leading shock.[6] They are 3-D and made up of a complex chain of shocks and reaction zones, called cells, that are shown in Figure 10. These cells are the characteristic length of detonations and the cell size, λ, is typically measured as the widest part of the cell perpendicular to the direction of propagation. They are formed by the paths taken by the triple point of the detonation.

As seen in the blowup portion of Figure 10, the triple point is the intersection of the Mach stem and transverse shock from a newly formed reaction zone and the incident shock wave from an older reaction zone. As the detonation progresses downstream, the triple point traces out a fish scale pattern. By tracking these fish scale patterns with soot foil experiments, researchers were able to successfully determine the approximate cell size for different fuel/oxidizer mixtures.[7]

These tests showed multiple trends in cell size that dictate certain geometric constraints in detonation devices. They show that in order to successfully maintain a

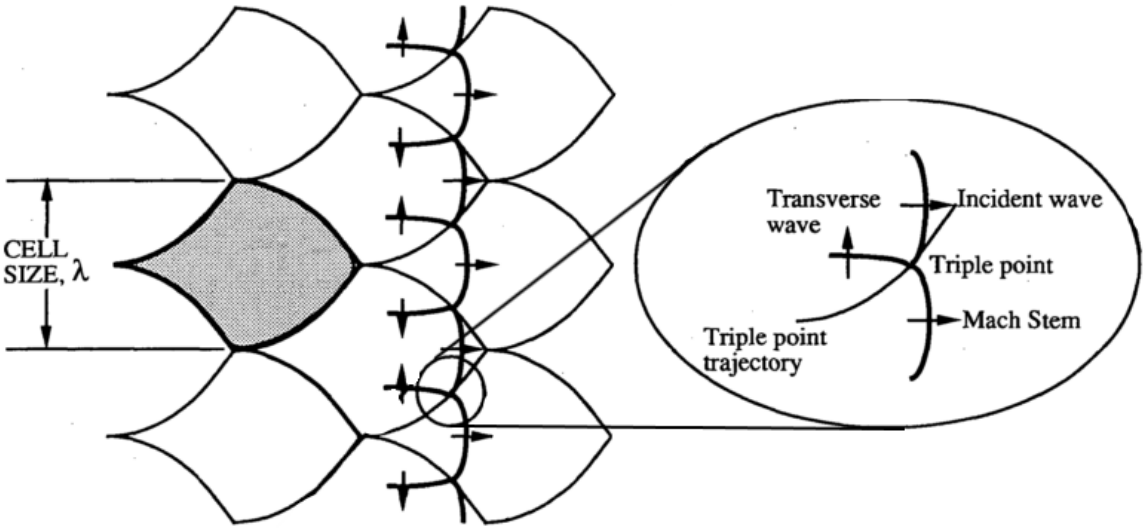

Figure 10. 2-D detonation structure.[7]

propagating detonation wave, at least one dimension must be between 4 λ and 17 λ and one of the other directions must be at least one cell size.[6] However, this means that only one of the dimensions of the detonation channel can be less than a cell size to enable a detonation wave to still propagate.

Another trend shown by Ciccarelli et al. is the correlation of equivalence ratio, ϕ, initial pressure, and initial temperature of the detonation. In particular they showed that detonation cell size was smallest at a stoichiometric ϕ of 1, and grew as the equivalence ratio moved to either more lean or more rich conditions. Their results also showed that increasing the initial pressure or temperature decreased in cell size.[7] These results are the standard for designing a detonation engine and help set constraints on the geometry for the RRDE.

2.1.5 Deflagration to Detonation Transition.

In order to achieve a detonation of a fuel air mixture one of two events is required. The first is a high energy ignition source that provides the activation energy for the mixture to achieve detonation directly, which is on the order of 10-1000 kJ of

energy. The second is through the use of a phenomena known as Deflagration to Detonation Transition (DDT). This process typically has two methods that lead to a detonation: one, with a shock or multiple focused shocks that provide the energy for auto-ignition, and two, through high mixing which increases the burn rate of the mixture. This self-propagating cycle can eventually generate a compression wave that can then auto-ignite the mixture, leading to a detonation wave.[8]

PDEs typically operate on using a DDT section opposed to a direct ignition approach. This is due to the massive amount of energy that is required for direct ignition since the minimum energy for direct initiation is proportional to the cube of the cell size. Direct ignition is typically done using a exploding wire which is one time use.[7] DDT devices are also crucial for the operation of an RDE. These devices are usually referred to as a pre-detonator as they create the initial hammer-shock that starts the detonation wave.

One proven device that uses the flame acceleration method is the Shchelkin spiral. This device consist of a tube with a section that has a spiral around the inner radius of the tube. This spiral provides an obstacle to the flow which allows for the DDT process to occur. These devices have proven to create a successful detonation in a shorter distance compared to smooth wall tubes.[9]

New et al. tested the effects of changing the geometry of a Shchelkin spiral.[9] They varied the blockage ratio and the length of the spirals. Their results show that the higher blockage ratios allowed for successful DDT in shorter length configuration, but the longer, lower blockage ratio configuration did produce a higher peak thrust. In the case of starting an RDE, thrust production is not of concern. However, having a more compact pre-detonator is valuable.

Knox et al. tested a DDT devices that operated using fluidic obstacles instead of physical obstacles, like the spiral section in a Shchelkin spiral.[10] Figure 11 shows a

layout of the design they tested and the conventional design with which they compared. Their novel design used a circumferential jet of air as the flow obstacle. They showed that the fluidic obstacle provide 240% higher turbulence intensity over the conventional obstacle in cold flow testing. The fluidic obstacles also allowed for a higher probability of DDT at lower initial tube pressures. Lastly, they showed the fluidic obstacle had a much lower pressure loss compared to the physical obstacle, and increasing blockage ratio for the physical obstacle led to high pressure losses. This result aligned well with the thrust losses seen by New et al.[9]

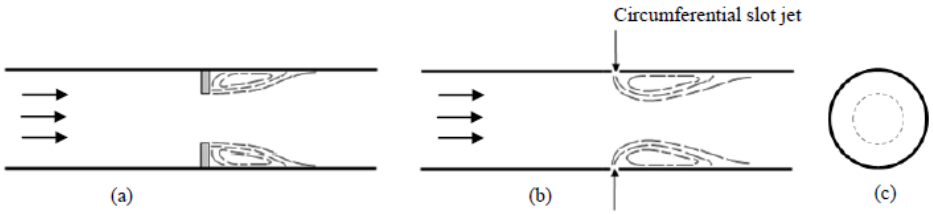

Figure 11. Conventional and Fluidic DDT Devices.[10]

2.2 Detonation Engines

Detonation Engines are Pressure Gain Combustion devices that use a detonation process in an attempt to achieve the benefits of detonation combustion. For the purposes of this thesis two categories of detonation engines engines will be discussed, Pulse Detonation Engines and Continuous or Rotating Detonation Engines. PDE operate on a fill-fire-purge cycle and typically use a DDT section to transition to a detonation. More detail on how these devices work will be given in Section 2.2.1. RDEs operate on a constant detonation wave that propagates around a circular channel. The fill-fire-purge cycle of the PDE is eliminated with RDE devices, which removes cycle frequency constraints and allows for more steady exit conditions. RDEs also provide a more compact design with increased power density versus a PDE.[11] A more in depth discussion of RDEs is given in Section 2.2.2.

2.2.1 Pulse Detonation Engines.

Pulse Detonation Engines are a type of detonation engines that operates under a fill-fire-purge cycle. These engines typically have a main combustion chamber, a DDT section, and a long tube where the exhaust exits. The cycle starts when fuel and oxidizer are injected into the main chamber where a spark ignites the mixture. Next, the combustion event travels through the DDT devices and exits the tube end as a detonation wave. Finally, the chamber and tube are purged to remove the products of combustion. Therefore, during each cycle there is only a short period of time where the actual detonation wave is propagating and the majority of the time is spent in the other potions of the cycle, thus reducing the benefit of the detonation. Furthermore, the cyclic nature of a PDE leads to the unsteadiness at the exit of PDEs.[11]

PDEs were first theorized in the 1940's by Hoffman[12] and the late 1950's by Nicholls et al.[13] Nicholls et al. tested a hydrogen/air PDE and measured the specific thrust, F_s, and specific impulse, I_{sp}, of the device. Where specific thrust is given by:

$$F_s = \frac{F}{\dot{m}_{air}} \tag{6}$$

where $\dot{m}_{air}$ is the mass flow rate of air, and specific impulse is given by:

$$I_{sp} = \frac{F}{\dot{m}_f g_0} \tag{7}$$

where $\dot{m}_f$ is the mass flow rate of fuel and g_0 is the gravitational constant. They tested the PDE over a range of mass flow rates varying from 0.011 $\frac{\text{kg}}{\text{s}}$ to 0.021 $\frac{\text{kg}}{\text{s}}$ and operating frequencies varying from less than 10 Hz up to 35 Hz. Their results showed an increase in thrust and specific impulse as the cycle frequency increased up to a frequency of 24 Hz for the lower mass flows and up to 30 Hz for the highest mass flow before it began decreasing. They postulated this was due to a fraction of the new fuel and oxidizer being able to propagate down the channel before the detonation was initiated.[13]

More recently, the Detonation Engine Research Facility, (DERF) at the Air Force

Research Lab (AFRL) at Wright Patterson Air Force Base (WPAFB) has conducted multiple studies on PDE performance and optimization. One study, by Schauer et al., conducted at the DERF used a hydrogen and air PDE using a weak ignition and DDT section in order to achieve a detonation. Their results showed the DDT section drastically reduced the length of the PDE tube needed in order to achieve detonation before the tube exit. Their work also showed that maximum thrust occurred around an equivalence ratio of one or slightly higher and efficiency increased as the equivalence ratio was decreased.[14]

PDEs showed promise for detonation combustion as a tool for increasing engine performance over CPCs, however, there were also some shortcomings of PDEs including low cycle frequencies, highly unsteady operation, and overall length of the devices.[15] These issues with PDEs paved the way for the need and development of continuous detonation devices.

2.2.2 Rotating Detonation Engines.

Continuous detonation devices have been theorized as a method of reaping the benefits of pressure gain combustion without the cyclical frequency limits with PDEs.[16] A common continuous detonation device used currently is the Rotating Detonation Engine. This device consisted of an annular channel where the detonation wave propagates circumferentially around the channel, as seen in Figure 12. As the detonation wave propagates around the channel a fuel/air mixture is injected from the bottom (Head) end. This mixture is detonated in the channel and the products exit out of the exhaust (Nozzle) end.

Figure 13 is an unrolled view of the RDE's detonation channel. This view allows for more detailed view of the structures within a detonation wave in an RDE. Region A corresponds to the detonation wave itself. Region B is the oblique shock that

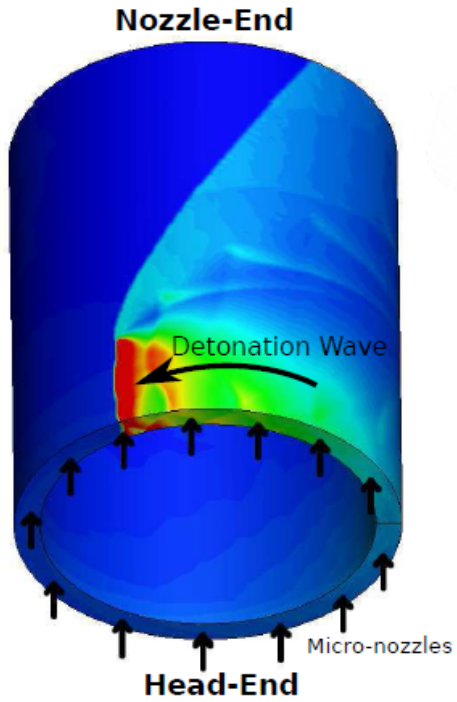

Figure 12. Computational Fluid Dynamics solution of an RDE. [17]

forms due to the expansion of the combustion products behind the detonation wave. Region C is the slip line where the fresh products from the detonation wave meet with older products once they pass thru the oblique shock. Region D is a secondary shockwave that originates from the intersection of the detonation wave and the oblique shock. Region E is the border between the detonation products and the fresh reactant mixture being injected into the channel. Region F corresponds to the region where the pressure from the detonation blocks the injection process momentarily. Region G shows the reactant flow injection, unimpeded by the detonation.

Figure 14 shows the path that the flow takes as it passes through the detonation wave. This figure divides the incoming flow into three regions. The first region, Detonation-A, contains the flow that passes through the detonation wave and then passes through the oblique shock as the detonation wave makes its second pass. The next region, Detonation-B, is the flow that passes through the detonation wave but

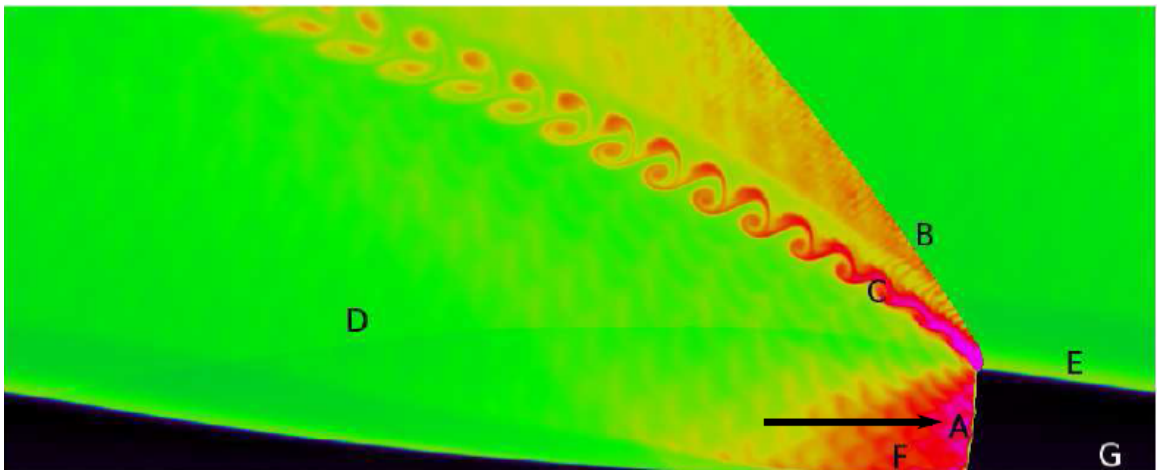

Figure 13. Unrolled RDE showing detonation wave features. A) Detonation wave, B) Oblique shockwave, C) Slip line between freshly detonated products and older products, D) Secondary shockwave, E) Region of mixing between reactant mixture and product gases, F) Region with backflow/blocked injection, G) Reactant mixture. [17]

exits the channel prior to the oblique shock on the second pass. The final region, Non-Detonation, is the a region of the flow that does not pass through the detonation wave, but only passes through the oblique shock. The flow from the Non-Detonation region combusts after the oblique shock and forms the slip line. This is important because a larger Non-Detonation region means more combustion outside of the detonation, which leads to a decrease in the pressure gained from combustion. This in turn leads to a decrease in the efficiency compared to a detonation where all the reactants were detonated.

2.2.2.1 RDE History.

Rotating Detonation Engines were first theorized in the 1960s by Cullen et al.[18] and Voitsekhovsky.[19] These engines featured a circumferential annulus in which a continuous detonation wave could propagate, similar to the layout shown in Figure 12. Cullen et al. tested a RDE operating on both hydrogen-oxygen and methane-oxygen. They noticed the detonation wave would circle the channel in both directions at initiation, giving them no directional control over the detonation wave. To combat

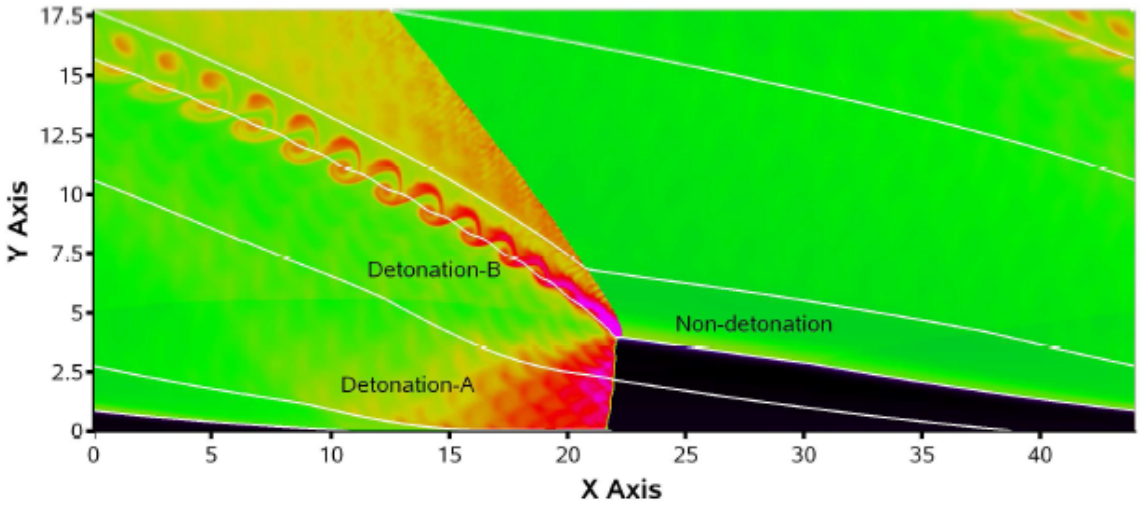

Figure 14. Unrolled RDE showing detonation wave and path of the flow. [17]

this they installed a breakable diaphragm that would block one direction off and they were able to control the direction of travel of the detonation wave.[18] Their study showed the feasibility of RDEs and paved the way for continued research.

Bykovskii et al. tested a RDE on multiple gaseous and liquid fuel types. They presented the results for their RDE operating on oxygen and kerosene, diesel, methane, and hydrogen. All of which showed successful detonation propagation and wave speeds roughly 70% of CJ velocity.[20] This research showed the ability of RDE to operate on multiple fuel types with a similar geometric design.

Suchocki et al. tested a 76.2 mm diameter hydrogen-enriched air RDE at the DERF and ran the device through a range of mass flow rates and equivalence ratios. Their results showed as they increased the mass flow rate from 0.75 $\frac{\text{kg}}{\text{s}}$ to 0.85 $\frac{\text{kg}}{\text{s}}$ the RDE became more unsteady and began transitioning from one detonation wave to two detonation waves and when increased passed 0.85 $\frac{\text{kg}}{\text{s}}$ the RDE operated on primarily two waves. Once the RDE entered predominately two wave operation the unsteadiness dropped back down to levels seen at the lower mass flow rates for the single wave operation.[21]

2.2.2.2 RDE Performance.

It is important to understand where previous RDEs best operate in order to accurately predict how a novel design will function. The studies in this section explore several RDE geometries and characterize their operating conditions. They examine changes in several aspects of the RDE including: size, channel width, nozzling, equivalence ratio, and mass flow rate, and characterize how these changes effects the operability of an RDE.

Shank et al. designed a large, modular RDE device to allow for multiple configurations to be tested. Their device featured capabilities to change the channel width, fuel injection scheme, fuel type, and oxidizer type. Their initial result for hydrogen and air showed successful detonations only at mass flow rates greater than 120 $\frac{\text{lbm}}{\text{min}}$ and slightly rich equivalence ratios.[15]

Dyer et al. tested a 508 mm diameter RDE operated on ethylene-air and hydrogen-air.[16] They initially had problems initiating a detonation with the ethylene-air but did have success using hydrogen-air due to its smaller cell size and increased detonability. However, they did note that the hydrogen, which has a much larger flammability limit, may promote flame-holding in the channel, a typical failure mode in RDEs. They postulated that the increase in flammability limits allowed for more consistent operation because the less well-mixed hydrogen-air pockets were still able to detonate. Their results also showed one, two, and multiple wave operation as they varied mass flow from less than 3.2 to 4.1 $\frac{\text{kg}}{\text{s}}$, a trend that agrees with previous research.[21]

Fotia et al. measured the specific thrust and the specific impulse for an RDE with multiple nozzle exit configurations which included a bluff body exit and an aerospike nozzle. They tested the aerospike nozzle with a varying range of exit geometries: fully open, 20% area reduction and 40% area reduction. Their results showed that all of the configurations without a choke nozzle had similar specific thrust and specific impulse

results, but having a choked nozzle led to an increase in both of these measures. This was due to increased static pressure in the detonation channel which increased the post detonation pressure; therefore, increased the exit pressure of the RDE allowing for more specific thrust and specific impulse. This resulted in the ability to achieve a similar output thrust and specific impulse with a choked RDE operating at a lower fuel rate of 0.76 $\frac{kg}{s}$ compared to an open nozzle RDE operating at 1.14 $\frac{kg}{s}$.[22]

Fotia et al. next operated a hydrogen-air RDE and varied the channel width, mass flow rate, equivalence ratio, air injection ratio, and nozzle area ratio. Their study provided insight into the geometric effects on RDE performance. A key conclusions from their study was increasing either the channel width from 7.6 mm to 22.9 mm or the mass flux through the RDE from 86.5 to 173 $\frac{\mathrm{kg}}{\mathrm{m^2s}}$both showed an increase in the corrected thrust. However, the larger, 22.9 mm channel width showed a specific impulse roughly 70% lower than that of the other channel. Another takeaway was adding a more restrictive nozzle improved the specific impulse for all channel widths. Their research also showed as they increased the mass flow rate, the specific thrust and specific impulse increased, a similar trend shown throughout the literature. Finally, they showed operation at an equivalence ratio at or slightly above one had the highest specific thrust value.[23]

2.2.3 Radial RDE.

Conventionally, RDEs have a similar layout as discussed in Section 2.2.2 and shown in Figure 12. An alternative, disk-shaped, design was theorized and tested. Radial RDE designs typically inject fuel and oxidizer from the outer radius. The reactants are then combusted and exit the device in the center. Figure 15 highlights the key difference in the two designs; the conventional RDE (a) and the Radial RDE (b). The first key difference is the reactants in the conventional RDE maintains an axial

flow path throughout the device, where the RRDE injects the reactants in the radial direction then turns the flow axially at the channel exit. In both cases; however, the detonation runs circumferentially around the channel.[24]

RRDEs provide an advantage over conventional RDE in a few specific cases. The first is the radial layout allows for possible integration of RRDEs in location where a conventional RDE would not fit. Another distinct advantage of RRDEs is they are better suited for operation with a radial inflow turbine. The flow is already radial in a RRDE; therefore, turning of the exhaust flow is not necessary.

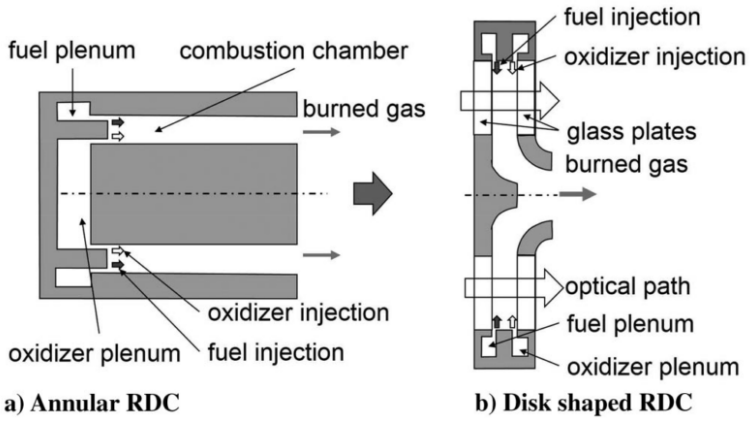

Figure 15. Conventional, Annular RDE (a) and Radial RDE (b).[24]

Figure 16 shows a more detailed view of the flow features of a Radial RDE, where fuel and oxidizer are injected separately from the outer radius, represented by the light blue. Next, the reactants mix in the channel before detonating, represented by the light green. Similarly to conventional RDEs, the detonation wave propagates circumferentially around the channel, but unlike conventional designs, the RRDE detonation wave extends radially instead of axially. This is shown by the red region. Finally, the combustion products leave the center of the device, shown in orange.

This type of design was initially tested by Bykovskii et al. Their device injected air and fuel in radially from the outer circumference, similar to the device Nakagami et al. tested. Bykovskii et al. showed their device operated successfully using a

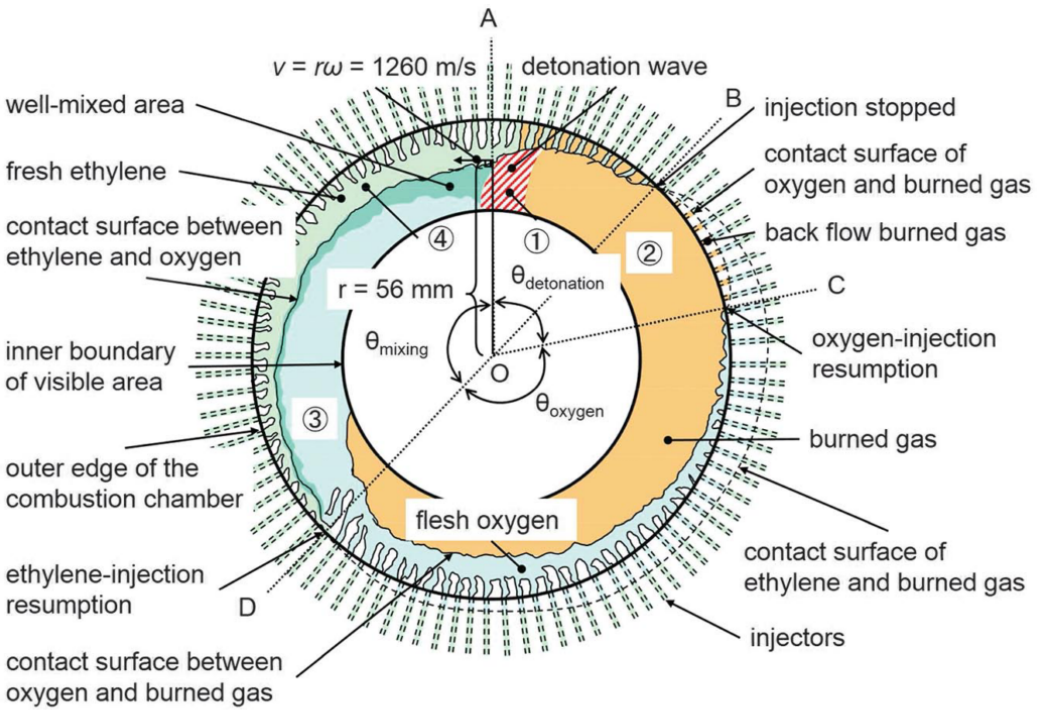

Fig. 5 Schematic of the phenomena in the disk-shaped RDC.

Figure 16. Flow path structure of a Radial RDE.[24]

mulititude of fuels, discussed in Section 2.2.2.1.[20] This research gives confidence in the ability for a RRDE to operate, and showed the potential to expand to other fuel types.

More recent studies using the RRDE layout have been conducted by Nakagami et al.[24] and Higashi et al.[25] Nakagami et al. tested the device shown in Figures 15 and 16. They studied the detonation wave visually by installing glass plates at the radial location where the detonation wave propagated. They conducted three different visual experiments; self-luminescence, shadowgraph and Schlieren. The self-lumination captures showed the combustion within the detonation wave and allowed for the calculation of the wave speed. The shadowgraph imaging showed the injection pattern for the fuel and oxidizer injectors which allowed for determining when the ports began re-injecting after the detonation wave passed. Finally, the Schlieren imaging showed the structure of the detonation wave. Figure 17 shows a Schleren

image of the detonation wave. It shows similar detonation wave structure compared to the conventional RDE suggesting these devices function similarly despite the shape change.[24]

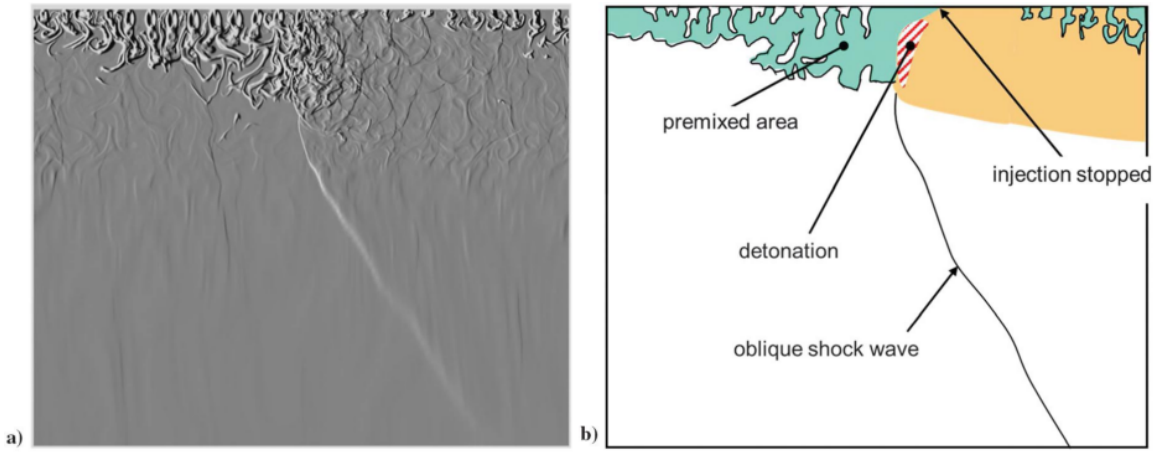

Figure 17. Detonation wave structure of a Radial RDE.[24]

Higashi et al. tested a RRDE that brought in either air or pure oxygen through the center of the device using a centrifugal compressor attached to a free-spinning bottom plate, Figure 18. Hydrogen was injected at the exit of the compressor and the mixture was detonated. The products then exited through a row of turbine blades attached to the same plate as the compressor. This design concept represents a possible self-sustaining RRDE.[25]

Higashi et al.'s device was tested by spinning up the compressor plate section using an electric motor. Once a sufficient RPM was reached the motor was disconnected using a clutch, and then the RRDE was ignited. Their results showed an RPM increase as soon as the detonation was established which showed the feasibility of the device.

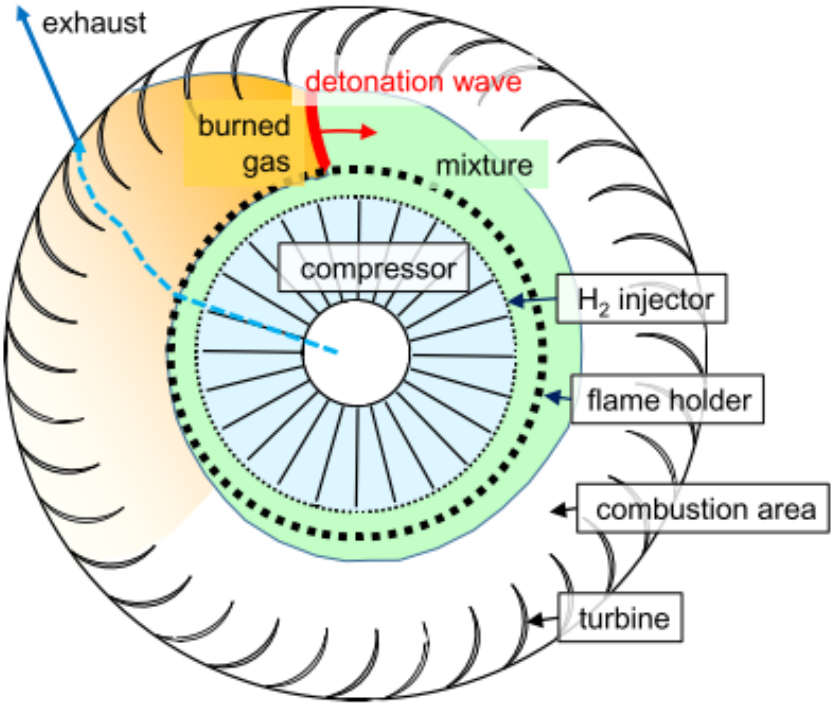

Figure 18. Compressor driven Radial RDE with turbine row.[25]

2.3 Turbine Integration

Once the operability of these PGCs was established, the next step in the process was to couple them with turbines for work extraction. This task poses many possible issues, including unsteady, non-uniform flow, high-temperature and high-pressure exhaust, and possible supersonic flow at the turbine entrance. The unsteady flow of PDEs is of concern due to the fact that the turbine will not be at a constant RPM throughout its operation, which could be a detriment to its efficiency.[26] The issue with non-uniform flow could lead to an imbalance in loading on the turbine. Having high-temperature exhaust is commonplace in gas turbine engines, and they handle this by running cooling flow or film cooling to the turbine to maintain structural strength at these high temperatures. However, in PGCs the exhaust gas pressure is higher than the pressure entering the combustor. This makes film cooling tricky

due to the fact that the film cooling air is typically taken from the final stage of the compressor that is at a higher pressure than the turbine. Lastly, the possibility of having supersonic flow at the turbine could lead to losses due to shocks in the flow.[11] Despite all of these issues, multiple tests were conducted coupling PGCs to both radial and axial turbines.

2.3.1 PDE Turbine Integration.

The first step taken in coupling a PGC to a turbine started with PDE devices. PDEs are highly unsteady due to the frequency they operate at and the fact that the cycle requires a purge between each detonation. Rouser et al. examined the differences in power generation using an automotive turbocharger coupled with a PDE operating at 10 Hz and a conventional CPC.[27] During the test, they measured a cyclic variation in the turbine operating RPM as shown in Figure 19. Their results showed that a PDE coupled with the turbine maintained a power level higher than the CPC throughout the entire cycle, despite the variable RPM. They also showed that the average specific power of the PDE was 41% higher than the CPC operating at the same mass flow rate of 8 $\frac{\text{lbm}}{\text{min}}$. Specific power, P_s, is defined as:

$$P_s = \frac{P}{\dot{m}} \tag{8}$$

where P is the power output and $\dot{m}$ is the mass flow rate. This gives confidence in the ability of the PDE-turbine integration to provide a more efficient way of power generation compared to CPCs.

Rouser et al.'s study also showed an interesting phenomenon where the RPM of the turbine actually peaked just slightly after the detonation front arrived at the turbine. They reexamined this in their next work where they theorized that there was mass storage occurring before the turbine as the detonation wave passes.[28] This explains why the instantaneous turbine RPM peaks just after the wave passes in Figure 19, and

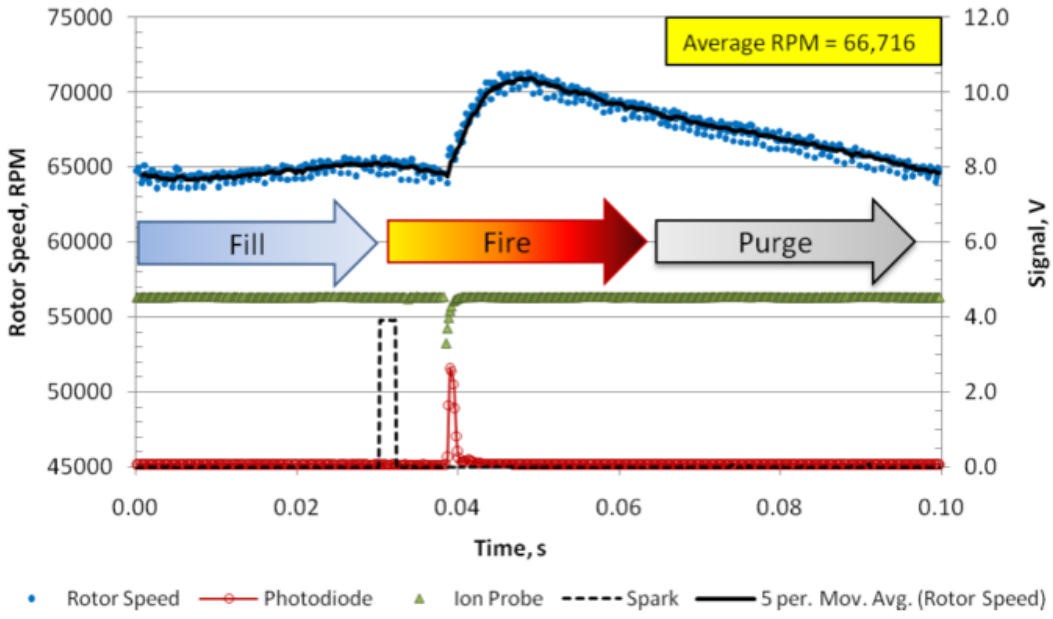

Figure 19. Turbine Operation with PDE Combustor.[27]

why the specific power remains high throughout the cycle. By maintaining a roughly constant output RPM, this improves the possibility of operating a compressor at its design point at near steady conditions, or provides a sources of constant work for the use in a generator. Rouser et al. also noticed significant bearing wear when operating due to the rapid angular acceleration of the turbocharger every tenth of a second. This bearing wear eventually lead to premature failure of the bearings.

Glaser et al. attempted to avoid the unsteadiness and heat transfer issues by coupling multiple PDEs to an axial turbine. They were able to run six PDEs, firing sequentially, and ran the exhaust through a channel where the cooler purge flow mixed with the exhaust before entering the turbine. The cooling air not only lightened the temperature load on the turbine, but the mixing also allowed for a more uniform flow. Similar to Rouser et al.'s results, they were able to show improved specific power output with the PDE system over a CPC system operating at the same turbine inlet temperature.[29]

These results show that the theorized benefits of PGCs can be realized. First,

the PDEs where able to acheive a higher specific power over their CPC counterparts. Next, the output power remained relatively constant despite the fluctuations in RPM in the turbine. Finally, the turbines in these test did not fail at the high-temperature and high-pressure flow exiting the combustor over these shorter runs.

2.3.2 RDE Turbine Integration.

The next step in pairing Detonation Engines with turbines was to try to reduce the unsteadiness of the flow entering the turbine. This was accomplished by coupling RDEs with turbine and comparing them with conventional combustors. Tellefsen,[30] DeBarmore et al.,[31] and Naples et al.[26] all studied aspects of a turbine operating in RDE exhausts and the results of these studies are presented.

Tellefsen conducted a study examining the effects of coupling an axial flow turbine to an RDE.[30] His process included getting the turbine up to speed by running cold flow through the system before initiating the detonation. He was only able to achieve detonations when using enriched air and at equivalence ratios between 1.1 and 1.4. This experiment also measured the pressure at the inlet and exit of the turbine and showed the inlet pressure fluctuated at 8.6 kHz when the exit pressure only fluctuated at 5.75 kHz, which indicated that some of the unsteadiness of the flow was damped out by the turbine. Another interesting result from Tellefsen's study was despite the large fluctuations in pressure through the turbine, the compressor saw predominately steady operating pressures throughout the test runs. Lastly, he measured the turbine RPM throughout the run, and it showed large variation in instantaneous RPM over the run, which was expected due to the unsteadiness of the RDE exhaust. However, the average turbine RPM remained relatively constant during the run once detonation had full established.

DeBarmore et al. examined the effects of inserting a Nozzle Guide Vane (NGV)

cascade into the exhaust of an RDE.[31] The guide vanes they used were from a T63 gas turbine engine. They were able to achieve a detonation in the RDE with a near stoichiometric mixture of hydrogen and air. By measuring the pressure fluctuations both upstream and downstream of the guide vanes, they were able to determine that the pressure fluctuation from the passing detonation wave propagates through the guide vanes and would propagate to the turbine, had one been included in the test.

Naples et al. eventually tested the T63 gas turbine engine coupled to an hydrogen/air RDE and compared it to the T63 operating using its conventional CPC operating on hydrogen. They operated the RDE/turbine setup without cooling for 20 minutes and showed no signs of damage to the turbine. Their results also showed an increase in turbine power output with the RDE over a range of engine RPM settings. These results give confidence in operability of a RDE coupled to a turbine, and reduces the concern of not actively cooling the turbine blades.[26]

2.3.3 Radial RDE Turbine Integration.

Integrating a turbine with a Radial RDE is a challenging tasks and has only been done by Higashi et el.[25] Their device was discussed in more detail in Section 2.2.3 and shown in Figure 18. Their device was able to produce an increase in RPM once the electric motor was disconnected due to the detonation in the combustion channel. Two main drawback of their design were that the compressor was not optimized and they saw a drastically different exit flow angle out of the turbine than what was expected. The non-optimal compressor was a detriment to the efficiency of the cycle, but maximum cycle efficiency was not the main goal of this study. The real issue was with the large deviation in exit flow angle for the turbine. They designed the turbine with an exit flow angle of 70° while the achieved angle was 27°. They hypothesized that this was due to separation in the turbine which would not allow for the expected

turbine performance to be seen, but offered no comment on the reason behind the flow separation. This research is important for the understanding of how a turbine blade row behaves behind a detonation in a RRDE. While the design tested in this paper does not operate in the same inside-out method as the one shown in Higahsi et el., their test showed the effects of blades in the wake of a RRDE detonation wave.

2.4 Radial-Inflow Turbines

Radial turbines are rotating pieces of turbomachinery that extract work out of a flow field in a similar fashion to axial turbines. However, these devices operate by also turning the flow from initially radial 90° to exit axially. This distinction between the two turbines, as well as the benefits of radial versus axial turbines, is discussed in Section 2.4.1. Because these turbines are operating a high rotational velocities, it is necessary to turn the incoming flow in order to match the required inlet flow condition in the turbine. Why this is necessary and how this has been accomplished in the literature is discussed in more detail in Sections 2.4.2 and 2.4.3.

2.4.1 Radial Turbine Performance.

Radial turbines offer a benefit over axial turbines in specific applications such as low mass flow operating conditions and in situations that require a compact design.[32] The efficiency advantage of these devices over axial turbines occurs at lower mass flow rates and is due to the differences in expansion process through the turbines. In axial turbines the flow stays at roughly the same radial distance throughout its expansion process which means the relative total pressure and temperature are constant through the blade passage; however, in radial turbines as the flow travels radially inward the relative total pressure and temperature decrease. This results in radial turbines operating at lower velocities for a given expansion.[32]

To quantify where radial turbines operate optimally a performance parameter known as specific speed, N_s, is used, defined as:

$$N_s = \frac{NQ^{\frac{1}{2}}}{H^{\frac{3}{4}}} \tag{9}$$

where N is the rotational speed of the turbine, Q is the volumetric flow rate, and H represents the ideal work, or head, of the turbine. Radial turbines operate most efficiently at a specific speeds ranging from 0.2 to 0.6, where axial turbines operate at specific speeds greater than 1.0.[32]

While specific speed of the turbine drives operating efficiency of the turbine, a structural limit exist that dictates the maximum RPM of the device. This limit is based on the maximum tip speed of the turbine and typically ranges from 350 $\frac{\text{m}}{\text{s}}$ to 500 $\frac{\text{m}}{\text{s}}$ depending on the turbine material and the operating temperature.[33] This limit is important to keep the centrifugal stress of the turbine below its limit and avoid issues with creep or structural failure.

Finally, blade loading is another important aspect of the operation of all forms of turbomachinery, espcially radial turbines. Blade loading is essentially the "lift" that the turbine blade is producing due to the differences in pressures on the pressure and suction side of the blade. Figure 20 shows the pressure and suction sides of a turbine cascade as well as the blade loading profile of a blade. It is important to note the area between the curves represents the total force on the blade and the difference in height of the curves at an given point represents the force acting at that particular point. In radial turbines it is important to maintain a lower value of blade loading at the entrance of the turbine and increase blade loading as the flow is turned through the passage.[32]

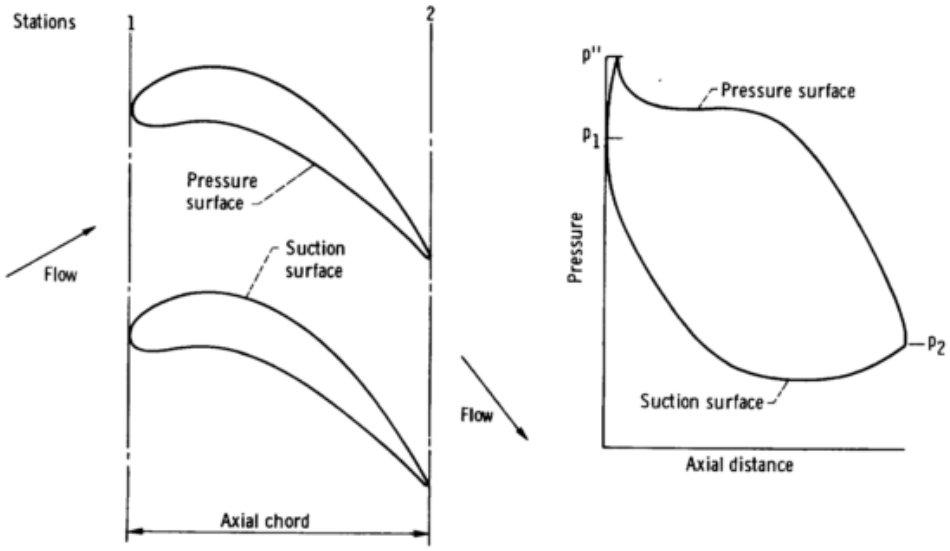

Figure 20. Loading Profile of a Turbine Blade.[32]

2.4.2 Velocity Triangles.

Because radial turbines are rotating turbomachines, the relative inlet velocity that the blades see is different than the actual inlet velocity in the absolute frame of reference. To understand this relationship, two dimensional velocity triangles are used as seen in Figure 21. In this figure V is the absolute velocity entering the turbine, U is the rotational velocity of the turbine tip, and W represents the relative velocity, as seen by the blade. The relative velocity show in Figure 21 is actually flowing against the direction of motion of the blades. This is done to decrease the loading on the blades at the inlet.[32]

In all radial turbines this tangential component of the absolute velocity is needed in order to match the tangential velocity of the blade tip. There are two main methods to achieve the tangential velocity. The first method uses a scroll, or volute, that takes in the flow from a pipe and progressively decreases the volume as the flow is directed around the the turbine. This application is typical of automotive turbocharger turbines and relies on proper design of the scroll to do all of the flow turning. The other method involves the use of guide vanes before the entrance of the turbine. This

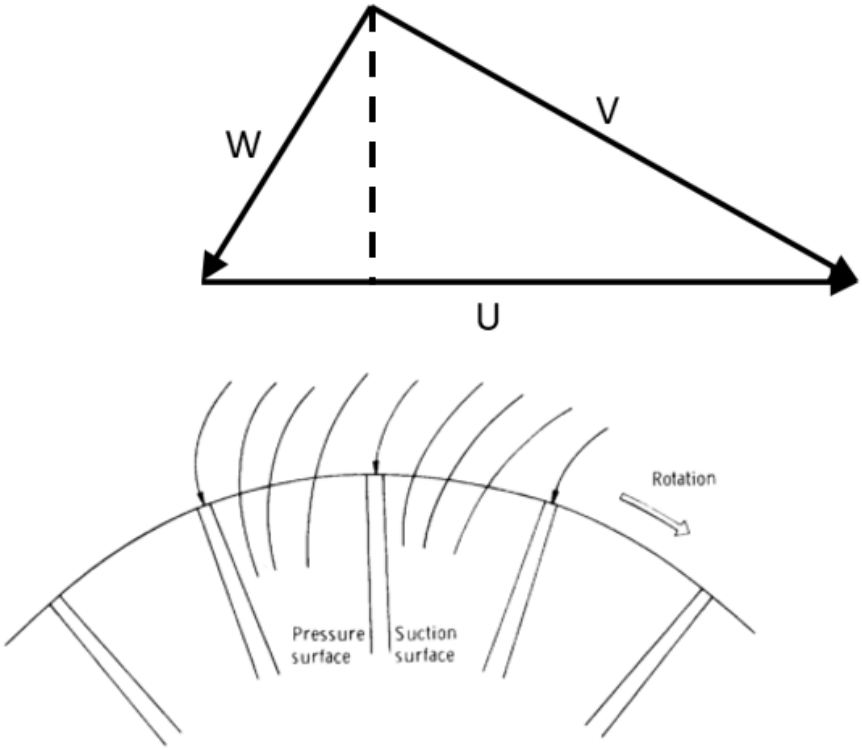

Figure 21. Velocity Triangle of a Radial Turbine. Adapted from Glassman et al.[32]

method directly turns the flow much like a the guide vanes before an axial turbine.

2.4.3 Stator Blade Design.

As discussed in Section 2.4.2, radial inflow turbines require a tangential velocity component in order to operate. To achieve this tangential velocity one of two devices is needed. The first is to design a spiral housing with decreasing volume to condition the flow and impart a change in the velocity. The second method is through the use of NGVs, which utilize the curvature and angle of the blades to turn the flow.[32]

Harold Rohlik discuses radial inflow turbine NGV design philosophies in Chapter 10 of Turbine Design and Application.[32] He suggested that, in general, the NGVs used in radial inflow turbines have low solidity, σ, and low aspect ratio, AR. Solidity is the ratio of the blade chord length, c, to blade spacing, s, and is given by the

equation:

$$\sigma = \frac{c}{s} \tag{10}$$

Aspect ratio is the ratio of the blade height, h, to it chord length, c and is given by the equation:

$$AR = \frac{h}{c} \tag{11}$$

Rohlik also discuses the effects of pre-swirl on the NGVs. He defines pre-swirl as the tangential velocity component before the NGVs. If the flow has sufficient pre-swirl then little chamber is needed for the blade profile of the NGVs since the flow has a significant tangential velocity component coming into the blades; therefore, less turning is required out of the blades, themselves.[32] This principle allows for statorless radial turbines that use a scroll and the conservation of angular momentum to attain the proper tangential velocity for the rotor.

Reichert et al. present a design procedure for transonic and supersonic nozzle guide vanes for radial inflow turbines.[34] Their method solves the flow field by breaking the airfoils into two parts. The first in the converging section which accelerates the incoming flow to the sonic condition. The second section is the diverging section which, depending on the conditions specified downstream, either accelerates the flow supersonic or slows the flow to subsonic velocities. For supersonic exit flow, they suggest turning the flow during the converging section and minimizing the turning of the supersonic-diverging section.

2.5 Pressure Measurement Techniques

One of the bigger difficulties in measuring the pressure in an RDE is the high temperatures in the channel. This restricts the use of conventional pressure measurement devices like Pitot tubes and Kiel probes. These devices are limited to short duration

runs or they risk the possibility of melting. Stevens et al. testied the measurement capabilities of three different devices: a Kiel probe, a Capillary Tube Average Pressure (CTAP) device, and an Infinite Tube Pressure (ITP) device.[35] Their results showed the feasibility of the CTAP and ITP devices for attaining pressure measurements in the hostile conditions of an RDE channel; however, the Kiel probe melted during testing, reaffirming the need for pressure measurement devices that are shielded from the channel itself. The following sections will discuss these two devices in more detail and offer the benefits and drawbacks of both, as well as possible applications.

2.5.1 Capillary Tube Average Pressure.

Capillary Tube Average Pressure devices consist of a long, narrow diameter tube connected on one end to a pressure transducer. Figure 22 shows a schematic of a CTAP device. This device is fairly simple and protects the pressure transducer from the temperatures in the channel. It records a time averaged pressure of the channel, and because of the length of the tube, most of the noise in the signal is damped out before reaching the pressure transducer. However, the damping of the signal does not allow CTAPs to detect minor fluctuations in the pressure, which hurts their transient response.[35]

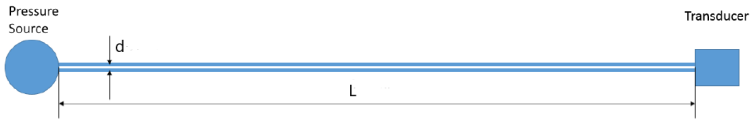

Figure 22. Capillary Tube Average Pressure Device. Adapted from Stevens et al.[35]

Fotia et al. used a row of CTAP devices mounted axially along the channel of an RDE to gain insight of the regions within the channel. The CTAPs showed a region of mixing at lower pressure in the beginning of the channel, followed by a region of higher pressure that corresponded to the detonation region. Lastly, the CTAPs show an exhaust region in which there was a steady decrease in pressure from the end of the

detonation region to the exit of the RDE.[22] This measurement technique allows for close approximation of where the detonation occurs within the channel if no visible access is available.

Fotia et al. then examined the effects of varying the length and tube diameter on the pressure response in CTAPs mounted in the air plenum of a RDE. Their results showed that for tubes with an inner diameter less than 0.010 in the attenuation of the unsteadiness of the signal was increased as the static pressure was increased. They also showed that as the length of tube was increased the frequency response from the signal was reduced to the point where the frequency of the signal was lost and the pressure settled on the average value of pressure of the input signal. Finally, they showed that as the diameter of the tube was decreased the attenuation of the signal was increased; therefore, a long tube of minimal diameter is wanted to eliminate the frequency variation of the RDE pressure signal.[1]

2.5.2 Infinite Tube Pressure.

Infinite Tube Pressure devices are similar to CTAPs in the sense that they protect the pressure transducer from the high temperatures; however, they differ in how they operate. ITP probes consist of a long tube that typically exhaust to ambient and a teed off section near the pressure source where the pressure transducer is attached. Figure 23 shows the layout of an ITP probe. By using this design ITP probes are able to collect the transient pressure measurements that the CTAP could not. If designed with the proper length, the pressure transducer does not create a resonator, which allows these devices to minimize the noise in the signal caused by the reflections of the pressure waves in the tube and improves the quality of the transient pressure measurement.[36] Englund et el. also mentions that the tube should have no sharp turns and have a constant cross-sectional area in order to avoid pressure reflections.

He also suggest that having the transducer tee off closer to the pressure source will lessen the magnitude of of the oscillation from any reflection.

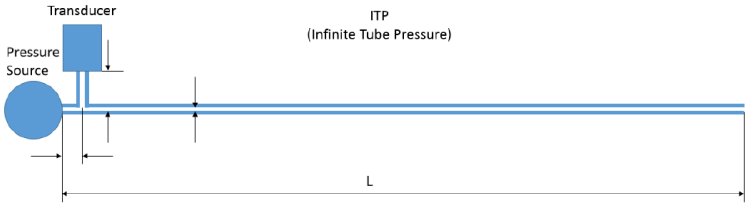

Figure 23. Infinite Tube Pressure Device. Adapted from Stevens et al.[35]

Stevens et al. showed their ITP probe was able to capture the transient pressure fluctuations within the RDE but they noticed that their ITP probe had significant noise in the signal that manifested in pressure fluctuations not associated with the passing detonation waves.[35] They postulate this was due to the tee they used to connect the tubes and pressure transducer. The tee had a change in cross-sectional area that may have caused it to act like a resonator, leading to the noise in the signal.

Naples et al. examined the response of an ITP probe in a variety of configurations. They showed that as the standoff length from the teed section was increased, and the subsequent volume between the transducer face and the main tube increased, the pressure response was weakened. However, the initial temporal response of the pressure wave was relatively unchanged, but the larger cavity volume took longer to reach the pressure of the test section. This fact allows ITP probes to be used to track the arrival of the detonation wave, but not its actual pressure. Finally, they noticed as the volume of the teed section was changed and the natural frequency of the ITP probe teed section changed, the pressure traces showed the variation in natural frequency was shown in the pressure wave reflections, but they cited this was a much smaller effect.[37]

III. Experimental Setup

This chapter will discuss the methodology of the design and testing process for the Radial RDE. It will include an introduction to the test facility, Section 3.1, the equipment used for testing and the test setup, Section 3.3, a detailed description of the design process, Section 3.2, the test procedures and test matrix, Section 3.4, and the uncertainty analysis for this thesis with example calculations, Section 3.5.

3.1 Facility

The test facility used for this project was the Detonation Engine Research Facility, (DERF), owned by the Air Force Research Lab, (AFRL) at Wright-Patterson Air Force Base, (WPAFB) in Dayton, Ohio. The critical capabilities and a brief overview of this research facility will be discussed further in Section 3.1.1. Within the DERF are several test stands which allows a variety of detonation engine research to be conducted in parallel. The specific test stand used to test the Radial RDE, along with its features is discussed in Section 3.1.2.

3.1.1 Detonation Engine Research Facility.

The Detonation Engine Research Facility is a test bay owned by the Turbine Engine Division of AFRL at WPAFB. It was originally designed for large scale turbojet engine testing, but now solely focuses on detonation engine and pressure gain combustion research. Because it was designed to test full scale turbojet engines the building features a large test cell with a fuel room isolated from the rest of the test bay. A schematic of the DERF is shown in Figure 24. Its control room is protected by two feet of reinforced concrete to protect the research team. High pressure air for the facility is stored in tanks separate from the test cell and fuel room. The facility is

also plumed to handle high pressure hydrogen which is supplied from a tuber trailer located behind the facility.

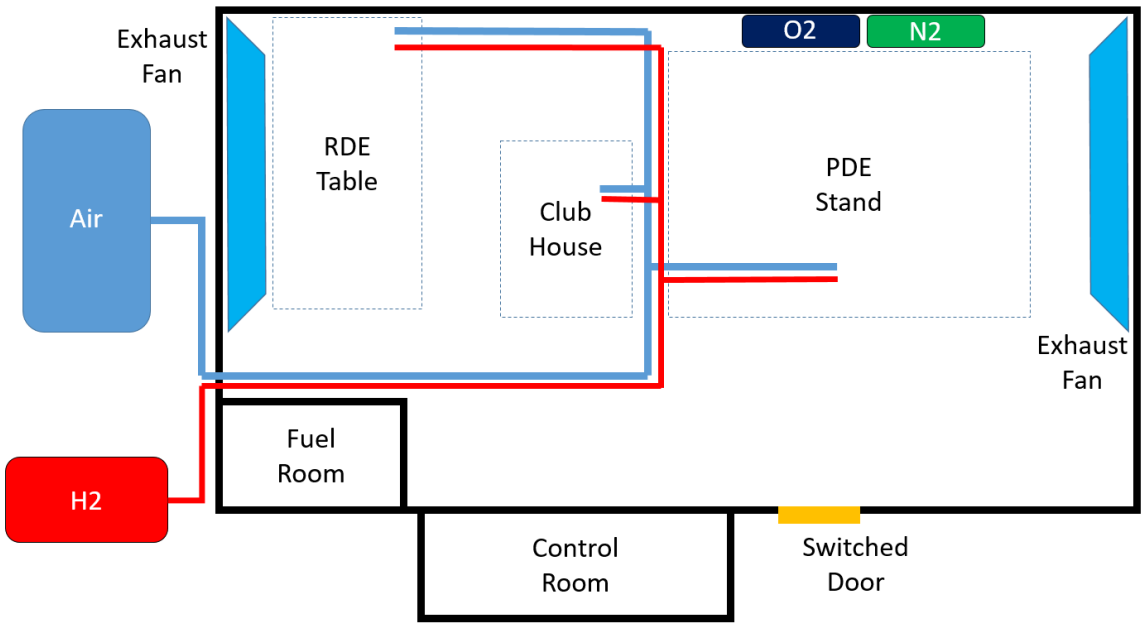

Figure 24. Detonation Engine Research Facility Layout.

The test cell features three main areas of testing: the RDE Table, the Club House, and the PDE Stand. The RDE Table is where the majority of the current RDE testing is conducted. This area features a heated fuel/air line, a small thrust stand, and the ability to have multiple experiment setups at once. The RDE Table was used by Fotia et al.[23] for testing multiple gaseous fuels in an RDE. The Club House area features a couple of test stands where the majority of the optical testing occurs due to the increased space. It also features a pre-mixed RDE test stand used by Andrus et el.[38] to conduct testing on many pre-mixed RDE designs. The PDE Stand features a large thrust stand and was the location of the majority of the early PDE research conducted at the DERF. The PDE Stand is where Schauer et al.[14] conducted their PDE studies and also where Naples et al.[26] conducted testing of the T63 turbine. This location was where the testing of the RRDE occurred and more detail on its layout will be given in Section 3.1.2.

Control of all of the test cell stands is done remotely from the control room. The control room has multiple safety features including a camera constellation with the ability to view the entire bay, valve control switches to cut off fuel or air flow and a switch on the test cell door that must be fully closed to operate any test stand. The test stands are controlled by the *LabView 2012* software, which is a program that collects and records data during each run. The computer used for the data collection was a National Instruments *PXIe-1085* which allowed for the use of eight channels of high speed analog input and sixteen channels of low speed analog input. For this project the high speed channels operated at a collection rate of 1 MHz and the low speed channels operated at 90 Hz.

3.1.2 Radial RDE Test Stand.

For this research, the PDE Stand was utilized, seen in Figure 25. The PDE Stand has its own high pressure air (light blue) and hydrogen (red) line which were used for the RRDE tests. It also featured a separate hydrogen (red) and oxygen (dark blue) lines for the pre-detonator which was used to ignite the RRDE. More detail about the pre-detonator will be discussed in Section 3.4.1. Next, the PDE stand featured nitrogen lines used to regulate and actuate the valves in the system. There were low pressure nitrogen lines used to control the solenoid valves. The air line was regulated upstream of the test stand and then brought up to the PDE stand, it was at this location where the air control valve was located with the sonic nozzle just after the valve. The hydrogen line was regulated at the PDE stand. This line used high pressure nitrogen to regulate the flow, which was done because the nitrogen would not react if there was a leak.

Figure 26 shows a side view of the test stand with the existing air and fuel lines that bring the gases to the PDE stand. The air control valve and the line leading to

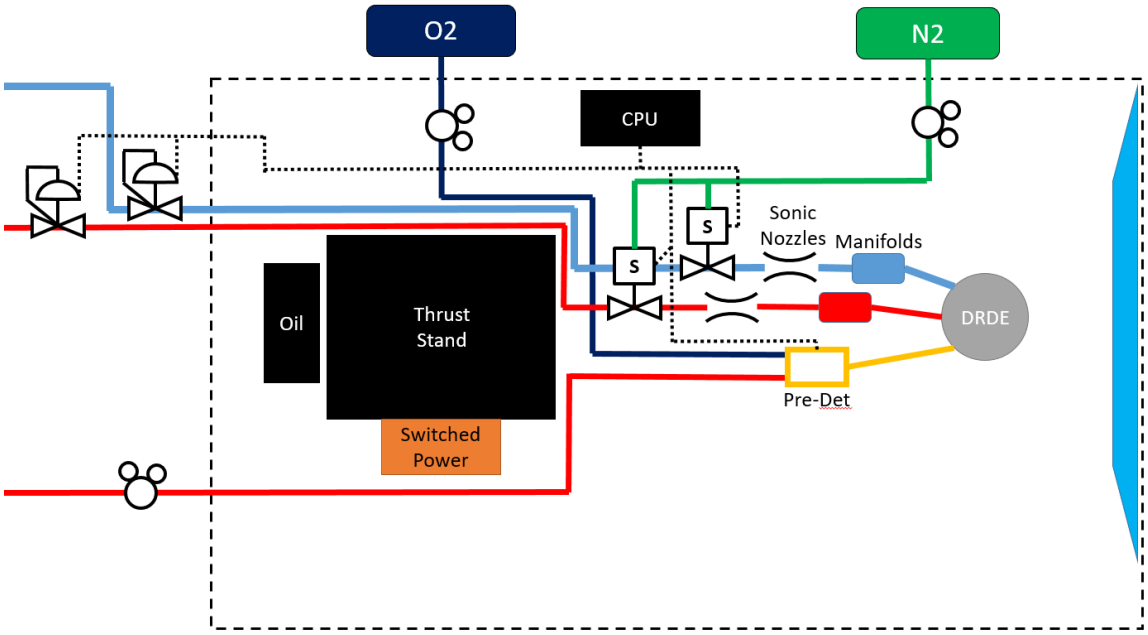

Figure 25. PDE Stand Layout.

the air sonic nozzle is clearly visible. After the sonic nozzle the air line runs to the air manifold, which will be discussed more later in this section. Also visible is the location of the fuel control valve which is before the fuel sonic nozzle. The rest of the fuel line is shown in 27 (b) with the fuel sonic nozzle leading to the fuel manifold.

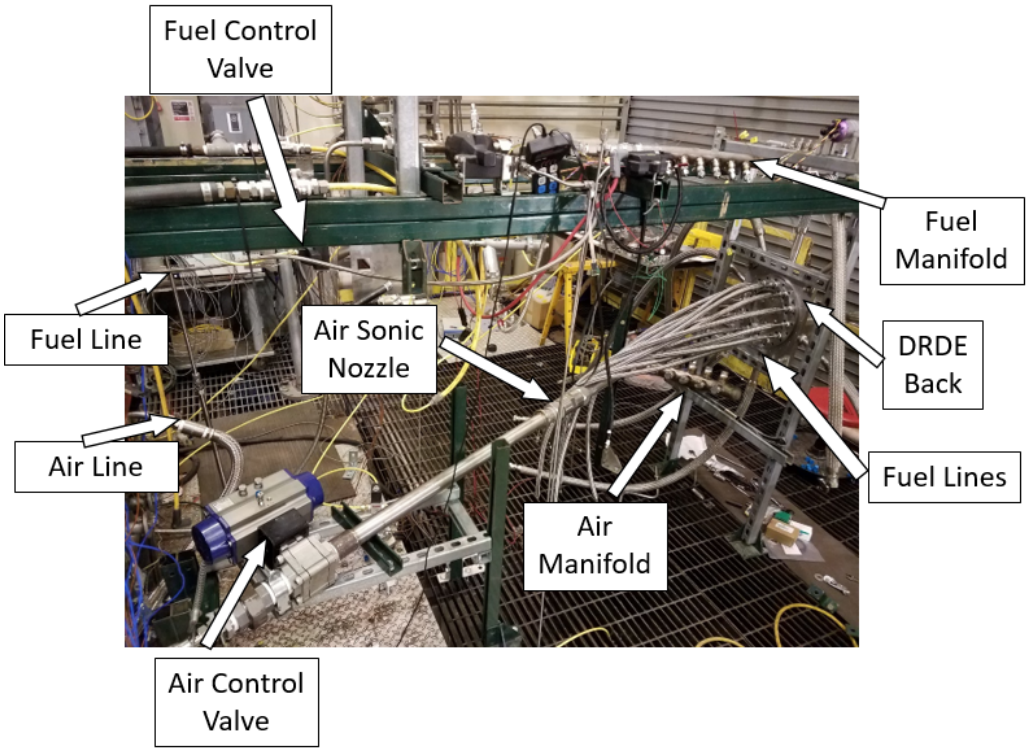

Figure 26. PDE Stand Configured for Radial RDE.

With the locations of the air and hydrogen lines and the mass flows required for this project, a new manifold for each was needed along with flexible air and fuel lines to bring the air and fuel to the RRDE. These manifolds are shown in Figure 27 (a & b) and they show the 10 flex lines used for the air, (a) and the 12 flex lines used for the fuel, (b). Figure 27 (c & d) shows the flex lines attaching to the RRDE itself. In (c) the 10 air lines are located at the outer radius of the RRDE and they are separated by 36°. These air lines are all 19.05 mm in diameter. The number of flex lines was determined based on achieving an even flow injection around the RRDE and to ensure the minimum area of the air flow was not the flex lines themselves, but in the RRDE. Shown in (d), the 12 fuel lines mount to the back of the RRDE and are separated by 30°. These line were all 9.5 mm in diameter, and the number was dictated in the same manor as the air lines.

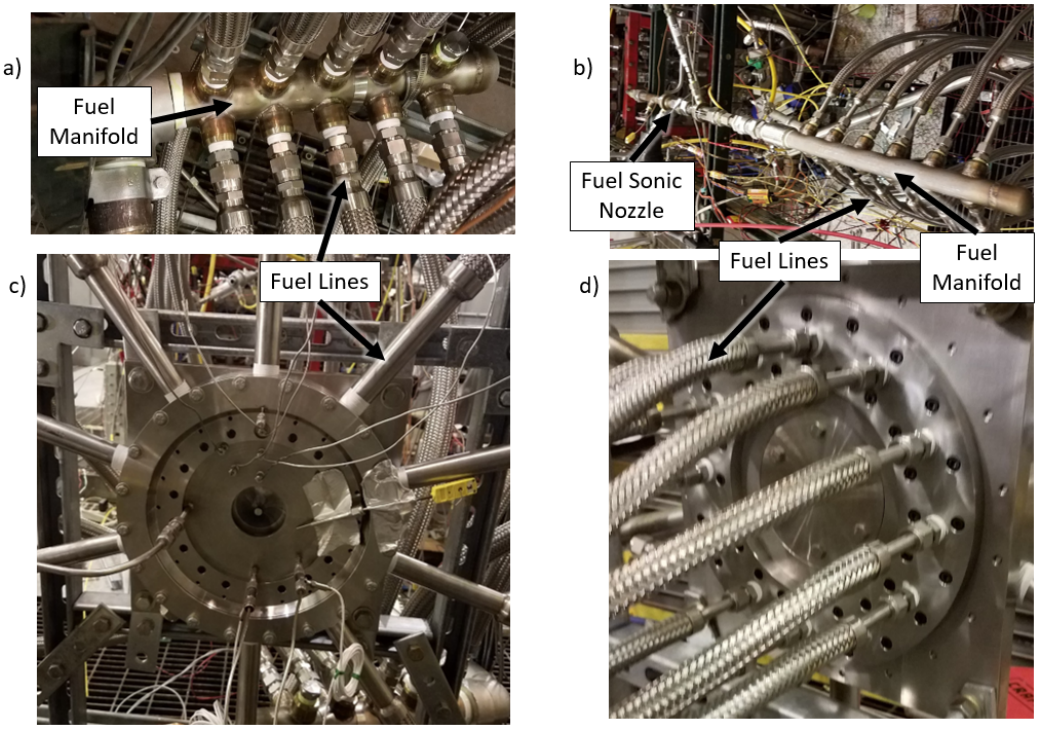

Figure 27. Radial RDE Front and Back with Manifolds.

The PDE Stand also has an oil system, Figure 29, which was used to oil the turbocharger during testing. This oil system features a pump that can be regulated to the oil pressure required by the turbocharger, an automotive oil filter, and a return sump used to collect the oil returning from the turbocharger. The setup used during the turbine testing, minus the compressor inlet measurement piping, is shown in Figure 28. The compressor inlet and outlet piping were the same used by Rouser et al. but this test did not include the laser tachometer.[27] Instead a magnetic RPM sensor was used, which was included in the Garrett Turbo RPM kit. Because of the width of the compressor housing, the fuel lines were altered by using elbow fittings at the back of the RRDE instead of straight fittings. This was the only major change from the original setup. The turbo was situated such that the oil feed line was on the top and the oil return line at the bottom. This was done to help remove the oil from the turbocharger with the help of gravity. It should be noted that the

turbocharger is typically water cooled in automotive applications, but due to the short run times and long cooling periods between runs, the decision to solely rely on oil to cool the turbocharger was made. The final additions to the turbocharger set were the compressor inlet and exit measurement devices. The actual devices will be discussed in more detail in Section 3.3, but the setup featured measurements of mass flow, RPM, compressor inlet temperature and pressure, and compressor exit temperature and pressure. This was nearly identical to the setup used by Rouser et al.[27]

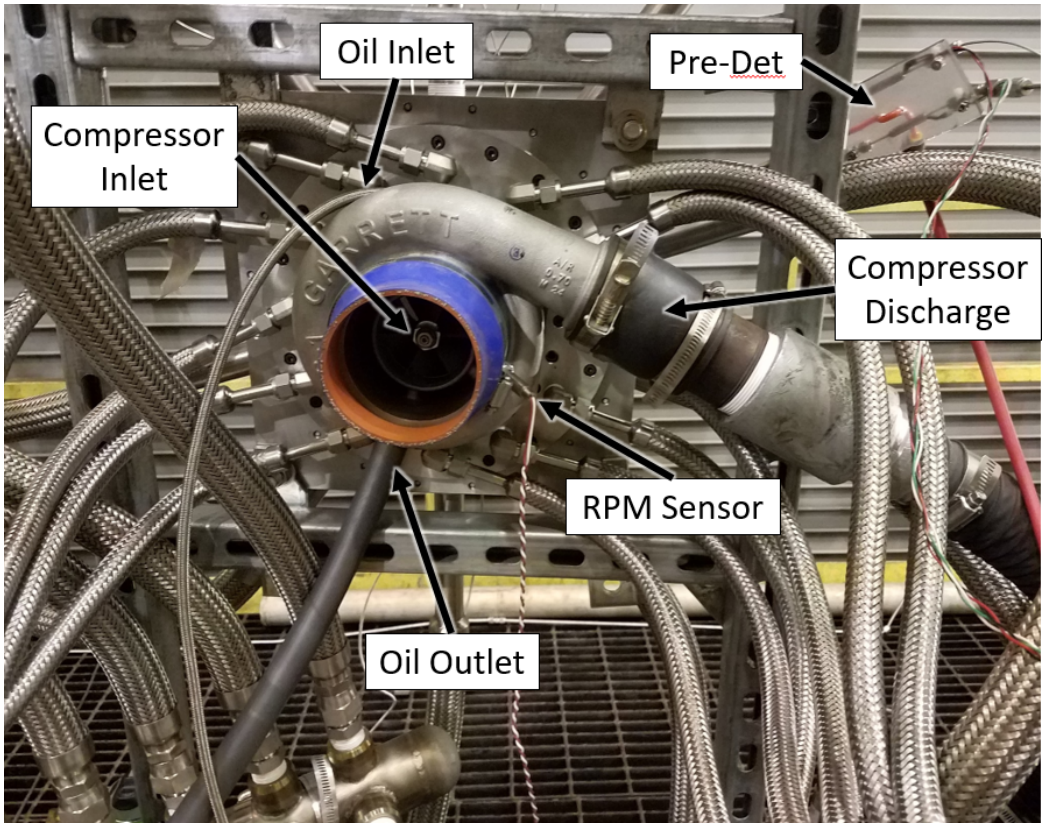

Figure 28. Radial RDE Setup with Turbocharger.

The controls for this test setup were done using *RDE Table5* which was installed on a computer dedicated to the PDE Stand. This computer controlled the regulators, valves, and spark plug for the pre-detonator. It also recorded data for the multitude of pressure and temperature measurements done on the RRDE. The placement and

characteristics of these devices will be discussed further in Section 3.3.

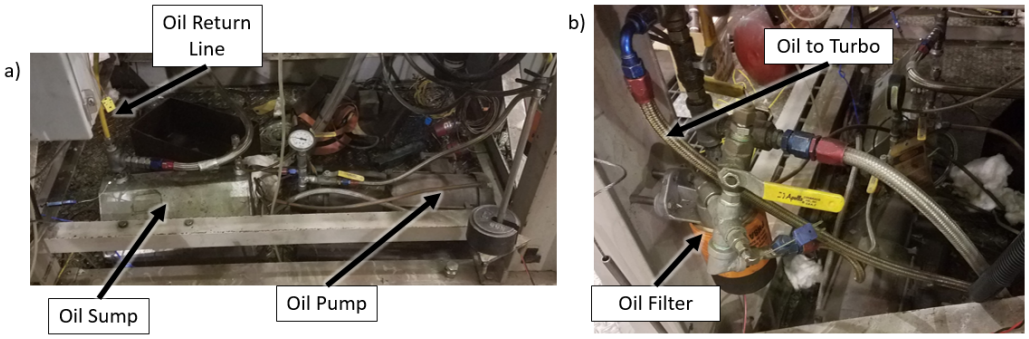

Figure 29. PDE Stand Oil Lines. (a) oil sump and pump & (b) oil filter

3.2 Radial RDE Design

This section discusses the design of the Radial RDE. To best understand the challenges faced during the design process, an understanding of the geometry of the RRDE as well as the fundamental operating principles is needed. This section will provide a brief overview of the RRDE layout and why this geometry was selected before discussing the design constraints and the final design.

Figure 30 (a) shows a cartoon sketch of a conventional RDE. The defining features of a RDE are the air injector or throat, A_t, the detonation channel, A_c, and the nozzle, A_n. The throat is where the air is injected into the detonation channel, and also where the fuel is injected and mixed with the incoming air. Next, the mixture enters the channel where it is detonated. The combustion products then exit out of the channel through the nozzle. A Radial RDE operates in a similar fashion, where air and fuel area injected and mixed, as suggested in Figure 30 (b). The mixture enters a similar detonation channel, but now must turn 90° before exiting through the nozzle.

When examining RDE geometry, the width of the detonation channel, the throat area ratio, AR_t, and the nozzle area ratio, AR_n, are often used to compare performance between different devices. The same holds for the RRDE geometry. It was

designed with the ability to vary the channel dimensions and the area ratios for the throat and nozzle. The details of how this is done will be discussed in more detail in Section 3.2.2.

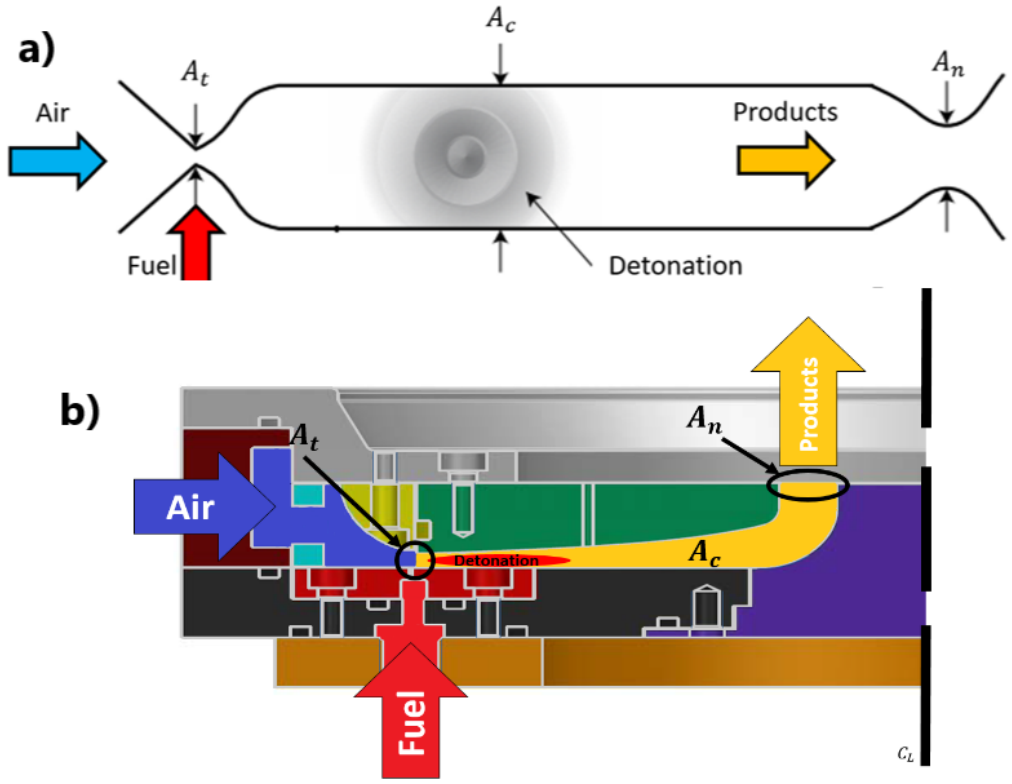

Figure 30. Flow Path Characteristic of a RDE and RRDE. (a) typical RDE flow features & (b) Radial RDE flow features.

To achieve a better understanding of the notional flow path of a RRDE, a top down view is provided in Figure 31 (a). The path of the air flow is directed radially inward which is shown by the blue arrows. Figure 31 (b) shows a cross sectional slice taken through the center of the RRDE, with the air flowing from the outer radius. The detonation channel layout is shown with the white ring in (a) and the solid yellow section in (b). It is important to note that in (a) the channel is blocked from view and the white ring is a representation of the channel as if it were visible. In (a) the detonation wave is shown by the red line at the outer radius of the channel, with the coupled oblique shock, shown with the black line. This wave propagates in

a circumferential direction, shown by the black arrow. Like conventional RDEs, as long as fresh reactants are provided the detonation wave will continuously propagate around the channel. The products of combustion exit the channel through the nozzle, shown by the solid yellow ring in (a). Therefore, the products are exiting out of the page when viewing the RRDE from the top. The channel exit is highlighted in (b) by the yellow arrows representing the products of combustion. Once again the products turn 90° from the initial flow direction. It is this location where a radial inflow turbine was inserted.

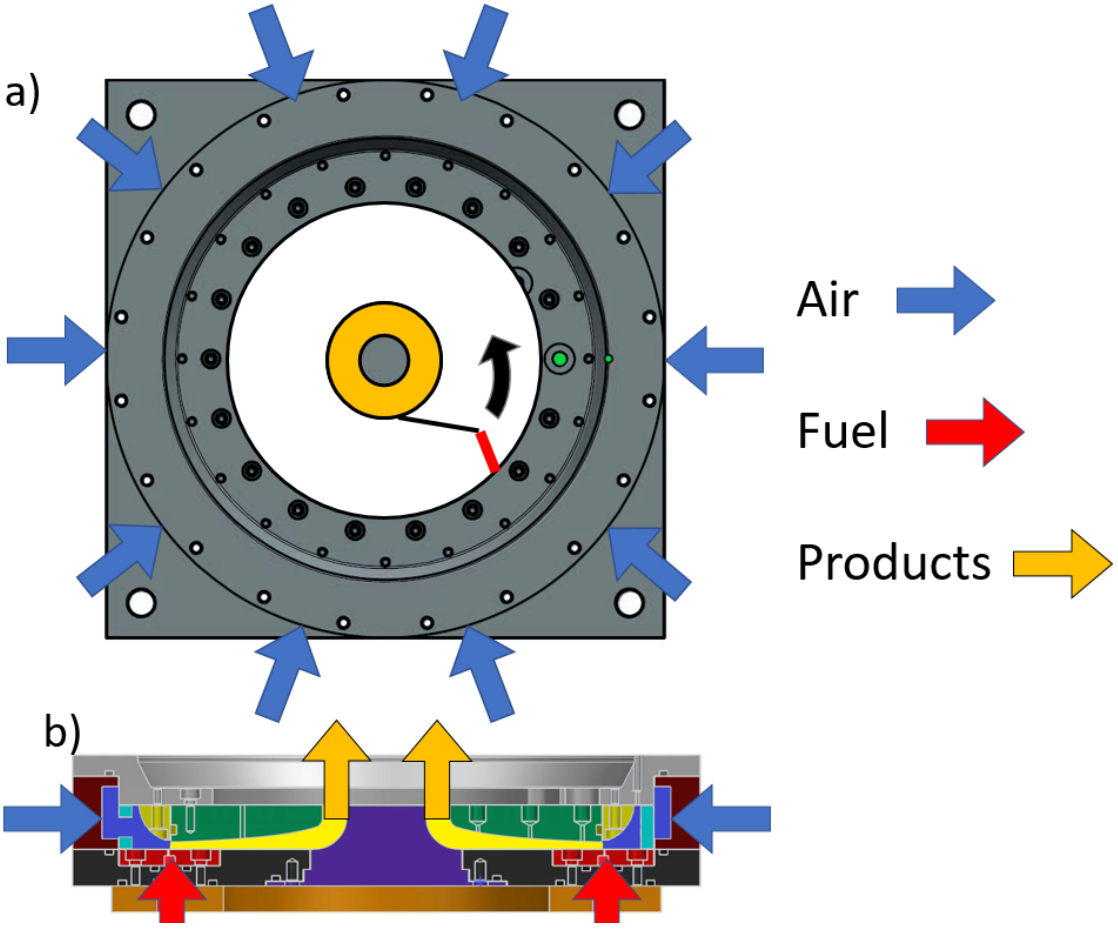

Figure 31. Schematic of Radial RDE Flow Path (Top View).

A firm grasp on the layout and operation of the RRDE provides a sense of the complexity of the design. The rest of this section will discuss the design constraints

for this project, Section 3.2.1, the final design and its features, Section 3.2.2, and the design of a channel and NGVs to mount with the turbocharger turbine, Section 3.2.3.

3.2.1 Design Constraints.

The design process of the Radial RDE started with a few initial constraints and design requirements. The purpose of the RRDE was to determine its feasibility as a compact APU. This involved serving as a testbed for the characterization of the operability of RRDEs as well as measuring its power output when coupled with the turbine. Because of these testing requirements, the RRDE needed to be a modular device that could easily swap pieces to test more configurations without having to create and manufacture a new RRDE. The modularity of the device allowed for a multitude of test variables which included the channel height, channel area, total mass flux, fuel injection scheme, air injection area ratio, nozzle area ratio, and nozzle guide vane layouts. Finally, the modularity allowed for the coupling of the selected turbocharger turbine.

The design constraints for the RRDE will be discussed in more detail in Sections 3.2.1.1 and 3.2.1.2. Sections 3.2.1.1 focuses on the selection of the turbocharger turbine for the RRDE which dictated the mass flow through the RRDE. Section 3.2.1.2 will discuss the sizing constraints that were selected for the RRDE based on a maximum allowable size of the device.

3.2.1.1 Turbocharger.

To create a higher power density APU, the Radial RDE need to be compact, but also it needed to produce on the order of 100 kW of power. To measure the power output of the RRDE a turbocharger was used. The turbocharger selected for

this project was a Garrett GT3582R, shown in Figure 32, which featured a 68 mm diameter radial inflow turbine with a turbine exit diameter of 62 mm. According to the Garrett Turbocharger Catalog, this turbocharger had a maximum mass flow rate of 0.55 $\frac{\text{kg}}{\text{s}}$ and a maximum operating speed of 130 kRPM.[39] This turbine was selected because it had a high mass flow rate for a commercially available turbocharger of this size. This is important because it helped keep the size at a minimum while providing a higher mass flow.

Figure 32. Garrett GT3582R Turbocharger.

Having a high mass flow is important because the power extracted from a turbine is a linear function of mass flow rate, which is given by the equation:[33]

$$\dot{W}_t = \dot{m} c_p \Delta T_t \tag{12}$$

where W_t is the power extracted from the turbine, c_p is the specific heat at constant pressure of the working fluid, and ΔT_t is the difference in total temperature of the fluid between the entrance and the exit of the turbine. Turbine power is also estimated

by:[33]

$$\dot{W}_t = \dot{m} {U_t}^2 \tag{13}$$

where U_t is the turbine blade tip speed. As mentioned in Section 2.4.1, the tip speed is limited by the material of the turbine and the properties of the working fluid and is typically limited to $350 - 500$ $\frac{\text{m}}{\text{s}}$. Tip speed is determined using Equation 14:

$$U_t = \omega r \tag{14}$$

where ω is the rotational speed of the turbine and r is the tip radius of the turbine. At its maximum RPM given by the manufacturer, the GT3582R has a maximum tip speed of 462.8 $\frac{\text{m}}{\text{s}}$. Due to the limited tip speed, to maximize turbine power the mass flow should also be maximized. Using Equation 13, an estimated maximum turbine power for the GT3582R of 118 kW. This is a rough estimate of the power extracted from the flows typically seen by an automotive turbocharger, and offered a good reference for the power extracted from the turbine coupled with the RRDE. The RRDE was designed around the selected turbocharger, and its size and operating window were dictated by the turbocharger's geometry, discussed in Section 3.2.1.2.

Now that the turbocharger was selected, the maximum mass flow rate through the RRDE was set. Like mentioned in Section 2.2.2.2, the mass flux, $\dot{m}''$, through the RRDE should be kept below a maximum of 300 $\frac{\text{kg}}{\text{m}^2\text{s}}$to achieve optimal performance. Therefore, the maximum mass flow rate, $\dot{m}$, of 0.55 $\frac{\text{kg}}{\text{s}}$ dictated the minimum channel area, A_c, of $2.3 * 10^{-3}$ m^2. The combination of the maximum mass flow rate and the minimum channel area correspond to a mass flux of 240 $\frac{\text{kg}}{\text{m}^2\text{s}}$through the channel, determined by Equation 15:

$$\dot{m}'' = \frac{\dot{m}}{A_c} \tag{15}$$

3.2.1.2 Size Constraints.

The initial sizing constraints for the RRDE design were primarily concerned with the overall size of the device, with the goal of achieving a compact design. This was set at a maximum outer diameter of 304.8 mm because a device of this size would be able to fit in a standard wing pod on an aircraft. This maximum outer diameter dictated other features of the RRDE, which included the length of the channel, size of air injection section, and the size of the turbine that could fit in the RRDE.

The overall radius of the RRDE had to fit a spacer ring at the outer radius where the air lines mount, an air distribution section before the injector, the injector, a detonation channel, and the turbocharger. To create the channel, a spacer ring was used which also served as the mount for the air lines which required 16.8 mm of width for the air line fittings. The minimum channel length determined for the RRDE was set at 76.2 mm due to the desire to insure the detonation wave occurs in the channel and not the exit of the RRDE. The region in the center of the RRDE was reserved for the turbocharger, and took up a radius of 34 mm. Given the maximum 152.4 mm radius and the previously mentioned size constraints, the left over space was for the air injection section was set to achieve a uniform flow distribution around the RRDE, which was 25.4 mm.

The overall height of the RRDE, when full assembled, was not constrained but it was kept to a minimum to increase the compactness of the RRDE. At its maximum, the RRDE is 7.6 cm tall. This gives a total volume of the RRDE of around $5.5 * 10^{-3}$ m^3.

3.2.2 Final Design.

With the design constraints implemented, a final Radial RDE design was accomplished. The results of the final design as well as a detailed description of all the

necessary parts is given in this section. Accounting for all of the requirements and geometric challenges, a final RRDE design was made. A detailed cross-sectional view of the ten pieces that make up the final design as well as its flow path is shown in Figure 33. This device has an outer diameter of 304.8 mm and an overall thickness of 76.2 mm. Figure 34 shows the RRDE in an exploded form to give a better understanding of how the pieces fit together and to define the nomenclature used to describe these pieces. Throughout this section each piece of the final RRDE will be discussed in more detail and the benefits of the RRDE's modularity will be highlighted.

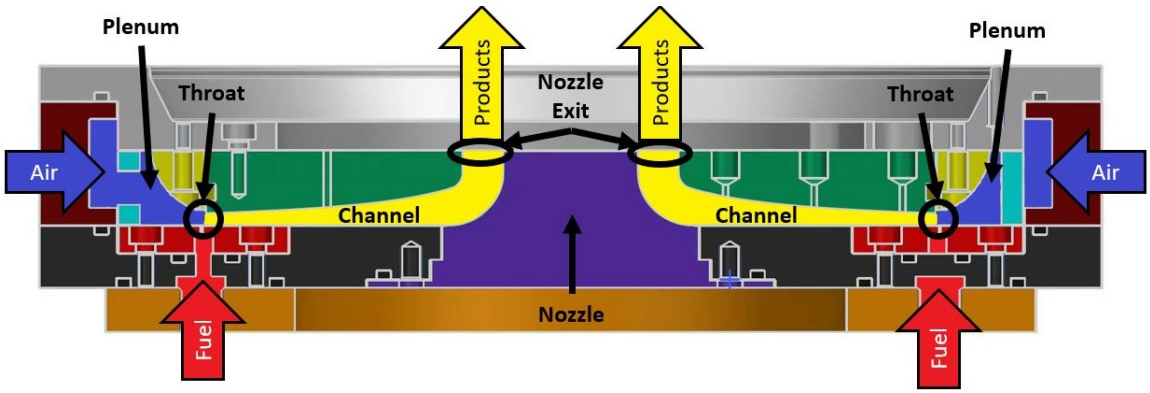

Figure 33. Cross Sectional Cut Away of the Final Radial RDE Design with Flowpath Highlighted.

The solid, dark blue region represents the air injection and stilling chamber for the RRDE. In this region the fresh air was brought in through the spacer ring (brown) by 10, 19.1 cm diameter air lines. These air jets were then broken up by the air distribution ring (light blue) which features 55, 12.7 mm diameter holes. At this point the air was well distributed and enters the stilling chamber itself which had a height of 2.16 cm at a radius of 12.2 cm, which corresponds to a flow area of 165 cm^2. This was the location where the pressure measurement in the air plenum was made. This pressure measurement along with other measurements on the RRDE will be discussed in Section 3.3. The air then flows into the throat, which had its height set by the throat ring (gold) and the shim rings (white).

Fuel was injected through the path shown by the solid red region. The fuel was first injected into the device through the fuel line mounting ring (orange), then it proceeded through a set of fuel distribution rings which were a part of the baseplate (black). Once properly distributed, the fuel was then injected at the throat by the fuel injector ring (dark red). The fuel/air mixture then proceeded to the channel, shown in solid yellow. In this region the detonation occurs. The combustion products then made a 90° turn with help from the nozzle (purple), before exiting the channel through the top of the RRDE. By controlling the size and location of the components in the region, of how the channel area, throat area ratio, and nozzle area ratio can be varied. This process will be discussed later in this section.

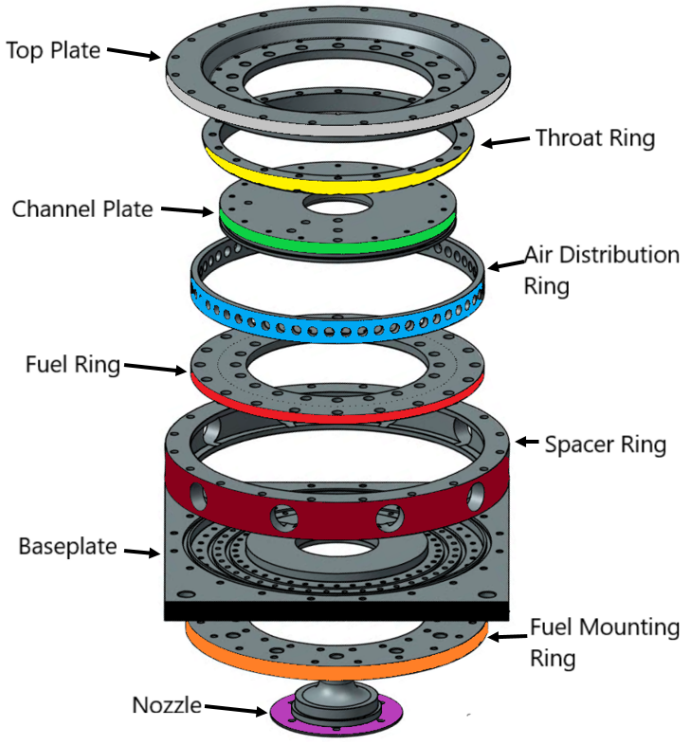

Figure 34. Radial RDE Exploded Isometric View. Similar Color Scheme as in Figure 33.

The top plate is shown with silver in Figure 33. Figure 35 shows a more detailed view of the top (a), side (b), and bottom (c) of the top plate. This devices has an

outer diameter of 304.8 mm with an inner diameter of 168.9 mm. It has an overall height of 24.1 mm with a step down in height towards the inner diameter to minimize the weight of the top plate but still allow the channel plate to remain at the correct height above the base plate. The holes filled with brown are the bolt hole that connect the top plate to the spacer ring, while the yellow and green holes represent where the throat ring and channel plate, respectively, are bolted to the top plate. The small hole towards the outer radius of the top plate is where a pressure transducer will mount to obtain the pressure in the stilling chamber of the RRDE. Finally, the larger semicircle and hole are where pressure transducers in the channel are mounted. These holes provide clearance for the fittings used to mount the pressure transducers.

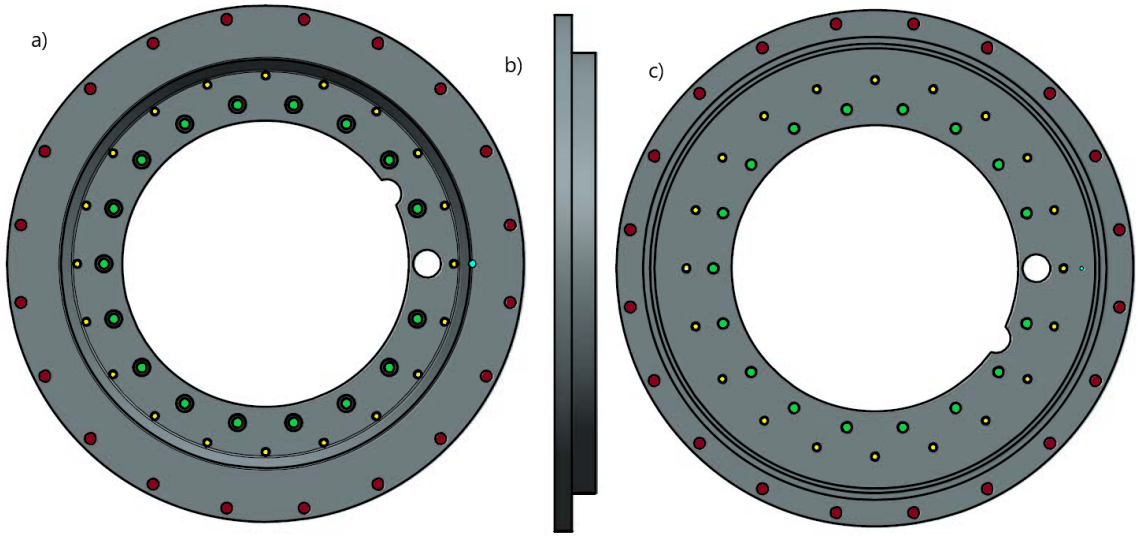

Figure 35. Radial RDE Top Plate. (a) Top View, (b) Side View, and (c) Bottom View.

The channel plate is shown in green in Figure 33, and a detailed view is given in Figure 37. Three different channel plates were used in this project, each with a different channel height and area. The heights of these channel plates were 3.5, 4.0, and 4.5 mm. These differences are highlighted in Figure 36 (a), (b), and (c), respectively.

Figure 37 is a representation of the 3.5 mm channel plate but a similar layout

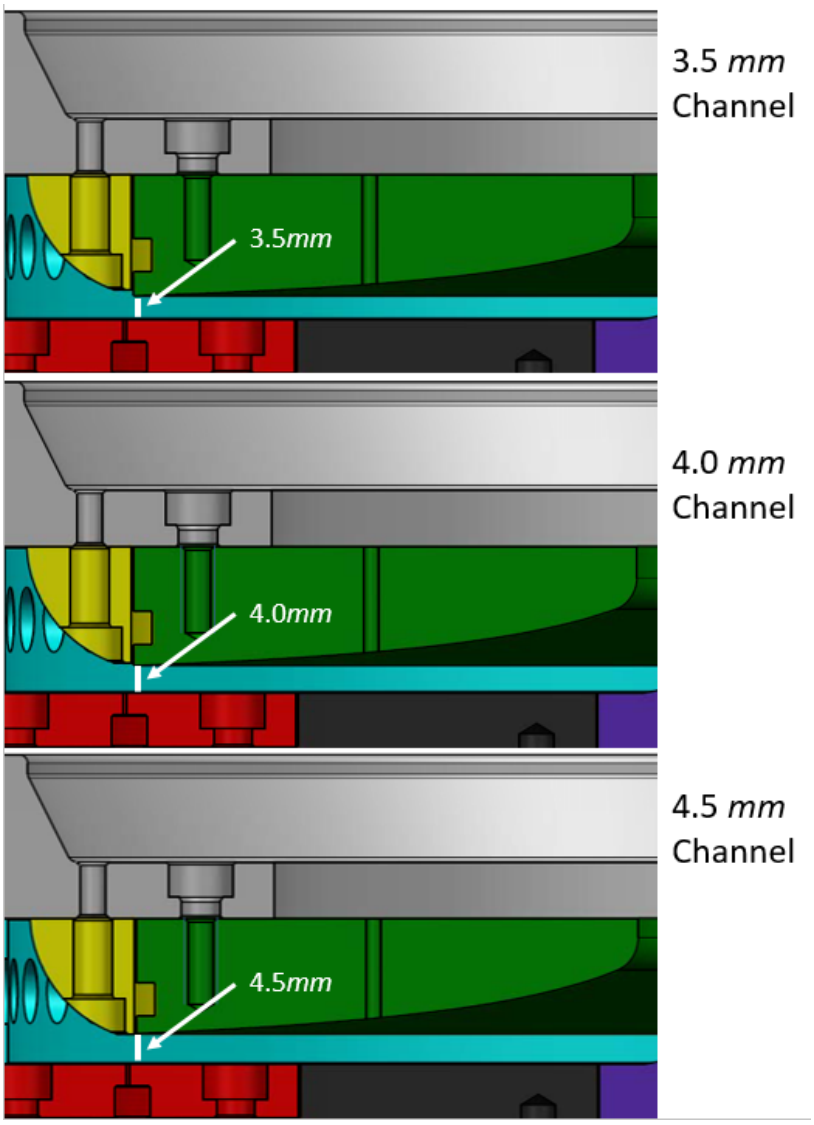

Figure 36. Channel Plates Evaluated.

is followed for the other two channel plates. All three channels are designed to be constant area from the outer radius of the channel up to the channel exit. Each channel plate has an outer diameter of 209 mm and an inner diameter of 62 mm, which is the same as the diameter of the exit of the turbocharger turbine. The silver holes towards the outer radius correspond to where the channel plate is bolted onto the top plate. These holes are only drilled and tapped 12.7 mm deep from the top of the plate to preserve the smooth channel curvature on the bottom of the plate.

The red holes are where the channel ITP pressure measurements lines mount and the green holes are where the channel CTAP lines mount. It should be noted that the green holes on the bottom of the channel plate are much smaller than the ones on top. This is due to the mounting scheme used for the CTAPs that involves using a $\frac{1}{16}$ in NPT fitting to connect the CTAP tube to the channel. The fitting does not continue through the channel so a through hole the size of the inner diameter of the CTAP tube is used to connect the end of the fitting mount to the channel. Finally, the yellow hole is where the pre-detonator mounts and is roughly at the start of the channel.

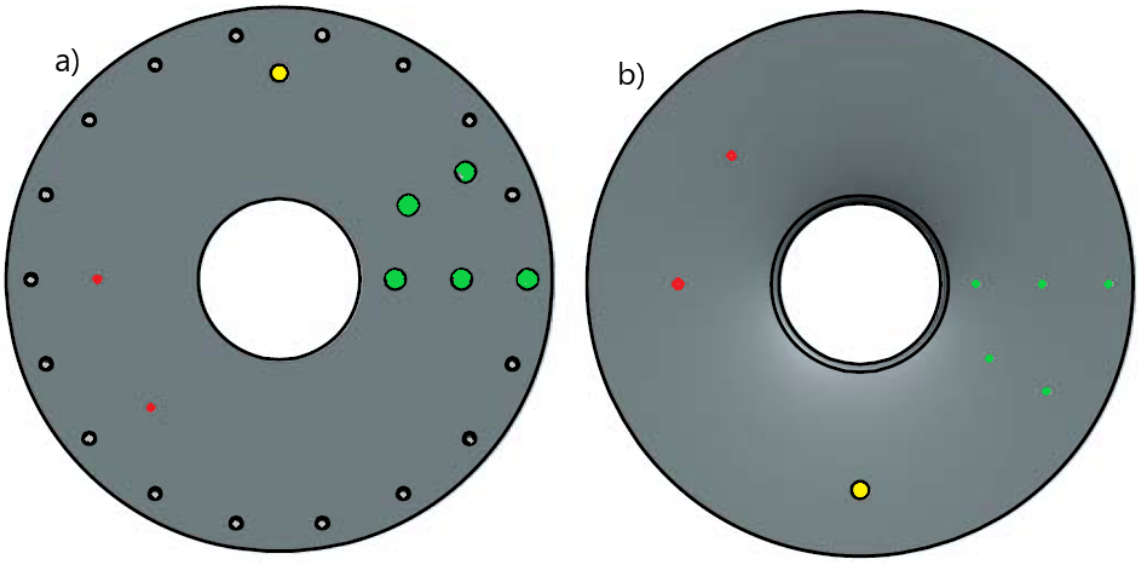

Figure 37. Radial RDE Channel Plate. a) Top View and b) Bottom View.

Represented by brown in Figure 33, the spacer ring is shown in more detail in Figure 38. The spacer ring is a 35.6 mm high ring with an outer diameter of 304.8 mm and an inner diameter of 260.4 mm. The spacer ring also acts as the mounting point for the air lines, ten $\frac{3}{4}$ in NPT mounts where used in the design and they are best shown in blue in Figure 38 (b) and (c). The black holes near the outer radius represent through holes where the bolts connect the top plate, spacer ring, and baseplate. It should also be noted that a large groove is cut out of the inside

of the spacer ring. This is to allow the incoming air to better disperse throughout the RRDE stilling chamber. This piece can be removed and replaced with a modified version with a different the number air line holes or by a different height depending of the air flow requirements.

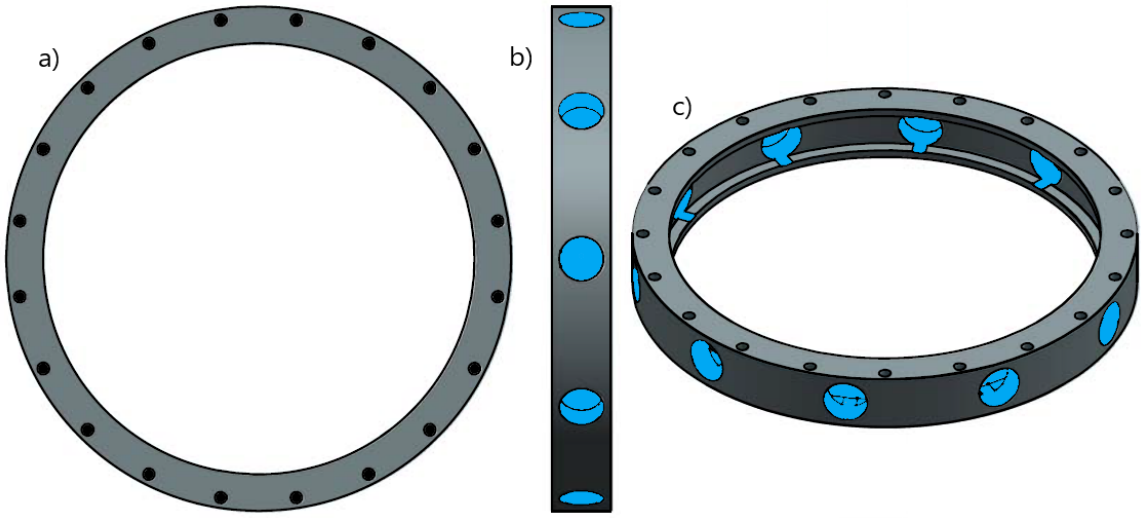

Figure 38. Radial RDE Spacer Ring. (a) Top View, (b) Side View, and (c) Isometric View.

The air distribution ring, shown in light blue in Figure 33, is shown in more detail in Figure 39. This ring is 21.3 mm tall with an outer diameter of 259.8 mm and an inner diameter of 247.2 mm. It sits just inside the spacer ring and its purpose is to force the incoming air from the spacer ring and spread it more evenly around the stilling chamber by increasing the number of holes from ten air mounting holes to fifty five air distribution holes, and decreasing the size of the holes to 9.5 mm. Care was taken to ensure the effective area of the air distribution ring holes, 39.2 cm^2, was slightly greater than the area of the holes in the spacer ring to prevent unnecessary restriction and to ensure the minimum area in the system was not in the distribution holes. This piece can be modified by changing the number and size of the holes to meet the air flow requirements.

In Figure 33 the gold represent the throat ring, which is shown in more detail in

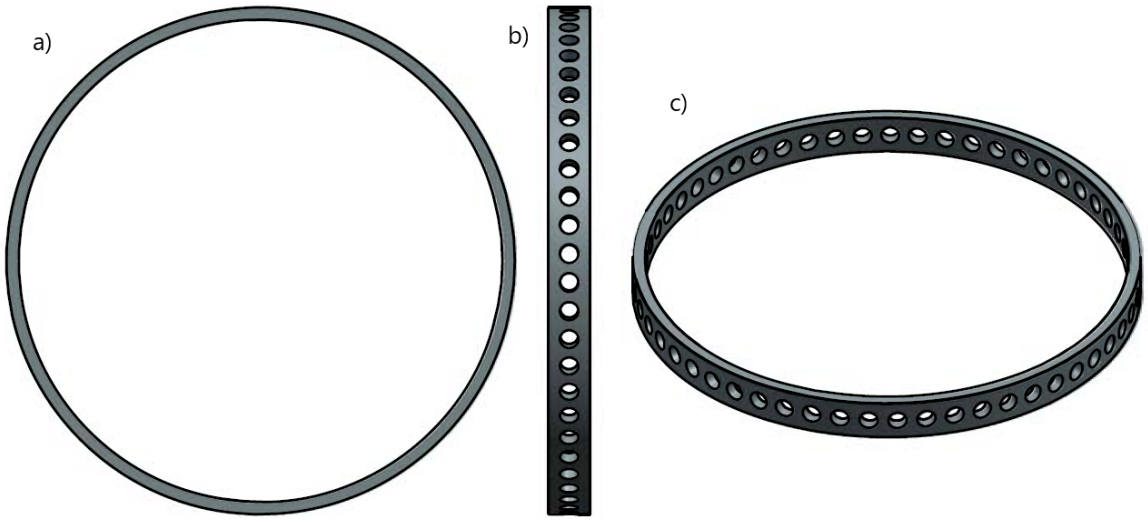

Figure 39. Radial RDE Air Distribution Ring. a) Top View, b) Side View, and c) Isometric View.

Figure 40. This ring is 17.1 mm tall with an outer diameter of 240.8 mm and an inner diameter of 209.6 mm. It features a curved portion where the area from end of the stilling chamber is gently restricted to form the throat of the RRDE. The throat ring creates the minimum area for the RRDE flow path at a radial distance of 106 mm. The silver holes represent where the throat ring mounts to the top plate. Although not pictured, the height above the baseplate where the throat ring sits is controlled with the use of shim rings that have the same diameters and layout as the throat ring, seen in Figure 40 (a), but vary in thickness.

By adding more shims to the RRDE throat ring, the height of the throat itself can be decreased leading to a decreased throat area. The final height of the throat ring was determined by wanting a wide open area ratio, $\frac{A_t}{A_c} = 1$, for the largest channel area without the use of shims. Where A_t is the throat area and A_c is the channel area. This ratio is commonly referred to as the injector area ratio. The size and number of shims were then selected to closely match the specific area ratios of interest. An example of the changing the throat area is shown in Figure 41. This is also shown in more detail in Section 3.4.2.

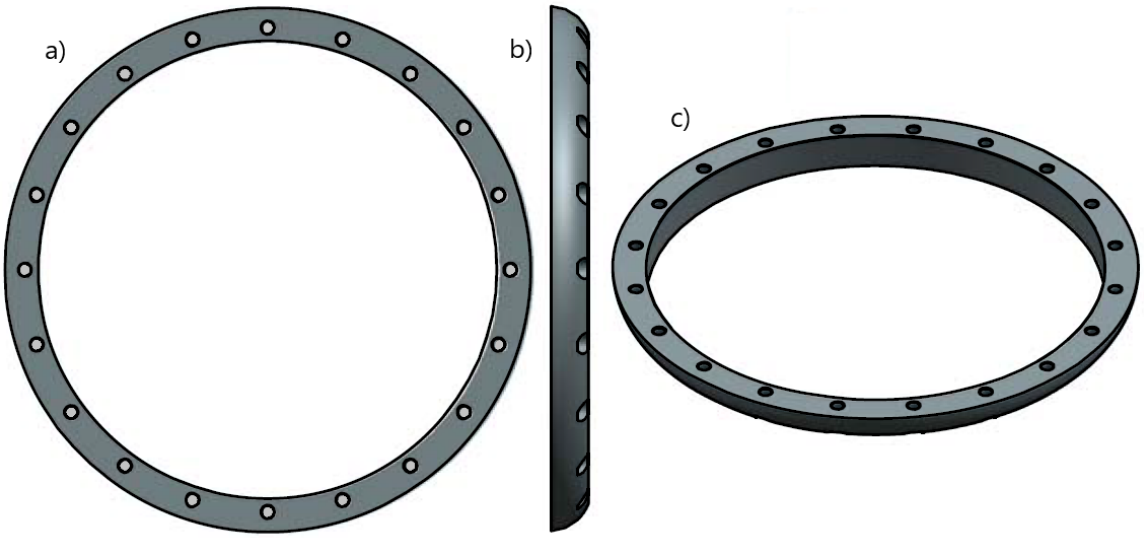

Figure 40. Radial RDE Throat Ring. (a) Top View, (b) Side View, and (c) Isometric View.

Shown in black in Figure 33, the baseplate is shown in more detail in Figure 42. This device is a 17.8 mm thick, 304.8 mm square that has a multitude of features. The center of the baseplate features a hole where the nozzles and turbocharger mount. The six bolt holes, purple in Figure 42 (b), just outside of the center are where the nozzles and turbocharger mount. The shape of this area was designed specifically for the turbocharger used in experimentation. The next feature is the alternating red and orange holes, where the red is for the fuel injector ring that mounts in the top (a) of the baseplate and the orange is for the fuel line mounting ring that attaches to the bottom (b) of the baseplate. There is a groove the height of the fuel injector ring cut into the top (a) of the baseplate to allow the fuel ring to lay in the baseplate without disruption to the flow. The ring of white holes are the fuel distribution holes that are a part of the baseplate and perform a similar task as the air distribution ring mentioned earlier. There are 41, 4.8 mm holes used to distribute the fuel which gave an area of 7.3 cm^2. The four outer holes are where the RRDE mounts to the test stand and the ring of brown holes in where the spacer ring and top plate mount.

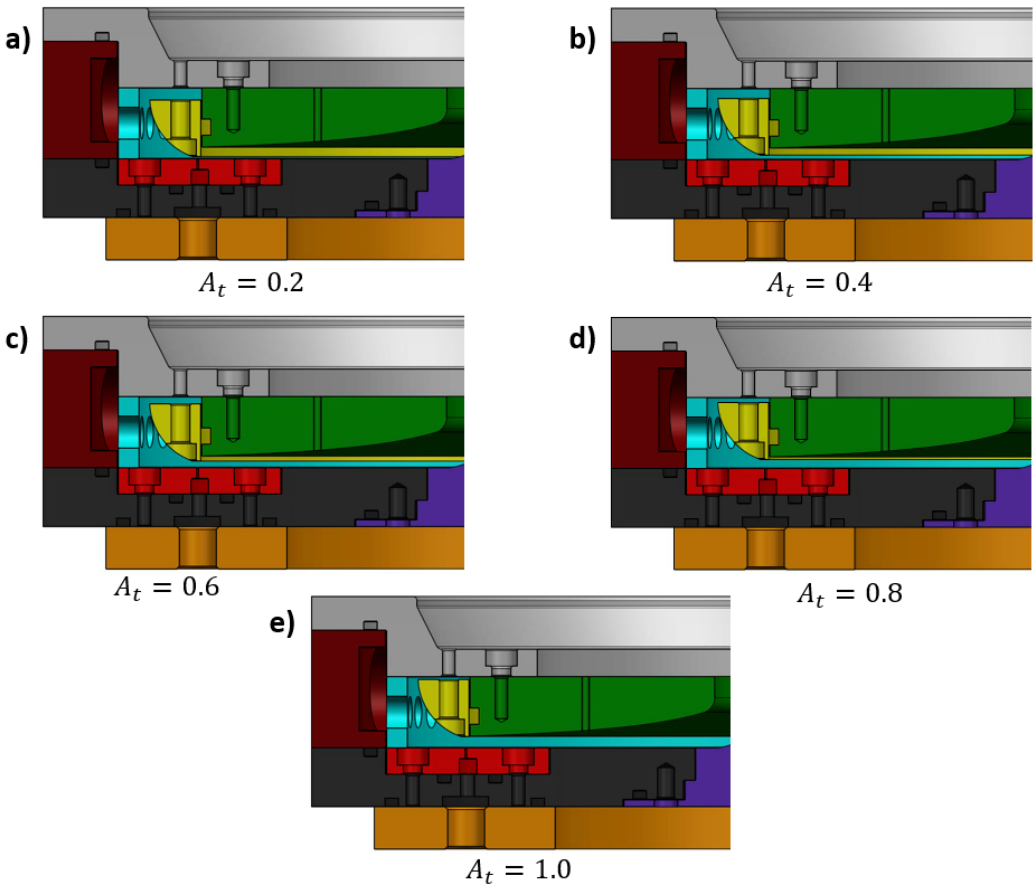

Figure 41. Possible Throat Area Ratios.

The fuel injection ring is represented by the dark red in Figure 33, and is shown in more detail in Figure 43. This ring is 7.9 mm thick with an outer diameter of 259.6 mm and an inner diameter of 161.9 mm. The two rings of larger black holes around the inner and outer radii are where the fuel ring bolts into the baseplate. The red groove shown in Figure 43 (b) acts as a plenum for the fuel before it is injected through the 120, 0.51 mm diameter fuel injector holes which give an area of 24.3 mm^2. These holes sit at a radius of 105.9 mm which where the throat ring creates the throat for the fuel injection. The fuel ring is sized so that it fits neatly into the groove cut from the top of the baseplate, Figure 42 (a). This was done to minimize the disturbance it would cause to the flow. The fuel injection ring can easily be modified by changing the number of holes and the size of those hole to give a different fuel injection scheme.

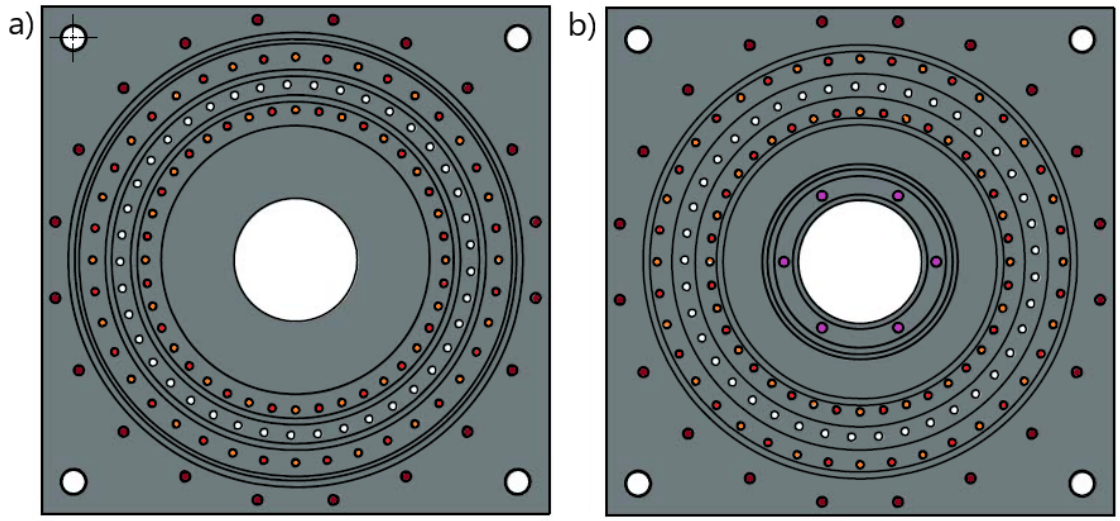

Figure 42. Radial RDE Baseplate. a) Top View and b) Bottom View.

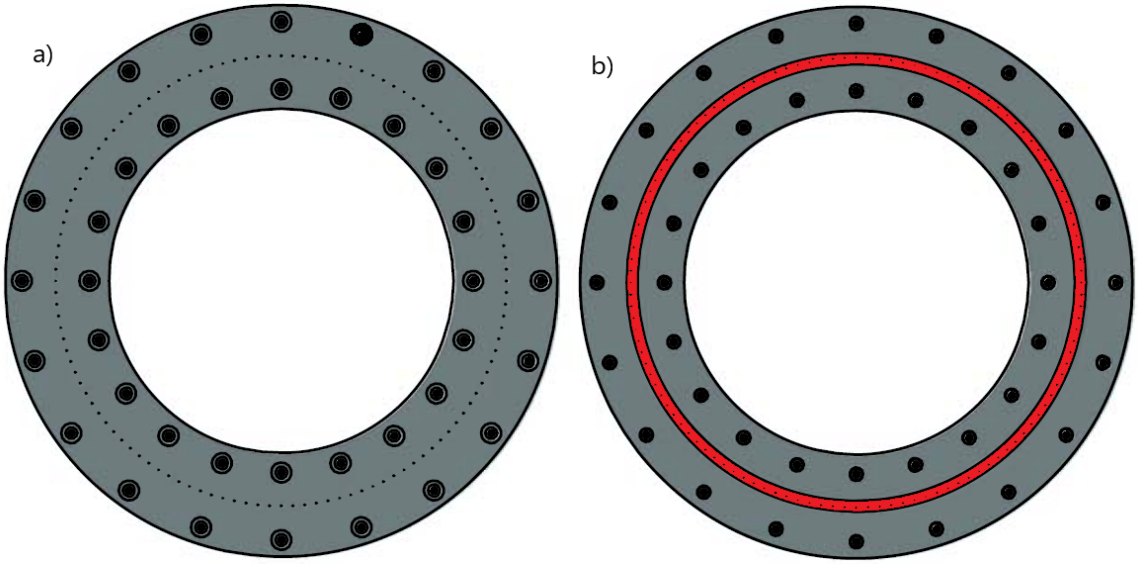

Figure 43. Radial RDE Fuel Injection Ring. (a) Top View and (b) Bottom View.

Shown in orange in Figure 33, the fuel line mounting ring is also shown in Figure 44 in more detail. This ring is 12.7 mm thick with an outer diameter of 267 mm and an inner diameter of 158.3 mm. It features 12, $\frac{3}{8}$ in NPT female threads where the $\frac{3}{8}$ in NPT fuel lines will mount. The black holes represent where the fuel line mounting

ring attaches to the baseplate. This piece can be modified to change the number and size of fuel lines depending of the fuel flow requirements.

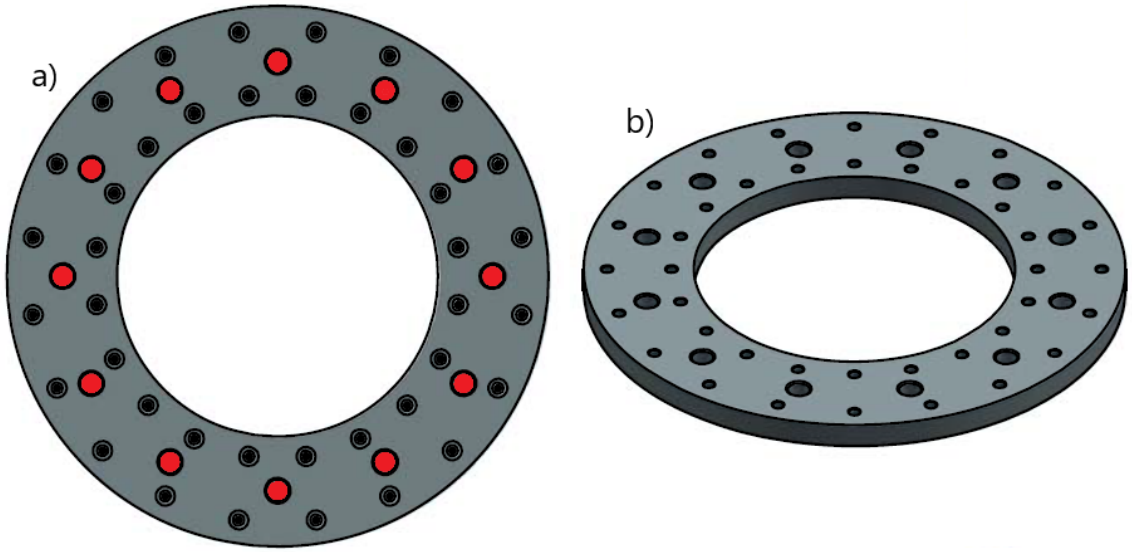

Figure 44. Radial RDE Fuel Line Mounting Ring. (a) Top View and (b) Bottom View.

The purple represent the nozzle in Figure 33. A more detailed view of a nozzle piece is shown in Figure 45. This is just one example of the many different nozzle pieces, each with a different exit curvature that corresponds to a different nozzle area ratio, which is the ratio of the nozzle minimum area versus the channel area, or $\frac{A_n}{A_c}$. The nozzle features six bolt holes where it mounts to the baseplate, the same mounting scheme used for the turbocharger. All of the nozzles have the same max outer diameter of 116.8 mm and the the same two diameters of the mounting section, shown in white, of 73.7 mm for the upper white section and 80 mm for the lower white section.

By changing the curvature of the nozzle exit curve, the area at the nozzle exit is changed. These nozzle curves were designed by using the radius of curvature at the end of the channel plate, shown in Figure 46. For the nozzle area ratio of 1.0 the curvature of the nozzle was set by using a circle with the same center as the radius of curvature of the channel exit. The radius of this larger circle is determined by

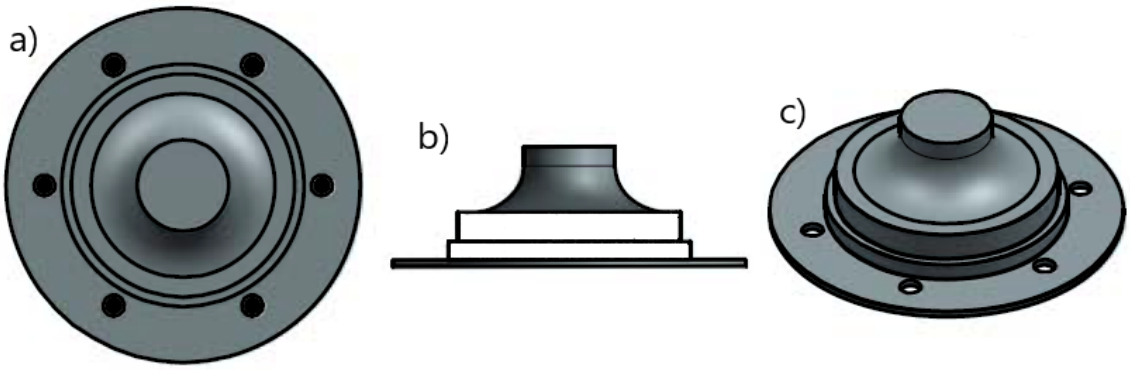

Figure 45. Radial RDE Nozzle. (a) Top View, (b) Side View, and (c) Isometric View.

ensuring the exit area of nozzle is the same as the channel area, where the nozzle exit area is the area between the concentric circles at the exit, when viewed from the top. This area is highlighted with the yellow line.

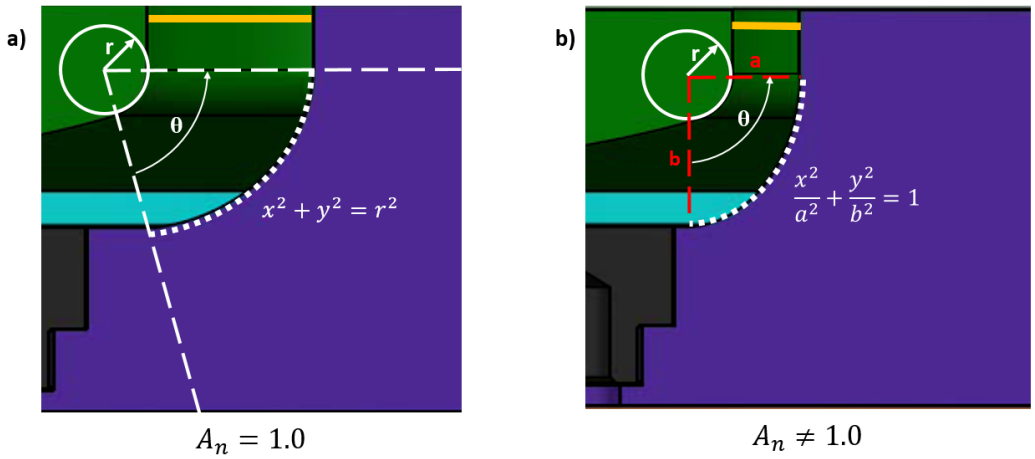

Figure 46. Nozzle Curvature Equations.

For cases with a nozzle area ratio less than 1.0 the nozzle curve was set by an ellipse with the same center as the radius of curvature for the channel exit. The semi-major axis, b, was the height of the center above the baseplate, black, and the semi-major axis was determined by matching the area at the exit to create the appropriate nozzle exit area ratio. This was a similar concept as the nozzle area ratio of 1.0; however, using an ellipse instead of a circle creates a constantly converging area up to the nozzle exit, yellow line, and ensures the nozzle exit area is the minimum area of the

nozzle. An example of changing the nozzle area ratio is shown in Figure 47, with the four nozzle area ratios used during testing.

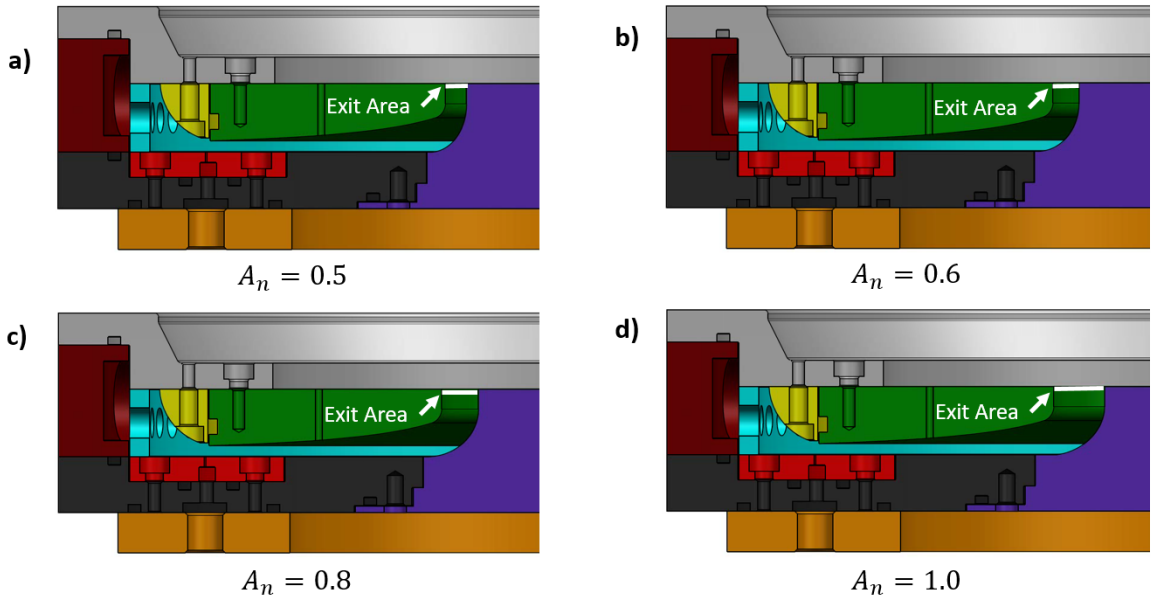

Figure 47. Nozzle Area Ratio Variation Tested.

3.2.3 Turbine Channel and Nozzle Guide Vane Design.

Radial inflow turbines require a tangential velocity component that matches the speed of the turbine itself, a fact discussed in Section 2.4.3. Despite the detonation wave propagating in the circumferential direction in the RRDE, the flow path remains relatively radial. This brought up the need for a row of NGVs before the turbine to turn the flow and achieve the tangential velocity component.

Three distinct NGV designs were accomplished through the uses of the *TurbAero* design program.[40] Each design featured 17 vanes to reduce the possible excitation of natural frequencies in the 10 blade turbine. These NGV profiles are shown in Figure 48 and each blade turns the flow from its primarily radial direction to a slightly tangential direction, which each NGV ring turning the flow at a different angle to impart a different tangential velocity on the flow. The airfoil profiles were designed

by the program by specifying the conditions ahead of the NGVs, the height of the NGVs, the vane thickness, the radial location of the start and end of the NGVs, the number of blades, and the desired chamber of the vanes.

To design the NGV rings the flow conditions were set at an estimated 1400 K and 2 atm with a mass flow rate of 0.53 $\frac{\text{kg}}{\text{s}}$. The vane height was held constant in the program and set to the same vane height as the turbocharger turbine inlet which was 13.9 mm with 17 vanes with a 2 mm maximum thickness. The outer radius of the NGV ring was set at 50.8 mm with an inner radius of 34.7 mm. The chamber input was used to manipulate the turning angle of the flow. With these inputs, the program produced the vane profile as well as certain flow exit conditions which included the exit angle of the flow. This design process was iterated to produce a specific exit flow angle that matched the tangential velocity of the flow to a given turbine tip velocity. This was set at 300, 400, and 500 $\frac{\text{m}}{\text{s}}$ for desired operating condition The NGV exit flow angles for these cases were 23.5°, 32°, and 39°, and are shown in Figure 48 as (b), (c), (d) respectively.

To easily swap and mount the NGVs, a ring layout was created than would insert into a channel plate designed specifically for the turbine. This channel is shown in Figure 49, and featured a slot cut out near the center radius where the NGV ring mounted. Like the previously designed channel plates, the turbine specific channel remained constant area through the channel section; however, the profile flattens where the NGV mounts. The turbine channel featured a starting height of 6.7 mm, which corresponds to an area of 44.3 cm^2.

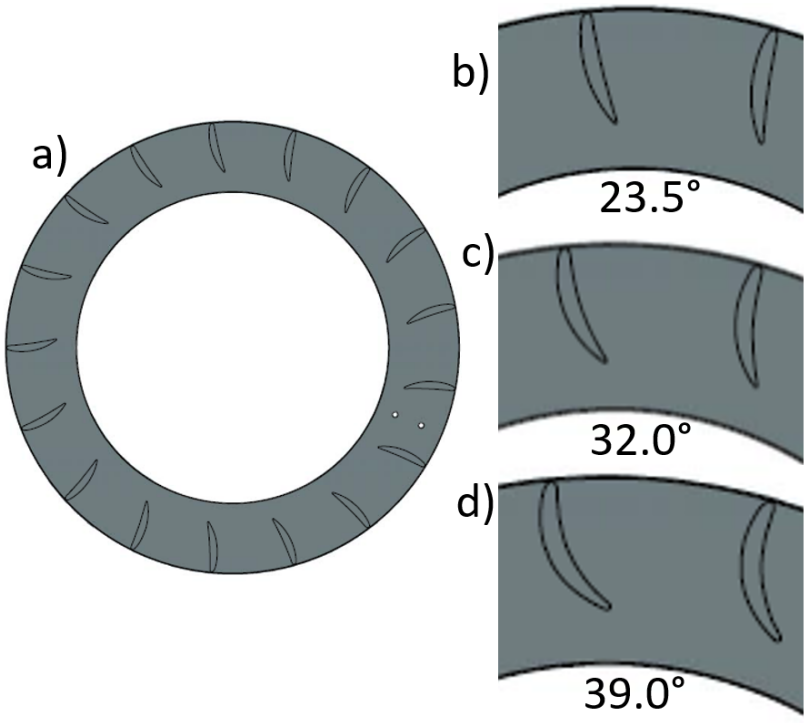

Figure 48. Nozzle Guide Vane Ring Designs.

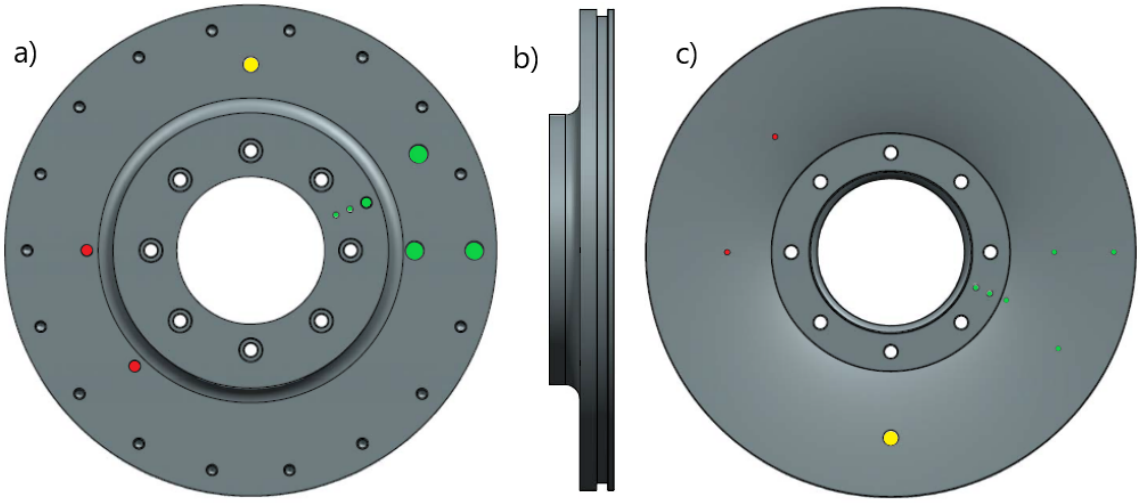

Figure 49. Radial RDE Turbine Channel (a) top, (b) side, and (c) bottom.

3.3 Equipment

There were a multitude of measurements taken on the Radial RDE. These mostly included pressure and temperature measurements of the flow itself. For the initial testing and characterization of the RRDE there were twelve pressure measurements and three temperature measurements taken. After characterization was complete, there were fifteen pressure measurements and five temperature measurements taken. The location, rational, and description of these measurements will be discussed in more depth throughout this section.

When characterizing the RRDE, the pressure measurements included six CTAPs located in the channel of the RRDE, shown with the green dots in Figure 50 (a). The smallest green dot represents a CTAP that measures the average pressure in the air plenum. This allowed for calculating the pressure losses through the throat of the RRDE. The other five CTAPs were located at different radial locations throughout the channel: 4.5, 5.7, 7.0, 8.3, and 9.5 cm. These location correspond to locations that are 6.0, 4.8, 3.5, 2.2, 1.0 cm, respectively, from where the channel starts at the outer radius of the channel plate. This setup allowed for determining the average channel pressure in the device, as well as, determine the rough location of the detonation wave. The two red dots in Figure 50 (a) represent the ITP pressure transducer locations. These devices were located at the same radius of 7.0 cm but were separated by 45°. ITPs gave the transient pressure response as the detonation wave passed through the channel, and by offsetting them by a known arc length, 5.5 cm, the speed of the detonation wave was calculated by analysis the phase lag between the two signals. Lastly, a thermocouple (blue) was attached to the top of the RRDE to show the temperature of the device itself, which was done to insure the RRDE was held at a safe operating temp.

Figure 50 (b) shows the sonic nozzle setup. This setup required measuring the

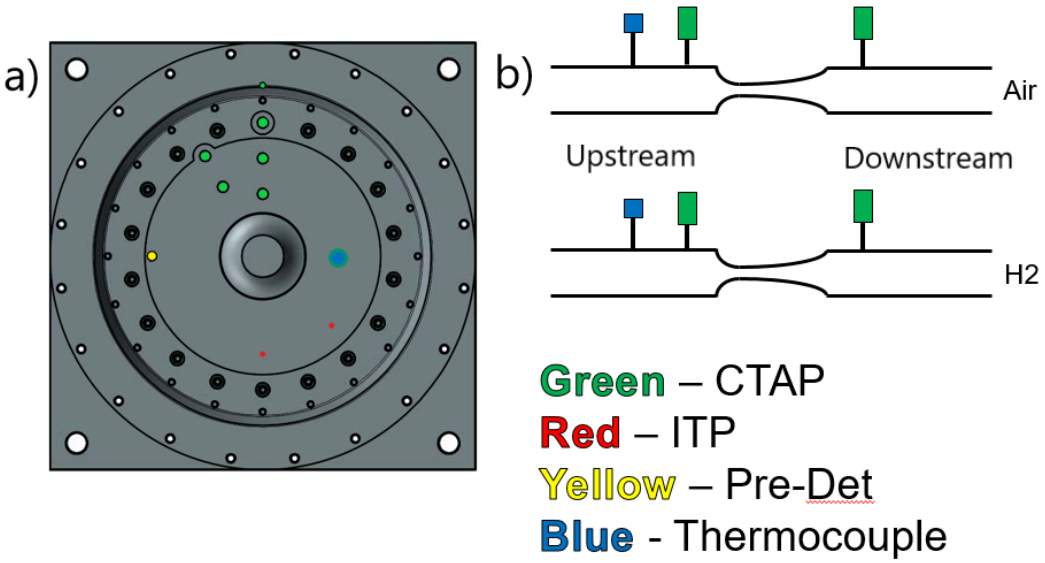

Figure 50. Schematic of Radial RDE Measurement Locations.

pressure and temperature upstream of the sonic nozzle orifice and then measuring the pressure downstream of the orifice. For this setup the air line used a sonic nozzle with a pipe diameter of 50.8 mm and a nozzle diameter of 8 mm which gave an area ratio of 40. The fuel line used a pipe diameter of 25.4 mm with a nozzle diameter of 3.2 mm which gave an area ratio of 64. With these area ratios it is acceptable to assume the upstream pressure and temperature are total quantities. This, combined with the area of the nozzle and the properties of air allows for the calculation of the mass flow, which will be shown in Section 3.5.

Table 1 shows the list of equipment used for the initial characterization of the RRDE. This table includes the device description as well as the uncertainty of the device, which will be discussed in more detail in Section 3.5.

There were additional measurements taken when running the RRDE coupled with the turbocharger. This included additional pressure and temperature measurements and an additional mass flow measurement calculating the mass flow through the turbocharger compressor section. With the turbocharger, the channel CTAP layout

Table 1. Radial RDE Measurement Devices.

Device	Brand	Part Number	Range	Uncertainty
Channel CTAPs	Omega	PX429-250A5V	$0 - 250$ *psia*	± 0.2 *psi*
Plenum CTAP	Omega	PX429-250A5V	$0 - 250$ *psia*	± 0.2 *psi*
Air Sonic Nozzle Upstream	Omega	PX429-2.5KA5V	$0 - 2500$ *psia*	± 2 *psi*
Air Sonic Nozzle Downstream	Omega	PX429-1.0KG5V	$0 - 1000$ *psig*	± 0.8 *psi*
Fuel Sonic Nozzle Upstream	Omega	PX429-3.5KA5V	$0 - 3500$ *psia*	± 2.8 *psi*
Fuel Sonic Nozzle Downstream	Omega	PX429-2.5KA5V	$0 - 2500$ *psia*	± 2 *psi*
Thermocouples	Omega	K-Type	$0 - 1608$ K	± 1 K
ITPs	Kulite	ETL-4-GTS-190-1000A	$0 - 1000$ *psia*	± 1 *psi*

changed slightly, shown in Figure 51. The plenum CTAP and the three CTAP furthest from the center remained the same; however because of the NGV ring section, the inner two CTAPs had to move. One was moved to just radial outboard of the NGV ring location and one was moved to the radial center of the NGV ring to collect pressure data as the flow moves through the NGV ring. An additional CTAP was added at the exit of the NGV ring to acquire the pressure entering the turbocharger turbine. The ITP and thermocouple location on the RRDE also remained the same.

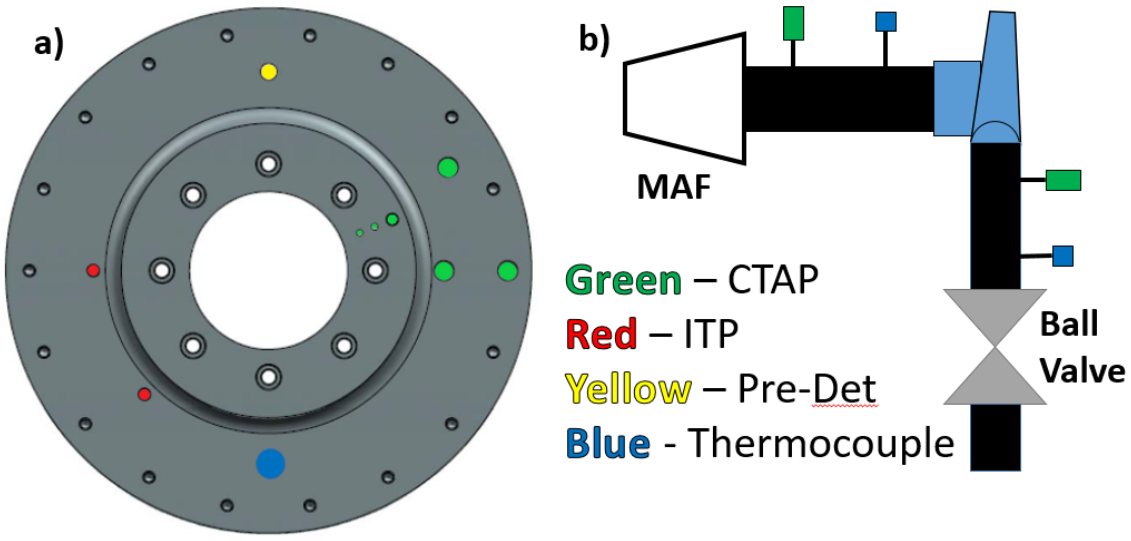

Figure 51. Measurement Setup for Turbine Channel.

With the addition of the turbocharger came new measurements needed to determine the power being extracted from the RRDE. Figure 51 (b) shows the additional

features added. The Mass Air Flow Sensor (MAF) was used to determine the mass flow rate through the turbocharger compressor. Two additional CTAPs and thermocouples were also included to measure the change in pressure and temperature through the compressor. Finally, an electromagnetic RPM sensor was mounted in the housing of the turbocharger compressor to acquire the rotational speed of the turbocharger throughout the run. These calculation and the uncertianty associated with these measurements will be discussed in Section 3.5. The new sensors needed with the turbocharger equipped is shown in Table 2.

Table 2. Additional Radial RDE Measurement Devices with Turbine Installed.

Device	Brand	Part Number	Range	Uncertainty
MAF	Pro M Racing	92	0-1.21 $\frac{kg}{s}$	$\pm 0.003 \frac{kg}{s}$
Compressor Upstream Pressure	Omega	PX429-030A5V	$0 - 30$ $psia$	± 0.024 $psia$
Compressor Downstream Pressure	Omega	PX429-150A5V	$0 - 150$ $psia$	± 0.12 $psia$
Compressor Thermocouples	Omega	K-Type	$0 - 1608$ K	± 1 K
RPM Sensor	Garrett/Honeywell	769366-001	150 $kRPM+$	N/A

3.4 Testing

This section focuses on the testing of the stand alone Radial RDE and the turbocharger coupled with the RRDE. Section 3.4.1 discusses the test procedures used when testing the RRDE. This includes the start up procedure, the procedures used during the run, and the safety steps involved. The test matrix used for testing and how it was accomplished will be discussed in Section 3.4.2.

3.4.1 Test Procedures.

This section focuses on the test procedures used when testing the Radial RDE. It includes examples of the test runs for both the stand alone RRDE as well as the RRDE with the turbine installed. This section will also include example calculations made for each run and the performance parameters used in this study.

A full test run for the RRDE was ten seconds of total run time and data collection taken at a frequency of 90 Hz, as seen in Figure 52. The test starts with opening the air valve roughly two seconds into the run. Once the air settles at a steady state value the fuel valve is opened at roughly four seconds. The fuel is allowed to steady for one second before the pre-detonator is fired which initiates the RRDE, shown in Figure 53. The pre-detonator is a device that injects a mixture of hydrogen and pure oxygen into a 4 way connector. This mixture is then ignited by a spark plug. The combustion process is initially a deflagration; however, through the use of a small screw obstructing the flow, or a long narrow tube section, the deflagration transitions to a detonation. This detonation wave then enters the channel of the RRDE, shown in Figure 54. The leading shock wave of this detonation wave then expands into the channel of the RRDE which initiates the detonation wave within the channel.

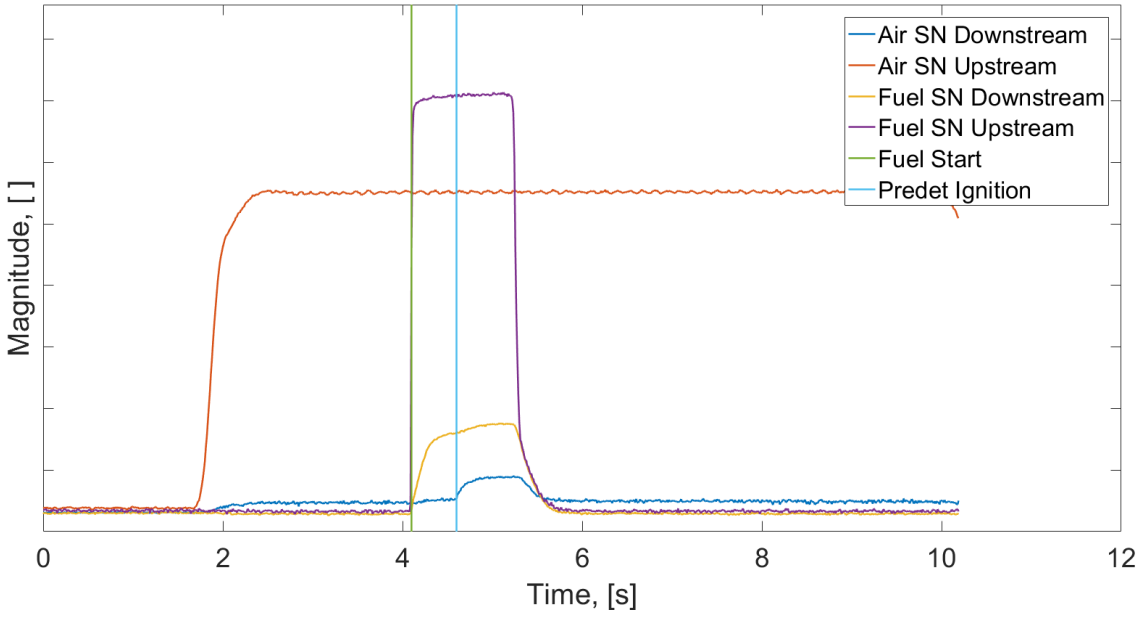

Figure 52. Example Test Run. Channel Height = 4.5 mm**,** AR_t **= 0.2,** AR_n **= 1.0,** $\dot{m}''$ **=** $75\frac{kg}{m^2 s}$**,** ϕ **= 0.9.**

After ignition the RRDE is allowed to run for roughly one second before the fuel valve is shut off. Finally, the last four or five seconds of the run are blowdown where the air is left on to cool down the RRDE. This also clears the RRDE of residual gases.

At the ten second mark the air valve is closed and data collection stops.

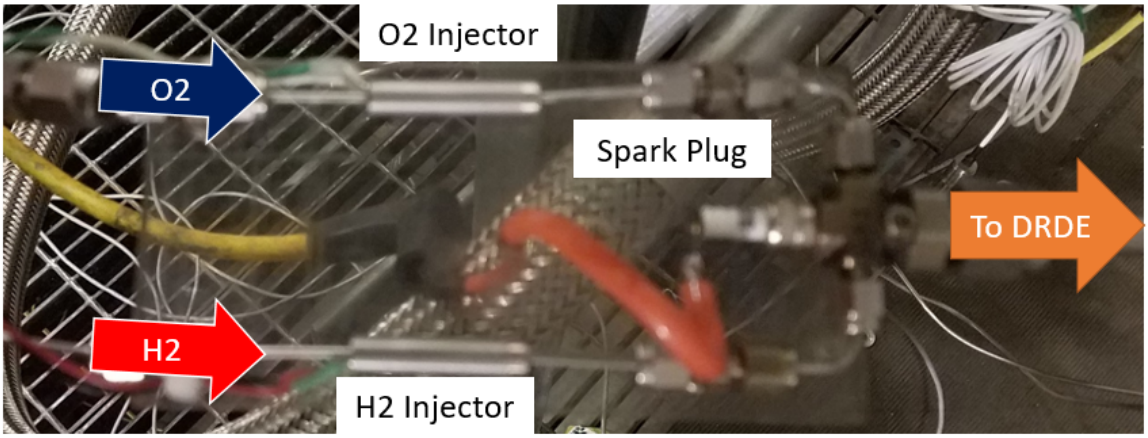

Figure 53. Pre-Detonator Layout.

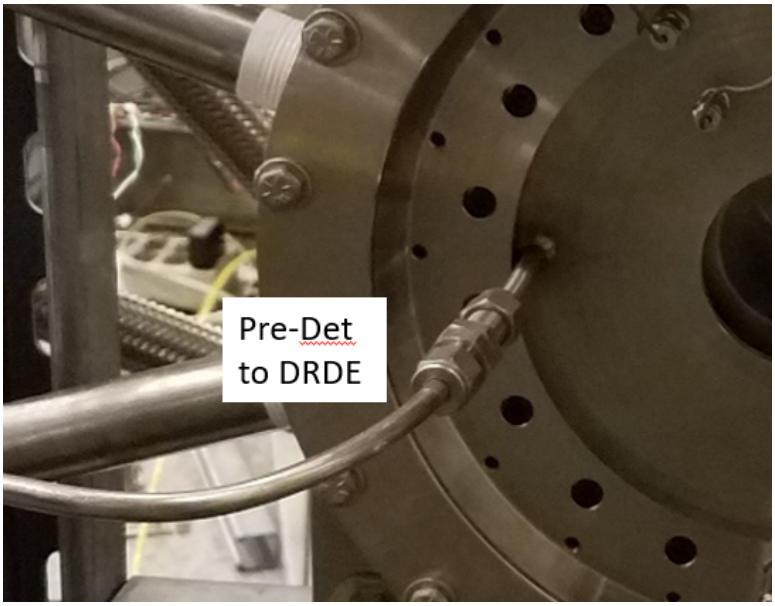

Figure 54. Front view of the Radial RDE.

Figure 55 shows an example the full run but only includes the channel and plenum CTAPS. At the pre-det ignition time there is a sharp rise in pressure in both the channel and the plenum. During this time the detonation applies a backpressure to the plenum as the detonation initiation. After the sharp rise in pressure the detonation stabilizes and the pressure values approach a steady state value. It is once

these values reach a steady value that the pressure measurements are made in the channel and allow for the creation of a channel pressure distribution plot.

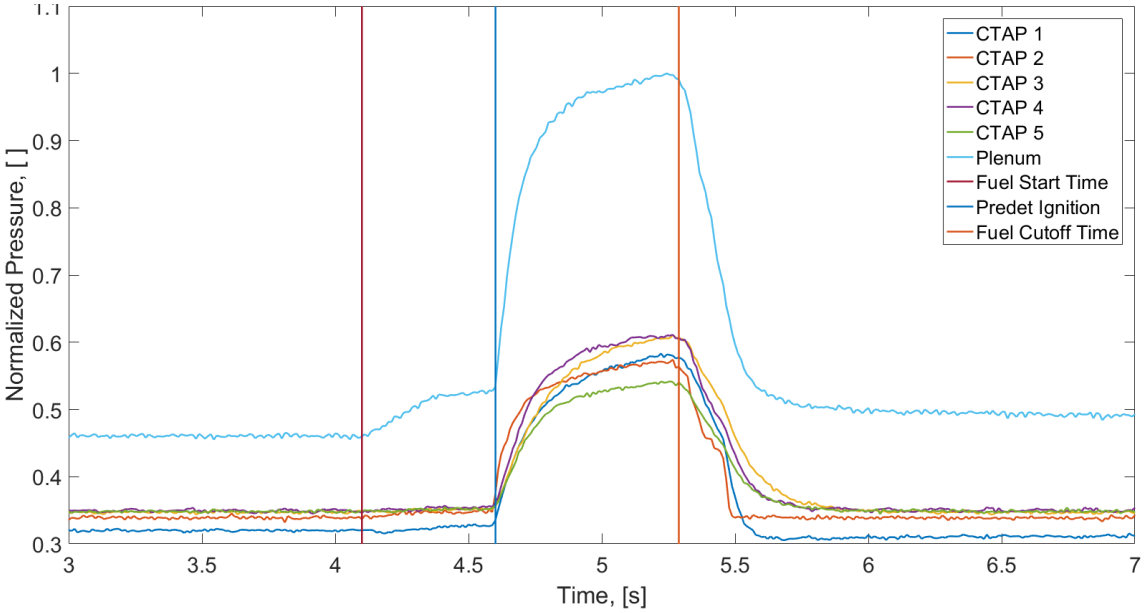

Figure 55. Test Run Channel Pressures. Channel Height = 4.5 mm**,** AR_t **= 0.2,** AR_n **= 1.0,** $\dot{m}''$ **= 75**$\frac{kg}{m^2 s}$**,** ϕ **= 0.9.**

Figure 56 shows screenshots from a video of a Radial RDE run. It shows the RRDE pre-ignition, (a), at ignition, (b), operating in a one wave mode, (c), and operating at a two wave mode, (d). During the run there was a noticeable change in both the brightness of the exhaust gas and a shift in the frequency of the operating sound, which corresponded to the transition from one to two waves.

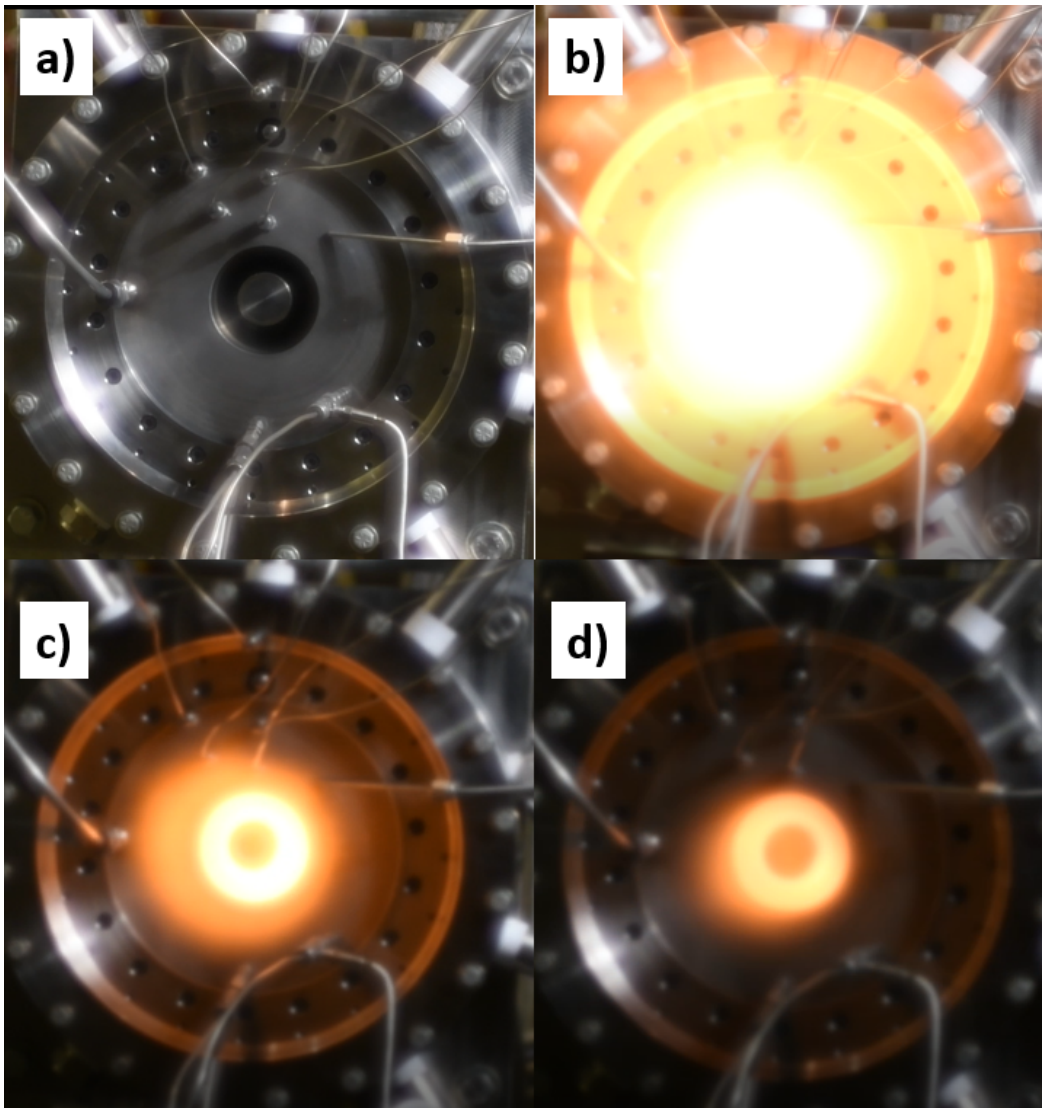

Figure 56. Radial RDE Operation. (a) pre-ignition, (b) at ignition, (c) one wave operation, & (d) two wave operation.

The run in Figure 56 exhibited two modes of operation, but there was also runs operating in a three wave mode. Figure 57 shows frames taken from high speed video showing all three modes of operation, with one wave, (a), two wave, (b), and three wave, (c).

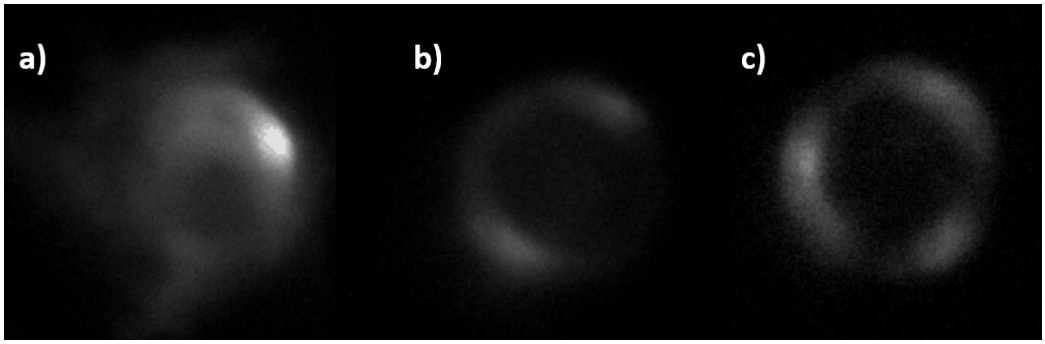

Figure 57. Radial RDE Mode Changes. (a) one wave, (b) two waves, & (c) three waves.

During select cases, the transition in wave modes was captured in the channel pressure traces. Figure 58 shows an example of the pressure traces during a transition from one to two wave mode operation. This plot shows the pressure in the channel grows as the detonation initiates and begins to settle into a one wave operating mode. Then there is a steep drop in all of the normalized channel pressures at roughly 4.7 s into the run where the RRDE transitioned from one to two waves. Once this transition occurs the channel pressures remain relatively constant throughout the run. Other cases that were able to capture this transition occasionally showed the channel pressure began to increase to a new steady state value after the transition. Finally, once the fuel was cutoff, the RRDE appears to transition back into one wave operating mode for a brief moment before extinguishing. This transition was also noticeable in the highspeed pressure data, which will be shown later in this section.

The two performance parameters that were examined for the stand alone RRDE were the injection pressure loss and the wavespeed. The injection pressure loss was calculated based on the channel pressure distribution. An example of the channel

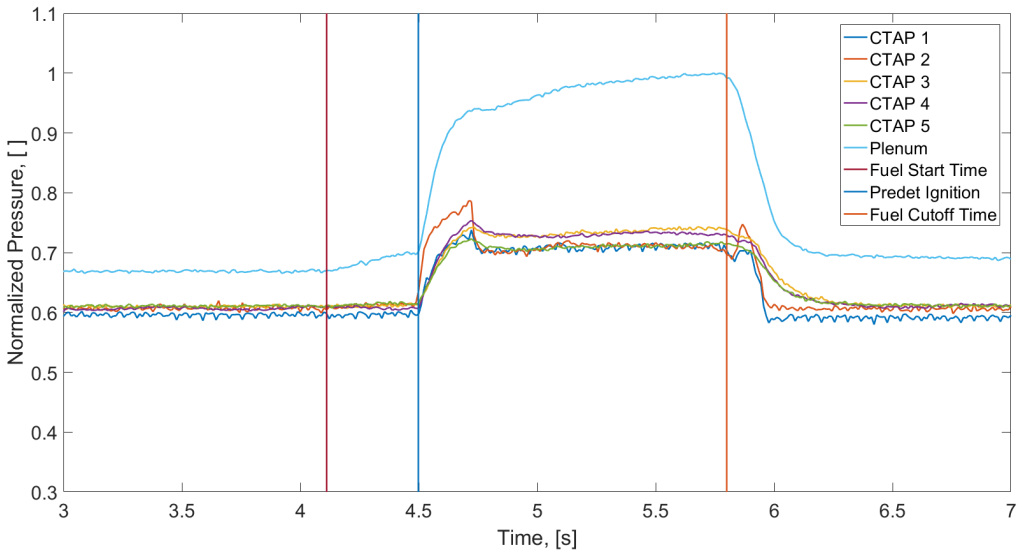

Figure 58. Channel Pressure Traces with One Wave to Two Wave Transition at 4.7s. Channel Height = 4.5 mm, AR_t = 0.2, AR_n = 0.6, $\dot{m}''$ = 50 $\frac{kg}{m^2 s}$, ϕ = 0.7.

pressure distribution is shown in Figure 59. This plot normalized the channel pressures by the plenum pressure during cold flow (blue) and during detonation (red). The cold flow distribution shows a drop in normalized pressure just after the injection, but a slight recovery to a roughly constant value as the flow progressed down the channel. The detonation flow shows a similar pressure drop just after the injector along with a rise in pressure as the flow progresses, but there is a peak value in channel pressure unlike the cold flow case. It should be noted that the as the detonation initiates, the plenum pressure increases due to the sharp back pressure being applied by the detonation. This is shown in Figure 55 where the increase in channel pressure is mirrored by an increase in plenum pressure. This peak roughly represents the location of the detonation wave which is nearest the middle CTAP. This CTAP has the same radial location as the ITP probes discussed in Section 3.3.

The pressure distribution plot also allows for the calculation of the pressure losses when detonating, which is the first performance parameter that is examined in this

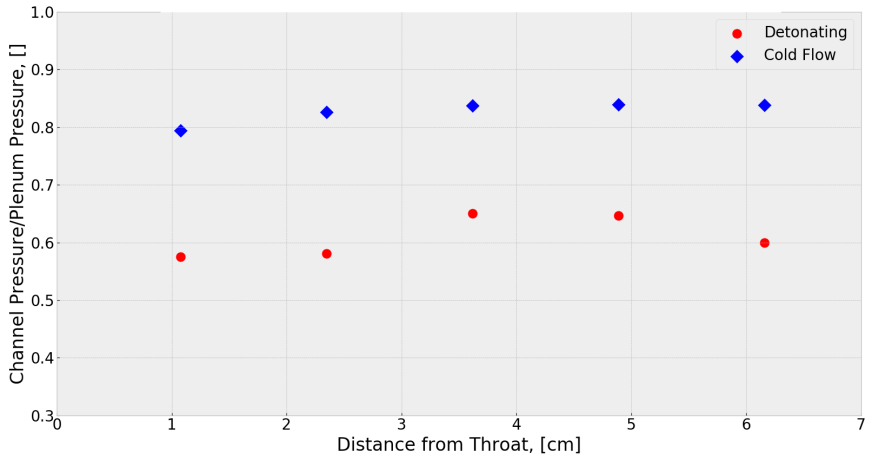

Figure 59. Example Channel Pressure Distribution. Channel Height = 4.5 mm**,** $AR_t = 0.2$**,** $AR_n = 1.0$**,** $\dot{m}'' = 75\ \frac{kg}{m^2 s}$**,** $\phi = 0.9$

study. This is done by using Equation 16:

$$dp_{inj} = \frac{P_{plenum} - P_{channel}}{P_{plenum}} \tag{16}$$

where P_{plenum} is the plenum pressure and $P_{channel}$ is the channel pressure measured at the CTAP furthest from the injector. For the example run the injector pressure loss was 43.6%.

The second performance parameter that was examined was the wavespeed of the detonation. This was done by examining the highspeed data from the ITP probes, shown in Figure 60. The sensors were triggered 0.1 seconds before the pre-det was fired, this section of the highspeed data before ignition is shown in the plot before the bold, black line. However, this section of the high speed data was not used in the wavespeed analysis. For the majority of the test runs the highspeed data was taken for 0.5 seconds at a 1 MHz data rate. Figure 61 shows a zoomed in view of the highspeed data, which shows the saw-tooth peaks that are typically seen for detonations.

The wavespeed measurement was determined with Equation 17:

$$wavespeed = 2\pi r f \tag{17}$$

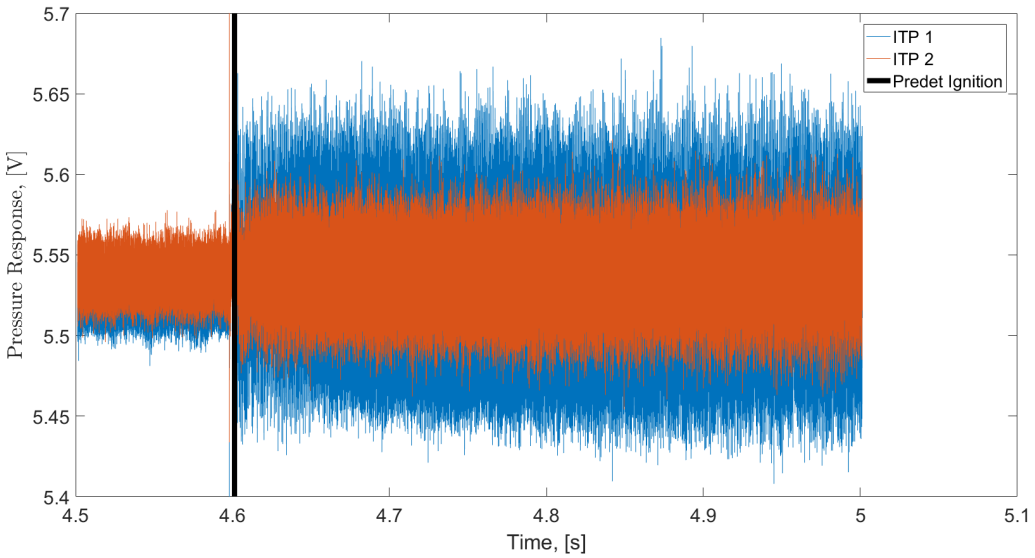

Figure 60. High Speed Pressure Data Full Plot. Channel Height = 4.5 mm**,** $AR_t = 0.2$**,** $AR_n = 1.0$**,**$\dot{m}'' = 75\ \frac{kg}{m^2 s}$**,** $\phi = 0.9$

where f is the frequency response of the ITP probes and r is the radius of the detonation wave. This frequency was determined by taking the Fast Fourier Transform (FFT) of the highspeed data. An example of the FFT for Figure 60 is shown in Figure 62. The large peak at roughly 3 kHz was represents the peak frequency of the detonation wave with its harmonic as the second largest peak at roughly 6 kHz.

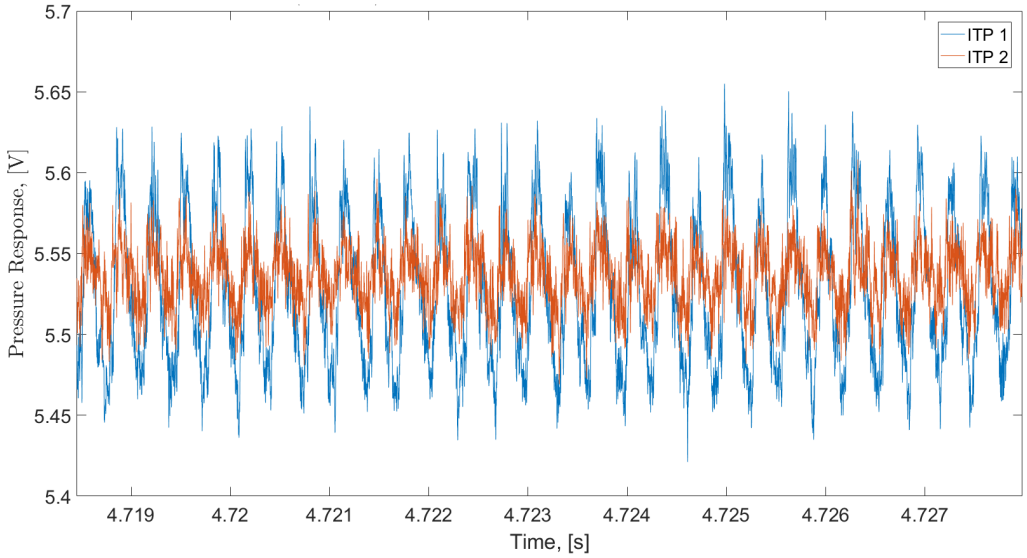

Figure 61. High Speed Pressure Data Zoomed. Channel Height = 4.5 mm**,** $AR_t = 0.2$**,** $AR_n = 1.0$**,**$\dot{m}'' = 75\ \frac{kg}{m^2 s}$**,** $\phi = 0.9$**.**

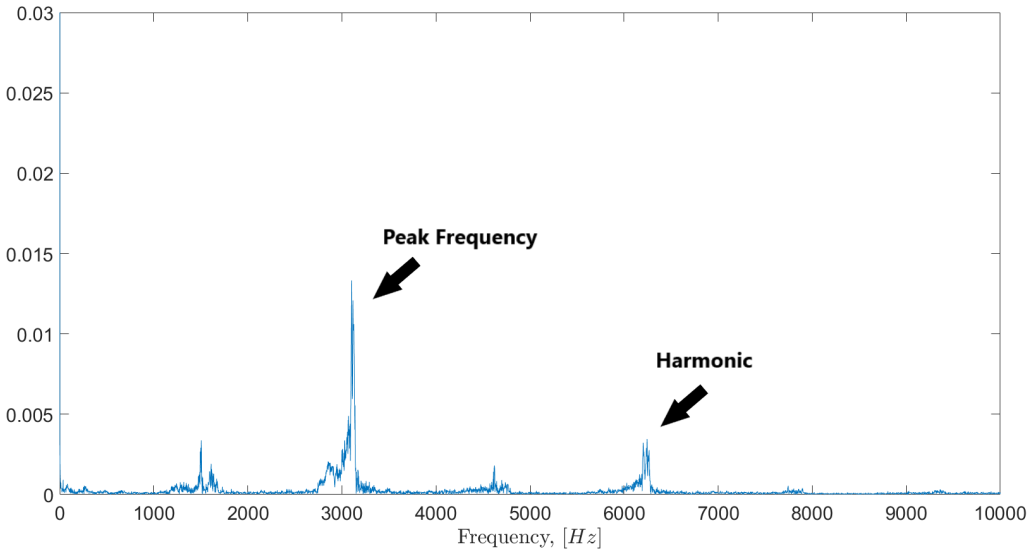

Figure 62. Example FFT for Full Run. Channel Height = 4.5 mm**,** $AR_t = 0.2$**,** $AR_n = 1.0$**,**$\dot{m}'' = 75\ \frac{kg}{m^2 s}$**,** $\phi = 0.9$

It should be noted that in order to capture the true wavespeed of the detonation, the exact radial location of the wave must be known. However, the exact location cannot be determined with the base configuration. For consistency in comparing different runs, the radial location of the ITP probes, 7.0 cm, was used. For most runs this assumption was reasonable when the channel pressure distribution was analyzed. This point was used for all wavespeed calculations to ensure a direct comparison between runs. However, using the locations of the first and last CTAPs, the actual wavespeed could be as much as 36% different from the wavespeed presented at the location of the ITP probes.

Like mentioned previously, the transition of the RRDE between operating modes was occasionally captured in the data. Figure 63 shows cases where the transition from one to two waves was captured, and also a case where two to three wave transition occurred. These plots used the high speed ITP data from the entire run which allowed for the capture of both wave mode operation. Subplot (a) shows the FFT containing one and two wave operating modes. This FFT shows a peak at roughly 3 kHz, which corresponds to the one wave operating mode, and another peak at over 4 kHz, which corresponds to the two wave operating mode. The plot also shows the harmonics of these two modes at higher frequency.

It would be expected that the frequency of the two wave mode would occur at twice the frequency of the one wave mode, and normalizing the frequency by the number of waves would result in a similar frequency as the one wave mode. This was not the case with the RRDE, which had a two wave normalized frequency roughly 70% of the one wave frequency. This could be due to a shift in the radial location of the detonation waves as the RRDE transitioned, which may have shifted the detonation wave further back into the channel which would correspond to a lower frequency per wave.

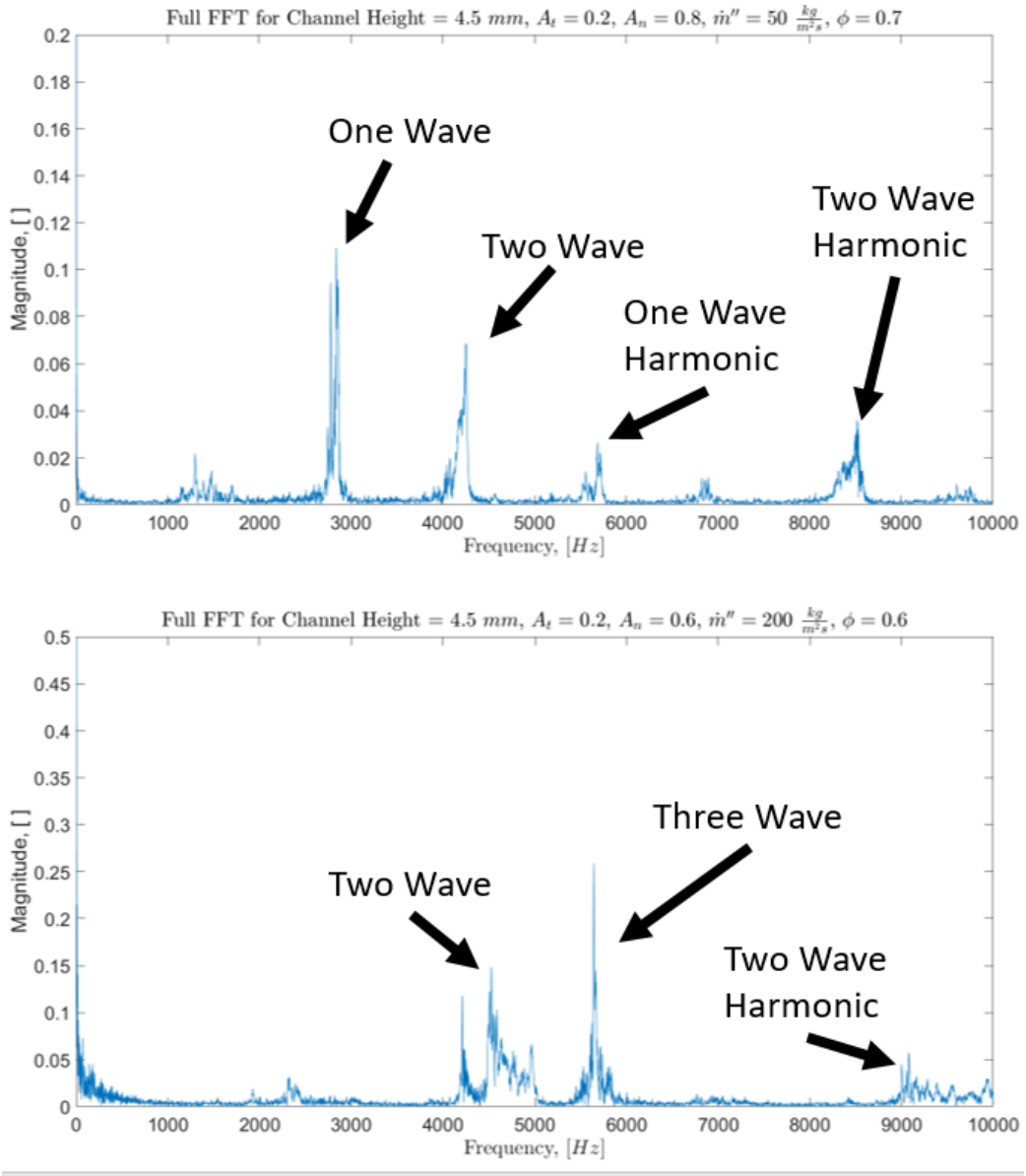

Figure 63. FFT of Operating Mode Transitions. (a) Channel Height = 4.5 mm**,** AR_t **= 0.2,** AR_n **= 0.8,** $\dot{m}''$ **= 50** $\frac{kg}{m^2 s}$**,** ϕ **= 0.7 & (a) Channel Height = 4.5** mm**,** AR_t **= 0.2,** AR_n **= 0.6,** $\dot{m}''$ **= 200** $\frac{kg}{m^2 s}$**,** ϕ **= 0.6.**

This phenomena is also shown in Figure 63 (b) where the RRDE transitioned from two to three wave mode. In this case the normalized frequency of the three wave mode was roughly 85% of the normalized two wave frequency. This suggested the detonation wave again shifted further back into the channel, but with less of a shift

compared to the one to two wave shift. The reason for analyzing the wave number include determination of wavespeed and determining the operating conditions that produce multiple wave. For these reasons the wavespeeds presented are normalized by the number of waves. In conventional RDEs, the wave number is largely a function of the fill height of the injection. The fill height is typically a function of mass flux, equivalence ratio, and back pressure on the channel. These same results are expected to appear in RRDE operation, too.

Figure 64 shows the one to two wave transition as in the pressure traces (a), Figure 58, compared to a spectrogram of the ITP data (b). The spectrogram plots the frequency response, y-axis, as a function of time, x-axis, of the high speed pressure data which allowed for a detailed view of the mode changes through the run. These plots are aligned with the same time scale and show the transition to two wave correlates between the low speed and high speed data. It should be noted that (b) shows a transition period, with one and two wave frequencies, that is not shown in the low speed pressure traces. The pressure traces only show the point at which the RRDE has fully transitioned into a two wave operating mode.

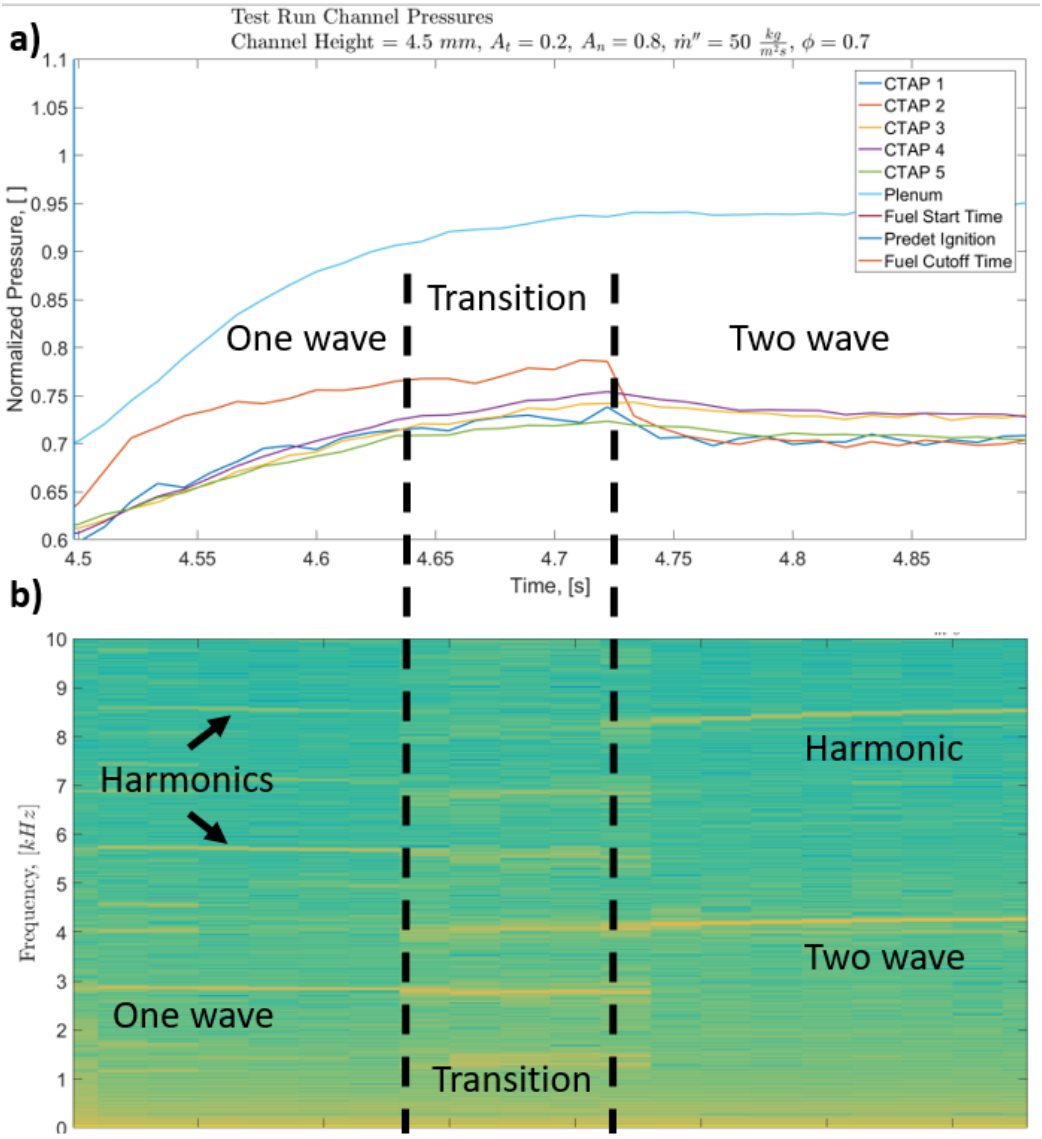

Figure 64. Pressure Trace and High Speed Spectrogram Wave Transition. Channel Height = 4.5 mm, $AR_t = 0.2$, $AR_n = 0.8$, $\dot{m}'' = 50 \frac{kg}{m^2 s}$, $\phi = 0.7$. (a) channel pressure plot & (b) high speed pressure spectrogram analysis.

To determine the performance of the RRDE as an APU there were two main measures used, the power output of the RRDE and its thermal efficiency. To calculate the power output from the turbine, the work done by the compressor side of the turbocharger was calculated, and by using the efficiency of the compressor and the mechanical efficiency of the shaft, the turbine output power could be backed out. This was a similar method as the one used by Rouser et al.[27] with the work given by Equation 18:

$$\dot{W}_t = \frac{\dot{m}_c c_p T_{t1}}{\eta_{mech}\eta_c}\left(\left(\frac{P_{t2}}{P_{t1}}\right)^{\frac{\gamma-1}{\gamma}} - 1\right) \tag{18}$$

where $\dot{W}_t$ is the power the turbine is sending to the turbocharger shaft, $\dot{m}_c$ is the mass flow rate through the compressor side of the turbocharger, c_p is the specfic heat at constant pressure for air, T_{t1} is the total temperature entering the compressor, η_{mech} is the mechanical efficiency between the tubine and compressor (assumed 0.99), η_c is the compressor efficiency, determined from the compressor operating map in Figure 65, P_{t1} is the total pressure entering the compressor, P_{t2} is the total pressure exiting the compressor. By using the operating point of the compressor based on the compressor pressure ratio, π_c, and the corrected mass flow of the compressor, $\dot{m}_{corr}$, the compressor efficiency can be determined.

The pressure and temperature measurements taken from the compressor side of the turbocharger were all static values; therefore, these values must be converted to total properties using Equation 19 and Equation 20:

$$T_t = T\left(1 - \frac{\gamma-1}{2}M^2\right) \tag{19}$$

$$P_t = P\left(1 - \frac{\gamma-1}{2}M^2\right)^{\frac{\gamma}{\gamma-1}} \tag{20}$$

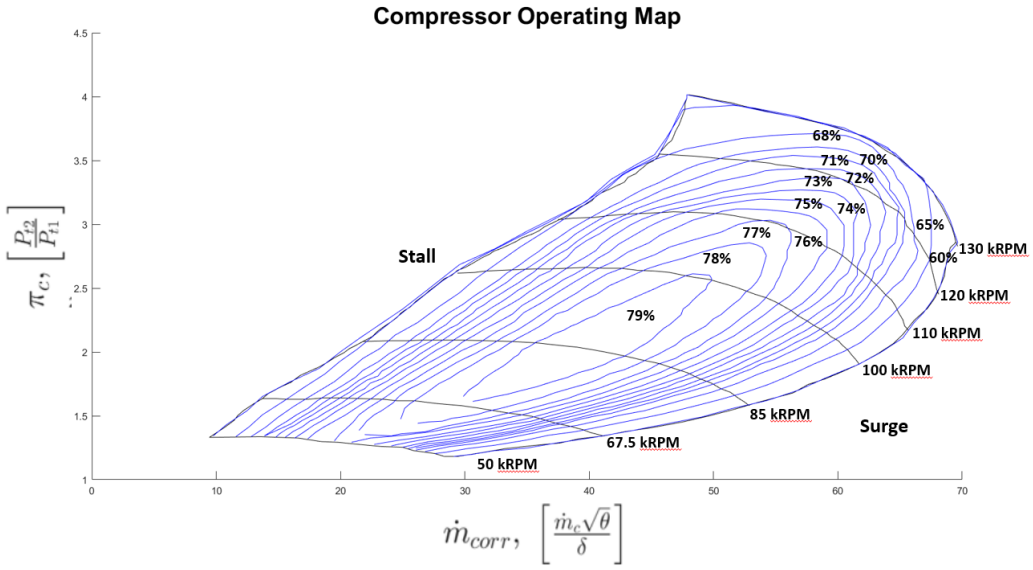

Figure 65. Compressor Operating Map. Digitized from [39].

This required the calculation of the Mach number given by Equation 21:

$$M = \frac{V}{a} \tag{21}$$

where V is the velocity and a is the speed of sound. The speed of sound was determined by the static temperature, Equation 22

$$a = \sqrt{\gamma RT} \tag{22}$$

The velocity was determined based on the mass flow rate, Equation 23:

$$V = \frac{\dot{m}}{\rho A} \tag{23}$$

where ρ is the density and A is the area. To get the density, the perfect gas law was used:

$$\rho = \frac{P}{RT} \tag{24}$$

where R is the specific gas constant. The static pressures and temperatures were taken as a mean value at the end of the RRDE operation. The full operating values are shown in Figure 66 and a zoomed view during the section where the mean was taken are shown in Figure 67. It is important to not that the static temperature

downstream of the compressor does not reach steady state during the run. However, when compared to the maximum downstream static temperature, the change in the measurement of power is negligible, and assuming the lower value at the end of the run will under-predict the power out of the turbine.

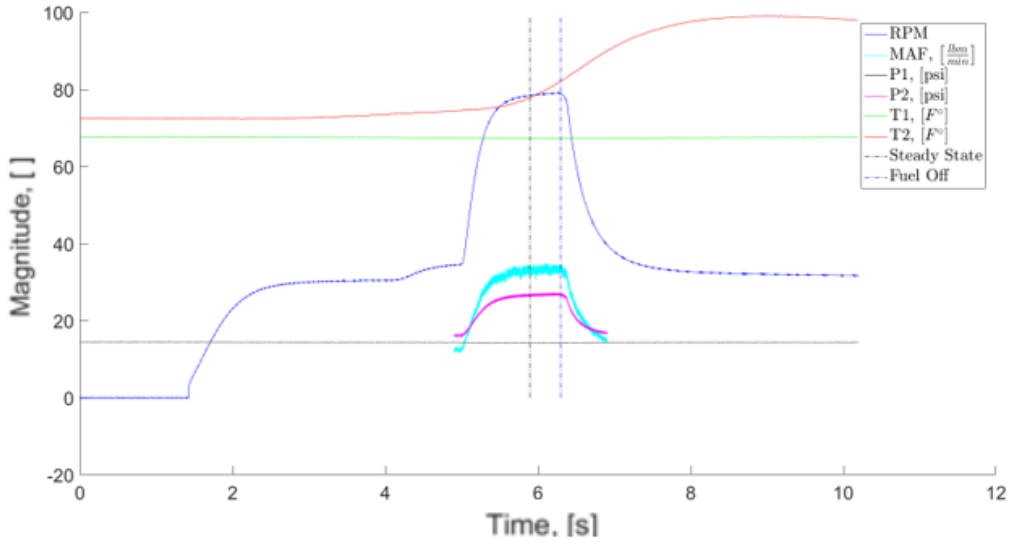

Figure 66. Turbine Run Power Measurements. Turbine Channel, AR_t = 0.2, NGV Angle = 39.0°, $\dot{m}''$ = 50 $\frac{kg}{m^2 s}$, ϕ = 0.5.

To provide comparison of the RRDE as an APU to other APUs, the specific power of the turbine is used. This is the ration of the power output to the input air mass flow rate and given by Equation 25:

$$\dot{W}_{t,s} = \frac{\dot{W}_t}{\dot{m}_a} \tag{25}$$

Specific power allows for a direct comparison to other APUs as well as estimates the mass flow rates need to achieve a given power output for a device.

The second of the two performance measures was the thermal efficiency of the RRDE, given by Equation 26:

$$\eta_{th} = \frac{\dot{W}_t}{Q_{in}} \tag{26}$$

where η_{th} is the thermal efficiency of the RRDE and Q_{in} is the input energy into the

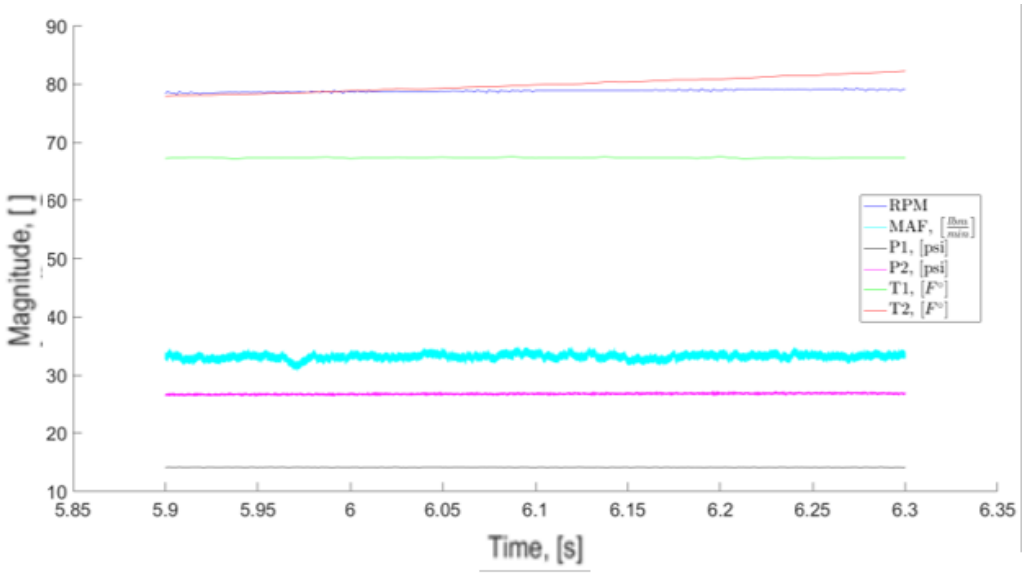

Figure 67. Turbine Run Power Measurements (zoomed). Turbine Channel, AR_t = 0.2, NGV Angle = 39.0°, $\dot{m}''$ = 50 $\frac{kg}{m^2 s}$, ϕ = 0.5.

RRDE from the combusting fuel and given by Equation 27:

$$Q_{in} = \dot{m}_f \ \mathbf{LHV} \tag{27}$$

where $\dot{m}_f$ is the mass flow rate of fuel and **LHV** is the lower heating value of that fuel. The thermal efficiency of the RRDE shows how well the RRDE can convert the energy available in the fuel into usable work.

In the Internal Combustion Engine (ICE) world the performance is typically measured in Brake Specific Fuel Consumption (BSFC), which is given by Equation 28:

$$BSFC = \frac{\dot{m}_f}{\dot{W}_t} \tag{28}$$

This is another relation between the power out of the turbine and the fuel input into the combustor. BSFC is inversely proportional to the thermal efficiency, Equation 26. This relation is shown in Equation 29, and shows the two are interchangeable; therefore, this project will report the efficiency of the RRDE using thermal efficiency. This relationship will allow for the comparison of the RRDE APU and other APUs/-generators in used today.

$$\eta_{th} = \frac{1}{BSFC \ \mathbf{LHV}} \tag{29}$$

3.4.2 Test Matrix.

Because of the modularity built into the Radial RDE, there exist an extensive list of possible test configurations. For this project, the key variables being investigated were: channel height, throat area ratio, nozzle area ratio, mass flow rate, and equivalence ratio. The variations in the geometric configurations were shown in Figure 36, Figure 41, and Figure 47, respectively. To determine the effects of channel height, three separate channels were made, discussed in Section 3.2.2. The nozzle ratio was varied by changing the nozzle with different nozzle exit area. For each channel, a nozzle array was designed so that the nozzle ratios of 0.5, 0.6, 0.8 and 1.0 were available. Examining the effects of throat area ratio variation was not conducted in this research so the throat area ratio was set at 0.2 for all channel configurations. These throat areas used an array of shim rings paired with a throat ring, another feature discussed in more detail in Section 3.2.2. Table 3 shows a detailed description of the number of shim rings needed to achieve the 0.2 throat area ratio for the tested channel configurations.

Table 3. Shim Thickness and Number needed for given Air Injection Area Ratios, $\frac{A_t}{A_c}$, for all Channel configurations tested.

Throat Area Ratio	0.2		
Channel Height	3.5 mm	4.0 mm	4.5 mm
Shim Thickness	Number of Shims		
0.127 mm	1	1	0
0.508 mm	1	1	1
1.220 mm	0	0	0
2.286 mm	1	1	1
Actual Area Ratio	0.220	0.193	0.200
% Difference	10.2%	3.6%	0.0%

Finally, the variability in mass flow rate and equivalence ratio were studied. Because the comparison of the three different channel heights meant comparing three different channel areas, having the same mass flux through the RRDE dictated the

mass flows tested. The tested mass fluxes were: 50, 75, 100, 125, 150, and 200 $\frac{\text{kg}}{\text{m}^2\text{s}}$. The equivalence ratio was then varied at each mass flux to get a sense of the operating map of the RRDE. The equivalence ratios were varied from 0.5 to 1.0 at an interval of 0.1.

When testing the RRDE with the turbocharger attached, the throat area ratio was set at 0.2, which was comparable to the throat ratio tested in the stand alone configuration. Because the turbine channel had a larger initial height the mass flux variation was limited to a max of 100 $\frac{\text{kg}}{\text{m}^2\text{s}}$at a maximum mass flow rate of 0.55 $\frac{\text{kg}}{\text{s}}$, which was set by the maximum mass flow rate for the turbocharger. The NGV turning angles tested were 23.5°, 32.0°, and 39.0°. At each NGV configuration a mass flux sweep was conducted at 50, 75, and 100 $\frac{\text{kg}}{\text{m}^2\text{s}}$, and each one of these mass fluxes was tested at an equivalence ratio sweep from 0.5 to 0.6. An equivalence ratio of 0.6 was set in an attempt to lower the combustion temperature and prolong the life of the turbine.

3.5 Uncertainty

The uncertainty analysis for this project was done using a partial derivative method described by Moffat.[41] To use this method, the equation for the value of interest was expanded so that each variable in the equation was either a measurement or a known constant. Next the partial derivative of the equation is taken with respect to each of the measurement values, referred to as the sensitivity. Finally, the root sum square of the products of the sensitivities and device errors was taken to acquire the uncertainty in the measurement. This was done in a similar manor for each of the calculated values examined in this product. Equation 30 was used for the air and fuel mass flow rates:

$$\dot{m} = C_D \frac{A_o P_t}{\sqrt{T_t}} \sqrt{\frac{\gamma}{R}} \left(\frac{\gamma + 1}{2} \right)^{\frac{\gamma+1}{2(\gamma-1)}} \tag{30}$$

where C_D is the discharge coefficient of the sonic nozzle, and assumed to be 0.99, A_o is the area of the sonic nozzle orifice, P_t is the total pressure, T_t is the total temperature, and R is the gas constant for the flow.

Mass flux wass measured using Equation 31:

$$\dot{m}'' = C_D \frac{A_o P_t}{2\pi r_c h_c \sqrt{T_t}} \sqrt{\frac{\gamma}{R}} \left(\frac{\gamma+1}{2} \right)^{\frac{\gamma+1}{2(\gamma-1)}} \tag{31}$$

where r_c is the radius of the start of the channel and h_c is the initial channel height.

Finally, the equivalence ratio was calculated using Equation 32:

$$\phi = \frac{\frac{f}{a}}{\left(\frac{f}{a}\right)_{st}} \tag{32}$$

where $\frac{f}{a}$ is the actual fuel/air mass ratio and $\left(\frac{f}{a}\right)_{st}$ is the stoichiometric fuel/air ratio.

By substituting in Equation 30 into the actual mass flows in Equation 32, Equation 33 is formed:

$$\phi = \frac{\frac{A_{of} P_{tf}}{\sqrt{T_{tf}}} \sqrt{\frac{\gamma_f}{R_f}} \left(\frac{\gamma_f+1}{2} \right)^{\frac{\gamma_f+1}{2(\gamma_f-1)}}}{\frac{A_{oa} P_{ta}}{\sqrt{T_{ta}}} \sqrt{\frac{\gamma_a}{R_a}} \left(\frac{\gamma_a+1}{2} \right)^{\frac{\gamma_a+1}{2(\gamma_a-1)}}} \frac{1}{\left(\frac{f}{a}\right)_{st}} \tag{33}$$

where the values correspond to either the fuel or air. This was done to achieve an equation solely of measurements or constants.

An example of the uncertainty process is shown for the mass flow rate, Equation 30. The measurement variables in this equation are the total pressure, P_t, and the total temperature, T_t. The partial of Equation 30 with respect to each of these variables is shown in Equations 34 and 35:

$$\frac{\delta \dot{m}}{\delta P_t} = C_D \frac{A_o}{\sqrt{T_t}} \sqrt{\frac{\gamma}{R}} \left(\frac{\gamma+1}{2} \right)^{\frac{\gamma+1}{2(\gamma-1)}} \tag{34}$$

$$\frac{\delta \dot{m}}{\delta T_t} = -C_D \frac{A_o P_t}{2 T_t^{\frac{3}{2}}} \sqrt{\frac{\gamma}{R}} \left(\frac{\gamma+1}{2} \right)^{\frac{\gamma+1}{2(\gamma-1)}} \tag{35}$$

these equations represent the sensitivity of the mass flow with respect to the measurement variables. Next, Equations 34 and 35 are inserted into Equation 36:

$$\delta \dot{m} = \sqrt{\left(\frac{\delta \dot{m}}{\delta P_t} \Delta P_t \right)^2 + \left(\frac{\delta \dot{m}}{\delta T_t} \Delta T_t \right)^2} \tag{36}$$

where ΔP_t is the error in the pressure transducer and ΔT_t is the error in the thermocouple. Equation 36 represents the total uncertainty in the measurement of the mass flow rate. The same technique was applied to the mass flux, Equation 31, and equivalence ratio, Equation 33. A summary of the uncertainties is given in Table 4, using example values from an actual test run and the uncertainties in the devices used from Table 1. This test run was done using the configuration of the 4.5 mm channel, a throat area ratio of 0.2, a nozzle area ratio of 1.0, a mass flux of 75 $\frac{\text{kg}}{\text{m}^2\text{s}}$, and an equivalence ratio of 0.9.

Table 4. Uncertainty Example.

Measurement	Value	Uncertainty	% Error
Air Mass Flow Rate, $\left[\frac{kg}{s}\right]$	0.224	$\pm 5.5 * 10^{-3}$	$\pm 2.44\%$
Fuel Mass Flow Rate, $\left[\frac{kg}{s}\right]$	$5.8 * 10^{-3}$	$\pm 1.56 * 10^{-4}$	$\pm 2.68\%$
Mass Flux, $\left[\frac{kg}{m^2 s}\right]$	75.7	± 6.7	$\pm 8.85\%$
Equivalence Ratio, [ ]	0.89	± 0.03	$\pm 3.62\%$

The error in wavespeed was calculated by dividing the highspeed pressure data from the ITPs into five segments while the detonation was propagating through the channel. Then an FFT was taken for each of these segments, shown in Figure 68, with a zoomed in version focusing on the frequency of interest in Figure 69. These FFTs were taken using the same run as in Table 4. The standard deviation in the peak frequency for each FFT was found. By using a Student T score for a sample size of five and a 95% confidence interval, the error in the wavespeed was determined. The mean wavespeed thoughout the run was 1364.1 $\frac{\text{m}}{\text{s}}$ with an error of 37.2 $\frac{\text{m}}{\text{s}}$, which gave a percent error of 2.73%. This percent error was assumed to be the same error for all runs.

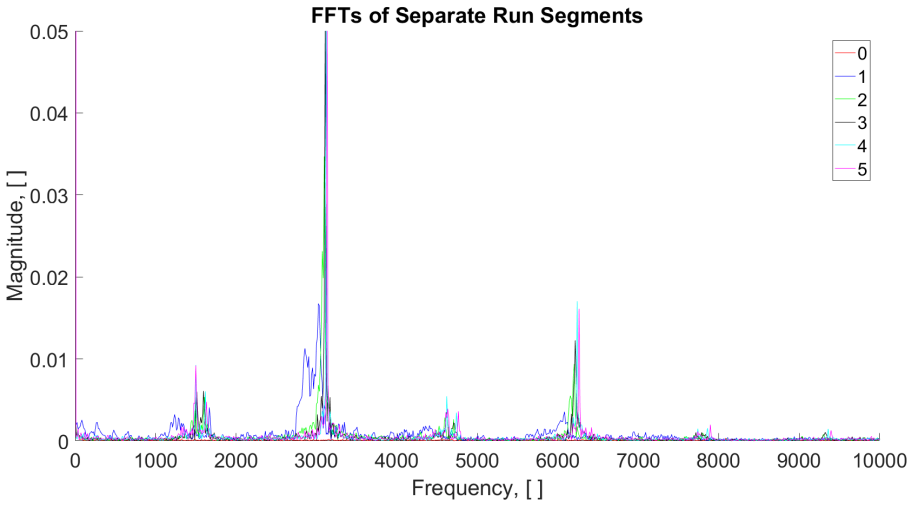

Figure 68. FFT for Segments of Radial RDE Run.

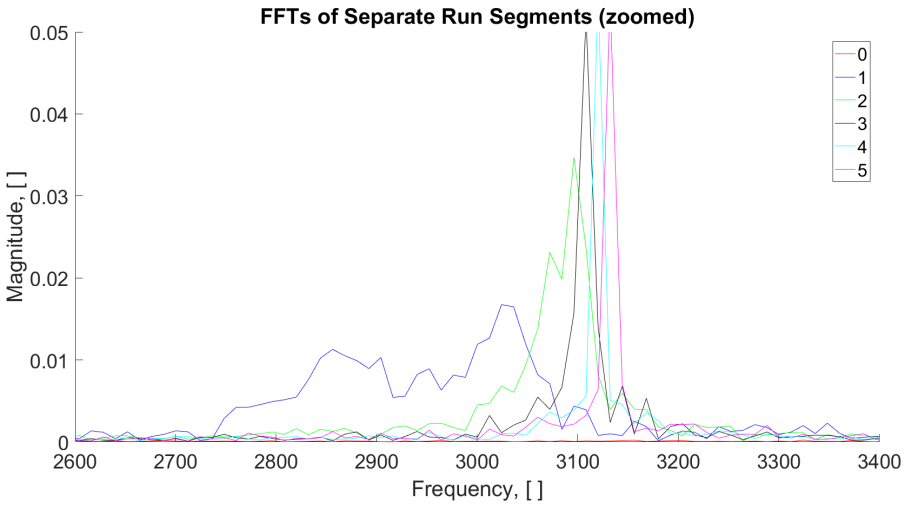

Figure 69. FFT for Segments of Radial RDE Run (zoomed).

A repeatability analysis was conducted for the Radial RDE stand alone operation. This data was collected at the operating condition with the 4.5 mm channel, a throat area ratio of 0.2, a nozzle area ratio of 1.0, a mass flux of 50 $\frac{\text{kg}}{\text{m}^2\text{s}}$, and an equivalence ratio of 1.0. Five separate points were taken on multiple days during testing and also at multiple times during testing. Table 5 shows the results of the repeatability error using a Student T distribution based on a 95% confidence interval. Before examining the data it should be known that these test points are at low mass flow rates for

both the fuel and the air. At these low flow rates the regulating valves for both the fuel and air have issues exactly regulating the pressure upstream of the sonic nozzle. This made it difficult to run at the exact same mass flow rates at different times. This was likely the biggest contribution to the repeatability error in mass flux and equivalence ratio shown in Table 5. Higher mass flow rates were expected to have a lower repeatability error.

Table 5. Repeatability.

Measurement	Mean	2σ	% Error
Mass Flux, $\left[\frac{kg}{m^2 s}\right]$	51.4	± 5.4	$\pm 10.5\%$
Equivalence Ratio, [ ]	1.00	± 0.09	$\pm 9.3\%$
Pressure Loss, [ ]	0.27	± 0.05	$\pm 18.8\%$
Wavespeed, $\left[\frac{kg}{m^2 s}\right]$	1289	± 16.3	$\pm 1.3\%$

Figure 70 shows the plots of wavespeed and pressure loss versus the mass flux and equivalence ratio. These are fitted with a trend line (blue dashed line) through the five points. Next, the trend line was shifted by the square root of the sum of the squares of the errors in the measurement devices for both axes. These new trend line were plotted for the maximum and minimum values (green dashed lines) and represent the error bar on the actual measurements of the five points. Subplots (a & b) show the wavespeeds all fell within the error plots, which indicated that the inability to control the exact mass flow and equivalence ratio of the test points was a less significant factor in repeatability error since the measurement of wavespeed was not based on mass flow or equivalence ratio, but the response frequency of the high speed pressure data.. Subplot (c) shows that the pressure loss data were outside of the error bars which indicates that the difficulty in setting the test conditions had a significant effect on the error associated with the pressure loss repeatability error. This can also be seen in (d) where the the points fall along the error bars with less margin than (a & b), which also indicates there is an effect in the error due to the

inability to pick the test point, and it is on the order of the error of the measurement devices.

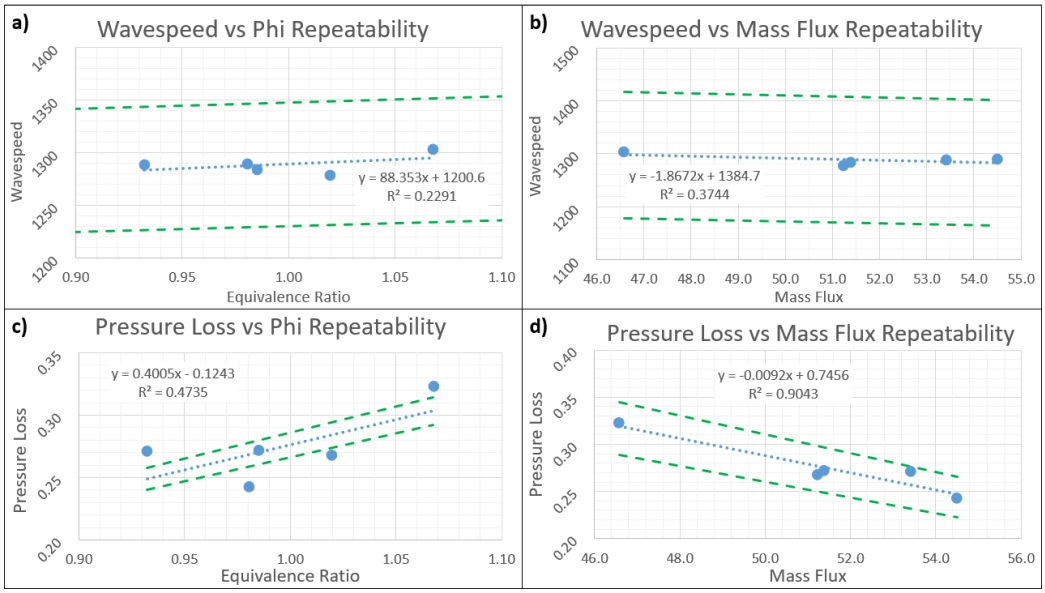

Figure 70. Repeatability Analysis.

The error in the power out of the Radial RDE and its thermal efficiency was conducted in the same manor shown earlier. To do this the formula for power was reduced into a form containing only measured values and constants. This was done by combining Equations (18-22), which yields Equation 37:

$$\dot{W}_t = \frac{c_p \dot{m} T_1 \left(\frac{RT_1\dot{m}^2+2\gamma(A_1P_1)^2-\gamma RT_1\dot{m}^2}{2\gamma(A_1P_1)^2}\right)\left(\left(\frac{P_2\left(\frac{RT_2\dot{m}^2+2\gamma(A_2P_2)^2-\gamma RT_2\dot{m}^2}{2\gamma(A_2P_2)^2}\right)^{\frac{\gamma}{\gamma-1}}}{P_1\left(\frac{RT_1\dot{m}^2+2\gamma(A_1P_1)^2-\gamma RT_1\dot{m}^2}{2\gamma(A_1P_1)^2}\right)^{\frac{\gamma}{\gamma-1}}}\right)^{\frac{\gamma-1}{\gamma}} - 1\right)}{\eta_c \eta_{mech}} \tag{37}$$

where T_1 and P_1 are the static temperature and pressure entering the compressor and T_2 and P_2 are the static temperature and pressure exiting the compressor.

The error in chemical energy was based on the error in the fuel mass flow rate. For the error in the thermal efficiency the combination of the error in turbine power and error in the chemical energy available were combined taking the square root of the sum of the squared errors. These errors for the turbine performance are shown

in Table 6. This example run was using the configuration with a throat area ratio of 0.2, with the 39° NGV ring, at a mass flux of 50 $\frac{\text{kg}}{\text{m}^2\text{s}}$, and at an equivalence ratio of 0.5.

Table 6. Uncertainty Example for Turbine Performance.

Measurement	Value	Uncertainty	% Error
Turbine Power, $[kW]$	18.6	± 0.3	$\pm 1.76\%$
Chemical Energy, $[kW]$	404.1	± 17.7	$\pm 4.4\%$
Thermal Efficiency, [ ]	4.73%	$\pm 0.22\%$	$\pm 4.72\%$

IV. Results and Discussion

This chapter will discuss the results acquired during testing of the Radial RDE. The first half of the chapter will discuss the operation of the RRDE as a stand alone device. This part of the research showed consistent detonation operation for a variety of configurations and studied the effects of varying the parameters of channel height, nozzle area ratio, mass flux, and equivalence ratio. These results completed the second objective of this project, which was to operate the RRDE and determine its operating characteristics. The effects of the four test parameters on the channel pressure distributions will be discussed in Section 4.1. These results show the completion of the second objective of this project, and show the viability of the RRDE as a detonation engine. Section 4.2 discusses the results of the RRDE operation as the different parameters were varied. This was a global analysis of every test run and did not account for the interaction with other parameter variation. Section 4.5 will discuss a more detailed analysis of the performance of the RRDE at the channel height of 4.5 mm and at all of the nozzle area ratios (0.5, 0.6, 0.8, and 1.0). These configuration were tested at all mass fluxes and equivalence ratios, which allowed for the creation of a rough operating map of the RRDE. A more detailed discussion of the subtle effects of varying the channel height and nozzle area ratio, that were not already discussed in Section 4.2 or Section 4.5, will be examined in Section 4.3 and Section 4.4, respectively. These result will also show that the RRDE may operate in a more steady fashion relative to conventional RDEs, showing the benefits of the radial flow scheme. Finally, the work presenting in these sections offer insight on a novel design that had yet to be tested in the United States.

The successful characterization of the Radial RDE as a stand alone device allowed for the second half of this chapter, which will focus on the operation of the turbocharger when coupled with the RRDE. Section 4.6 will discuss the performance

of the turbine-RRDE pair and examine the effects of varying the mass flow, the equivalence ratio, and the exit flow angle of the NGVs ahead of the turbine. The examination of these results will show the accomplishment of the third objective for this project. These results also serve as the starting block for the continued exploration of the RRDE as a compact APU. This configuration represents the first of its kind in the world, and showed that this RRDE APU could outperform conventional APUs in power density and response time.

4.1 Pressure Distributions

Before attempting to pair the Radial RDE with the turbocharger and test it as an APU, it was necessary to characterize the operation of the RRDE as a stand alone combustor. This determined the flow conditions in which the RRDE operated to give the bounds of the possible APU operating conditions. It also enabled determination of how a design change would effect the RRDE and subsequent APU. This section discusses the effect of varying the geometry and flow conditions on the pressure distribution in the of the RRDE. When examining the channel pressure, both the cold flow and detonating profiles were considered. The cold flow distributions were taken after the air flow was turned on and reached a steady value. The detonating pressure distributions were created from the same cases as the cold flow cases, but at the time where the detonation has stabilized within the channel. These measurements were taken by the CTAPs at the five radial location described in Section 3.3, and it should be noted that the CTAPs measure an average static pressure; therefore, the normalized pressure that will be presented were the static channel pressure referenced to the total pressure in the plenum.

First, the effects of varying the height of the detonation channel on the pressure distributions were examined. Figure 71 shows the cold flow pressure distributions for

all three channel heights (3.5, 4.0 & 4.5 mm) at the same mass flux of 125 $\frac{\text{kg}}{\text{m}^2\text{s}}$. From this plot it is clear that the smaller channel height reduced the pressure lost through the air injection process. The shape of all of the pressure distributions remains the same for each channel height. The cause of the shift in pressure distribution plots could be due to the decrease in the mass flow, which corresponds to a decrease in injection pressure at the plenum.

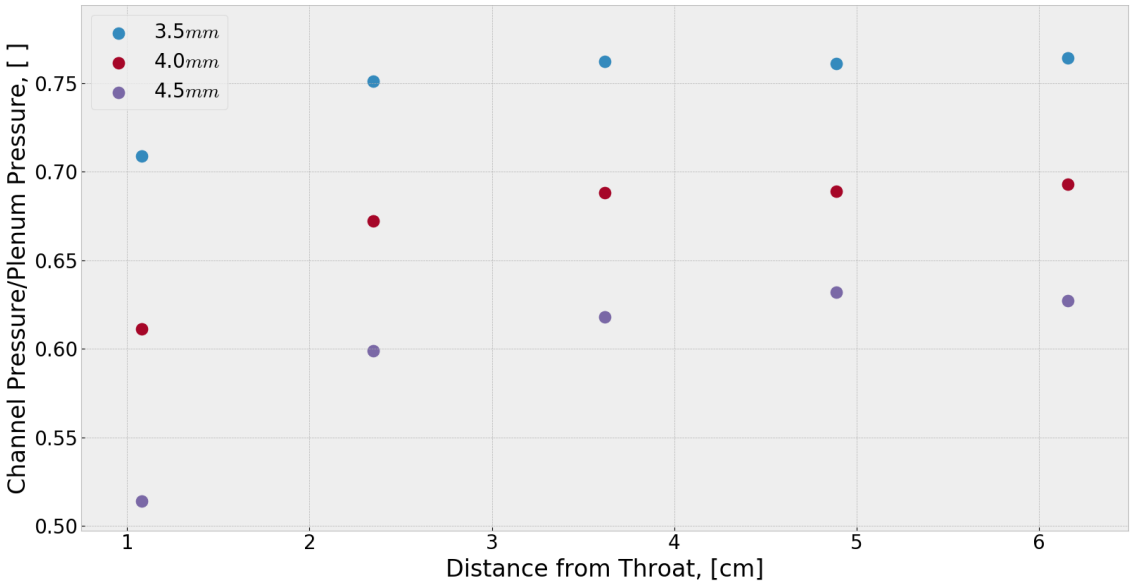

Figure 71. Cold Flow Channel Pressure Distribution at Multiple Channel Heights: $AR_t = 0.2$**,** $AR_n = 1.0$**,** $\dot{m}'' = 125\frac{kg}{m^2 s}$**,** $\phi = 0.7$**.**

With an understanding of the cold flow pressure distributions, the pressure distribution when the RRDE was detonating were examined in Figure 72. This plot shows the pressure distributions for the two smaller channel heights had the same shape, while the 4.5 mm channel had a large dip at the second CTAP from the injector. Also, for the two smaller channels the pressure in the final CTAP was higher than that of the second to last CTAP. This was not the case for the 4.5 mm channel, where the pressure continuously dropped from the third CTAP to the final CTAP. The suspected reason was attributed to the two wave operation experienced with the

smaller channels, versus the one wave mode of the 4.5 mm channel. When the RRDE transitions from one to two waves, it appears that the detonation wave was pushed back further into the detonation channel. A more detailed of the mechanisms behind this phenomena will be discussed in Section 4.2. This thought is shown clearly in Figure 72, with the two wave modes having a peak pressure closer to the air injector.

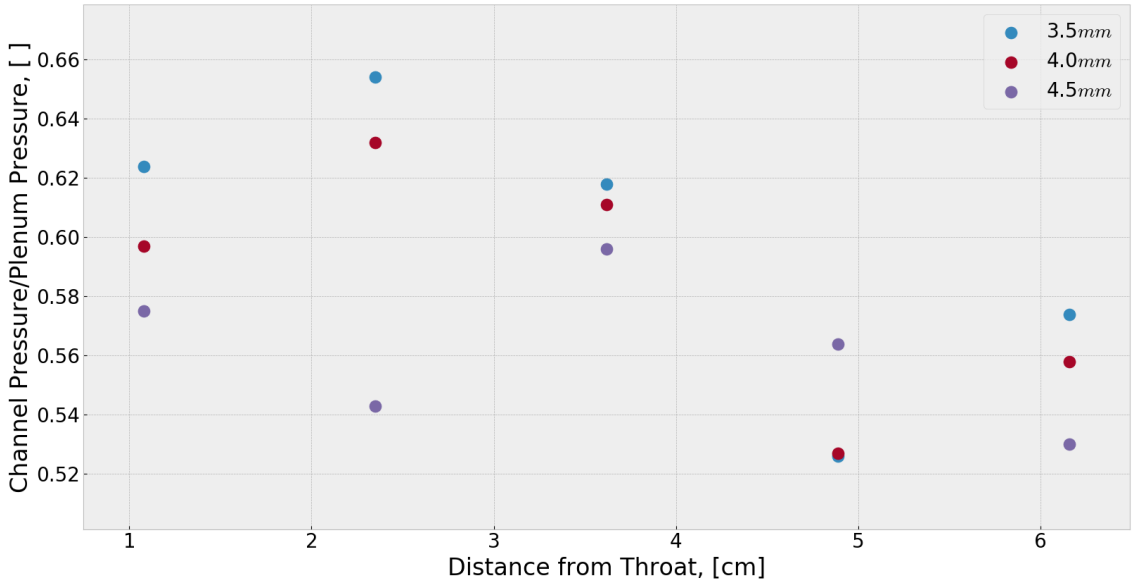

Figure 72. Detonating Channel Pressure Distribution at Multiple Channel Heights: $AR_t = 0.2$**,** $AR_n = 1.0$**,** $\dot{m}'' = 125\frac{kg}{m^2 s}$**,** $\phi = 0.7$**.**

Next, the effects of varying the nozzle area ratio on the pressure distributions was examined. Figure 73 shows the effects the nozzle area ratio had on the cold flow pressure distributions within the channel downstream of the throat. The shape of the distribution was not changed regardless of the nozzle. The magnitude of these cold flow plots also remained relatively unchanged, but as the nozzle area ratio was decreased there was a slight increase in the normalized channel pressure. This could be attributed to the normalized pressure measurement relating the static channel pressure to the total pressure in the plenum, before injection. The higher back pressure from the more restrictive nozzles would lower the velocity in the channel which would

lower the channel mach number, thereby increasing the static to total pressure ratio.

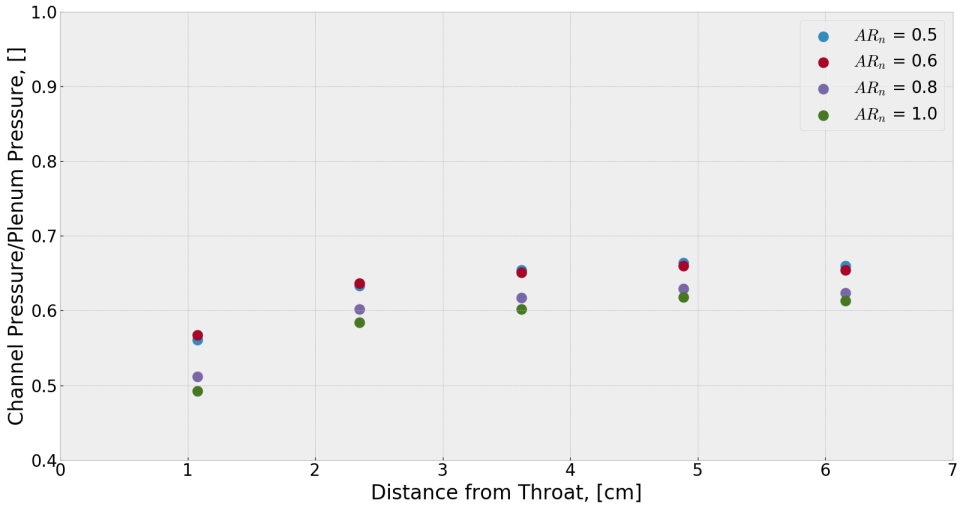

Figure 73. Cold Flow Channel Pressure Distribution at Multiple Nozzle Area Ratios: Channel Height = 4.5 mm**,** $AR_t = 0.2$**,** $\dot{m}'' = 125\frac{kg}{m^2 s}$**,** $\phi = 1.0$**.**

Figure 74 shows the detonating channel pressure distributions for the same cases as Figure 73. Keep in mind the increase in plenum pressure as the detonation ignites, though the magnitude of these pressures cannot be discussed. This increased plenum pressure was used to normalize the detonation channel pressure, a fact discussed in Section 3.4.1. Much like the previous plot, the shape of the pressure distribution remained similar for each nozzle area ratio. However, the magnitude of the channel pressure distributions were noticeably different. The 0.6 nozzle area ratio shows the highest normalized pressure in the channel, which could indicate that this was where the best performance would occur. This presumption will be shown throughout this section and in Section 4.5 and was likely due to a sweet spot in the back pressuring of the channel. The nozzle area ratio of 0.6 provides enough back pressure to the channel to increase the detonability of the device, but does not apply enough back pressure to restrict the injection of the fresh reactants.

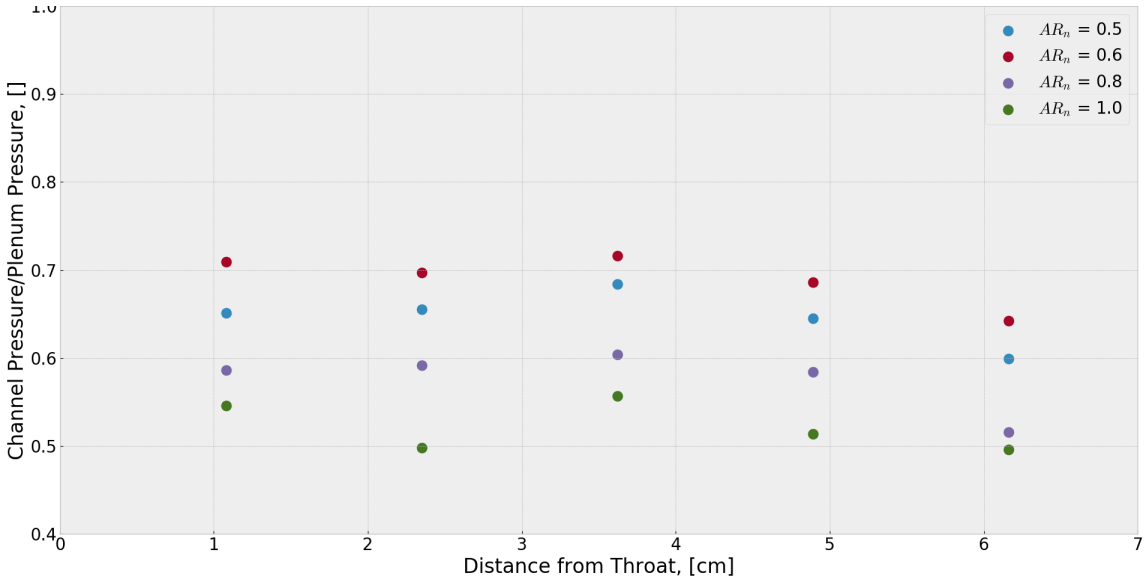

Figure 74. Detonating Channel Pressure Distribution at Multiple Nozzle Area Ratios: Channel Height = 4.5 mm**,** $AR_t = 0.2$**,** $\dot{m}'' = 125\frac{kg}{m^2 s}$**,** $\phi = 1.0$**.**

Figure 75 shows the channel pressure distribution plots as the mass flux is varied. This plot shows that for an increase in mass flux, there was an decrease in the normalized pressure. These pressure distribution lines resemble that of a subsonic isentropic expansion after a nozzle, Figure 76. The lines (G & H) represent subsonic flow after the throat of the nozzle, where (H) corresponds to the case where the flow does not reach the sonic condition at the throat and (G) corresponds to the case where flow is sonic at the throat, but remains subsonic during expansion. The area of the channel itself is constant but there was likely a recirculation zone extending off of the back face of the throat ring, which would act like a nozzle as the effective area is reduced by this zone. This was the reason attributed to the shape of the pressure distributions resembling that of an isentropic nozzle.

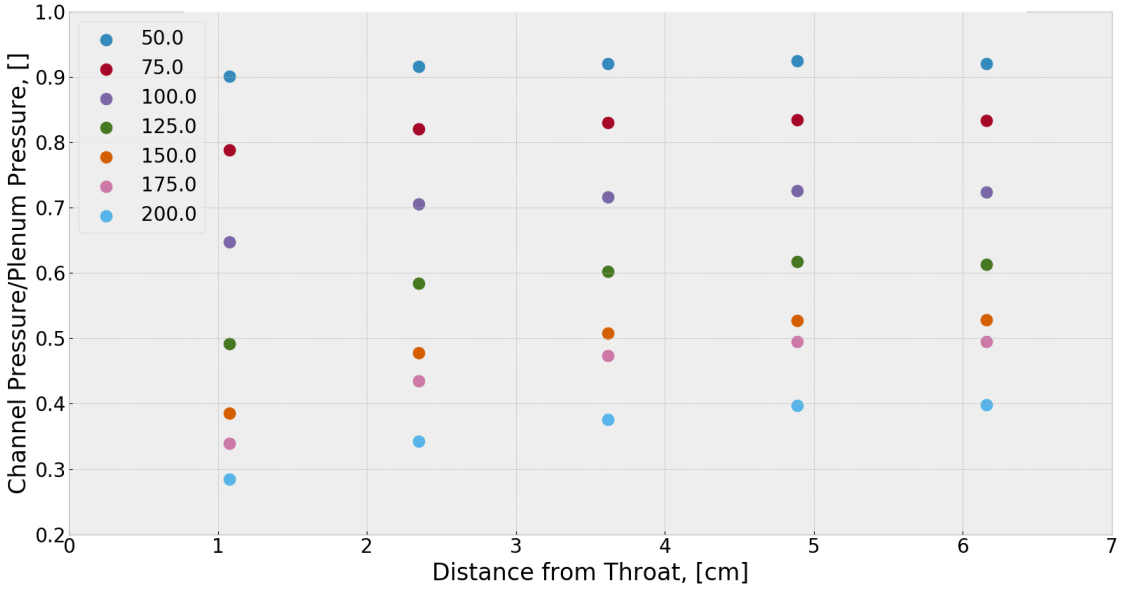

Figure 75. Cold Flow Channel Pressure Distribution vs Mass Flux: Channel Height = 4.5 mm**,** $AR_t = 0.2$**,** $AR_n = 1.0$**,** $\phi = 1.0$**.**

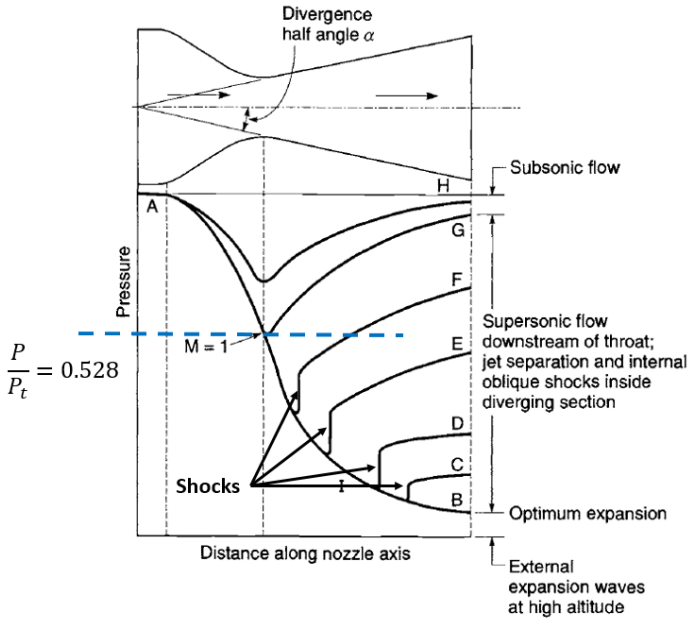

Figure 76. Isentropic Nozzle Plots. Modified from [42]

As the pressure in the plenum was increased, the magnitude of the pressure distributions change, but the shape remains that of subsonic flow through a nozzle from

Figure 76 (G). In an ideal nozzle, a pressure ratio below 0.528 corresponds to supersonic flow; however, when examining the magnitude of the pressure distributions for a mass flux greater than 125 $\frac{\text{kg}}{\text{m}^2\text{s}}$, the pressure ratios fall at or below the sonic pressure ratio, but the shape of these distributions remain that of a subsonic nozzle, Figure 76 (G), or supersonic flow that was shocked down to subsonic either before the first CTAP or between the first and second CTAP, Figure 76 (F). The pressure ratio versus Mach number line in Figure 77, which is plotted for isentropic flow. The shape of the distributions would indicate subsonic flow, but the magnitude indicated supersonic flow, but only if the flow were isentropic. Therefore, it was assumed that the injection of the flow at higher mass flow rates had significant losses which were attributed to the recirculation zone that would likely increase in strength as the mass flux was increased or due to losses as the flow was shocked down to subsonic velocities. The determination of which one of these mechanisms caused the pressure loss was not determined. Comparing the injector to the sonic nozzles used for air and fuel metering, Equation 30, the injector would have a discharge coefficient much lower than the roughly ideal nozzle used for metering. This explains the magnitude of the pressure distributions changing but the shape remaining the same, because there are high losses associated with the air injection scheme.

Figure 78 shows the detonating channel pressure distributions when mass flux is varied. This shows similar trends as the cold flow case where the shapes of each distribution remains roughly the same, but the magnitudes were different and vary directly with the mass flux between 20% at the first CTAP after injection and roughly 75% at the final CTAP. This sharp decrease in pressure loss was attributed to losses in the injection scheme of the RRDE.

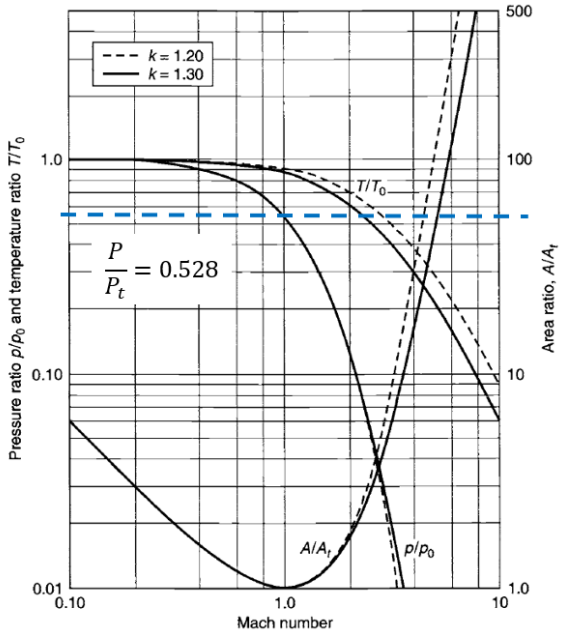

Figure 77. Isentropic Flow Plots. Modified from [42]

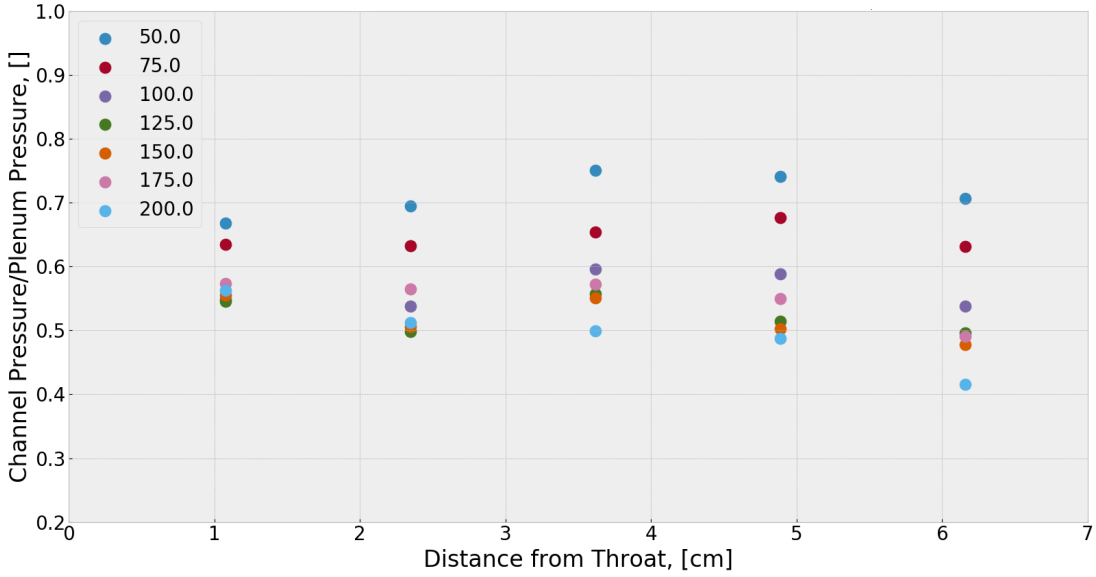

Figure 78. Detonating Channel Pressure Distribution vs Mass Flux: Channel Height = 4.5 mm**,** $AR_t = 0.2$**,** $AR_n = 1.0$**,** $\phi = 1.0$**.**

Finally, the effect of varying the equivalence ratio on the pressure distribution were examined. Figure 79 shows the cold flow channel pressure distribution when the

equivalence ratio was varied. This plot shows that as the equivalence ratio was varied there was a minimal effect on the shape and the magnitude of the channel pressure distributions. This slight variation in the pressure loss were attributed to a slight increase in the losses due to the mixing of the fuel and air at the injector.

Figure 80 shows the detonating channel pressure distributions when the equivalence ratio was varied. Like Figure 79 the shape of the channel pressure distribution was similar for all equivalence ratios, but the magnitudes varied by up to 20%, especially at the CTAP locations closer to the injector and by roughly 10% at the CTAPs furthest from the injector. This was most evident at the two lower equivalence ratios of 0.5 and 0.6 where the pressure distribution showed higher pressure throughout the channel. This could be attributed to the higher losses at the injector from mixing the fuel and air. As the injection pressure of the fuel increases with the increased fuel flow, so does the losses from the mixing of the air and fuel jets. This means operating at a lower equivalence ratio will improve the pressure loss performance of the RRDE, which was desirable for the APU operation mode as well.

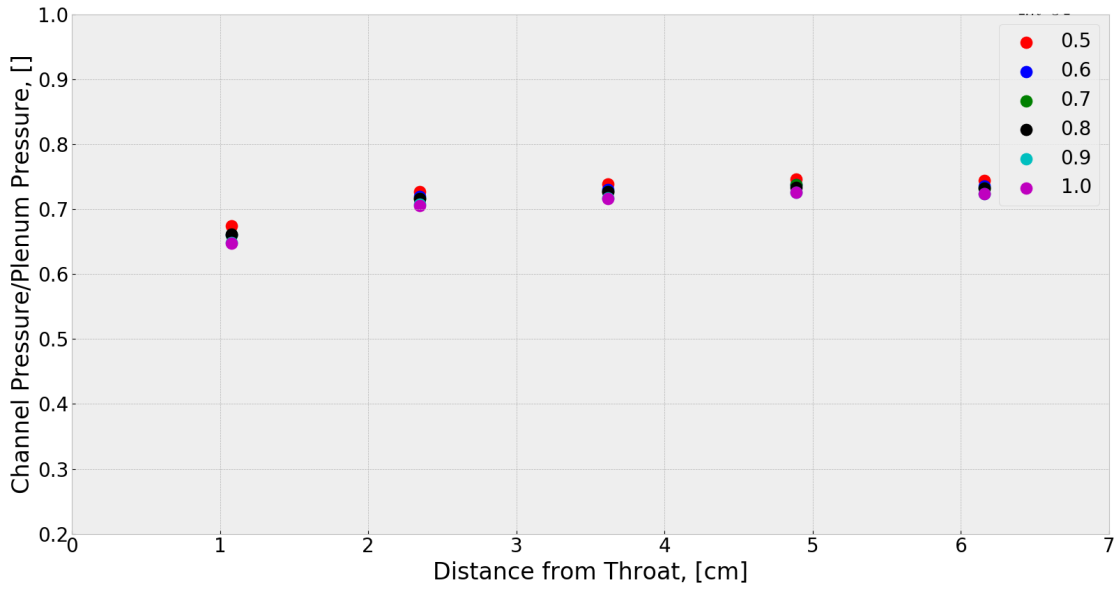

Figure 79. Cold Flow Channel Pressure Distribution vs Equivalence Ratio: Channel Height = 4.5 mm**,** $AR_t = 0.2$**,** $AR_n = 1.0$**,** $\dot{m}'' = 100\ \frac{kg}{m^2 s}$**.**

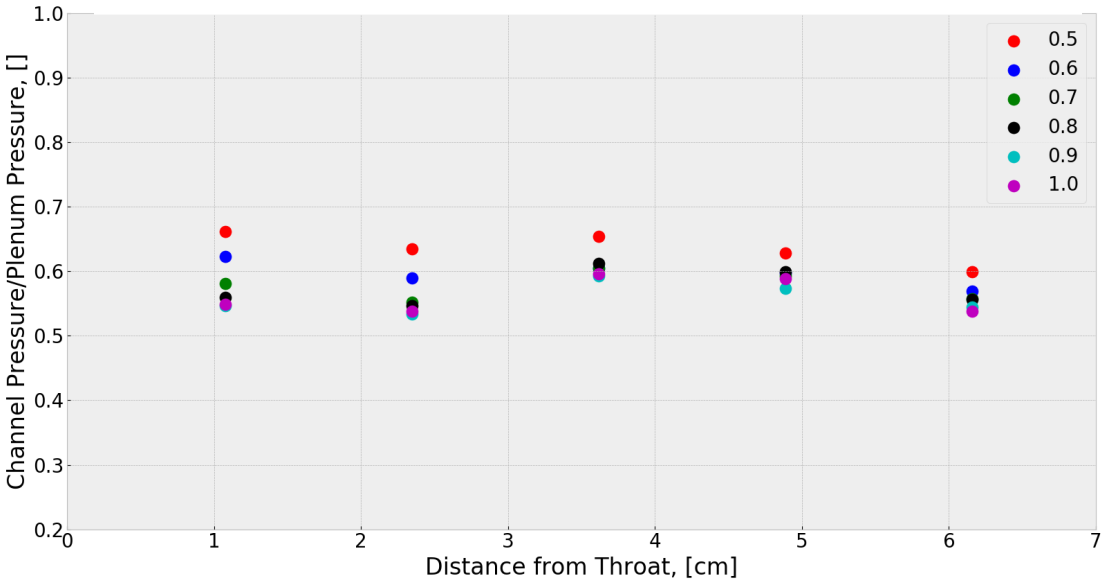

Figure 80. Detonating Channel Pressure Distribution vs Equivalence Ratio: Channel Height = 4.5 mm**,** $AR_t = 0.2$**,** $AR_n = 1.0$**,** $\dot{m}'' = 100\ \frac{kg}{m^2 s}$**.**

4.2 Radial RDE Operation

This section will examine the effects of varying the flow conditions of the Radial RDE, which included mass flux and equivalence ratio. These results are plotted for the entirety of the data set, and the general trends were shown. The examination of the effects of varying the mass flux showed strong correlation with the pressure loss and wavespeed. The wavespeed variation with mass flux for all runs is shown in Figure 81. This plot clearly shows that when the runs are broken up by the number of waves, there are three distinct trend lines that can be formed. These trend lines were given by Equation 38 for the one wave mode, Equation 39 for the two wave mode, and Equation 40 for the three wave mode.

$$\frac{V_a}{V_{CJ}} = 7.2 * 10^{-4}\dot{m}'' + 0.653 \tag{38}$$

$$\frac{V_a}{V_{CJ}} = 5.8 * 10^{-4}\dot{m}'' + 0.517 \tag{39}$$

$$\frac{V_a}{V_{CJ}} = 7.5 * 10^{-4}\dot{m}'' + 0.361 \tag{40}$$

where V_a is the actual wavespeed and V_{CJ} is the CJ velocity.

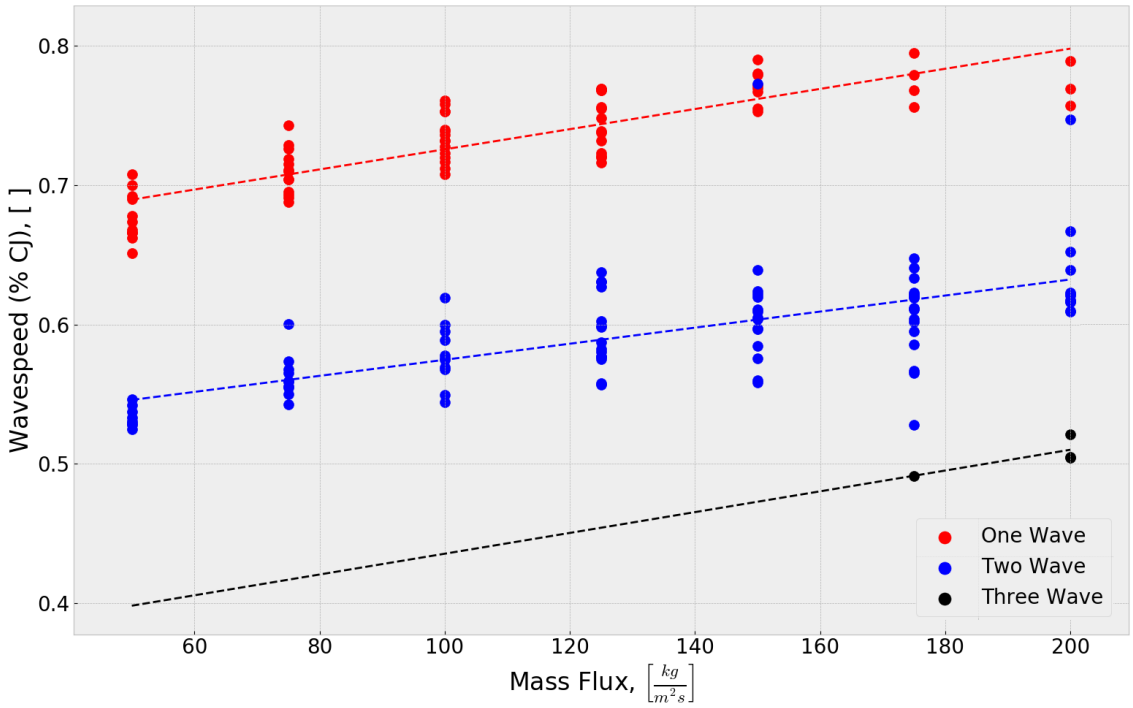

Figure 81. General Wavespeed (% CJ) versus Mass Flux for all runs.

Further examination of the effects of mass flux on the wavespeed of the device showed a clear correlation with the wavespeed and the mass flux at which the RRDE was operating. This was shown in Figure 82 for a nozzle area ratio of 0.6 operating at an equivalence ratio of 1.0; however, similar trends were also noticed for the other nozzle areas and equivalence ratios. This trend suggested that an increase in the mass flux would also correspond to an increase in the measured wavespeed. The cause of this could be due to the changing of the fill height of the RRDE as more fresh reactants enter the channel per unit time, or due to the increase in channel pressure as the injection pressure increases with mass flux. As the mass flux increased, more fresh reactants were injected into the channel, but if the actual wavespeed is roughly constant, the detonation wave may move closer to the exit of the RRDE to match the fresh reactants, which shows as an increase in the measured frequency of the wave pass. However, as the channel pressure increases, so to could the wavespeed. The

exact cause of this phenomena could not be determined with any certainty with the measurements taken for this project.

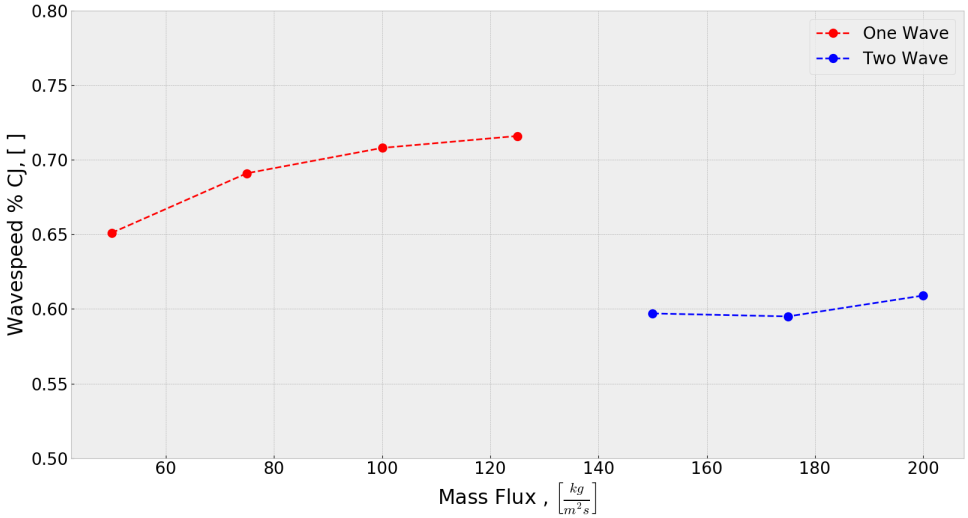

Figure 82. Wavespeed (% CJ) versus Mass Flux: Channel Height= $4.5mm$**,** $AR_t = 0.2$**,** $AR_n = 0.6$**,** $\phi = 1.0$**.**

In conventional RDEs, as the mass flux was increased, an unsteadiness in the flow appeared until the wave transition into a higher wave mode where it returned to the baseline unsteadiness of the lower wave mode at a lower mass flux.[21] This may be due to secondary combustion zones and periodic transition to other wave modes. While the extact cause of this unsteadiness is unknown, it could suggest there are areas in the operation of a conventional RDE prone to high unsteadiness. When the injection scheme is radial, like the RRDE, the detonation wave may be able to account for the change in the inflow of reactants by moving the location of the wave itself, a trait not shared with convention RDEs due to the roughly fixed radius of the channel, set by the inner and outer walls. An example of this phenomena is shown by Figure 83 for a single wave case as the mass flux is increased. However, this only stands as a possible reasoning for a possible decrease in unsteadiness in a Radial

RDE, and cannot be confirmed as the exact reason with the measurements taken in this experiment. This could also be attributed to an increase in the channel pressure at an increased mass flux.

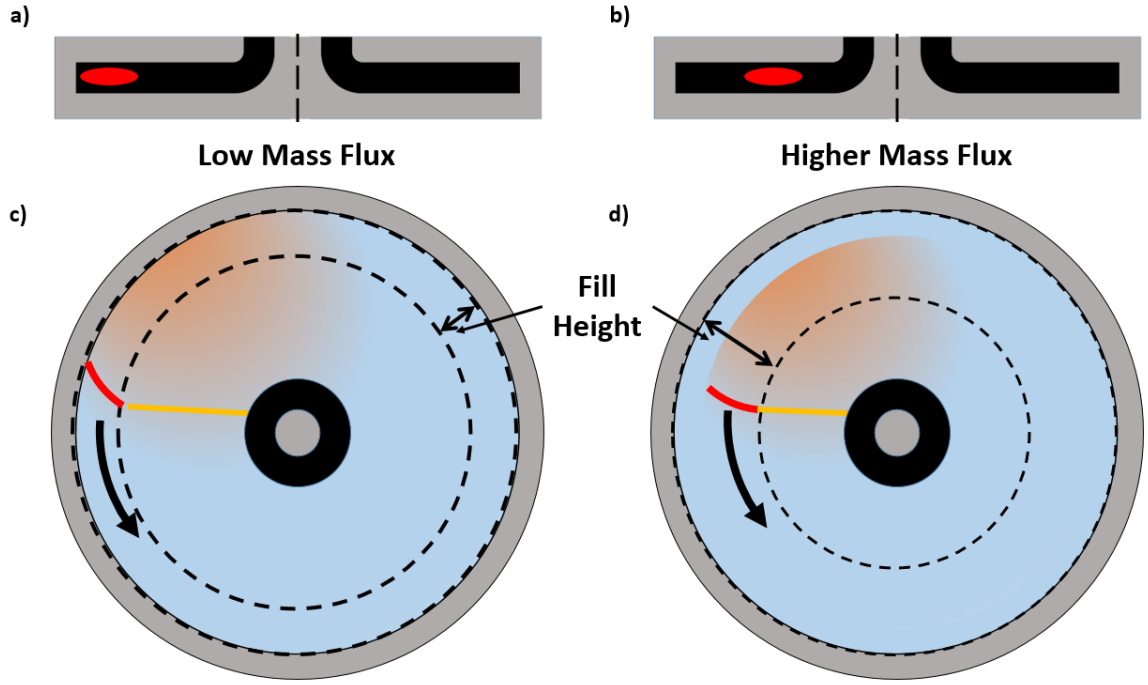

Figure 83. Detonation Wave Location Variation with Mass Flux. (a) side view low mass flux, (b) side view high mass flux, (c) top view low mass flux, & (d) top view high mass flux.

These two theories, combined with the possible change in location as the wave transitioned to a higher wave mode, Figure 84, may explain the wavespeed increases with mass flux at the single wave mode, then transitions to a two wave mode at a given mass flux, and then continues to increase in wavespeed at the two wave mode. As the mass flux is increased to a certain point for a given configuration and equivalence ratio, the RRDE can physically support a higher wave mode. As the RRDE transitions to the higher wave mode, it would make sense that the fill height of the incoming reactants would then decrease, moving the detonation wave further to the outer radius of the channel. This would then appear as a decrease in the

frequency response per wave at a higher wave number. The possible shifting of the detonation wave location suggested that the RRDE may offer improved operability over conventional RDEs, in terms of combustion unsteadiness. This could be due to the additional unconstrained radial dimension which allows the detonation wave to equilibrate in its optimal location within the channel depending on the operating condition of the RRDE.

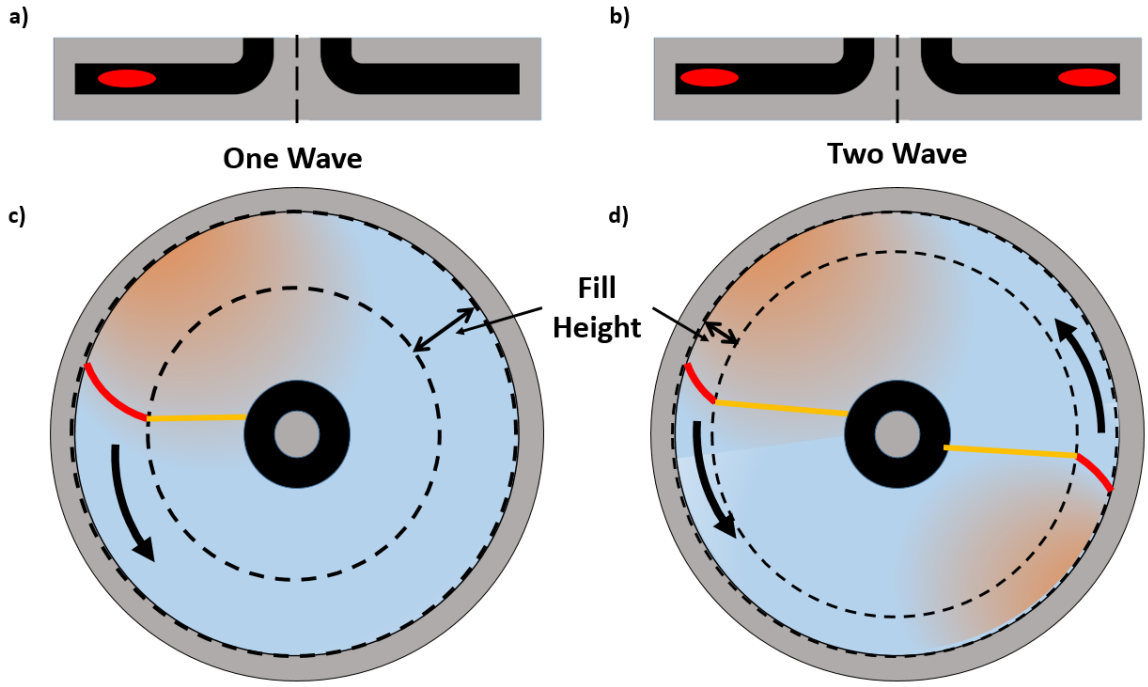

Figure 84. One Wave to Two Waves Transition Schematic (a) side view one wave, (b) side view two waves, (c) top view one wave, (d) top view two waves.

Figure 85 shows the pressure loss versus mass flux plot for all runs. This plot shows similar trends as the increase in mass flux produces an increase in pressure loss, but these trend lines do not have as high of correlations as the wavespeed plot in Figure 81. These trend lines are given by Equation 41 for the one wave mode, Equation 42 for the two wave mode, and Equation 43 for the three wave mode.

$$dp_{inj} = 1.69 * 10^{-3}\dot{m}'' + 0.217 \tag{41}$$

$$dp_{inj} = 1.02 * 10^{-3}\dot{m}'' + 0.222 \tag{42}$$

$$dp_{inj} = 6.7 * 10^{-4}\dot{m}'' + 0.183 \tag{43}$$

For the trend lines that were created there is also evidence that transitioning from a single wave operating mode to a two or three wave operation mode lowered the pressure lost through the RRDE. This suggest it might be beneficial to operate in a higher wave mode if possible to minimize the pressure loss.

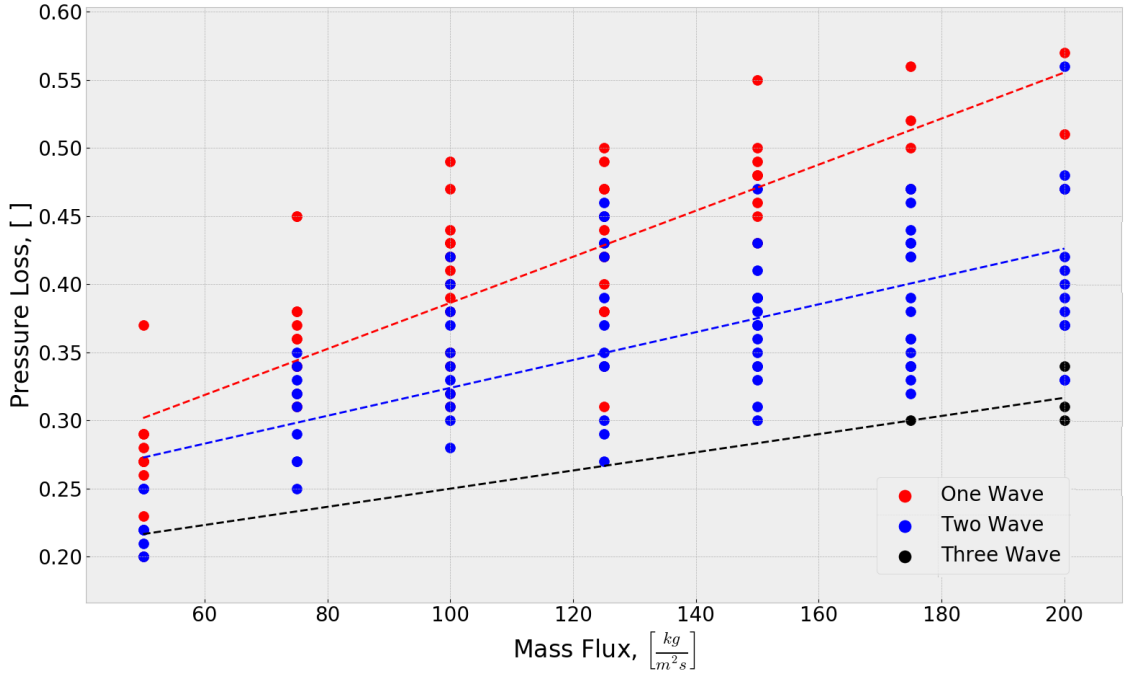

Figure 85. General Pressure Loss versus Mass Flux for all runs.

Finally, the effects of varying equivalence ratio was examined, with Figure 86 showing the wavespeed versus equivalence ratio plot. It should be reemphasized that these wavespeed are normalized by the CJ ideal wavespeed. This is most important when comparing the wavespeed to the equivalence ratio, because in 1-D detonation theory, the CJ wavespeed is largely a function of the equivalence ratio. This means it would be expected that the trend lines for these plots were perfectly flat; however, due

to the possilbe shifting of the detonation wave throughout the channel, these trend lines do have a slope and the one wave trend line actually shows a loss in wavespeed as the equivalence ratio is increased. It should be noted the poor correlation of the one and two wave trend lines. This suggests that other factors, such as mass flux, may be better predictors of performance, but the equivalence ratio does have some effect. The trend lines were given by Equation 44 for the on wave operating mode, Equation 45 for the two wave operating mode, and Equation 46 for the three wave operating mode.

$$\frac{V_a}{V_{CJ}} = -1.13\phi + 0.829 \tag{44}$$

$$\frac{V_a}{V_{CJ}} = 1.23\phi + 0.511 \tag{45}$$

$$\frac{V_a}{V_{CJ}} = 5.7 * 10^{-2}\phi + 0.469 \tag{46}$$

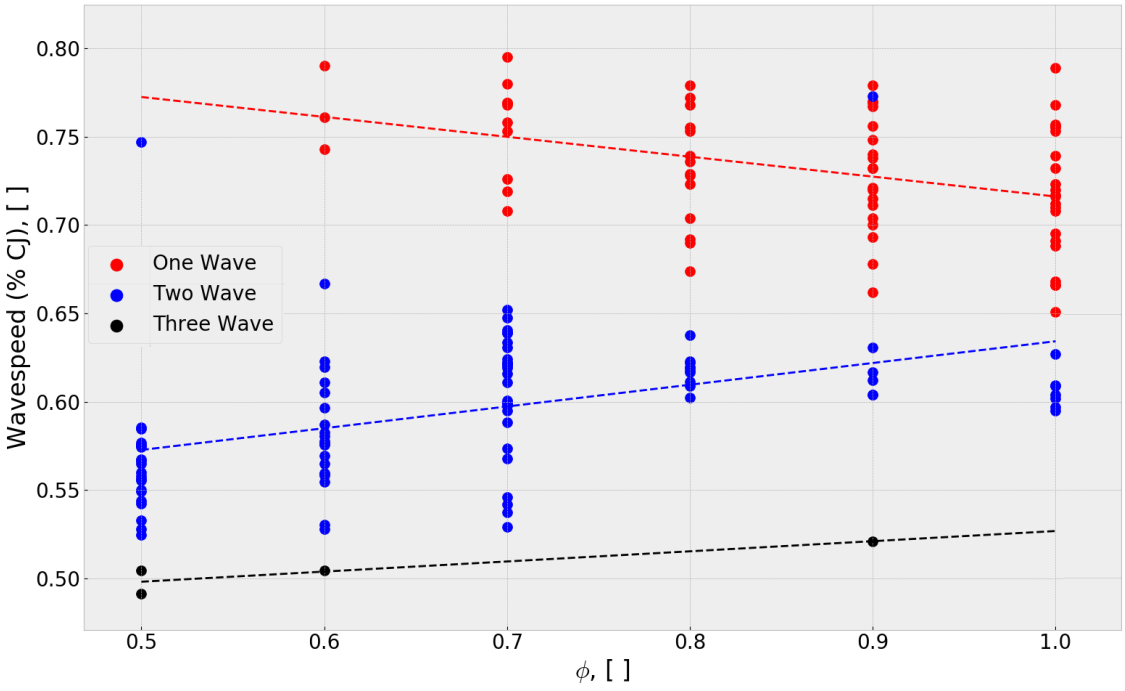

Figure 86. General Wavespeed (% CJ) versus Equivalence Ratio for all runs.

Further examination of the equivalence ratio variation at a particular operating condition was shown in Figure 87 at a nozzle area ratio of 0.6 and a mass flux of 100 $\frac{\text{kg}}{\text{m}^2\text{s}}$. This plot shows two wave operation at the lower equivalence ratios of 0.5-0.7, followed by a transition to one wave operation at an equivalence ratio of 0.8. This trend was shown for nearly all mass fluxes and nozzles; though, the exact equivalence ratio of this transition was not the same for each case.

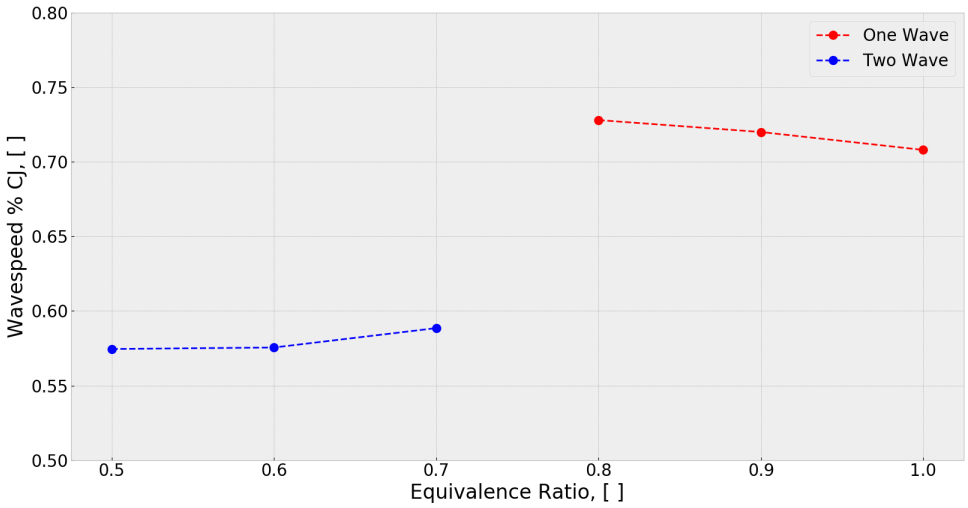

Figure 87. Wavespeed (% CJ) versus Equivalence Ratio: Channel Height$= 4.5mm$**,** $AR_t = 0.2$**,** $AR_n = 0.6$**,** $\dot{m}'' = 100\frac{\mathbf{kg}}{\mathbf{m^2 s}}$**.**

The explanation of why the RRDE transitioned from one to two wave may be due to the combination of rate at which the fresh reactant are supplied to the channel and the actual wavespeed of the detonation as the equivalence ratio is changed, which was illustrated by Figure 88. According to detonation theory the wavespeed should increase with an increase in equivalence ratio and at a set mass flux the fill rate would be expect to be roughly similar for all cases, with a slight increase in the fill rate due to the increase in injection pressure with the increase in fuel flow. When the RRDE is operating at a low equivalence ratio the expected wavespeed is lower and

the current fill rate supports two wave operation at the outer radius of the RRDE. When the equivalence ratio is increased, the expected wavespeed also increased and the fill rate increases slightly more. There becomes a point at which the physical dimensions of the channel can no longer support two waves for the given fill rate. This shifts the RRDE to a single wave operation. This single detonation wave may then shifts further towards the center of the RRDE to match the fill height, which could be the reason for the increased wavespeed when the RRDE transitioned from two to one wave. An effect opposite of that of increasing mass flux.

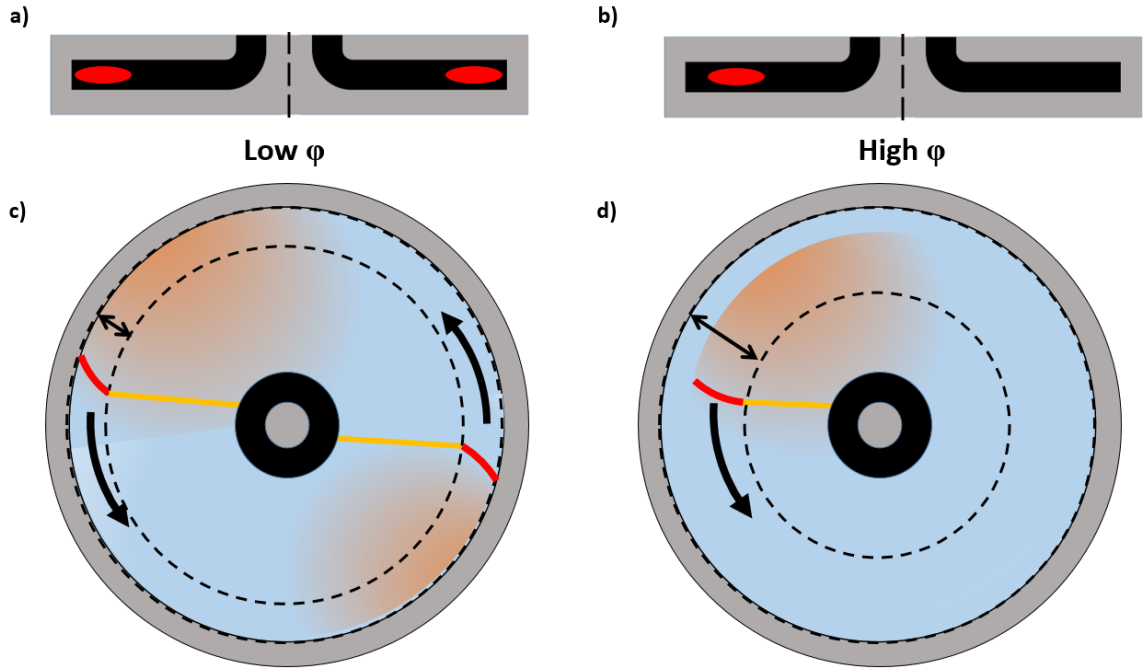

Figure 88. Equivalence Ratio Effect of Detonation Location. (a) side view one wave, (b) side view two waves, (c) top view one wave, (d) top view two waves.

Figure 89 shows the pressure losses versus equivalence ratio for all of the runs. This plot suggest that overall a higher equivalence ratio leads to more pressure loss, which could be an artifact of the higher injection pressure of the fuel and increased mixing between the fuel and air leading to higher losses during injection. However, when attempting to compare the pressure versus equivalence ratio at distinct wave modes,

the trend lines shown poor correlation once again for the one and two wave modes. An interesting fact is that the three wave mode actually shows perfect correlation, but with only three data points, this trend would likely not hold with additional three wave data points.

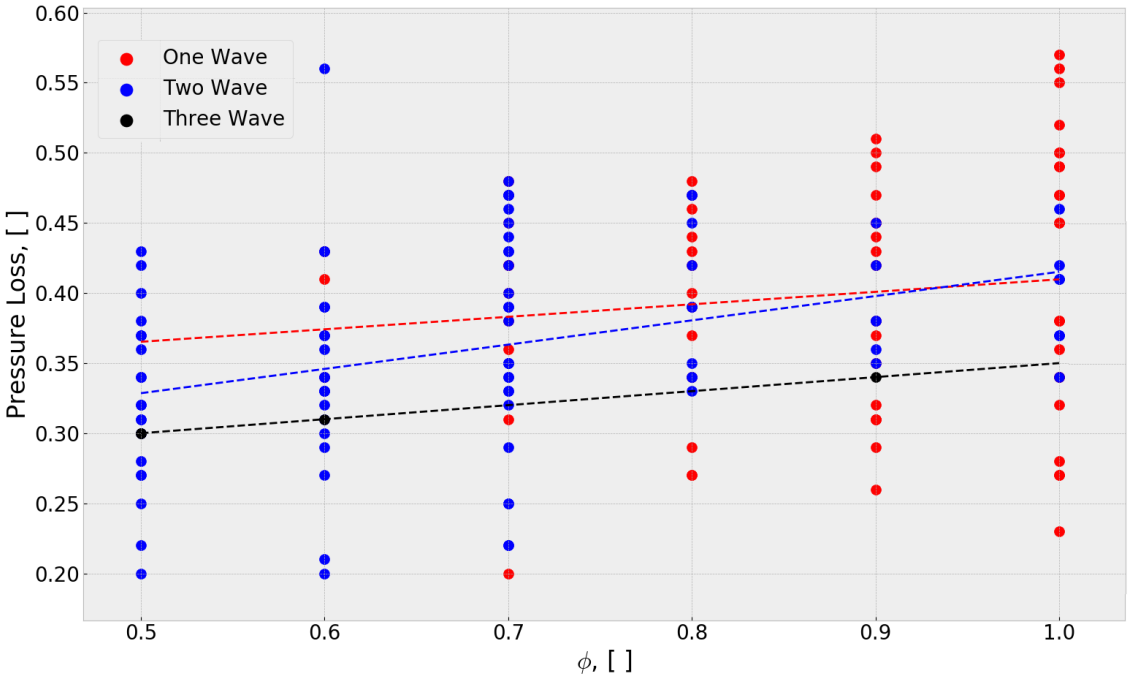

Figure 89. General Pressure Loss versus Equivalence Ratio for all runs.

These global results compare the performance of the RRDE to the independent variables investigated in this research. These results were conducted using all of the test runs and did not account for changes in the other independent variables. From this initial data examination it is clear that the mass flux had a signification effect on both the wavespeed and pressure loss, and showed high correlation which may allow for accurate prediction of future operation of the RRDE at other configurations. The equivalence ratio also showed some correlation to the wavespeed and pressure loss; however, these correlation were poor. From these results it could be theorized that the location of the detonation wave may shift around within the channel, which could

offer operability benefits for the RRDE as the detonation wave is not constrianed in the radial direct. Like mentioned previously, the measurements taken for this research were not able to confirm this theory, and further experimentation would be needed. Finally, further examination of the independent variables, accounting for the other independent variables, will be discussed in the subsequent sections.

4.3 Channel Height Variation

This section will discuss the performance of the stand alone Radial RDE and compare the effects of the geometric changes made between the configurations. For all of data presented in this section and the rest of this chapter, only points with confirmed detonation operation are shown. Finally, these results will occasionally be grouped based on the number of waves within the channel. Depending on the application of the RRDE, multiwave operation can be either beneficial or harmful to performance. Multiple waves within the channel usually corresponded to a higher channel pressure for a given mass flux, which could be beneficial; however, multiple waves also results in higher heat transfer to the device. For these reasons, when discussing the RRDE as a stand alone device the wave number will not be presented as a performance metric in the same sense as the wavespeed and pressure loss. Where increased wavespeed and decreased pressure loss constituted improved performance, an increase in wave number did not mean better performance, unless it corresponded to improvements in the wavespeed or pressure loss.

Before discussing the detailed results of the geometric variations, a more general analysis will be conducted. The following investigations show the wavespeed, as a percentage of Chapman-Jouguet velocity, and the pressure versus each of the channel configurations. Figure 90 shows wavespeed versus the height of the channel for the entire data set taken for the stand alone RRDE. No clear trends were visible other

than the fact that two lower channel heights of 3.5 and 4.0 mm were predominately two wave operation mode. However, it can also be seen that there were significantly more test points for the 4.5 mm channel, and the lack of test points at the two smaller channel heights could account for the lack of other wave modes. More detail on the effects of the channel height on the wavespeed will be discussed in Section 4.3.

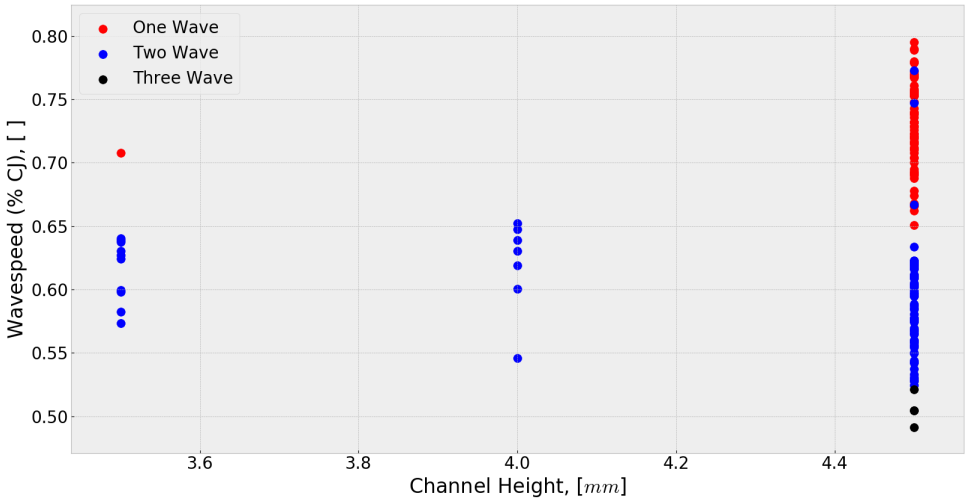

Figure 90. General Wavespeed (% CJ) versus Channel Height for all runs.

Figure 91 shows a plot of the pressure loss versus the channel height. Much like the previous figure, there were few trends correlated the pressure loss with the channel height. From a global standpoint there seemed to be little difference in the pressure loss performance with other channel heights, and this could be a product of matching the mass flux for each channel.

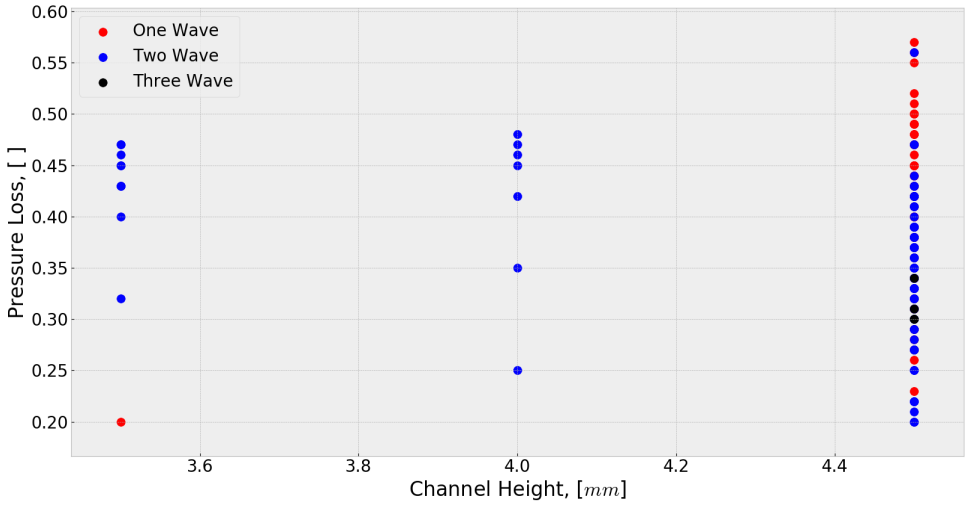

Figure 91. Pressure Loss versus Channel Height for all runs.

Changing the height of the channel has been shown to change the performance of RDEs, even at a constant mass flux. This was shown by Fotia et al. when comparing three channel widths of 7.62, 16.25, and 22.86 mm.[23] Their results shows there was an optimal channel height to operate at to maximize the specific impulse of the RDE they were operating. Though specific impulse was not a performance measurement used in this study, since the RRDE was not designed to be a thrust producing device, an optimal channel height could also be shown for the RRDE operation. The channel heights tested in this experiment were 3.5, 4.0, and 4.5 mm, and the operational differences between the three will be discussed in more detail in this section. The common flow condition of a throat area ratio of 0.2, a nozzle area ratio of 1.0, and an equivalence ratio of 0.7 was used for the following comparisons of the different channels.

Figure 92 plots the wavespeed versus the channel heights at multiple mass fluxes. It should be noted that at the larger channel height of 4.5 mm, equivalence ratio of 0.7, and at a mass flux of 50 $\frac{\text{kg}}{\text{m}^2\text{s}}$the RRDE was not able to detonate. This fact

alone suggest restricting the channel height improves the detonability of the RRDE. It should be noted that at an equivalence ratio of 0.7 and the 75 and 200 $\frac{\text{kg}}{\text{m}^2\text{s}}$mass fluxes, the 4.5 mm channel does not show points on this plot; however, this was due to a lack of data points taken at these conditions, not due to an inability to detonate. When examining the majority of the points, it is clear that the two lower channel heights were operating predominately in a two wave mode, versus the one wave mode of the 4.5 mm channel. The one exception to this trend is at a mass flux of 50 $\frac{\text{kg}}{\text{m}^2\text{s}}$. At this mass flux, the 3.5 mm channel was operating in a one wave mode, while the 4.0 mm channel was able to transition to a two wave mode, and the 4.5 mm channel was not able to detonate at this condition. This suggest there could be an optimal channel height that will increase the detonability of the RRDE, without restricting it to a lower wave number operation mode.

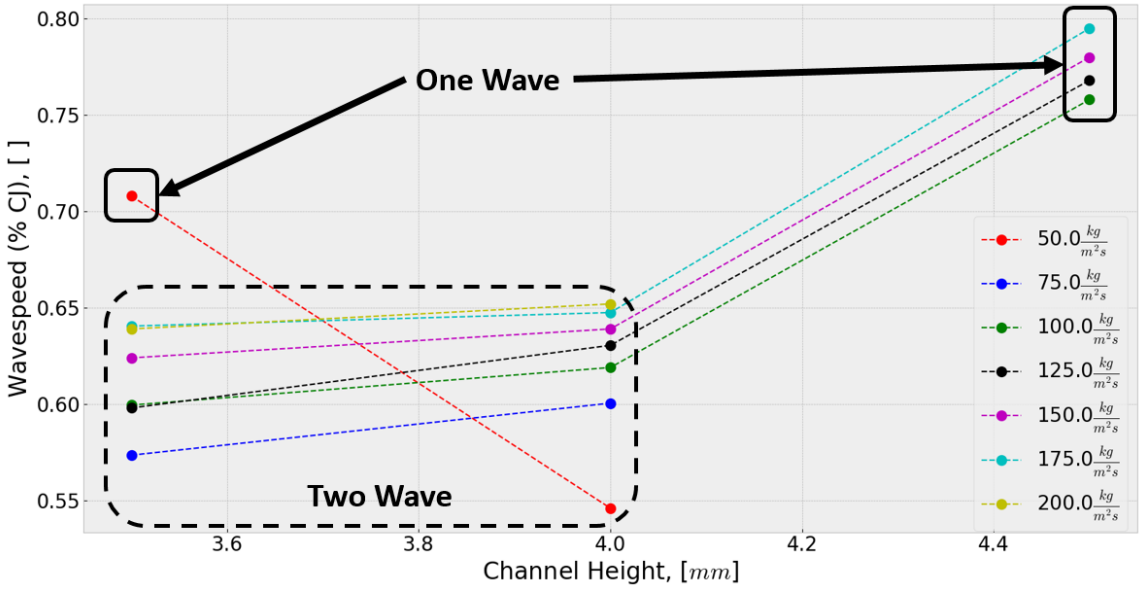

Figure 92. Wavespeed versus Channel Height: $AR_t = 0.2$, $AR_n = 1.0$, $\phi = 0.7$.

Figure 93 show the pressure loss performance versus the channel height for the same test points as Figure 92. There was a trend of decreased pressure loss as the channel height was decreased. The reason for the general trend of improved pressure

loss performance with a decrease in channel height could stem from the interaction between the reduced losses from the lower pressure air injection and the increased wavespeed performance increasing the exit pressure.

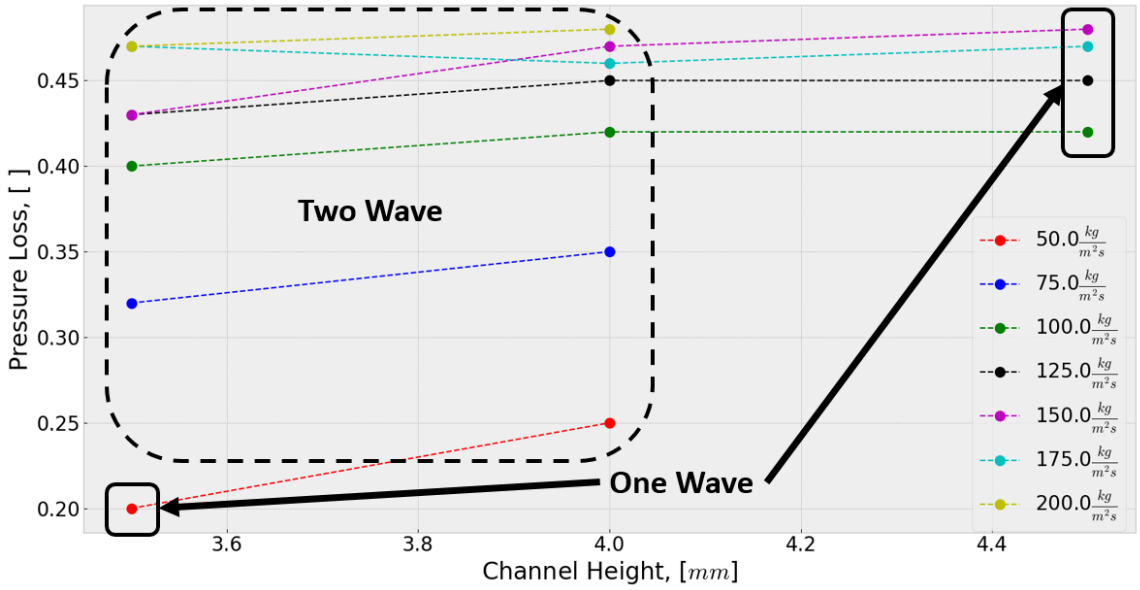

Figure 93. Pressure Loss versus Channel Height: $AR_t = 0.2$, $AR_n = 1.0$, $\phi = 0.7$.

4.4 Nozzle Area Variation

The nozzle area ratio is known to control the back pressure on the channel of RDEs; therefore, investigating this parameter was vital for understanding the operation of the Radial RDE. As the nozzle area ratio was decreased, an increased back pressure was applied to the RRDE. In conventional RDEs this increased pressure leads to an increase in both performance and detonability.[22] As outlined in Sections 3.4.2 and 3.2.2, the nozzle area ratios used were 0.5, 0.6, 0.8, and 1.0. The following results were conducted using the 4.5 mm channel at a constant throat area ratio of 0.2. The wavespeed versus nozzle area ratio is shown in Figure 94, and shows the 0.6 nozzle area ratio appears to have the lowest wavespeeds compared to the other nozzles. This could be an artifact of the detonation wave itself being pushed further towards the

outer radius of the RRDE with this configuration. It is also clear that the 0.6 nozzle ratio was the only configuration able to produce three wave operation, which could be attributed to this nozzle applying enough back pressure on the channel to allow the wave to transition without applying too much back pressure and restricting the injection of fresh reactants. It also appears that the 0.6 nozzle area ratio had a lower wavespeed for all runs compared to the other nozzle area ratios. Once again, this is likely due to an optimal back pressuring of the channel which shifted the detonation wave further back into the channel without restricting injection.

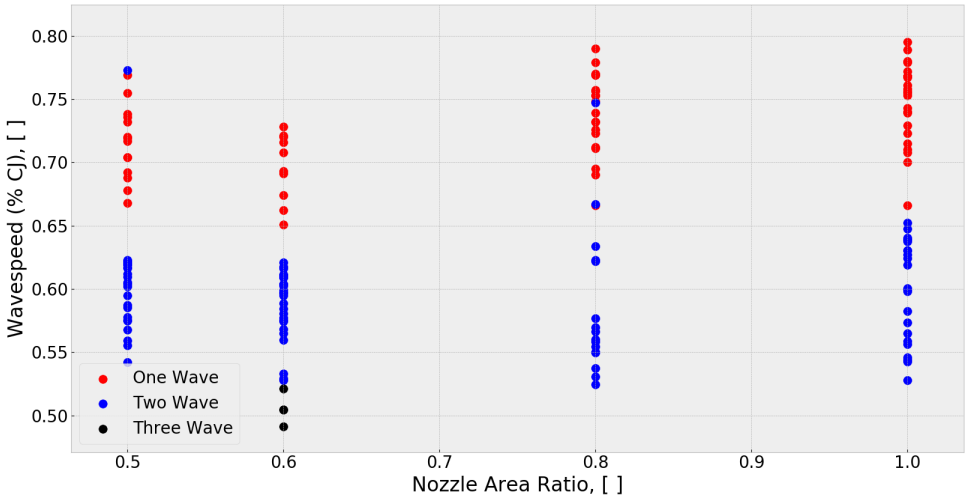

Figure 94. General Wavespeed (% CJ) versus Nozzle Area Ratio for all runs.

The pressure loss versus nozzle area ratios is plotted in Figure 95. This plot suggest the two more restrictive nozzle area ratios of 0.5 and 0.6 had a lower pressure loss overall, but had a similar minimum pressure loss as the two higher nozzle area ratios of 0.8 and 1.0. From this plot it seems that the two more restrictive nozzles out performed the less restrictive cases from a pressure loss perspective.

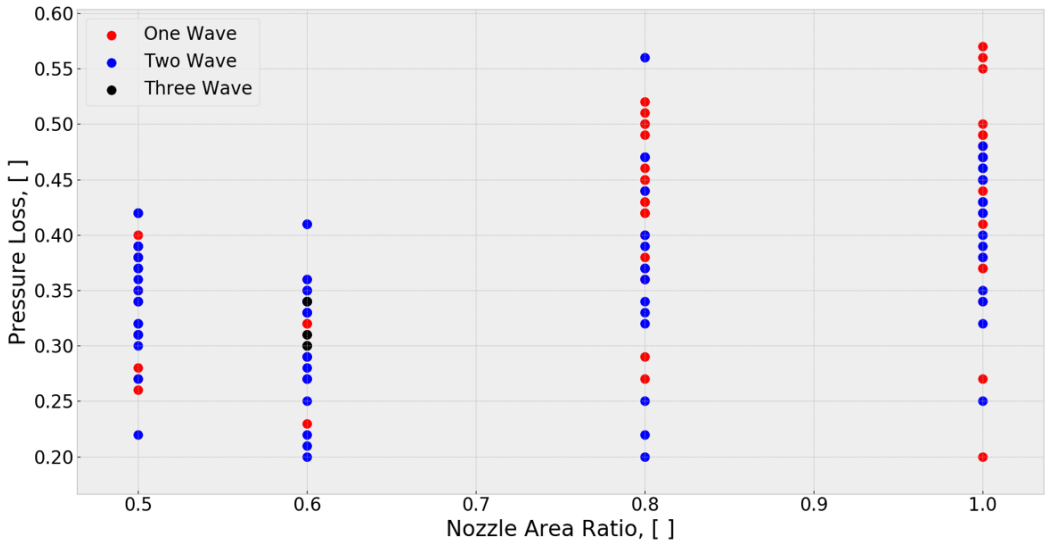

Figure 95. General Pressure Loss versus Nozzle Area Ratio for all runs.

Figure 96 shows a plot of the wavespeed versus the nozzle area ratio for all mass fluxes at an equivalence ratio of 0.7. This equivalence ratio was chosen as it roughly represented the center of the equivalence ratio data. The plot was sectioned off into one wave and two wave operation, and a clear division in the two wave modes was shown. This was expected from the analysis done in Section 4.5. The first noticeable trend in the plot was the fact that at the nozzle area ratio of 0.6, the RRDE exclusively operated with two wave, which was not the case at the other nozzle area ratios. It can also be shown that at a given mass flux and operating mode, changing the nozzle area ratio had little effect of the wave speed of the RRDE; although, a slight drop off in wave speed is noticed when moving from the 0.5 nozzle area ratio to the 0.6 nozzle area ratio. This indicated the most restrictive 0.5 area ratio nozzle may not allow the detonation wave to move as freely within the channel as the more open nozzle area ratios.

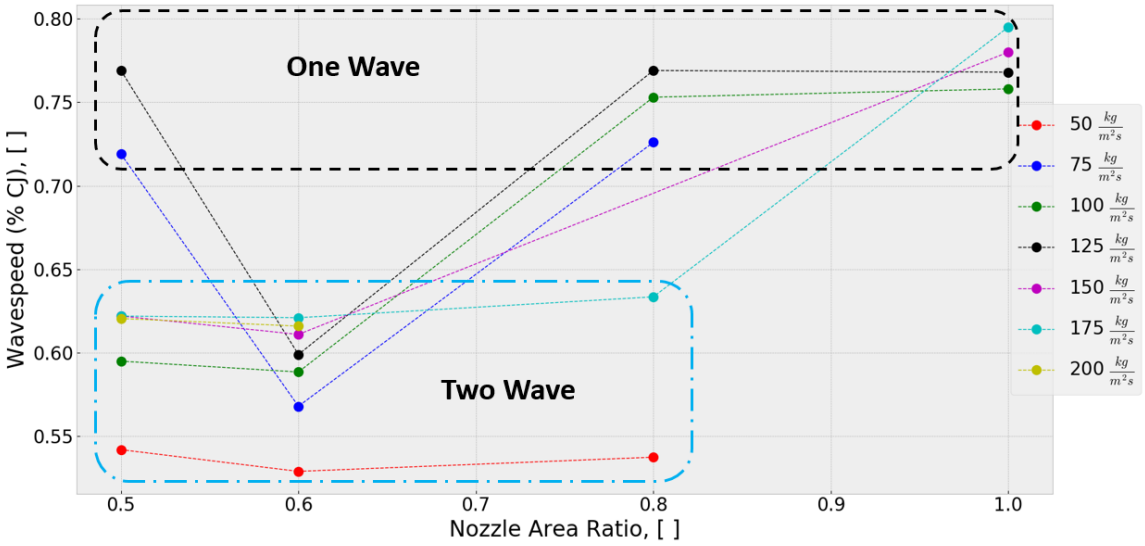

Figure 96. Wavespeed vs Nozzle Area Ratio: Channel Height = 4.5 mm**,** $AR_t = 0.2$**,** $\phi = 0.7$**.**

Figure 97 shows the pressure loss performance of the RRDE as the nozzle area ratio was varied. An attempt to neatly divide this plot into one and two wave operating modes proved fruitless, as there was no clear correlation between the pressure loss and operating mode. The most notable trend shown in this plot was at all mass fluxes except 50 $\frac{\text{kg}}{\text{m}^2\text{s}}$, the 0.6 nozzle area showed the lowest pressure loss, indicating it provided the ideal amount of back pressure to the channel to improve the detonability of the RRDE, but also allow for improved injection of the fresh reactants.

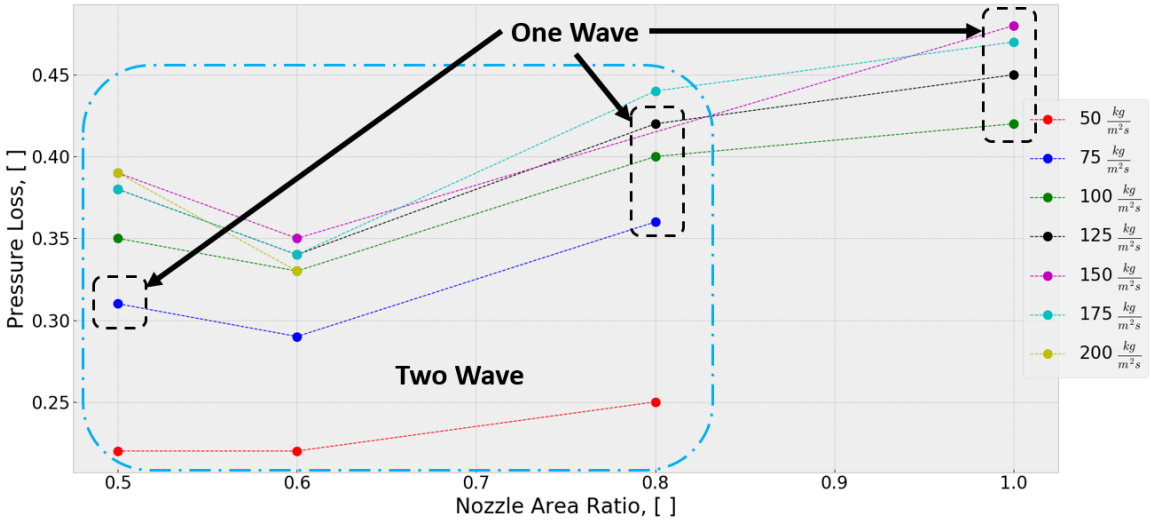

Figure 97. Pressure Loss vs Nozzle Area Ratio: Channel Height = 4.5 mm**,** $AR_t = 0.2$**,** $\phi = 0.7$**.**

4.5 Performance Maps

To best understand the optimal operating conditions for the Radial RDE an operating map was created based on the mass flux and equivalence ratio. In Figure 98 wavespeed is the performance metric of interest at a nozzle area ratio of 0.5. This plot shows the operating map for this configuration and is plotted by the mass flux and equivalence ratio, with the darker colors representing higher wavespeed as a percentage of the Chapman-Jouguet velocity. This chart is also broken up into one and two wave operating modes to show the clear drop off in wavespeed as the RRDE transitions from one to two waves. However, there is a single point were this trend does not hold, which is at a mass flux of 175 $\frac{\text{kg}}{\text{m}^2\text{s}}$and an equivalence ratio of 0.9. This point followed similar trends as other two wave cases, but its wavespeed would suggest it may be in a three wave operating mode. Further analysis of the trends shown later in this section removed this point because it was an outlier in the data. This plot accomplished the goal of showing operatibility of the RRDE at various flow

condition and also provide insight into where the wave mode transition; however, a more detailed analysis was also conducted.

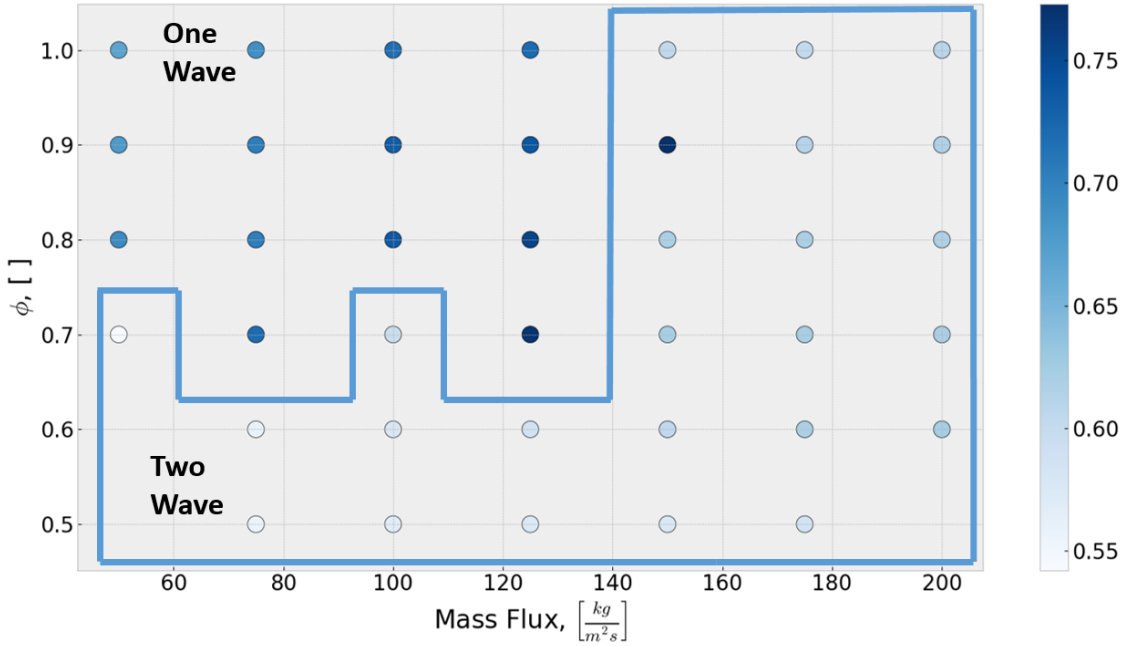

Figure 98. Wavespeed Performance: Channel Height = 4.5 mm, $AR_t = 0.2$, $AR_n = 0.5$. Color coded with wavespeed as metric.

Figure 99 shows the wavespeed as a percentage of CJ velocity versus mass flux for the nozzle area ratio of 0.5. This plot is taking three cuts from Figure 98 at equivalence ratios of 0.5, 0.7, and 1.0 (red, blue, and green respectively). These equivalence ratios were selected to provide a proper representation of the all equivalence ratios, without causing excessive clutter. This was done to examine the variations with mass flux in more detail for this configuration. This plot also differentiates between the one wave (circles) and two wave (diamonds) operating modes. Analysis of this data included adding linear trend lines to the distinct wave mode/equivalence ratio combinations, and also a trendline of all of the points within a single wave mode (black dotted). For this setup, there is the same clear division in the wavespeeds of the operating modes, but within each operating mode there is reasonable linear fit to

predict the performance of the RRDE based on wavespeed and wave number. These fits become even more accurate when the equivalence ratio is taken into account. For this configuration, these linear fits provide a relatively accurate estimate of the expected wavespeed, provided the expected wave number is known. The one wave operating mode the trendline is given by Equation 47 and the two wave operating mode is given by Equation 48:

$$\frac{V_a}{V_{CJ}} = 9.4 * 10^{-4}\dot{m}'' + 0.627 \tag{47}$$

$$\frac{V_a}{V_{CJ}} = 4.5 * 10^{-4}\dot{m}'' + 0.527 \tag{48}$$

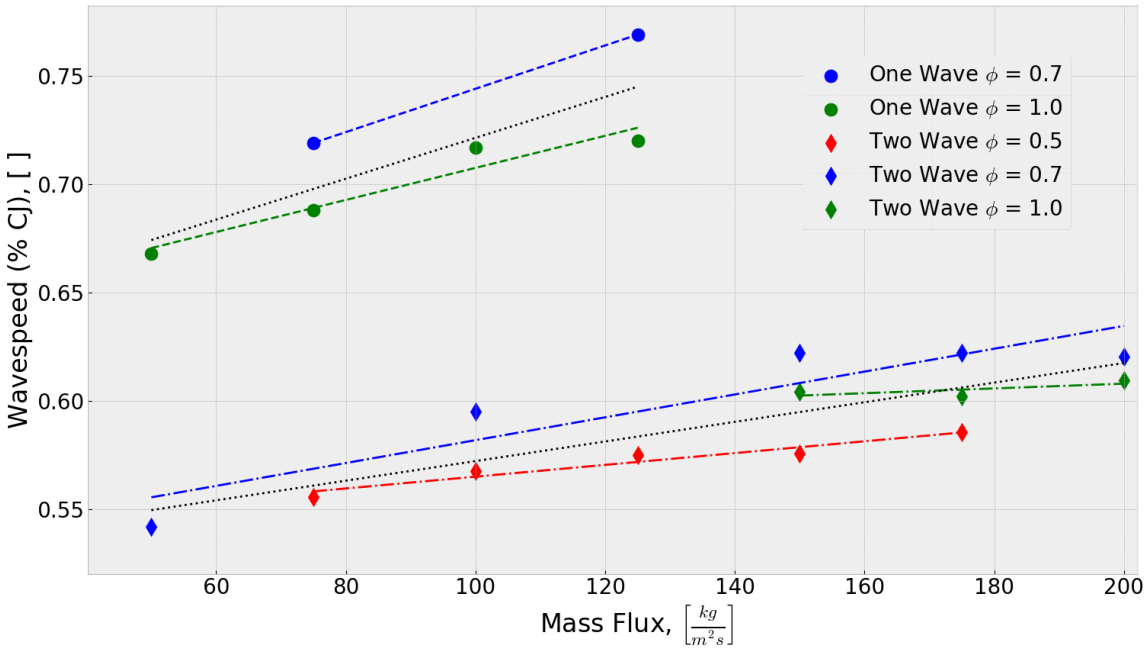

Figure 99. Wavespeed versus Mass Flux: Channel Height = $4.5\ mm$**,** $AR_t = 0.2$**,** $AR_n = 0.5$ **at** ϕ **= 0.5, 0.7, & 1.0.**

A similar analysis was conducted for the 0.5 nozzle configuration but now comparing the wavespeed and equivalence ratio at mass fluxes of 50, 125, and 200 $\frac{\text{kg}}{\text{m}^2\text{s}}$(red, blue, and green, respectively), shown in Figure 99. These mass fluxes were selected to provide an accurate representation of all of the mass fluxes, but not clutter the plots.

Like the previous plot, the plot is broken into the one wave (circles) and two wave (diamonds) operating modes. Once again, linear trendlines are fit to the one wave and two wave modes, both for the full data set and mass flux dependent. These results show that for the one wave operating mode there is a distinct decrease in wavespeed and the equivalence ratio increased. Section 4.2 discussed the fact that expectations would suggest these trendlines remain relatively flat; however, the movement in the detonation wave was left un-characterized, which may account for this unexpected result. When accounting for the mass flux at which the RRDE is operating, the trendlines offer great accuracy in the prediction of the wavespeed; though, grouping the one wave cases together shows a less accurate trendline. The two wave cases at a mass flux of 200 $\frac{\text{kg}}{\text{m}^2\text{s}}$show similar agreement with the one wave cases, where the wavespeed decreased with an increase in the equivalence ratio. However; the addition of the two wave cases at the lower mass fluxes shifted the trendline, giving it a positive slope. This highlighted that the mass flux was the dominate parameter.

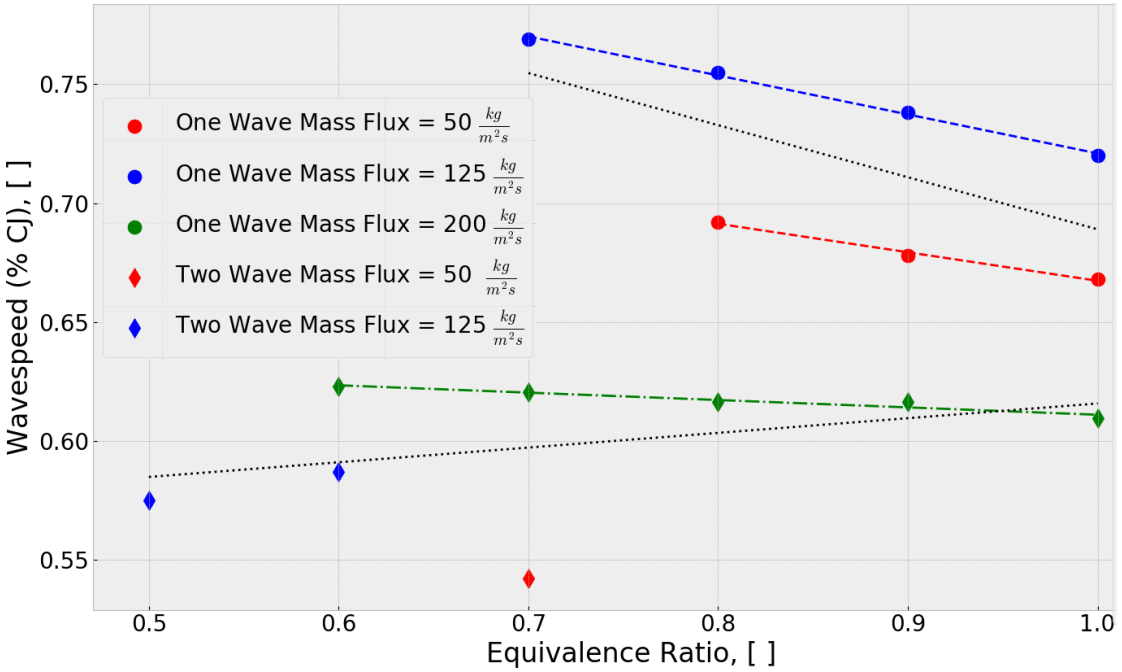

Figure 100. Wavespeed versus Equivalence Ratio: Channel Height = $4.5\ mm$**,** $AR_t = 0.2$**,** $AR_n = 0.5$ **at** $\dot{m}''$ **= 50, 125 & 200** $\frac{kg}{m^2 s}$**.**

Figure 101 shows the full pressure drop performance, defined in Section 3.4.1, of the RRDE at the 0.5 nozzle area ratio with the darker color being lower pressure loss. While this plot is still divided by operating mode, there is less correlation with the pressure loss versus the operating mode. There is a trend pointing to lower mass flux and lower equivalence ratio leading to a lower pressure loss. This aligns with the fact that there is less mass moving through the air injector at higher mass fluxes and fewer losses due to mixing of air and fuel at the lower equivalence ratios. A more detailed examination of this data was also conducted to find subtleties missed with this consolidated plot.

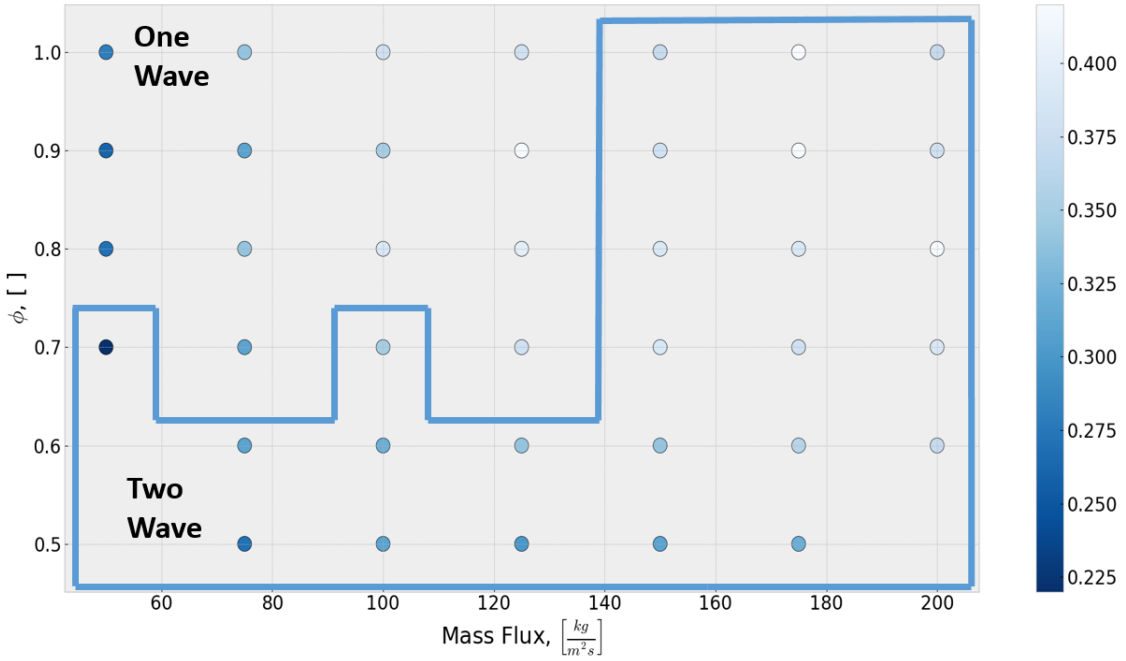

Figure 101. Pressure Loss Performance: Channel Height = $4.5\ mm$**,** $AR_t = 0.2$**,** $AR_n = 0.5$**. Color coded with pressure loss as metric.**

Much like the wavespeed plots, Figure 102 took the same equivalence ratio slices of 0.5, 0.7 and 1.0 (red, blue, and green, respectively) and compared the pressure loss versus mass flux. This operating wave mode was also noted in the same way for the one (circle) and two (diamond) wave modes. However; the wave mode of operation had little effect on the pressure loss of the RRDE at this configuration. For this reason, the trendlines were not fit to the individual wave mode/equivalence ratio combinations, but rather fit to the points at a constant equivalence ratio. These trendlines show good agreement between the pressure loss through the RRDE and the mass flux at which its operating. These trendlines offer relatively accurate prediction of the pressure loss and are given by Equation 49 for an equivalence ratio of 0.5, Equation 50 for an equivalence ratio of 0.7, and Equation 51 for an equivalence ratio of 1.0.

$$dp_{inj} = 4.0 * 10^{-4} \dot{m}'' + 0.252 \tag{49}$$

$$dp_{inj} = 9.9 * 10^{-4}\dot{m}'' + 0.223 \tag{50}$$

$$dp_{inj} = 6.0 * 10^{-4}\dot{m}'' + 0.288 \tag{51}$$

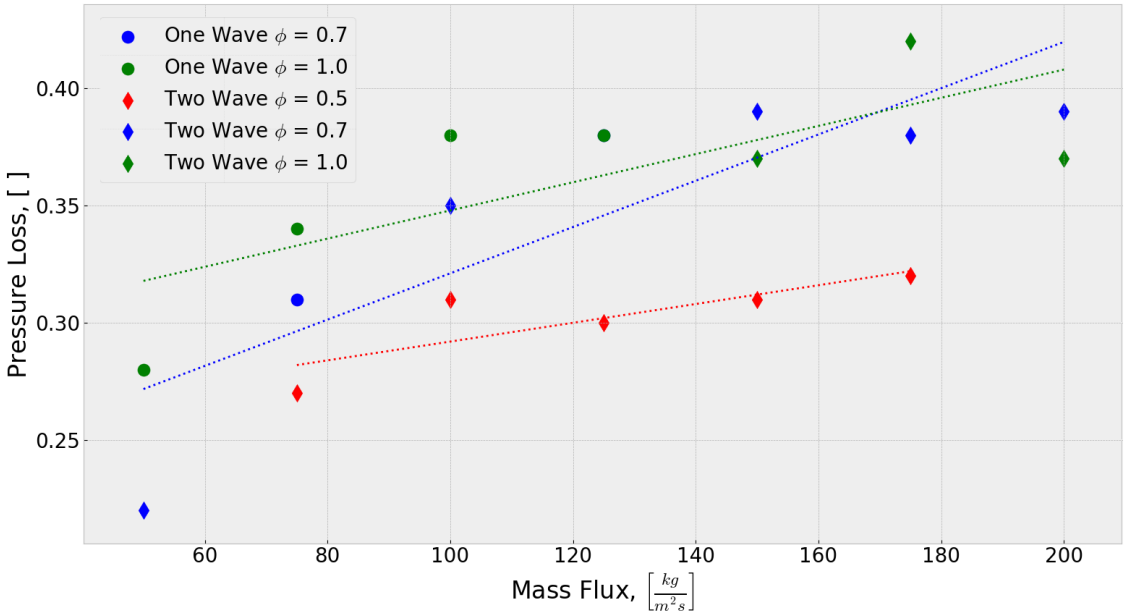

Figure 102. Pressure Loss versus Mass Flux: Channel Height = $4.5\ mm$**,** $AR_t = 0.2$**,** $AR_n = 0.5$ **at** ϕ **= 0.5, 0.7, & 1.0.**

Figure 102 shows the pressure loss performance versus equivalence ratio for the 0.5 nozzle area ratio configuration and taken at the same mass fluxes of 50, 125, and 200 $\frac{\text{kg}}{\text{m}^2\text{s}}$. This plot grouped the data by mass flux for the creation of the trendlines shown. At the mass fluxes of 50 and 125 $\frac{\text{kg}}{\text{m}^2\text{s}}$, the trendlines showed good agreement with the data and could be used predict the pressure loss, but the trendline for the higher mass flux of 200 $\frac{\text{kg}}{\text{m}^2\text{s}}$showed almost no correlation. The curve fits for the 50 and 125 $\frac{\text{kg}}{\text{m}^2\text{s}}$mass fluxes were given by Equation 52 and Equation 53, respectively.

$$dp_{inj} = 0.170\phi + 0.113 \tag{52}$$

$$dp_{inj} = 0.189\phi + 0.299 \tag{53}$$

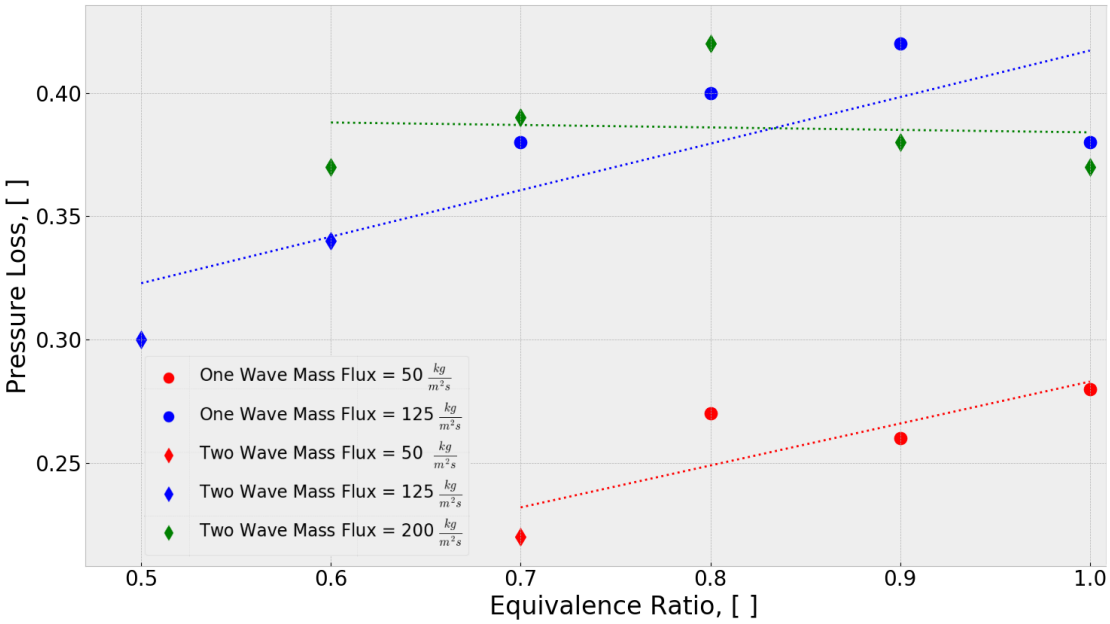

Figure 103. Pressure Loss versus Equivalence Ratio: Channel Height = $4.5\ mm$**,** $AR_t = 0.2$**,** $AR_n = 0.5$ **at** $\dot{m}''$ **= 50, 125 & 200** $\frac{kg}{m^2 s}$**.**

Figure 104 takes the performance data from Figure 98 and Figure 101 and compares the pressure loss performance versus the wavespeed that the RRDE was operating for the 0.5 nozzle area ratio. This plot was broken up into two distinct section, the red corresponds to one wave operation and the blue corresponds to two wave operation. There are simple linear curve fits on both sets of data that show the relation between the wavespeed and pressure loss. From these two data sets it was shown that an increase in wavespeed correlated to an increase in pressure loss; however, this was not indicative that the increase in wavespeed was causing the increase in pressure, but the two were correlated. This relationship meant there was a tradeoff between the pressure loss performance and the wavespeed, which could lead to an optimal operation regime. It should be noted that the trendlines were drawn out arbitrary lengths and the discontinuity between the two did not necessarily correspond to the point of transition. To estimate the expected pressure loss for a given the wavespeed

as a percent of CJ velocity, Equation 54 should be used for one wave operation and Equation 55 should be used for two wave operation. The slopes of the two trendlines were relavitvely close, suggesting that an increase in wavespeed would correlate to an increase in the pressure loss of similar magnitude regardless of the wave number.

$$dp_{inj} = 1.42\frac{V_a}{V_{CJ}} - 0.673 \tag{54}$$

$$dp_{inj} = 1.80\frac{V_a}{V_{CJ}} - 0.725 \tag{55}$$

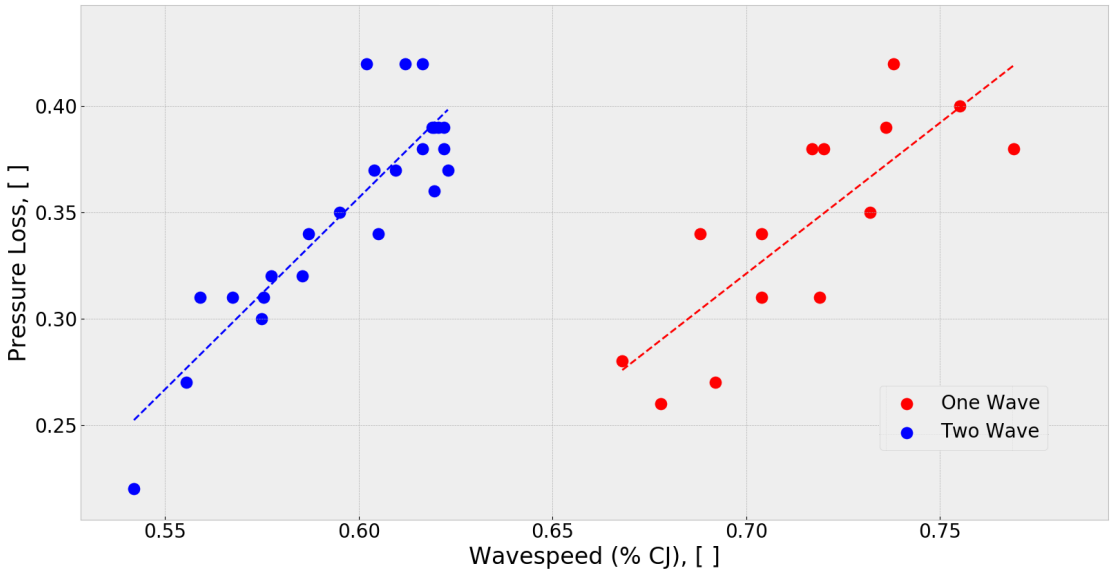

Figure 104. Pressure Loss vs Wavespeed: Channel Height = 4.5 mm**,** $AR_t = 0.2$**,** $AR_n =$ 0.5**.**

Figure 105 shows the performance plot at a nozzle ratio of 0.6. This plot shows a third operating mode where the RRDE transitioned from two to three waves. In general the transition regimes occur as the equivalence ratio is decreased and as the mass flux is increased, except for a singular point at a mass flux of 200 $\frac{\text{kg}}{\text{m}^2\text{s}}$and an equivalence ratio of 0.9. The reason why this lone point exist was not determined, but it does not appear to be an outlier in the data, and aligns well with the other three wave operation points.

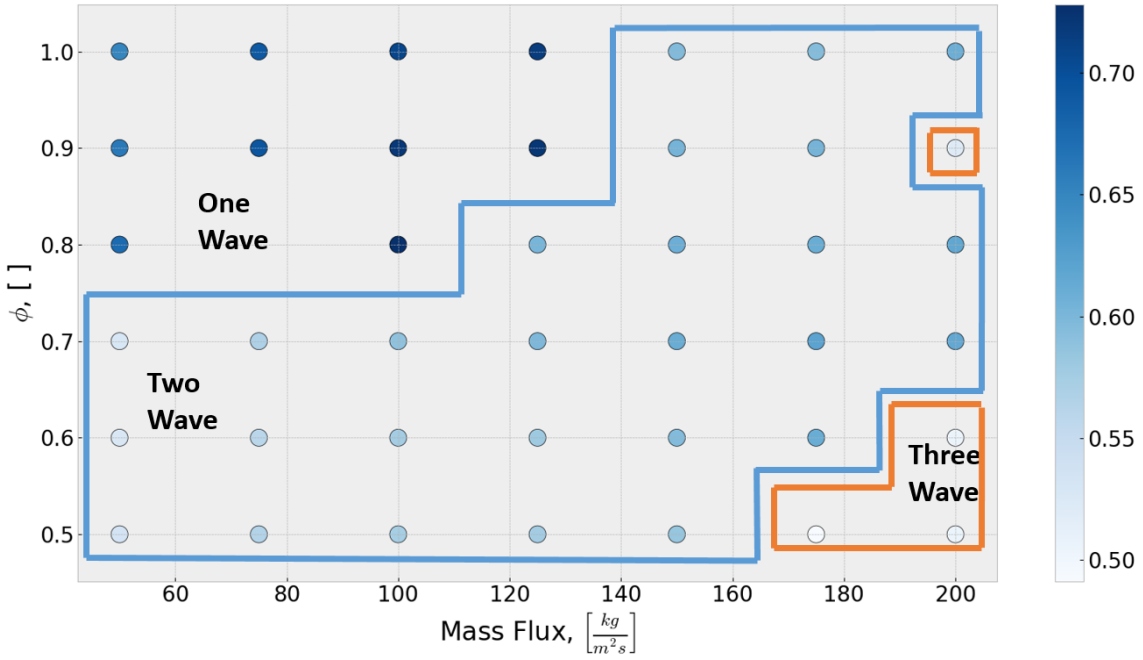

Figure 105. Wavespeed Performance: Channel Height = $4.5\ mm$**,** $AR_t = 0.2$**,** $AR_n = 0.6$**. Color coded with wavespeed as metric.**

Figure 106 shows the pressure loss performance map at the nozzle area ratio of 0.6. This plot also shows an increase in pressure loss as the mass flux and equivalence ratio increase. This plot also highlights the independence of operating mode and pressure loss, and it shows the same trend where the lower pressure losses occur at low mass flux and low equivalence ratio.

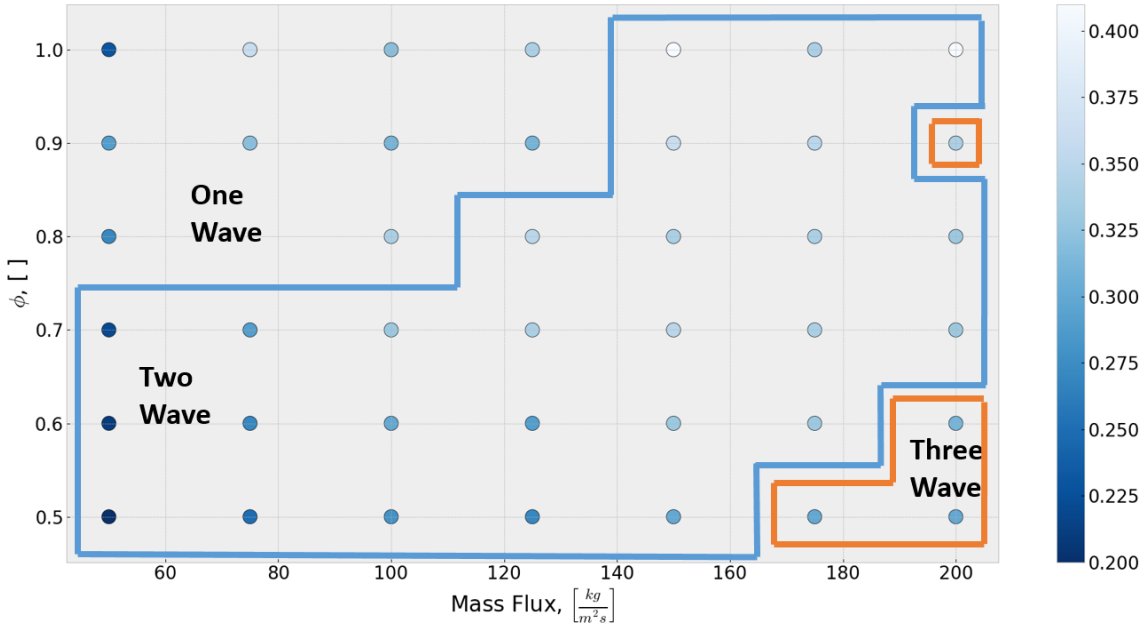

Figure 106. Pressure Loss Performance: Channel Height = $4.5\ mm$**,** $AR_t = 0.2$**,** $AR_n = 0.6$**. Color coded with pressure loss as metric.**

Figure 107 shows a plot of the pressure loss versus wavespeed for the 0.6 nozzle area ratio. This plot shows the same trends as Figure 104 but now included another set of data operating in a three wave mode (black). Like Figure 104, as the modes transition the slope of the trendline decreases. However, when transitioning from two to three waves, the pressure loss does not drop back down to the pressure loss at the lower end of the two wave mode like it did when going from one to two wave. This means transitioning from two wave to three wave may not be as beneficial. To estimate the pressure loss at a given wavespeed, as a percentage of CJ velocity, Equation 56 should be used for a one wave mode, Equation 57 for a two wave mode, and Equation 58 for a three wave mode.

$$dp_{inj} = 1.02\frac{V_a}{V_{CJ}} - 0.398 \tag{56}$$

$$dp_{inj} = 1.72\frac{V_a}{V_{CJ}} - 0.697 \tag{57}$$

$$dp_{inj} = 1.39\frac{V_a}{V_{CJ}} - 0.391 \tag{58}$$

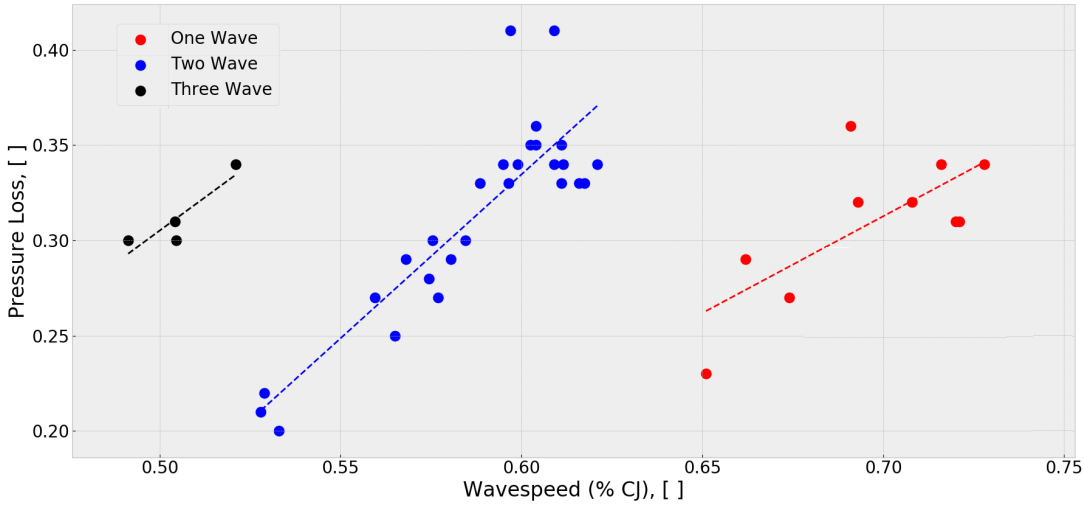

Figure 107. Pressure Loss vs Wavespeed: Channel Height = 4.5 mm**,** $AR_t = 0.2$**,** $AR_n =$ 0.6**.**

Figure 108 shows the wavespeed performance at a nozzle area ratio of 0.8. This plot shows the divide between one wave and two wave occurs at an equivalence ratio between 0.6 and 0.8 for all mass fluxes. It should be noted that the point at an equivalence ratio of 0.6 and a mass flux of 150 $\frac{\text{kg}}{\text{m}^2\text{s}}$was determined to be a single wave operation; however, these tests were only conducted at on test per point. This could mean this point may operate at two waves should this test point be conducted once more. If this were the case then an equivalence ratio of 0.6 would serve as a strict dividing line between the one and two wave operation in the mass flux regime of 75-150 $\frac{\text{kg}}{\text{m}^2\text{s}}$.

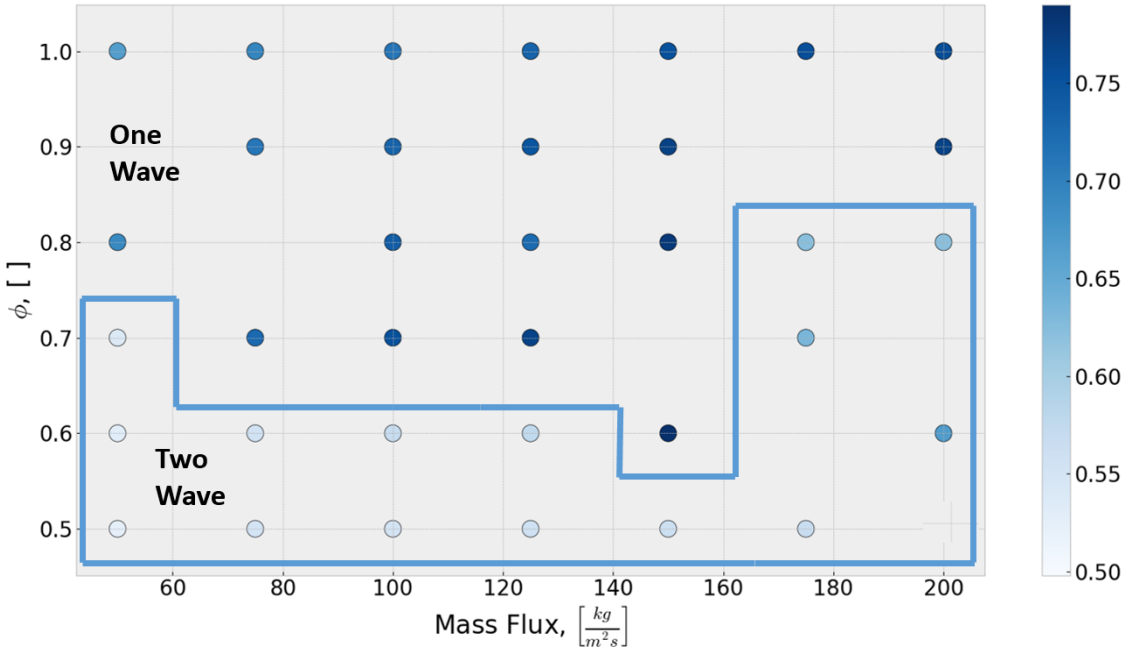

Figure 108. Wavespeed Performance: Channel Height = $4.5\ mm$**,** $AR_t = 0.2$**,** $AR_n = 0.8$**. Color coded with wavespeed as metric.**

Figure 109 shows the pressure drop performance at a nozzle area ratio of 0.8. This plot shows the same trends as the other pressure loss plots where the pressure losses are reduced at the lower mass fluxes and equivalence ratios; however at a mass flux of 50 $\frac{\text{kg}}{\text{m}^2\text{s}}$, the pressure loss is less than that of the one wave modes at the same mass flux. This indicates a clear benefit in operating in a two wave mode for this configuration.

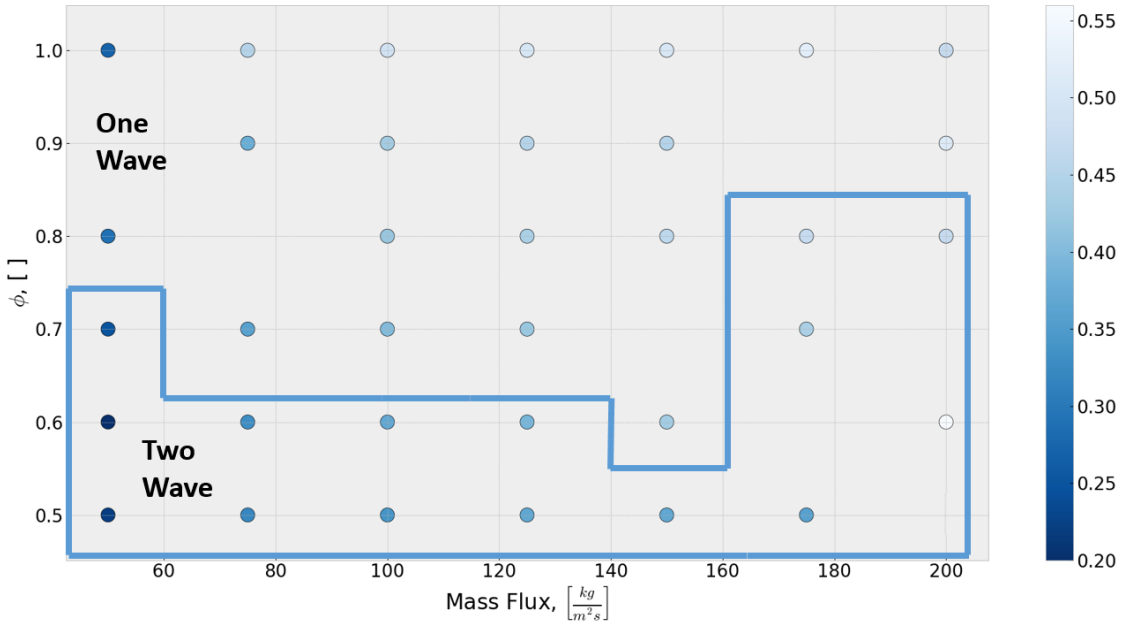

Figure 109. Pressure Loss Performance: Channel Height = $4.5\ mm$**,** $AR_t = 0.2$**,** $AR_n = 0.8$**. Color coded with pressure loss as metric.**

Figure 110 shows the pressure loss versus wavespeed plot with the 0.8 area ratio nozzle. This plot shows the correlation between pressure loss and wavespeed was high for the two wave cases, but the correlation at one wave case was not as accurate due to the large spread in the data at a single wave mode. These trendlines are given by Equation 59 for the one wave operating mode, and Equation 60 for the two wave operating mode. It should be noted that the that slope of the two wave trendline is almost double that of the one wave line. This indicated an increase in the wavespeed when operating in a two wave mode would show a significantly larger increase in pressure than if a similar increase in wavespeed was noticed at a one wave mode.

$$dp_{inj} = 1.25\frac{V_a}{V_{CJ}} - 0.887 \tag{59}$$

$$dp_{inj} = 2.18\frac{V_a}{V_{CJ}} - 0.887 \tag{60}$$

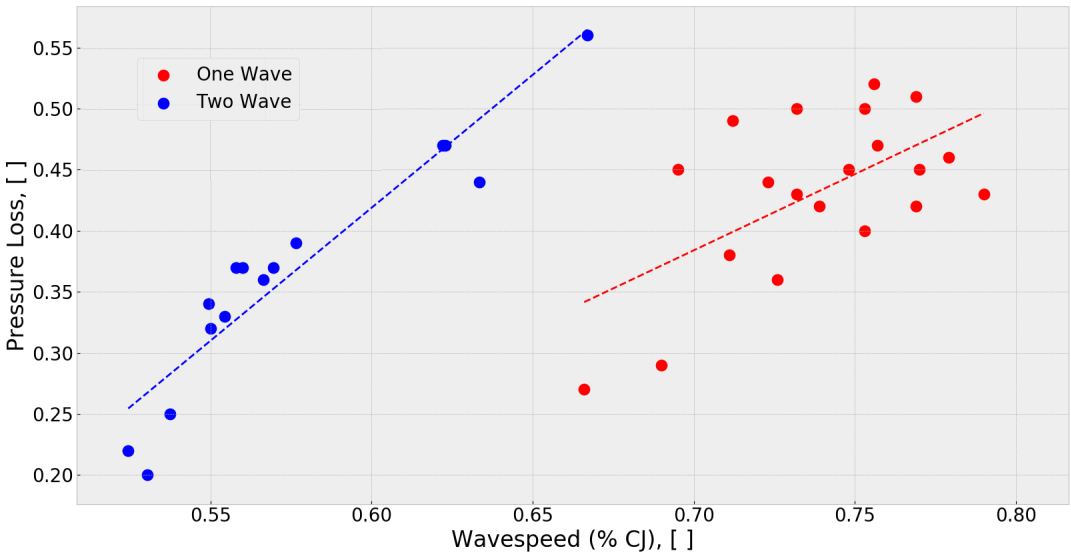

Figure 110. Pressure Loss vs Wavespeed: Channel Height = $4.5\ mm$**,** $AR_t = 0.2$**,** $AR_n = 0.8$**.**

Finally, Figure 111 shows the wavespeed performance map at the wide open nozzle area. This plot shows the small regime of two wave operating mode towards the middle of the plot. It should be noted that there was a lack of data points taken at the mass flux of 200 $\frac{\text{kg}}{\text{m}^2\text{s}}$, which was due to not running the RRDE at these cases, not because it failed to detonate. Overall, it was increasingly difficult for the configuration to transition from one wave to two wave, which was due to the lack of back pressure provided by the 1.0 nozzle area ratio. Also, at the lowest mass flux of 50 $\frac{\text{kg}}{\text{m}^2\text{s}}$, the RRDE did not detonate below an equivalence ratio of 0.9. This set the first operability limit seen during testing of the RRDE, since the RRDE was able to detonate successfully throughout the range of mass fluxes and equivalence ratios tested for all other configurations.

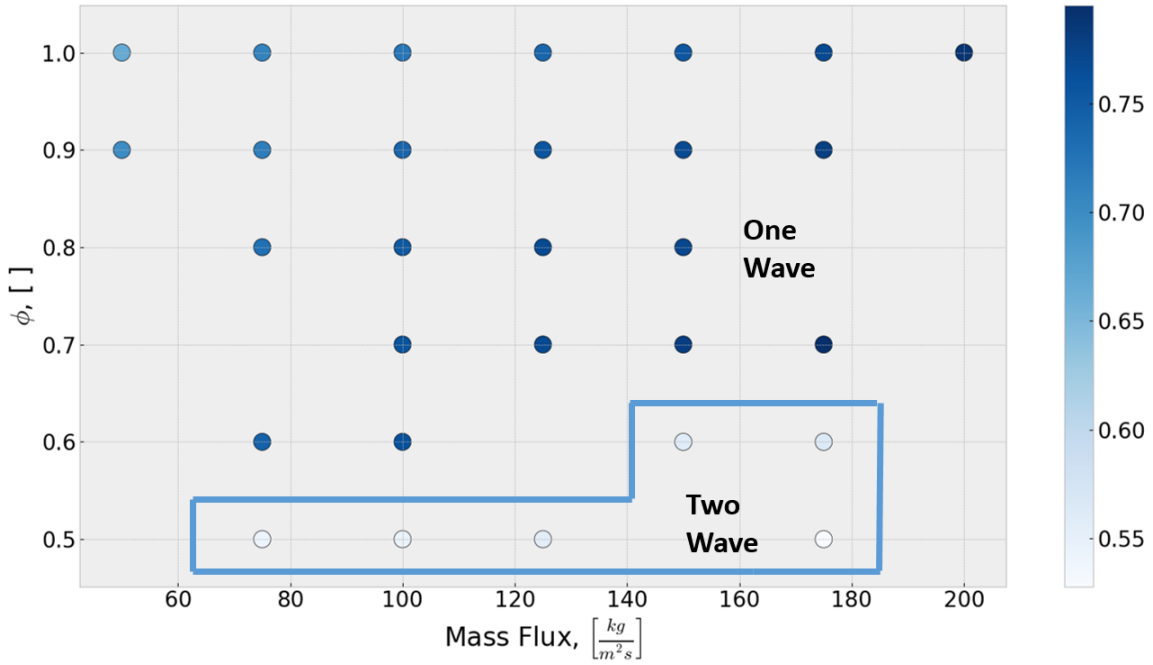

Figure 111. Wavespeed Performance: Channel Height = $4.5\ mm$**,** $AR_t = 0.2$**,** $AR_n = 1.0$**. Color coded with wavespeed as metric.**

Figure 112 shows the pressure drop performance with the wide open nozzle. This plot shows the similar trend in pressure loss versus mass flux and equivalence ratio; however at the mass flux of 50 $\frac{\text{kg}}{\text{m}^2\text{s}}$the RRDE was not able to detonate at equivalence ratios under 0.9. This represents the lower boundary of the operating window for the RRDE at this test configuration. Like the other nozzle configurations the pressure losses did not seem to depend on the wave number at which the RRDE was operating.

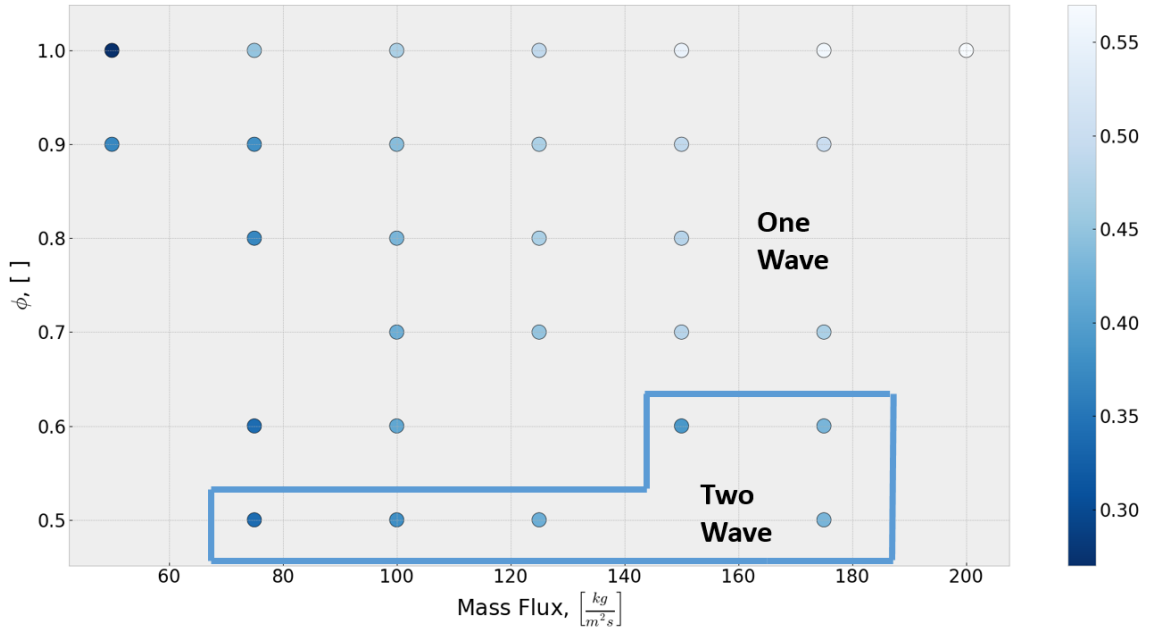

Figure 112. Pressure Loss Performance: Channel Height = $4.5\ mm$**,** $AR_t = 0.2$**,** $AR_n = 1.0$**. Color coded with pressure loss as metric.**

Figure 113 shows the final plot of pressure loss versus wavespeed. This plot shows a highly correlated trendline for the two wave mode, but a lower correlation at all for the one wave mode. The two wave mode plot removed an outlier (black) that caused the data to be correlated. Like the 0.8 nozzle area ratio, this plot shows the two wave mode had a slope nearly twice that of the one wave mode, suggesting the pressure losses will increase more dramatically with an increase in wavespeed at two waves. Finally, the trendlines for these plots are given by Equation 61 for the one wave mode and Equation 62 for the two wave mode.

$$dp_{inj} = 1.64\frac{V_a}{V_{CJ}} - 0.780 \tag{61}$$

$$dp_{inj} = 3.17\frac{V_a}{V_{CJ}} - 1.36 \tag{62}$$

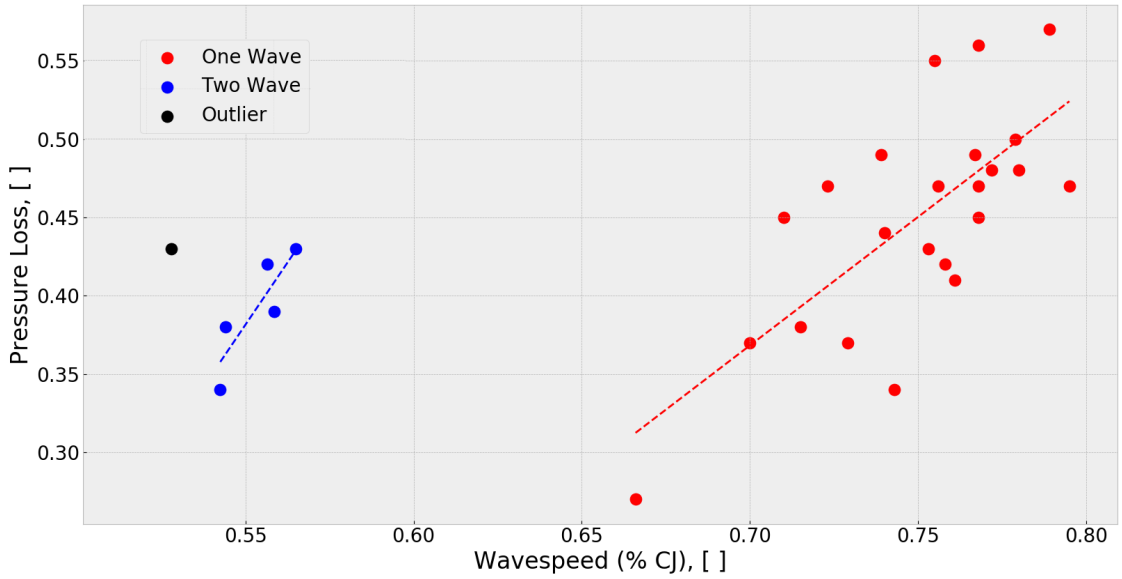

Figure 113. Pressure Loss vs Wavespeed: Channel Height = 4.5 mm**,** $AR_t = 0.2$**,** $AR_n =$ 1.0**.**

This section examined the operating map of the RRDE at a channel height of 4.5 mm, at a throat area ratio of 0.2, and at the nozzle area ratios of 0.5, 0.6, 0.8, and 1.0. The performance parameters of the wavespeed as a percentage of CJ velocity and the pressure loss through the RRDE were examined in detail, and the effect of varying the mass flux and equivalence ratio were examined. Restricting the nozzle area from 1.0 to 0.8 showed an increase in the operability map, especially at the mass flux of 50 $\frac{\text{kg}}{\text{m}^2\text{s}}$that struggled to detonate with the wide open nozzle. This shift in nozzle area also showed a growth in the region of two wave operation, which was also shown when varying the nozzle area ratio from 0.8 to 0.6, which also shown three wave operating mode cases; however, when changing the nozzle area ratio to 0.5, the three wave operating mode disappeared and the two wave operating region decreased as well. This indicated the 0.6 nozzle area ratio provided the ideal back pressure on the RRDE where the injection of fresh reactants was not restricted.

The examination of the effect of the equivalence ratio on the wavespeed was in-

conclusive. There were cases where increasing the equivalence ratio increased the wavespeed, as a percentage of CJ velocity, and other cases where the wavespeed was decreased. The cause of this could be attributed to the shifting the location of the detonation wave that would not allow for an accurate comparison.

Finally, the pressure loss performance was examined as a function of mass flux and equivalence ratio. This analysis found strong correlations between the pressure loss and both the equivalence ratio and the mass flux. An increase in either corresponded to an increase in pressure loss. This was likely due to an increase in the velocity of the flow as the mass flux is increased, which would decreased the static pressure measurement at the CTAPS, and an increase in losses through the injector if either the mass flux or the equivalence ratio was increased.

The pressure loss was also compared to the wavespeed and a correlation was found showing an increase in wavespeed corresponded to an increase in the pressure loss through the RRDE for a given operating mode. It is unlikely that the pressure loss was caused by the wavespeed increase, or vise versa, but rather an artifact of the flow conditions and geometry. However, this does indication there may be a trade-off between the pressure loss and the wavespeed of the device.

4.6 Radial RDE Turbine Integration

This section will discuss the completion of third objective of this project, the results of the integration of the turbocharger and Radial RDE, and the performance of this device as a compact APU. Successful operation of the RRDE as an APU represented the first of its kind ever researched. The main parameters of interest were the specific power output of the turbine and the thermal efficiency of the device. These results will be compared versus the nozzle guide vane turning angle, the mass flux, and the equivalence ratio at which the RRDE is operating, Section 4.6.1, Section 4.6.2,

and Section 4.6.3, respectively. Subsequently, a brief examination of the survivability of the turbine and RRDE will be conducted to show the feasibility in the continued use of this device, Section 4.6.4. Finally, the performance of the RRDE APU will be compared to that of other APUs in use today and insight into possible improvements will be discussed in Section 4.6.5. With the current configuration the RRDE APU already showed promise as a compact APU by providing instant power output while having a power density as much as $10x$ over conventional APUs with which it was compared.

4.6.1 Nozzle Guide Vane Variation.

The NGV ring ahead of the turbine conditions the flow before it enters the turbine. The exit flow angle of the vanes and the velocity of the exhaust gas will dictate the rotational speed of the turbine. This combined with the mass flow pushed through the turbine correlate well with the power output of the turbine, which was discussed in Section 3.2.1.1. This section will examine the effects of different flow turning angles on the power output of the RRDE.

Figure 114 shows the specific turbine power output versus the turning angle of the NGV ring. This plot shows that at the mass flux of 50 $\frac{\text{kg}}{\text{m}^2\text{s}}$as the NGV turning angles increases so does the specific power extracted from the turbine. However, at a mass flux of 75 and 100 $\frac{\text{kg}}{\text{m}^2\text{s}}$going from 32.0° to 39.0° showed a slight decrease in power. This trend was also seen at the equivalence ratio of 0.6 but at a higher specific power, which indicated that between these NGV flow angles there was a peak in specific power, and to increase the specific power, an increase in either the mass flux or equivalence ratio would be needed.

Figure 115 shows the thermal efficiency of the RRDE as the NGV turning angle is changed. This plot mirrors the results shown in Figure 114 due to the fact that the

equivalence ratio was held constant. Therefore, the thermal energy is similar and the thermal efficiency would be most effected by a change in turbine power output.

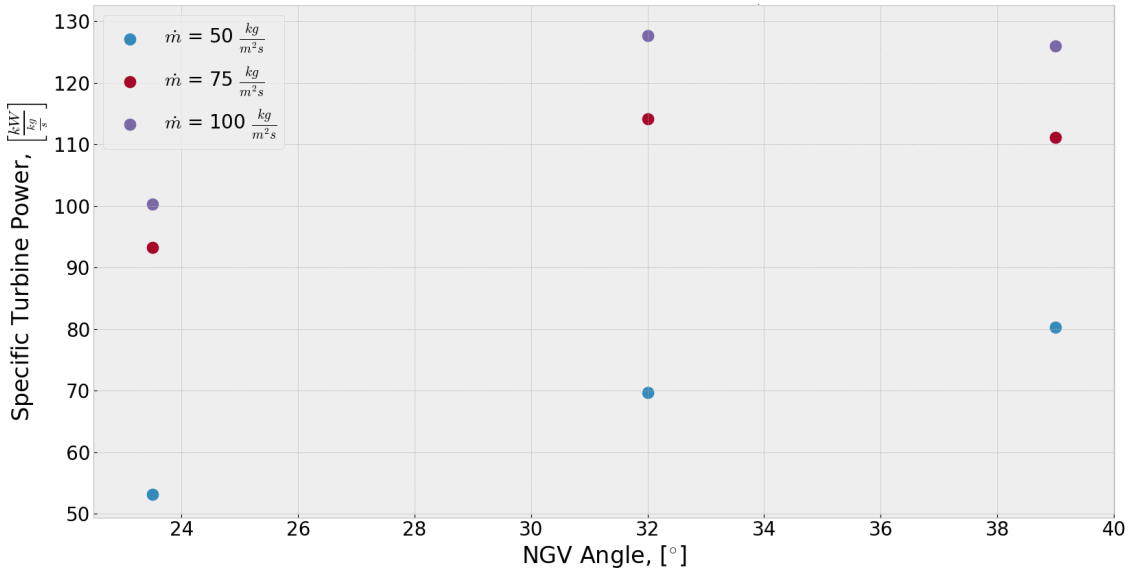

Figure 114. Turbine Power vs Flow Turning Angle: Turbine Channel, AR_t = 0.2, ϕ = 0.5.

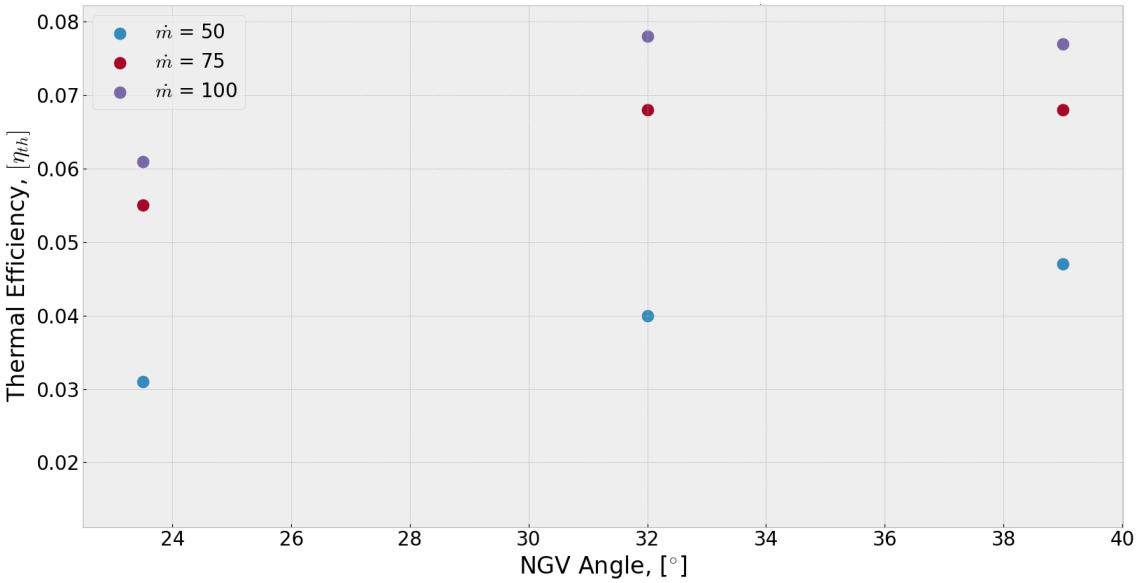

Figure 115. Thermal Efficiency vs Flow Turning Angle: Turbine Channel, AR_t = 0.2, ϕ = 0.5.

These results showed that the NGV rings tested may have found an optimal operating condition for the RRDE APU. At the conditions tested, the 32° NGV tuning angle produced a higher specific power relative to the other NGV turning angles. This result was also echoed in the thermal efficiency. Further research into NGV vane layouts could provide additional insight into the optimization of the RRDE APU. Finally, the operating RPM of the tests cases were compared to the designed

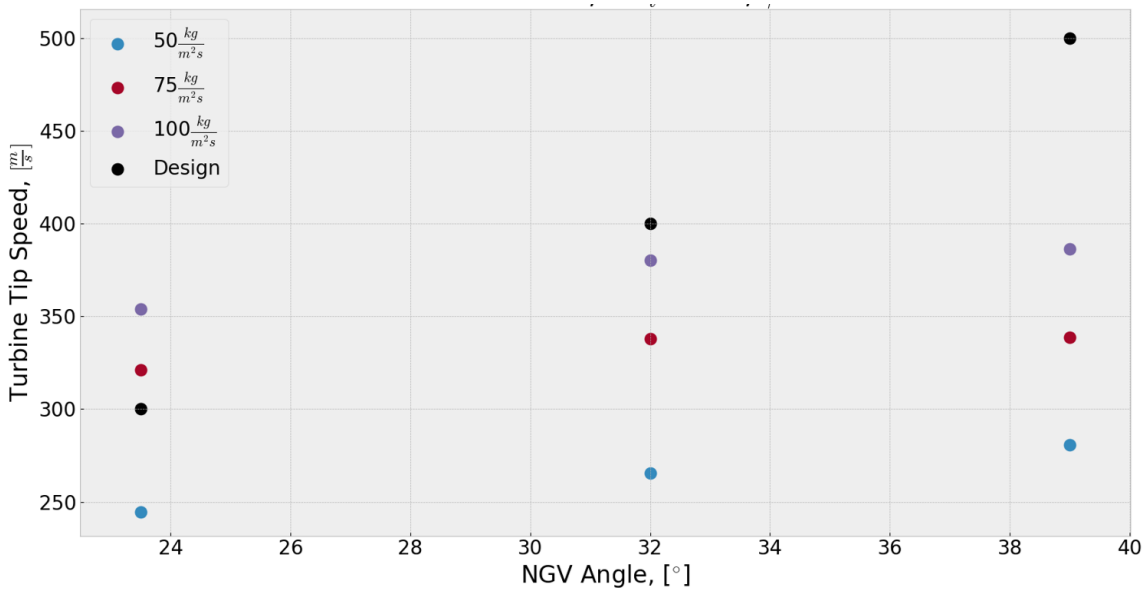

Figure 116. Turbine RPM vs Flow Turning Angle: Turbine Channel, AR_t = 0.2, ϕ = 0.5.

RPM of the NGV ring cascades. These results are shown in Figure 116, and it can be seen that the design RPM seldom matched the actual RPM of the turbine. At the two lower NGV turning angles of 23.5° and 32.0°, the actual RPM was close to the designed RPM in certain flow cases; however, at the highest NGV turning angle, the actual RPM was less than 80% of the design RPM. This is most likely caused by the conditions in the channel upstream of the NGV cascade did not match the conditions prescribed during the design of the NGV rings. There could also have been other interactions with the detonation wave and the NGV cascade that are not well understood.

4.6.2 Mass Flux Variation.

Examination of the effects of varied mass flux on the two APU performance parameters, specific power and thermal efficiency, was conducted. These tests were conducted as mass fluxes of 50, 75, and 100 $\frac{\text{kg}}{\text{m}^2\text{s}}$. These values were selected in an attempt to match the flow conditions of the stand alone Radial RDE. The 100 $\frac{\text{kg}}{\text{m}^2\text{s}}$mass flux was set as the maximum because it also corresponded to the maximum operational mass flow rate for the turbocharger. Equation 13 hinted at the correlation between the mass flow rate of rotating turbo-machinery and the power extracted from the device, so it would be expected that the power output from the turbine would increase as the mass flow increase. This is the reasoning behind normalizing the power by the input mass flow and comparing the specific power of the turbine for analysis.

Figure 117 shows the effects of varying the mass flux on the specific power extracted from the turbine at an equivalence ratio of 0.5. This relationship was shown at the three NGV turning angles of 23.5°, 32.0°, and 39.0° (blue, maroon, and purple, respectively). From this plot, it is clear that increasing the mass flux through the RRDE increased the work extracted from the turbine. This is due to an increase in the velocity of the flow, which would apply a larger force pushing on the on the blades of the turbine, thereby increasing the force being applied to the turbocharger shaft. This increase in the applied force corresponds to an increase in the torque on the turbocharger shaft, and an increase in the power output by Equation 63 and was also included in the discussion from Section 3.2.1.1 with reference to the mass flow rate.

$$\dot{W}_s = \frac{2\pi}{60}\tau RPM \tag{63}$$

where $\dot{W}_s$ is the shaft power and τ is the torque applied to the turbocharger shaft.

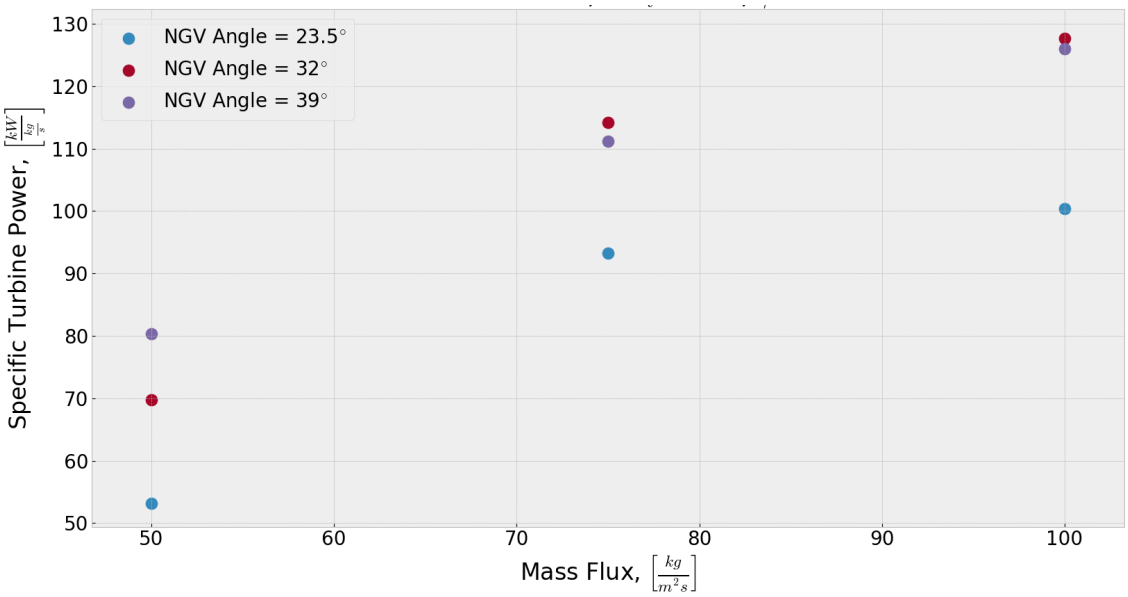

Figure 117. Turbine Power vs Mass Flux: Turbine Channel, $AR_t = 0.2$, $\phi = 0.5$.

Figure 118 shows the thermal efficiency of the same points from Figure 117. This plot shows that with an increase in mass flux there is also an increase in thermal efficiency; however, the slope of these lines decrease as the mass flux was increased. This would indicate a maximum thermal efficiency would occur at a higher mass flux for these configurations at this equivalence ratio. It should be noted that at the mass fluxes of 75 and 100 $\frac{\text{kg}}{\text{m}^2\text{s}}$, the thermal efficiency of the RRDE was roughly the same for the 32° and 39° NGV turning angles.

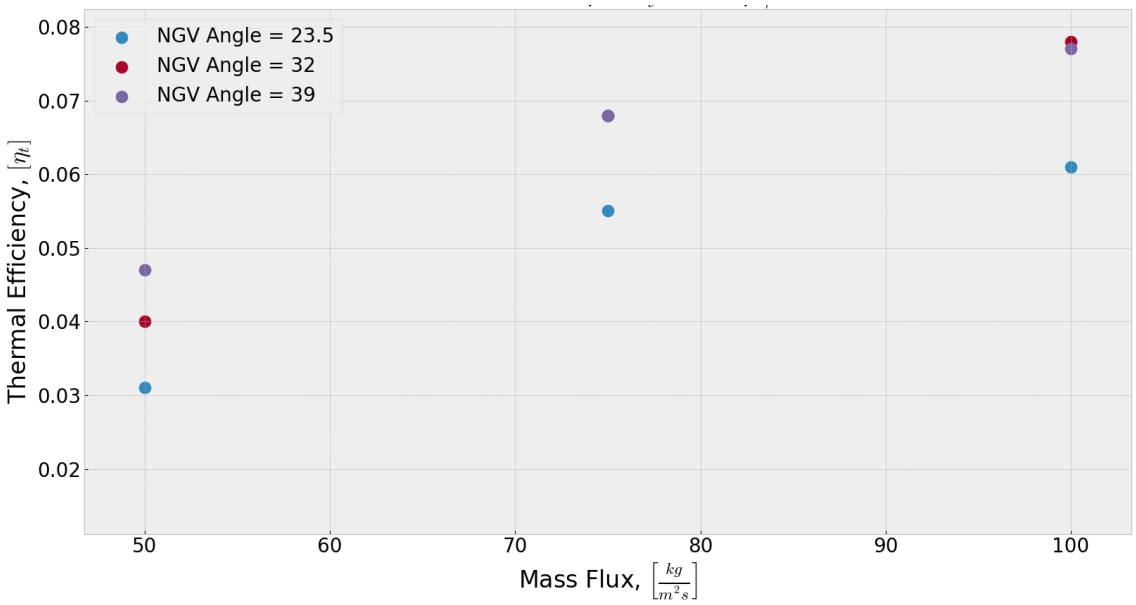

Figure 118. Thermal Efficiency vs Mass Flux: Turbine Channel, $AR_t = 0.2$, $\phi = 0.5$.

The results of this section indicated that as the mass flux was increased the specific power output and thermal efficiency of the APU also increased. This result was expected based on formulations of power output of other turbo-machines. Further increases in mass flux should increase the specific power output; however, logic dictates there would be maximum specific power the turbine can output based on its size and maximum operating RPM.

4.6.3 Equivalence Ratio Variation.

Next, the effects of varying the equivalence ratio of the APU was examined. These tests were conducted at an equivalence ratio of 0.5 and 0.6, which was kept low to mitigate the post detonation temperatures the turbine blades would face and increase survivability. Figure 119 shows the specific power versus equivalence ratio plotted for all of the mass fluxes at the 39.0° NGV turning angle. This plot was typical for the rest of the NGV ring configurations and shows a slight increase in work as the equivalence ratio was increased. This result is expected due to the increase in

channel temperature and pressure as the equivalence ratio increased. This channel temperature was not calculated but detonation theory provides that an increase in equivalence ratio will increase the post detonation temperature. Due to the roughly constant volume combustion process in detonations, this increase in temperature also increases the pressure in the channel, which could allow the turbine to operate at a higher pressure ratio if it were expanding to the same exit conditions.

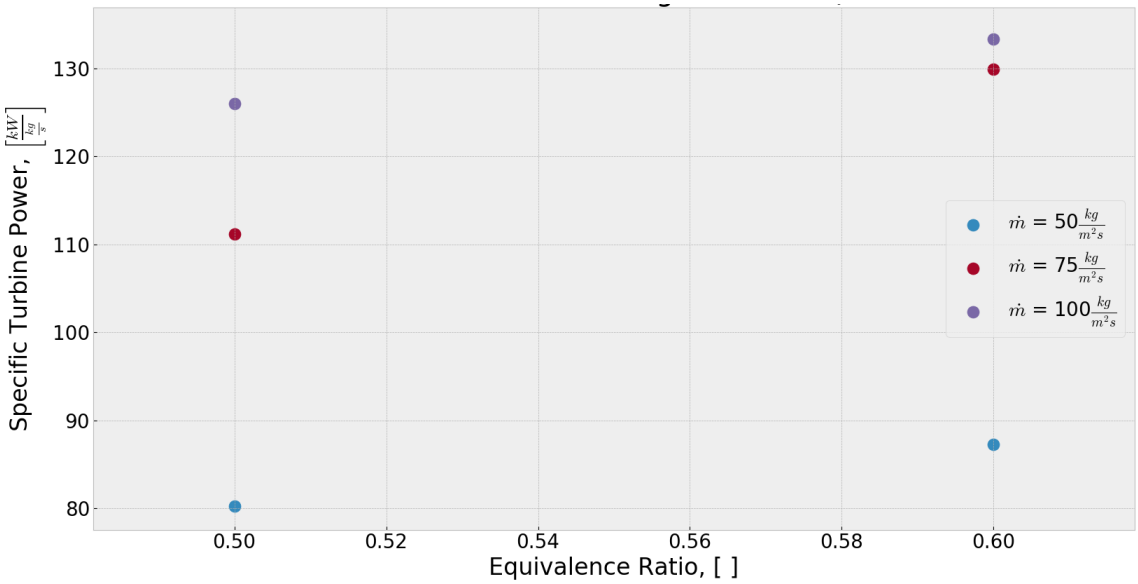

Figure 119. Turbine Power vs Equivalence Ratio: Turbine Channel, AR_t = 0.2, NGV Angle = 39.0°.

Figure 120 shows a plot of the thermal efficiency from the same points shown in Figure 119. At the two lower mass fluxes, changing the equivalence ratio slightly decreased the thermal efficiency. At the higher mass flux an increase in the equivalence ratio from 0.5 to 0.6 saw a significant decrease in thermal efficiency. From Figure 119, it was clear that at the 100 $\frac{\text{kg}}{\text{m}^2\text{s}}$mass flux the work did not significantly increase as the equivalence ratio increased. As the equivalence ratio increased, the fuel flow increased providing more thermal energy available from combustion. This caused the thermal efficiency to drop because there was a disproportionate increase in thermal

energy relative to the power output of the turbine. This could suggest the turbine is exhausting a large amount of usable energy as waste.

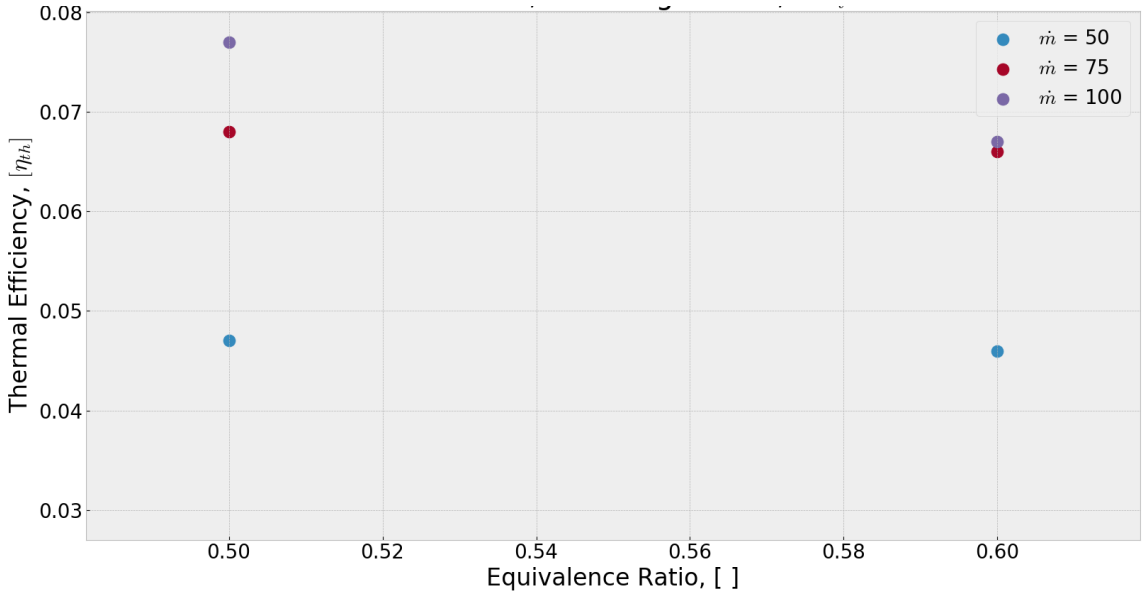

Figure 120. Thermal Efficiency vs Equivalence Ratio: Turbine Channel, AR_t = 0.2, NGV Angle = 39.0°.

4.6.4 Turbine Damage Assessment.

The post detonation environment is highly unsteady and provides high heat loads to the detonation engines. When coupling a detonation engine, like the Radial RDE, to a turbine, concerns arise with the survivability of the turbine because it was rotating at 100+ kRPM. This section will examine the effects of operating a turbine behind the exhaust of the RRDE and the damages seen after multiple runs.

Figure 121 shows a run with the turbocharger turbine. This figure shows the pre-ignition conditions where the turbine was being driven by air, (a). When the RRDE was ignited there was a period of deflagration (b) combustion before the detonation wave had established, (c). The turbine then came up to a steady state operating RPM and started to heat up and glow red hot, (d). Although the turbocharger was spun

up to a steady RPM with the initial air flow, when the detonation ignited the RPM jumped by 200-300%. This rapid acceleration put a large amount of stress on the bearings in the turbocharger; however, examination of the turbocharger between runs did not reveal any noticeable damage to these bearings. The only damage noticed during real time operation was the occasional spark ejected out in the RRDE exhaust, shown by the faint yellow streaks in the white box in (b). From this camera angle, the cause of the sparks was unknown.

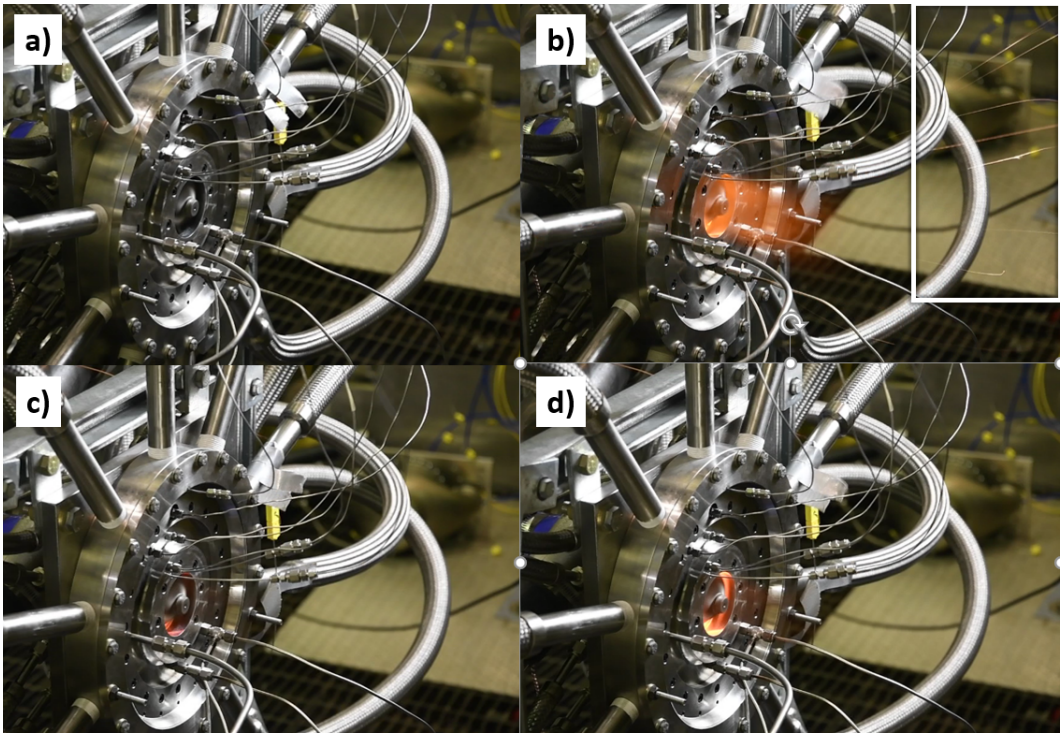

Figure 121. Turbine Operation Screenshots.

Figure 122 shows high speed imaging of the turbine operation. This figure shows the steady operation on the air flow, (a), the ignition of the RRDE, (b), the deflagration mode with the plume exiting the turbine, (c), and the detonation operation at select points throughout the run, (d - g). These latter figures highlight the increase in heating of the turbine blades. This camera angle also allowed for the determination of the origin of the sparks during previous runs. There was a select spot where the

turbine was rubbing against the exit of the RRDE, (d & e), with a spark exiting from that location shown in (e).

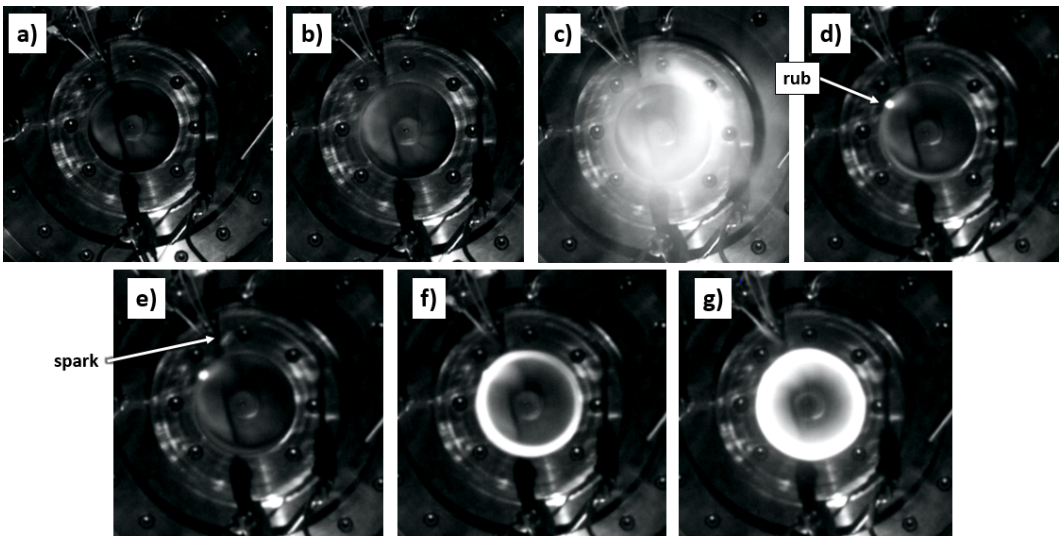

Figure 122. Turbine Operation Highspeed Video Screenshots. (captured at 4 kHz)

Figure 123 shows the examination of the turbine channel exit after the sparks were noticed. This shows the spot where the rotor was contacting the channel. Examination of this spot revealed ridges sticking out of the stainless channel. It is suspected that these ridges were what the turbine was rubbing against. Before additional turbine testing was conducted, these ridges were sanded smooth to prevent further damage.

Figure 124 shows the turbine blades after the sparks were noticed. This revealed a small band of damage on the blades in the same location where the ridges appeared on the turbine channel exit. These areas of damage were also sanded smooth to minimize addition rubbing. There was also noticeable discoloration of the turbine blades along the tips of the blades. This is to be expected when after successive operation of the turbine.

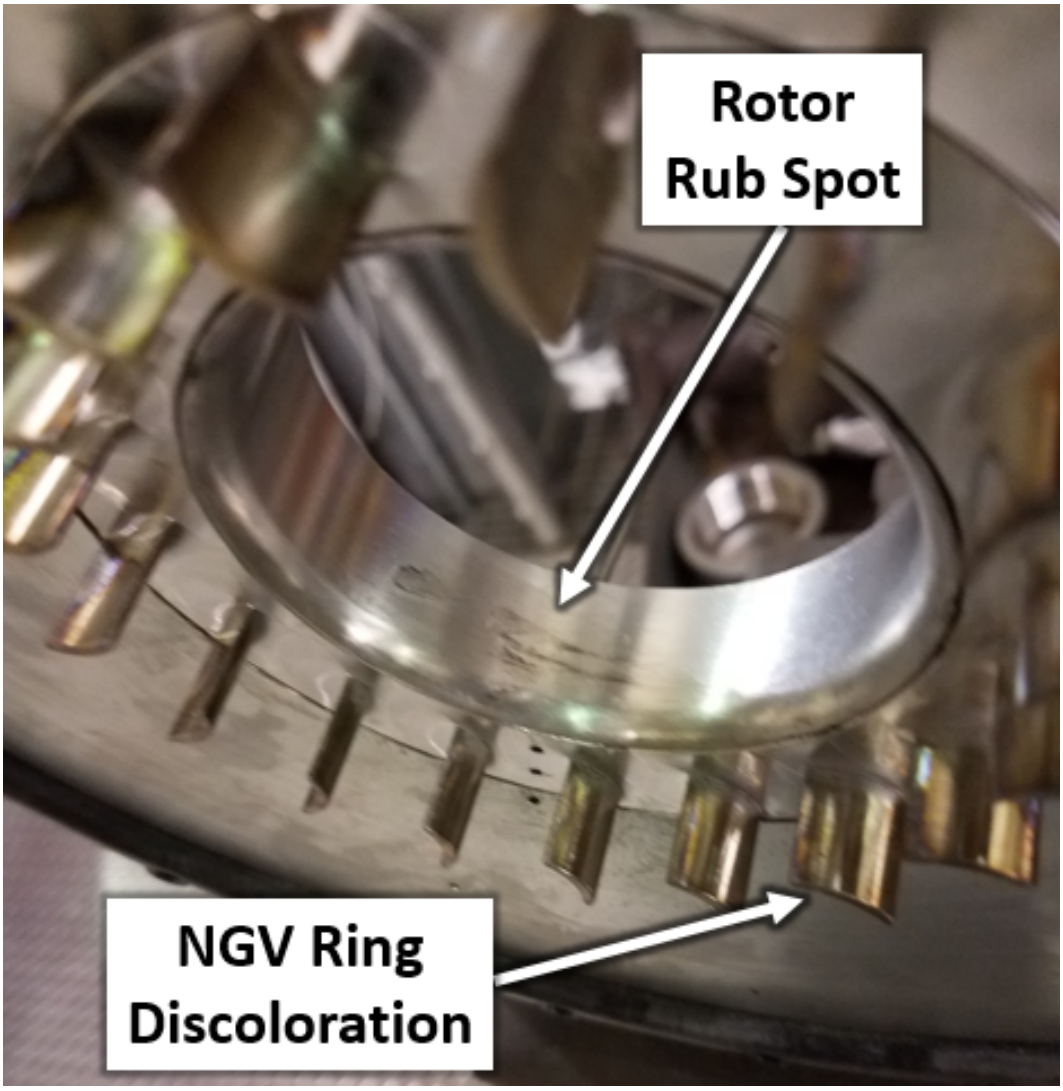

Figure 123. Damage to Turbine Channel Plate Exit from Rubbing.

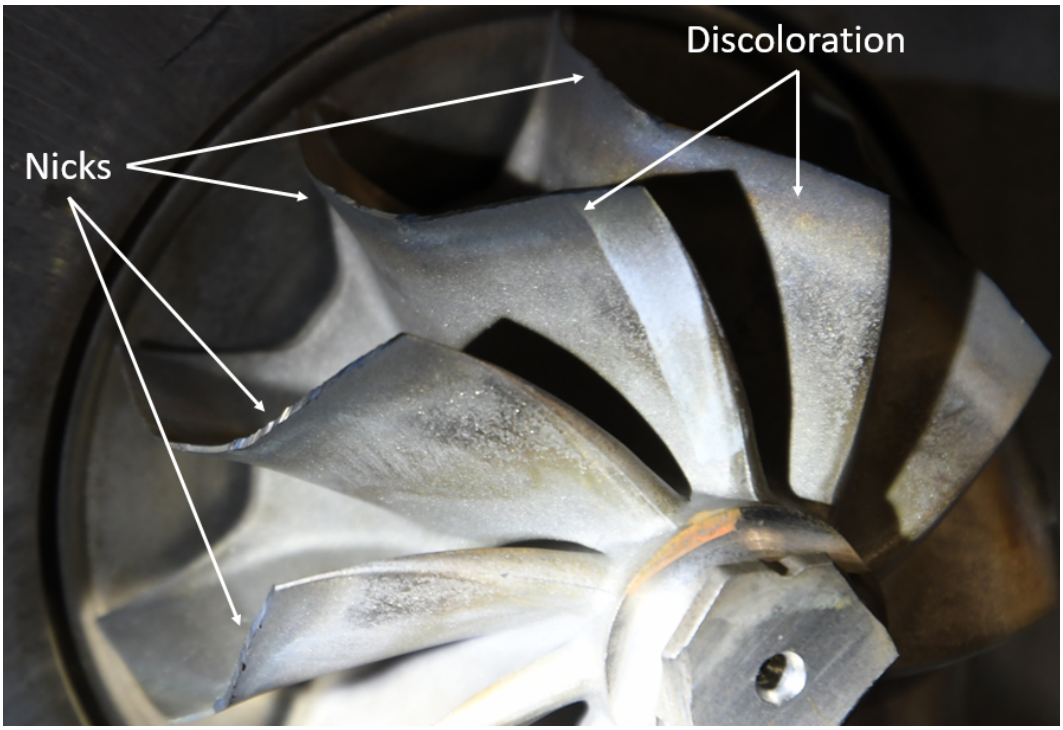

Figure 124. Damage to Turbocharger Turbine from Rubbing.

Figure 125 shows infrared imaging of the RRDE during operation. This camera was not calibrated so the exact temperature was unknown but the magnitude of the temperature difference during the run is highlighted. Though the exact temperature were not know the ambient conditions before the RRDE ignition was roughly 300 K while a thermocouple in the exhaust flow of the turbine measured exhaust temperatures of roughly 1250 K. This figure shows the RRDE before the run was started, (a), the start of the air flow, (b), the pre-ignition condition, (c), the ignition, (d), detonation operation, (e), max turbine temperature, (f), fuel cutoff, (g), blowdown, (h), and the end of the run, (i). This figure highlights the heat that is being imparted onto the turbine blades during the run. This high heat loading could lead to increased fatigue of the turbine blades for longer duration operation. Also, these large swings in operating temperature could also fatigue the turbine, leading to a reduced operating life.

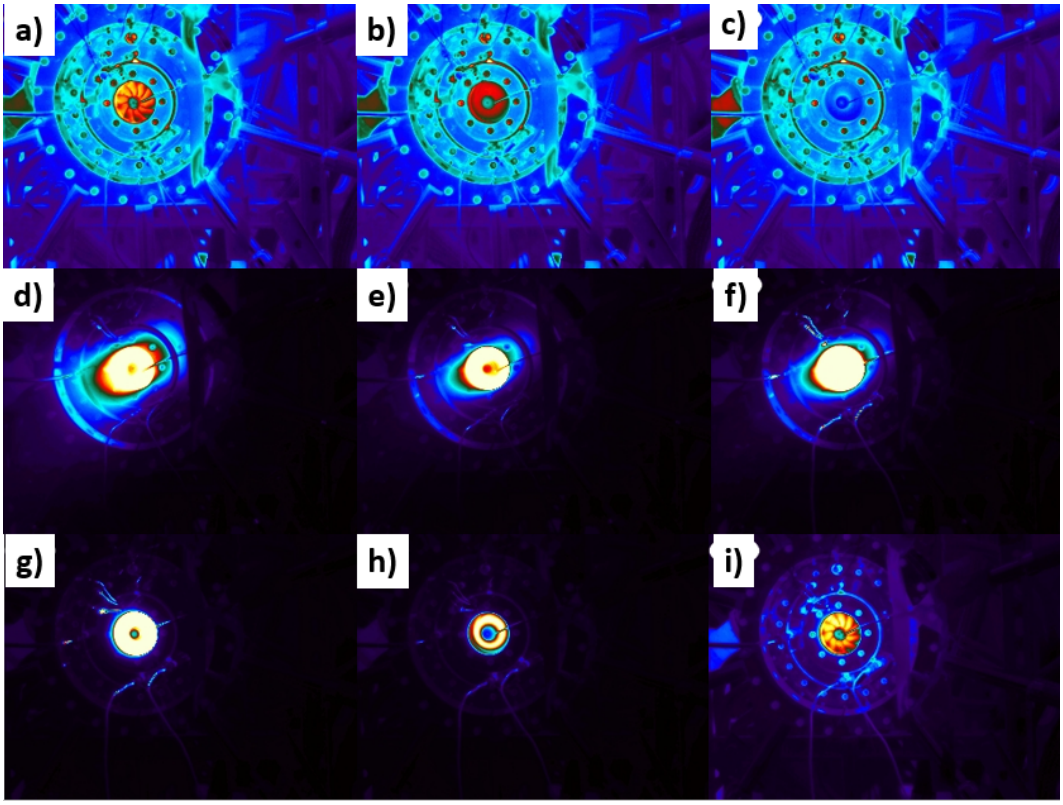

Figure 125. IR Turbine Operation Video Screenshots. (captured at 10 Hz)

After nearly 30 seperate runs, the turbine appeared to operate as expected, with only minor damage to the blade tips from slight rubbing. This could be prevented by higher precision machining and improved designing of the channel plate which housed the turbine. Tight clearances must be used to maximize the power extraction from the turbine, so any slight defect could cause the rubbing that was seen during operation. Another worry was the sharp increases in RPM that the turbine would see during operation, which were as much as 200% increase in PRM over a time frame of 0.1-0.2 s. Despite these rapid accelerations the bearing assembly continued to operate without any noticeable damage. These results give confidence that the APU can be operated repeatably without significant damage to the device.

4.6.5 Turbine Performance.

To determine the efficacy of the Radial RDE APU, it was necessary to compare it to commercial APUs in use today. This comparison was done using parameters: power density, APU specific power, thermal efficiency and turbine specific power. The power density relates the power output of the device to its overall volume and is given by Equation 64 and will be displayed with units of $\frac{\text{kW}}{\text{L}}$:

$$Power\ Density = \frac{\dot{W}_{out}}{V_{APU}} \tag{64}$$

where $\dot{W}_{out}$ is the output power of the APU and V_{APU} is the total volume of the APU. The APU specific power relates the mass of the APU and the APU's power output, and it is given by Equation 65 and shown with units of $\frac{\text{kW}}{\text{kg}}$:

$$APU\ Specific\ Power = \frac{\dot{W}_{out}}{m_{APU}} \tag{65}$$

where m_{APU} is the mass of the APU.

To compare the RRDE APU, the highest power output configuration was examined and its thermal efficiency was used to avoid skewing the data. This test case was conducted at a mass flux of 100 $\frac{\text{kg}}{\text{m}^2\text{s}}$, an equivalence ratio of 0.6, and using the 32.0° NGV turning angle. The power output was 69.5 kW, which was a specific power of 152.6 $\frac{\text{kW}}{\frac{\text{kg}}{\text{s}}}$ for the turbine, and had a thermal efficiency of 7.7%. The volume of the RRDE was 5.56 L and was estimated using the maximum radius and total height of the device. The mass of the RRDE APU was 41 kg and was estimated by subtracting the rough flow volume of the RRDE from the total volume, and multiplying the result by the density of stainless steal and then adding the mass of the turbocharger. It should be noted that the volume and mass of the RRDE would be underestimated due to the need of oil supply and the generator needed for sustained runs and the conversion of shaft power to electrical power. With these dimensions, the power density of the APU was 12.5 $\frac{\text{kW}}{\text{L}}$ and the APU specific power was 1.70 $\frac{\text{kW}}{\text{kg}}$.

The APUs used for comparison are shown in Table 7, and their performance is shown (if known). From this table is is clear that the RRDE offers a significant advantage in power density over the gas turbine APU. This advantage varied between 500 and 2000% compared to the other APUs. This is a significant reduction in the power density of the APUs, which was one of the main benefits of a detonation engine APU. The APU specific power of the RRDE was on the order of that of the other APUs. This was due to the large factors of safeties designed into the RRDE for lab testing, and the fact that it was designed for modularity. A reduction in weight would be expected for future design iterations, that would also correspond to an increased APU power density. The thermal efficiency of the RRDE was much lower that the thermal efficiencies of the other APUs. There were numerous reasons this may have occurred, including the flow may have significantly more availible work that is exhausted out of the turbine, using a commercial turbine designed for automotive uses, improper spacing, turning angle, and vane number in the NGV cascade, and the turbine exhaust has a noticeable radial component as it exits the turbine, which harms turbine performance. Solutions to these issues could increase the RRDE APU thermal efficiency to be on the order of the gas turbine APU efficiencies. Finally, the turbine specific power for the RRDE APU is greater than the conventional APUs. This result was expected due to the roughly constant volume detonation cycle.

Table 7. Performance Data of Commercial APUs.

APU	Power Density, $\left[\frac{kW}{L}\right]$	APU Specific Power, $\left[\frac{kW}{kg}\right]$	Thermal Efficiency, [ ]	Turbine Specific Power, $\left[\frac{\frac{kW}{kg}}{s}\right]$
Honeywell 36-155 [43]	0.37	1.11	-	120.8
PW 206 [44]	1.89	3.89	23.4%	-
PW 207 [44]	2.20	4.27	27.2%	-
T62-32 [45]	0.61	1.85	-	119.6

These results not only accomplished creating the first ever detonation engine powered APU, but the also showed the efficacy of this device and its improvements over

conventional APUs. The testing and characterizing of the RRDE APU also achieved the third and final objective of this project. However, addition improvements to the RRDE will be needed to further this development and implementation of this device.

V. Conclusion

This project endeavored to create a compact, energy dense, rapid response Auxiliary Power Unit with the capability of powering high output, airborne directed energy weapons. This new APU would need to meet size constraints for a fighter class aircraft. Years of continued research on Pressure Gain Combustion devices, especially Detonation Engines, provided the inspiration for such a device; however, a new flow scheme was needed for this project to assist with creating a more compact device that more easily pairs with a radial inflow turbine. This project serves as the first attempt at testing this novel layout in the United States. Design of a Radial Rotating Detonation Engine that met the constraints set by the size of the turbine and the overall size of the device was the first objective of this project. This goal was achieved through multiple design iterations, with the final design being presented in this project. The new Radial RDE was also designed in a modular fashion that would allow for multiple test configurations and enabled the installation of the turbine without additional modification to the RRDE. Finally, this device served as a testbed for the novel radial inward RDE flow path, and facilitates continued research into the operation of this device with other fuels, injection schemes, and other geometric layouts.

The second research objective for this project was to extensively test the RRDE though a number of configurations and flow conditions. Successful detonation operation of the RRDE was achieved and an operating map was created for this device. Test were conducted on the variation in the height of the detonation channel, the nozzle area ratio, the mass flux through the device, and the equivalence ratio at which the device was operated. These tests showed a nozzle area ratio of 0.6 provided the most competitive operating point for the RRDE, and allowed for a wide range of operability, a reduction in injector pressure loss, and an increase in wave speed and wave number over the other nozzle conditions. The results also showed higher mass

fluxes and lower equivalence ratios allowed the detonation wave to transition to higher wave numbers; however, in order to reduce the pressure loss through the injector a lower mass flux was required. This leads to design tradeoffs that should be taken into account for future designs and for testing with the turbine.

Section 4.3 examined the effects of varying the channel height of the RRDE and showed the two shorter channel heights of 3.5 and 4.0 mm allowed the RRDE to operate in regimes that would not detonate with the larger, 4.5 mm channel. Section 4.4 discussed the variance in nozzle area ratio and its effect on the RRDE. In terms of wavespeed, there was a clear improvement when adding back pressure to the RRDE through the used of a more restrictive nozzle. There also appeared to be an optimal nozzle area ratio of 0.6 that allowed for the highest wave number, highest wavespeed, and lowest pressure performance of all of the nozzle configurations of the RRDE.

Finally, Section 4.5 showed the operating map created for the RRDE at certain configurations and also the condensed detail of the mass flux and equivalence ratio sweeps that were conducted. These results showed a clear preference in the higher mass fluxes and lower equivalence ratios in terms of increasing wave number. An increase in equivalence ratio also showed an increase in wavespeed for a given wave number, which was expected based on detonation theory. Another trend was shown that as the mass flux and equivalence ratio were decreased, so was the pressure loss through the injection of this device. This may have been caused by a recirculation zone that was formed by the backward facing step of the air injector. As the mass flux through the injector increased so to would the size and strength of this recirculation zone, which would be beneficial for the mixing of the reactants but would negatively effect the pressure losses in the device.

A wide range of testing on the RRDE as a stand alone detonation engine provided insight into the efficacy of the device as a combustor. Overall this device performed in

a similar fashion to conventional RDEs but it also had some unforeseen operational characteristics. The first major difference in the operation of the RRDE was the fact that the location of the detonation wave may have shifted dramatically between runs and configurations. In a conventional RDE the radial location of the wave is constrained within the inner and outer body of the channel, which were only separated a few mm at most; however, the detonation waves in the RRDE were allowed to vary in radial location between the injector face and the nozzle exit. This gave the detonation wave roughly 7 cm of play. Since the measurement technique used to estimate wavespeed relied on the frequency of the high speed pressure transducers, the precise location of the detonation wave was needed to determine the exact wavespeed. This leads to trends discussed in the project such as the wave number normalized wavespeed dropping significantly when the device transitions to a higher wave number, which is thought to push the wave out to a further radius.

Because the exact location of the detonation waves were unknown, the wavespeeds presented were referenced to the what the wavespeed would be at the location where the high speed pressure measurements were taken. More investigation into the location of the detonation wave will provide additional insight into the operation of the RRDE and assist with improving performance of the device. Should the detonation wave be able to adjust the location at which it propagates with the RRDE, this could mean that the RRDE may offer improved operation over its annular counterparts.

The third, and final, objective for this project was to couple the Radial RDE with a radial inflow turbine and measure the power and efficiency of the device. This testing involved using an off the shelf, Garrett GT3582R automotive turbocharger and a specially designed channel plate that allowed for the use of multiple Nozzle Guide Vane configurations. Testing was done at a range of mass fluxes, equivalence ratios, and NGV turning angles. These results showed a clear trend that increased

mass flux produced more power, more efficiently. However, examination of the specific power showed a diminishing returns as the mass flow was increased. Variation in the equivalence ratio revealed a slight increase in power with an increase in equivalence ratio, but a decrease in thermal efficiency due to the disproportionate increase in the energy released from combustion over the increase in power extracted from the flow. Finally, examination of the nozzle guide vane variation showed an optimal flow turning angle existed based on the flow conditions within the channel. This was due to the nozzle guide vanes being designed for an arbitrary flow condition selected before the actual flow conditions within the RRDE were known.

Overall, the Radial RDE APU produced a maximum of almost 70 kW of power with an efficiency of 7.7%. It is important to note that this power was fully available less than 200 ms after ignition of the RRDE, giving nearly instant power. The maximum power output achieved with the RRDE APU gave it a volumetric power density of 12.6 $\frac{\text{kW}}{\text{L}}$ and a power to weight ratio of 1.71 $\frac{\text{kw}}{\text{kg}}$. These numbers were based on the volume of the stand alone RRDE and the mass of the RRDE and turbocharger only. When compared to other APUs of similar power output, this device offers nearly a $10x$ improvement in power density while achieving a similar power to weight ratio, all while being a first iteration of this novel detonation engine.

These initial results were promising, but there exists much room for improvement. First, the RRDE designed in this project was designed to be a testbed for research, not a finished product ready for installation. This led to a gross safety margin and a non-optimized design which could become much lighter and much more compact. Next, the turbine was an off the shelf part design for the flow conditions exiting an automotive internal combustion engine. A turbine designed for the flow conditions of the RRDE exhaust could lead to a significant improvement in the efficiency of the power extraction.

Another improvement exists with the design of the nozzle guide vanes. The geometry, spacing, and number of vanes could be optimized for the flow exiting the channel of the RRDE, with the effects of the oblique shock interacting with the vanes taken into consideration. This could lead to more power and a more efficient extraction process. The easiest improvement to make to the RRDE is to insure the exit flow of the turbine remains axial, which will improve the turbine performance, because initial results shows free expansion out of the turbine with a significant radial component. This also suggested there was more energy available in the flow that was being exhausted out of the turbine. Though it could harm the compactness of the device, additional turbine stages may be needed to see this device achieve more power and higher efficiencies.

With the data presented in this project, the RRDE offers the feasibility of a more compact APU that provides on demand power to fighter sized aircraft. The power density and the response time of this device already outclasses conventional APUs in use today, with the possibility of an improvement in power to weight with subsequent improvements in the design. Though this device is far from optimized, it has the potential to drastically reduce the size and weight of aircraft APUs in the aerospace realm, where more usable volume means more payload and weight savings equal fuel savings. This project opens the door for the possibility of a detonation engine based APU with a revolutionary improvement in the way aircraft are powered.

Bibliography

1. Fotia, M., Hoke, J., and Schauer, F., "Experimental Study of the Response of Capillary Tube Attenuated Pressure Measurements to High Amplitude, Non-Linear Forcing," *2018 AIAA Aerospace Sciences Meeting*, No. AIAA 2018-0634, 2018.

2. Bussing, T. and Pappas, G., "An Introduction to Pulse Detonation Engines," No. AIAA 1994-263, 1994.

3. Vutthivithayarak, R., Braun, E. M., and Lu, F. K., "Examination of the Various Cycles for Pulse Detonation Engines," No. AIAA 2011-6064, 2011.

4. Turns, S. R., *An Introduction to Combustion Concepts and Applications*, McGraw-Hill, New York, 2nd ed., 2000.

5. Kuo, K. K., *Principles of Combustion*, John Wiley & Sons, Inc, New Jersey, 2nd ed., 2005.

6. Babbie, C. A., King, P., Hoke, J., and Schauer, F., "Effect of Elevated Mixture Pressure and Equivalence Ratio on Hydrogen-Air Detonation Cell Size," *54th AIAA Aerospace Sciences Meeting*, No. AIAA 2016-0442, 2016.

7. Ciccarelli, G., Ginsburg, T., Boccio, J., Economos, C., Finfrock, C., Gerlach, L., Sato, K., and Kinoshita, M., "High-Temperature Hydrogen-Air- Steam Detonation Experiments in the BNL Small-Scale Development Apparatus," *NUREG/Cr-6213 BNL-NUREG-42414* , 1994.

8. Breitung, W., Chan, C., Dorofeev, S., Eder, A., Gelfand, B., Heitsch, M., Klein, R., Malliakos, A., Shepherd, E., Studer, E., and Thibault, P., "Flame Acceleration and Deflagration-to-Detonation Transition in Nuclear Safety," Tech. Rep. NEA/CSNI/R(2000)7, OECD Nuclear Energy Agency State-of-the-Art Report, 2000.

9. New, T. H., Panicker, P. K., Lu, F. K., and Tsai, H. M., "Experimental Investigations on DDT Enhancements by Shchelkin Spirals in a PDE," *44th AIAA Aerospace Sciences Meeting and Exhibit*, No. AIAA 2006-552, 2006.

10. Knox, B. W., Forliti, D. J., Stevens, C. A., Hoke, J. L., and Schauer, F. R., "A Comparison of Fluidic and Physical Obstacles for Deflagration-to-Detonation Transition," *49th AIAA Aerospace Sciences Meetign*, No. AIAA 2011-587, 2011.

11. Rankin, B. A., Fotia, M. L., Naples, A. G., Stevens, C. A., Hoke, J. L., Kaemming, T. A., Theuerkauf, S. W., and Schauer, F. R., "Overview of Performance, Application, and Analysis of Rotating Detonation Engine Technologies," *Journal of Propulsion and Power*, Vol. 33, No. 1, Jan 2017, pp. 131–143.

12. Hoffman, N., "Reaction Propulsion by Intermittent Detonative Combustion," *German Ministry of Supply, Volkenrode Translation*, Vol. 1, No. 1, 1940.

13. Nicholls, J. A., Wilkinson, H. R., and Morrison, R. B., "Intermittent Detonation as a Thrust-Producing Mechanism," *Journal of Jet Propulsion*, Vol. 27, No. 5, 1957, pp. 534–541.

14. Schauer, F., Stutrud, J., and Bradley, R., "Detonation Initiation Studies and Performance Results for Pulsed Detonation Engine Applications," *39th Aerospace Sciences Meeting and Exhibit*, No. AIAA 2001-1129, 2001.

15. Shank, J., King, P., Karnesky, J., Schauer, F., and Hoke, J., "Development and Testing of a Modular Rotating Detonation Engine," *50th AIAA Aerospace Sciences Meeting including the New Horizons Forum and Aerospace Exposition*, No. AIAA 2012-120, 2012.

16. Dyer, R., Naples, A. G., Kaemming, T. A., Hoke, J. L., and Schauer, F. R., "Parametric Testing of a Unique Rotating Detonation Engine," *50th AIAA Aerospace Sciences Meeting including the New Horizons Forum and Aerospace Exposition*, No. AIAA 2012-121, 2012.

17. Schwer, D. A. and Kailasanath, K., "Numerical Investigation of Rotating Detonation Engine," *46th AIAA/ASME/SAE/ASEE Joint Propulsion Conference & Exhibit*, No. AIAA 2010-6880, 2010.

18. Cullen, R. E., Nicholls, J. A., and Ragland, K. W., "Feasibility studies of a rotating detonation wave rocket motor." *Journal of Spacecraft and Rockets*, Vol. 3, No. 6, 1966, pp. 893–898.

19. Viotsehkovsky, B. V., "Stationary Spin Detonation," *Soviet Journal of Applied Mechanics and Technical Physics*, Vol. 3, 1960, pp. 157–164.

20. Bykovskii, F. A., Mitrofanov, V. V., and Vedernikov, E. F., "Continuous Detonation Combustion of Fuel-Air Mixtures," *Combustion, Explosion, and Shock Waves*, Vol. 33, No. 3, 1997, pp. 344–353.

21. Suchocki, J. A., Yu, S.-T. J., Hoke, J. L., and Naples, A. G., "Rotating Detonation Engine Operation," *50th AIAA Aerospace Sciences Meeting including the New Horizons Forum and Aerospace Exposition*, No. AIAA 2012-119, 2012.

22. Fotia, M. L., Schauer, F., Kaemming, T., and Hoke, J., "Experimental Study of the Performance of a Rotating Detonation Engine with Nozzle," *Journal of Propulsion and Power*, Vol. 32, No. 3, May 2016, pp. 674–681.

23. Fotia, M. L., Hoke, J., and Schauer, F., "Experimental Performance Scaling of Rotating Detonation Engines Operated on Gaseous Fuels," *Journal of Propulsion and Power*, Vol. 33, No. 5, Mar 2017, pp. 1–10.

24. Nakagami, S., Matsuoka, K., Kasahara, J., Kumazawa, Y., Fujii, J., Matsuo, A., and Funaki, I., "Experimental Visualization of the Structure of Rotating Detonation Waves in a Disk-Shaped Combustor," *Journal of Propulsion and Power*, Vol. 33, No. 1, 2016, pp. 1–9.

25. Higashi, J., Nakagami, S., Matsuoka, K., Kasahara, J., Matsuo, A., Funaki, I., and Moriai, H., "Experimental Study of the Disk-Shaped Rotating Detonation Turbine Engine," *55th AIAA Aerospace Sciences Meeting*, No. AIAA 2017-1286, 2017.

26. Naples, A. G., Hoke, J., Battelle, R. T., Wagner, M., and Schauer, F. R., "RDE Implementation into an Open-Loop T63 Gas Turbine Engine," *55th AIAA Aerospace Sciences Meeting*, No. AIAA 2017-1747, 2017.

27. Rouser, K. P., King, P. I., Schauer, F. R., Sondergaard, R., and Hoke, J. L., "Unsteady Performance of a Turbine Driven by a Pulse Detonation Engine," *48th AIAA Aerospace Sciences Meeting Including the New Horizons Forum and Aerospace Exposition*, No. AIAA 2010-1116, 2010.

28. Rouser, K. P., King, P. I., Schauer, F. R., Sondergaard, R., and Hoke, J. L., "Performance Evaluation of an Unsteady Turbine Driven by a Pulsed Detonation Combustor," *Proceedings of ASME Turbo Expo 2011*, No. GT2011-45396, 2011.

29. Glaser, A. J., Caldwell, N., and Gutmark, E., "Performance of an Axial Flow Turbine Driven by Multiple Pulse Detonation Combustors," *45th AIAA Aerospace Sciences Meeting and Exhibit*, No. AIAA 2007-1244, 2007.

30. Tellefsen, J., *Build Up and Operation of an Axial Turbine Driven by a Rotary Detonation Engine*, Master's thesis, Air Force Institute of Technology, 2012.

31. DeBarmore, N. D., King, P. I., Schauer, F. R., and Hoke, J. L., "Nozzle Guide Vane Integration into Rotating Detonation Engine," *AIAA Aerospace Sciences Meeting including the New Horizons Forum and Aerospace Exposition, 51st*, No. AIAA 2013-1030, 2013.

32. Glassman, A. J., Whitney, W. J., Stewart, W. L., Katsanis, T., McNally, W. D., Prust, H. W., Roelke, R. J., Goldman, L. J., Rohlik, H. E., Colladay, R. S., Szanca, E. M., and Schum, H. J., "Turbine Design and Application," Tech. Rep. 290, 1994.

33. Mattingly, J. D., *Elements of Propulsion Gas Turbines and Rockets*, The American Institute of Aeronautics and Astronautics, Inc., Reston, Virigina, 2nd ed., 2006.

34. Reichert, A. W. and Simon, H., "Design and Flow Field Calculations for Transonic and Supersonic Radial Inflow Turbine Guide Vanes," *Journal of Turbomachinery*, Vol. 119, No. 1, 1997, pp. 103.

35. Stevens, C. A., Fotia, M. L., Hoke, J. L., and Schauer, F. R., "Comparison of Transient Response of Pressure Measurement Techniques with Application to Detonation Waves," *AIAA Aerospace Sciences Meeting*, No. AIAA 2015-1102, 2015.

36. Englund, D. R. and Richards, W. B., "The Infinite Line Pressure Prod," Tech. Rep. 83582, 1984.

37. Naples, A., Hoke, J. L., and Schauer, F. R., "Quantification of Infinite Line Pressure Probe Response to Shocks and Detonation Waves," *2018 AIAA Aerospace Sciences Meeting*, No. AIAA 2018-1886, 2018.

38. Andrus, I. Q., King, P. I., Polanka, M. D., Schauer, F. R., and Hoke, J. L., "Design of a Premixed Fuel-Oxidizer System to Arrest Flashback in a Rotating Detonation Engine," *Journal of Propulsion and Power*, Vol. 33, No. 5, 2017.

39. Garrett, "Product Catalogue," Vol. 6, 2016.

40. Aungier, R., "TurbAero," 2006, Computer Program.

41. Moffat, R. J., "Describing the Uncertainties in Experimental Results," *Experimental Thermal and Fluid Science*, Vol. 1, No. 1, 1988, pp. 1–17.

42. Sutton, G. P. and Biblarz, O., *Rocket Propulsion Elements*, John Wiley & Sons, Inc, New York, 7th ed., 2001.

43. Honeywell, "36-155 Auxiliary Power Unit," Tech. Rep. N61-0820-000-000, Honeywell, Phoenix, 2008.

44. Agency, E. A. S., "Type Certificate Data Sheet EA E.017 PW206 & PW207 Series Engines," Tech. Rep. IM.E.017, European Aviation Safety Agency, 2009.

45. Pike, J., "Solar T62 Auxiliary Power Unit," `https://www.globalsecurity.org/military/library/policy/army/accp/al0993/le7.html`, 2005, Accessed: 01-10-2018.

REPORT DOCUMENTATION PAGE

Form Approved
OMB No. 0704–0188

1. REPORT DATE *(DD–MM–YYYY)*	2. REPORT TYPE	3. DATES COVERED *(From — To)*
02–03–2018	Master's Thesis	Sept 2016 — Mar 2018

4. TITLE AND SUBTITLE

DESIGN, BUILDUP AND TESTING OF A RADIAL ROTATING DETONATION ENGINE FOR A COMPACT AXILLARY POWER UNIT

5a. CONTRACT NUMBER

5b. GRANT NUMBER

5c. PROGRAM ELEMENT NUMBER

6. AUTHOR(S)

Riley Huff

5d. PROJECT NUMBER

5e. TASK NUMBER

5f. WORK UNIT NUMBER

7. PERFORMING ORGANIZATION NAME(S) AND ADDRESS(ES)

Air Force Institute of Technology
Graduate School of Engineering and Management (AFIT/EN)
2950 Hobson Way
Wright-Patterson AFB OH 45433-7765

8. PERFORMING ORGANIZATION REPORT NUMBER

AFIT-ENY-MS-18-M-266

9. SPONSORING / MONITORING AGENCY NAME(S) AND ADDRESS(ES)

Air Force Research Lab
5135 Pearson Road, Building 10
Wright-Patterson AFB OH 45433
DSN 255-6619, COMM 937-255-6619

10. SPONSOR/MONITOR'S ACRONYM(S)

AFRL

11. SPONSOR/MONITOR'S REPORT NUMBER(S)

12. DISTRIBUTION / AVAILABILITY STATEMENT

DISTRIBUTION STATEMENT A:
APPROVED FOR PUBLIC RELEASE; DISTRIBUTION UNLIMITED.

13. SUPPLEMENTARY NOTES

14. ABSTRACT

Current power generators consume a large portion of the aircrafts usable volume and they are also extremely heavy for the amount of power that they can produce. Therefore, a need for compact, lightweight Auxiliary Power Units (APU) with high power density has arisen. A novel solution to this problem comes in the form of coupling a Rotating Detonation Engine (RDE) with a turbine generator. A new type of RDE referred to as the Radial Rotating Detonation Engine (RRDE) has been developed to fill this need. This project marks the first radial flow RDE successfully operated in the United States, and also serves as the first instance of this layout being used for power extraction. Operation of the RRDE showed a possible shifting in the location of the detonation wave within the channel, which could improve the operability of the device. Finally, as an APU, the RRDE showed significant increases in power density, up to 10x, over conventional gas turbine based APUs. This development opens up a new opportunity for the Air Force to rapidly generate power with a high power density APU for use in various applications such as airborne directed energy weapons.

15. SUBJECT TERMS

Auxiliary Power Unit, APU, Compact, Detonation, Disk, Engine, Radial, Rotating Detonation Engine, RDE

16. SECURITY CLASSIFICATION OF:			17. LIMITATION OF ABSTRACT	18. NUMBER OF PAGES	19a. NAME OF RESPONSIBLE PERSON
a. REPORT	b. ABSTRACT	c. THIS PAGE			Dr. Marc D. Polanka, AFIT/ENY
U	U	U	U	198	19b. TELEPHONE NUMBER *(include area code)* (405) 922-0504; riley.huff@afit.edu